

# DISSERTATION

---

ZUR ERLANGUNG DES DOKTORGRADES DER NATURWISSENSCHAFTEN

## CLIMATE FORCING ON WATER COLUMN AND SEDIMENTARY ENVIRONMENTS OF AN ANCIENT SEMI-ENCLOSED BASIN: INSIGHTS FROM THE LATE MIOCENE (MESSINIAN) MEDITERRANEAN BASIN

VON MATHIA SABINO  
HAMBURG, 2021

Photo by M. Sabino ©

GUTACHTER:

**PROF. DR. JÖRN PECKMANN**

**PROF. DR. FRANCESCO DELA PIERRE**

---

FAKULTÄT FÜR MATHEMATIK, INFORMATIK UND NATURWISSENSCHAFTEN  
FACHBEREICH ERDSYSTEMWISSENSCHAFTEN, UNIVERSITÄT HAMBURG



# DISSERTATION

---

ZUR ERLANGUNG DES DOKTORGRADES DER NATURWISSENSCHAFTEN

**CLIMATE FORCING ON WATER COLUMN AND SEDIMENTARY  
ENVIRONMENTS OF AN ANCIENT SEMI-ENCLOSED BASIN:  
INSIGHTS FROM THE LATE MIOCENE (MESSINIAN)  
MEDITERRANEAN BASIN**

VORGELEGT VON

**MATHIA SABINO**

AUS TURIN, ITALIEN

AN DER FAKULTÄT FÜR MATHEMATIK, INFORMATIK UND NATURWISSENSCHAFTEN

FACHBEREICH ERDSYSTEMWISSENSCHAFTEN DER UNIVERSITÄT HAMBURG

---

HAMBURG, 2021



Als Dissertation angenommen am Fachbereich Erdsystemwissenschaften

Tag des Vollzugs der Promotion: 26.04.2021

Gutachter: Prof. Dr. Jörn Peckmann  
Prof. Dr. Francesco Dela Pierre

Vorsitzender des Fachpromotionsausschusses  
Erdsystemwissenschaften:

Prof. Dr. Dirk Gajewski

Dekan der Fakultät MIN:

Prof. Dr. Heinrich Graener



## **TABLE OF CONTENTS**

LIST OF PUBLICATIONS	VII
LIST OF ABBREVIATIONS	IX
ABSTRACT	1
KURZFASSUNG	3
CHAPTER 1 INTRODUCTION	6
1.1.    THE MEDITERRANEAN BASIN IN THE LATE MIOCENE	6
1.2.    THE MESSINIAN SALINITY CRISIS: STATE OF THE ART AND OPEN PROBLEMS	9
1.3.    LIPID BIOMARKERS: A TOOL FOR UNRAVELING THE GEOLOGICAL PAST	12
1.4.    THESIS OVERVIEW, RESEARCH QUESTIONS, AND SYNTHESIS OF THE KEY FINDINGS	15
CHAPTER 2 CLIMATIC AND HYDROLOGIC VARIABILITY IN THE NORTHERN MEDITERRANEAN ACROSS THE ONSET OF THE MESSINIAN SALINITY CRISIS	18
2.1.    ABSTRACT	18
2.2.    INTRODUCTION	19
2.3.    GEOLOGICAL AND STRATIGRAPHIC SETTING	20
2.4.    MATERIALS AND METHODS	23
2.5.    RESULTS	26
2.6.    DISCUSSION	29
2.7.    CONCLUSIONS	35
2.8.    ACKNOWLEDGMENTS	35
CHAPTER 3 THE RESPONSE OF WATER COLUMN AND SEDIMENTARY ENVIRONMENTS TO THE ADVENT OF THE MESSINIAN SALINITY CRISIS: INSIGHTS FROM AN ONSHORE DEEP-WATER SECTION (GOVONE, NW ITALY)	37
3.1.    ABSTRACT	37
3.2.    INTRODUCTION	37
3.3.    GEOLOGICAL SETTING	39
3.4.    MATERIALS AND METHODS	43
3.5.    RESULTS	46
3.6.    DISCUSSION	53
3.7.    CONCLUSIONS	59
3.8.    ACKNOWLEDGMENTS	59
CHAPTER 4 MARINE THAUMARCHAEOTA RECORD CARBON ISOTOPE EXCURSIONS IN THE NORTHERNMOST OFFSHOOT OF THE LATE MIOCENE MEDITERRANEAN BASIN	61
4.1.    ABSTRACT	61
4.2.    INTRODUCTION	61
4.3.    MATERIALS AND METHODS	63
4.4.    RESULTS AND DISCUSSION	65
4.5.    SUMMARY AND IMPLICATIONS	68
4.6.    ACKNOWLEDGMENTS	68
CHAPTER 5 SYNTHESIS AND FUTURE PERSPECTIVES	70
REFERENCE LIST	74
APPENDIX A	93
APPENDIX B	96
APPENDIX C	101
APPENDIX D	106
ACKNOWLEDGMENTS	120
VERSICHERUNG AN EIDES STATT – AFFIRMATION ON OATH	122





## LIST OF PUBLICATIONS

---

The thesis consists of two original articles (Chapter 2 and 3), both published in international, peer reviewed journals, and a third article (Chapter 4) currently under peer-review. For each of the articles my contribution was fundamental and is explained in detail in Appendix A. The original articles were slightly modified in their style to provide a consistent structure throughout the thesis. Figures were numbered continuously and references to Appendices are included.

**Sabino, M.**, Schefuß, E., Natalicchio, M., Dela Pierre, F., Birgel, D., Bortels, D., Schnetger, B., Peckmann, J., 2020. Climatic and hydrologic variability in the northern Mediterranean across the onset of the Messinian salinity crisis. *Palaeogeography, Palaeoclimatology, Palaeoecology* 545, article 109632. (Chapter 2)

**Sabino, M.**, Dela Pierre, F., Natalicchio, M., Birgel, D., Gier, S., Peckmann, J., 2020. The response of water column and sedimentary environments to the advent of the Messinian salinity crisis: insights from an onshore deep-water section (Govone, NW Italy). *Geological Magazine*, 1 – 17. (Chapter 3)

**Sabino, M.**, Birgel, D., Natalicchio, M., Dela Pierre, F., Peckmann, J. (submitted). Marine Thaumarchaeota record carbon isotope excursions in the northernmost offshore of the late Miocene Mediterranean Basin. (Chapter 4)

Data related to the already published articles were re-adapted from the author of the thesis for publication to the open access library PANGAEA (see Appendix A for details on contributions).

**Sabino, M.**, Schefuß, E., Natalicchio, M., Dela Pierre, F., Birgel, D., Bortels, D., Schnetger, B., Peckmann, J., 2020. Climate variability in the northern Mediterranean across the onset of the Messinian salinity crisis: insights from inorganic and organic geochemical proxies. PANGAEA.

**Sabino, M.**, Dela Pierre, F., Natalicchio, M., Birgel, D., Gier, S., Peckmann, J., 2021. Changes in water column and sedimentary environments at the onset of the Messinian salinity crisis: insights from an onshore deep-water section (Govone, NW Italy). PANGAEA.

Additionally, I contributed to a fourth publication during my doctoral studies (see Appendix A for further details), which however has not been included in this work.

Natalicchio, M., Dela Pierre, F., Birgel, D., Brumsack, H., Carnevale, G., Gennari, R., Gier, S., Lozar, F., Pellegrino, L., **Sabino, M.**, Schnetger, B., Peckmann, J., 2019. Paleoenvironmental change in a precession-paced succession across the onset of the Messinian salinity crisis: insight from element geochemistry and molecular fossils. *Palaeogeography, Palaeoclimatology, Palaeoecology* 518, 45–61. (not included)



## LIST OF ABBREVIATIONS

---

Al:	aluminum	OC:	organic carbon
APCI:	atmospheric pressure chemical ionization	P:	precipitation
Ar.:	Arnulfi	PB:	Piedmont Basin
Bioz.:	biozones	Pentac.	
BIT:	branched and isoprenoid tetraether index	sulfide:	pentacyclic sulfide
Bp-0:	acyclic biphytane	Ph:	phytane
Bp-1:	monocyclic biphytane	PLG:	Primary Lower Gypsum
Bp-2:	bicyclic biphytane	Poll. or	
Bp-3:	tricyclic biphytane	Pz.:	Pollenzo
BSTFA:	N,O-bis(trimethylsilyl)- trifluoroacetamide	R:	riverine runoff
Cald.:	caldarchaeol	SEM:	scanning electron microscopy
CPI:	Carbon Preference Index	Si:	silicon
Cren.:	crenarchaeol	SIM:	single ion mode
DAGE:	dialkyl glycerol ethers	SPM:	suspended particulate matter
DCM:	dichloromethane	SQ:	scientific questions
DGD:	diphytanyl glycerol diether	TC:	total carbon
DIC:	dissolved inorganic carbon	THM:	tetrahymanol
E:	evaporation	Ti:	titanium
EDS:	energy dispersive system	TIC:	total inorganic carbon
FAO:	first abundant occurrence	TLE:	total lipid extract
FID:	flame-ionization detector	TOC:	total organic carbon
G, Gov.,		TOM:	terrestrial organic matter
Gv.:	Govone	V-PDB:	Vienna Pee Dee Belemnite
GC:	gas chromatograph	V-SMOW:	Vienna Standard Mean Ocean Water
GDGT:	glycerol dibiphytanyl glycerol tetraether	XRD:	X-ray diffraction
HPLC:	high performance liquid chromatography	XRF:	X-ray fluorescence
IRMS:	isotope ratio mass spectrometer	Zr:	zirconium
IS:	internal standard		
Isorenier.:	isorenieratane	<u>Symbols:</u>	
kyr:	thousand years	$\delta^{13}\text{C}$ :	carbon stable isotope ratio
Ly:	lycopane	$\delta^{13}\text{C}_{\text{Bp}}$ :	biphytane carbon stable isotope ratio
Ma:	million years	$\delta^{13}\text{C}_{\text{DIC}}$ :	dissolved inorganic carbon stable isotope ratio
Med.:	Mediterranean	$\delta^{13}\text{C}_{n\text{-alk}}$ :	<i>n</i> -alkane carbon stable isotope ratio
MeOH:	methanol	$\delta^{18}\text{O}$ :	oxygen stable isotope ratio
MGI, II,		$\delta^2\text{H}$ :	hydrogen stable isotope ratio
III:	marine group I, II, III	$\delta^2\text{H}_{n\text{-alk}}$ :	<i>n</i> -alkane hydrogen stable isotope ratio
MS:	mass spectrometer	$\epsilon$ :	biosynthetic fractionation factor
MSC:	Messinian salinity crisis	$\Sigma$ :	sum
<i>n</i> -alk.:	<i>n</i> -alkane		



## ABSTRACT

---

The late Miocene (11.6 to 5.3 Ma) was characterized by a global trend of cooling and aridification. In such a scenario, the Mediterranean Basin was experiencing increasing tectonic restriction and climate fluctuations driven by changes in orbital parameters of the Earth (mostly precession). The concurrence of these factors ultimately led to the most dramatic paleoceanographic event in the history of the basin, the Messinian salinity crisis (MSC; 5.97–5.33 Ma). Although this event is known since more than 50 years, a detailed understanding of the environmental conditions established at the onset and during the MSC has not been reached yet. This is due to the inaccessibility of sediments deposited in the Messinian Mediterranean depocenters (> 1000 m paleodepth), the lack of modern analogs, and the scarcity of body fossils in the stratigraphic record. A so far rarely explored possibility to solve the riddle of the enigmatic environmental change accompanying the MSC onset is the study of sediments deposited at intermediate paleobathymetric depths (200–1000 m). In fact, these sediments represent the link to the still inaccessible early MSC sediments deposited in the depocenters of the late Miocene Mediterranean.

The aim of this thesis is to widen our knowledge on the paleoenvironmental conditions established at the MSC onset. Shale/marl couplets from intermediate paleobathymetric settings of the northernmost late Miocene Mediterranean sub-basin, the Piedmont Basin (NW Italy), were investigated. A multiproxy approach was applied, merging organic geochemical proxies (lipid biomarkers; compound-specific hydrogen ( $\delta^2\text{H}$ ) and carbon ( $\delta^{13}\text{C}$ ) stable isotopes) with inorganic geochemical proxies (Al, Si, Ti, and Zr; bulk-rock carbon ( $\delta^{13}\text{C}$ ) and oxygen ( $\delta^{18}\text{O}$ ) stable isotopes). Stratigraphic and petrographic studies complemented the investigations. One of the outcomes of this thesis is that prior to the onset of the MSC moister conditions prevailed at precession minima, resulting in enhanced riverine runoff. Such conditions favored phytoplankton blooms in the upper water column and led to a strong thermohaline stratification. Oxygen-depleted and sulfidic conditions developed at the seafloor and in the water column, occasionally extending into the photic zone, promoting deposition of organic-rich shales. Conversely, marls deposited at precession maxima when the climate was drier. The thermohaline stratification was disrupted towards the margins, where the water column was characterized by a dissolved inorganic carbon (DIC) pool with  $\delta^{13}\text{C}_{\text{DIC}}$  values ranging from  $-1\text{‰}$  to  $+2\text{‰}$ . Closer to the depocenter, however, thermohaline stratification and oxygen-depleted conditions at the seafloor and in the water column remained stable. Therefore, the deep-water body close to the depocenter was characterized by an estimated  $\delta^{13}\text{C}_{\text{DIC}}$  of about  $-6\text{‰}$ . After the MSC onset, no development of aridification or of hypersaline conditions was detected in the Piedmont Basin. Rather, an increase of humidity and freshwater input was identified in the northern Mediterranean, superimposed on analogous precession-paced climate and hydrologic variability as in pre-MSC times. Increasing humidity was due to an enhanced contribution of moisture sourced from the Mediterranean Sea to precipitation, coinciding with the exacerbation of the Mediterranean Basin restriction. Such conditions allowed the extension of stable thermohaline stratification towards the margin of the Piedmont Basin even at precession

maxima, excluding areas shallower than 200 m. Marine conditions persisted in the upper water column, where a  $^{13}\text{C}$ -enriched DIC pool developed, occasionally reaching  $\delta^{13}\text{C}_{\text{DIC}}$  values as high as +5‰. The enrichment was attributed to limited replenishment of remineralized DIC due to the stabilization of thermohaline stratification and export of  $^{12}\text{C}$  to the seafloor after phytoplankton blooms. Persistent water-column stratification at precession maxima, coupled to oxygen-depleted conditions at the seafloor, promoted organoclastic sulfate reduction. The latter triggered the precipitation of bacterially mediated dolomite in intermediate paleobathymetric settings while preventing the deposition of gypsum due to a faster rate of sulfate reduction *vs.* replenishment. Gypsum could presumably have precipitated at precession maxima since 5.97 Ma only where the thermohaline stratification was disrupted and the activity of sulfate reducing bacteria suppressed. This study highlights the sensitivity of ancient semi-enclosed basins to climate and hydrologic fluctuations. These fluctuations have the potential of altering the physicochemical properties of water bodies, in turn affecting sedimentary products and the carbon cycle.

## KURZFASSUNG

---

Das späte Miozän (von 11,6 bis 5,3 Ma) war durch einen globalen Trend hin zu einem kühleren und trockeneren Klima gekennzeichnet. Während dieser Zeit war das Mittelmeerbecken einer zunehmenden tektonischen Einschränkung und Klimaschwankungen ausgesetzt, die durch Änderungen der Umlaufbahnparameter der Erde (hauptsächlich Präzession) verursacht wurden. Das Zusammentreffen dieser Faktoren führte letztendlich zu dem dramatischsten paläozanografischen Ereignis in der Geschichte des Beckens, der messinischen Salinitätskrise (MSC; 5,97–5,33 Ma). Obwohl dieses Ereignis seit mehr als 50 Jahren untersucht wird, gibt es noch kein klares Verständnis hinsichtlich der Umweltbedingungen zu Beginn und während des MSC-Ereignisses. Dies ist auf die Unzugänglichkeit von Sedimenten zurückzuführen, die in den heutigen zentralen Ablagerungsräumen des Mittelmeeres liegen, und den messinischen Ablagerungsraum von > 1000 m Paläotiefe repräsentieren. Zudem fehlen moderne Analoga sowie ausreichende Körperfossilien in der stratigraphischen Überlieferung. Eine bisher kaum erforschte Möglichkeit, um das Rätsel der noch unbekanntenen Umweltveränderungen zu lösen, die mit dem Einsetzen der MSC einhergehen, ist die Untersuchung von Sedimenten, die sich in mittleren paläobathymetrischen Tiefen (200–1000 m) abgelagert haben. Tatsächlich stellen diese Sedimente die Verbindung zu den noch unzugänglichen und frühen MSC-Sedimenten dar, die in den damaligen zentralen Ablagerungsräumen des spätmiozänen Mittelmeers abgelagert wurden.

Ziel dieser Arbeit ist es, unser Wissen über die zu Beginn des MSC herrschenden paläoökologischen Bedingungen zu erweitern. Darauf basierend wurden Ton-/Mergel-Wechselfolgen aus intermediären paläobathymetrischen Bereichen des nördlichsten Teilbeckens des spätmiozänen Mittelmeers, dem Piemont-Becken (Nordwestitalien), untersucht. Es wurde ein Multiproxy-Ansatz angewendet, bei dem organisch-geochemische Proxies (Lipidbiomarker; verbindungsspezifische stabile Isotope von Wasserstoff ( $\delta^2\text{H}$ ) und Kohlenstoff ( $\delta^{13}\text{C}$ ) mit anorganischen geochemischen Proxies (Al, Si, Ti und Zr; stabile Isotope vom Gesamtgestein-Kohlenstoff ( $\delta^{13}\text{C}$ ) und Sauerstoff ( $\delta^{18}\text{O}$ )) kombiniert wurden. Stratigraphische und petrographische Studien ergänzten die Untersuchungen. Die Ergebnisse dieser Arbeit deuten darauf hin, dass vor dem Einsetzen der MSC feuchtere Bedingungen bei Präzessionsminima herrschten, was zu einem verstärkten fluviatilen Eintrag führte. Solche Bedingungen begünstigten die Phytoplanktonblüte in der oberen Wassersäule und resultierten in einer starken thermohalinen Schichtung. Am Meeresboden und in der Wassersäule entwickelten sich sauerstoffarme und sulfidische Bedingungen, die sich gelegentlich bis in die photische Zone erstreckten und die Ablagerung von organisch-reichen Tonen förderten. Umgekehrt lagerten sich Mergel bei Präzessionsmaxima ab, wenn das Klima – relativ gesehen – trockener war. Die thermohaline Schichtung wurde in Richtung der randlichen Beckenbereiche unterbrochen, sodass dort die Wassersäule durch einen Pool an gelöstem anorganischem Kohlenstoff (DIC) mit einem  $\delta^{13}\text{C}_{\text{DIC}}$  zwischen  $-1\text{‰}$  und  $+2\text{‰}$  gekennzeichnet war. In der Nähe des zentralen Ablagerungsraumes herrschten jedoch weiterhin eine stabile thermohaline Schichtung und sauerstoffarme Bedingungen am Meeresboden und

in der Wassersäule vor. Der tiefere Wasserkörper unter der Grenzschicht wies einen geschätzten  $\delta^{13}\text{C}_{\text{DIC}}$  von etwa  $-6\text{‰}$  auf. Nach dem Einsetzen der MSC konnte weder eine Aridifizierung noch die Entwicklung hypersaliner Bedingungen für das Piemont-Becken beobachtet werden. Vielmehr nahm sowohl die Luftfeuchtigkeit als auch der Süßwassereintrag im nördlichen Mittelmeerraum zu, gleichzeitig überlagert durch die Oszillationen eines präzessionsgesteuerten Klimas und der damit einhergehenden hydrologischen Variabilität, wie es bereits vor der MSC der Fall war. Die zunehmende Luftfeuchtigkeit hing mit einem verstärkten Beitrag der aus dem Mittelmeerraum stammenden Feuchtigkeit zu den lokalen Niederschlägen zusammen, was gleichzeitig mit der zunehmenden Restriktion des Mittelmeerbeckens zusammenfiel. Diese Bedingungen ermöglichten die Ausdehnung einer stabilen thermohalinen Schichtung bis in die randlichen Bereiche des Piemont-Beckens, selbst bei Präzessionsmaxima. Ausnahmen bildeten die Bereiche, die flacher als 200 m Wassertiefe waren. Die marinen Umweltbedingungen in der oberen Wassersäule blieben stabil und es bildete sich ein mit  $^{13}\text{C}$  angereicherter DIC-Pool, der mitunter  $\delta^{13}\text{C}_{\text{DIC}}$  Werte von bis zu  $+5\text{‰}$  erreichte. Die  $^{13}\text{C}$ -Anreicherung wird auf eine begrenzte Wiederauffüllung des remineralisierten DIC aufgrund der Stabilisierung der thermohalinen Schichtung und des Exports von  $^{12}\text{C}$  zum Meeresboden nach einer Phytoplanktonblüte zurückgeführt. Die anhaltende Schichtung der Wassersäule bei Präzessionsmaxima, gekoppelt mit sauerstoffarmen Bedingungen am Meeresboden, förderte den Abbau organischer Substanz durch mikrobielle Sulfat-Reduktion. Letzteres löste die Ausfällung von bakteriell induziertem Dolomit in intermediären paläobathymetrischen Bereichen aus und verhinderte gleichzeitig die Ablagerung von Gips, aufgrund einer schnelleren Sulfatreduktionsrate im Vergleich zur Ergänzung des Sulfatpools. Gips konnte vermutlich nur bei Präzessionsmaxima seit 5,97 Ma und nur dann ausfallen, wenn die thermohaline Schichtung gestört und die Aktivität sulfatreduzierender Bakterien unterdrückt war. Diese Studie hebt die Sensitivität von randlichen Becken gegenüber klimatischen und hydrologischen Schwankungen hervor. Letztere können die physikalisch-chemischen Eigenschaften der Gewässer verändern und sich somit wiederum auf die Sedimentprodukte und den Kohlenstoffkreislauf auswirken.





# Chapter 1

## INTRODUCTION

---

With an area of about  $2.5 \times 10^6$  km<sup>2</sup>, the Mediterranean Basin is currently the largest semi-enclosed basin on Earth. It is characterized by a pronounced climate gradient, defined by humid-temperate conditions in the northern sector passing to arid-subtropical conditions south-eastward (Lionello et al., 2012). Excess of evaporation ( $E$ ) relative to precipitation ( $P$ ) and riverine runoff ( $R$ ) results in a negative net hydrological budget ( $E - [P + R]$ ) in the modern Mediterranean Basin (Gladstone et al., 2007; Rohling et al., 2015). Rainfall is primarily derived from storms originating in the Mediterranean Basin itself, although North Atlantic storms extend into the basin, influencing mostly the north-western part of the basin (e.g., Kutzbach et al., 2014; Lionello et al., 2012; Rohling et al., 2015). Runoff is largely controlled by inputs from the Nile River (although its contribution has been strongly reduced after the construction of the Aswan High Dam), European rivers (Ebro, Rhone, and Po), and the Black Sea (Rohling et al., 2015). The excess of evaporation results in enhanced salinity (on average 37.5‰) compared to the global ocean (on average 35‰), which in turn controls the formation of Mediterranean deep waters in the cooler, northern areas of the basin (Gulf of Lion, Adriatic Sea, Aegean Sea; Li and Tanhua, 2020; Rohling et al., 2015). Sinking of denser water promotes a vigorous thermohaline circulation, seafloor oxygenation, and the formation of intermediate and deep-water masses (Rohling et al., 2015).

However, the study of the stratigraphic record of the Mediterranean area has revealed that the Mediterranean thermohaline circulation and hydrologic cycle had been periodically altered in the geological past (e.g., Rohling et al., 2015). The largest and most mesmerizing change occurred in the late Miocene, during the Messinian (7.25–5.33 Ma; Hilgen et al., 1995, 2000). At that time, the tectonic interaction between the African and Eurasian plates, superimposed to climate fluctuations, ultimately resulted in the deposition of the youngest salt body of regional extent on Earth, the Mediterranean Salt Giant (Camerlenghi and Aloisi, 2020; Roveri et al., 2014a).

### 1.1. The Mediterranean Basin in the late Miocene

The tectonic evolution of the Mediterranean Basin was dominated since the Cretaceous by the convergence between the African and Eurasian plates (Jolivet et al., 2006; Popov et al., 2006). The late Miocene (11.6 to 5.3 Ma) represents a crucial time interval in this evolution, since the basin was almost completely isolated from the global oceans. The tectonic isolation resulted first from the closure of the eastern gateway to the Indian Ocean at about 13.8 Ma (Bialik et al., 2019), followed by the tectonic shrinking of the western gateway to the Atlantic Ocean (Fig. 1.1; Capella et al., 2019, 2018; Flecker et al., 2015; Krijgsman et al., 2018). The isolation of the paleo-Mediterranean Basin was controlled by the westward drift of the Alboran Plate between the Iberian Peninsula and North Morocco, and its

tectonic uplift from about 8 Ma (Jolivet et al., 2006). These events led to the replacement of a wide gateway floored with oceanic crust with two narrower and shallower connections, i.e. the Betic and Rifian Corridors (Fig. 1.1; Capella et al., 2018, 2017; Krijgsman et al., 2018; Tulbure et al., 2017). The Betic and Rifian gateways regulated the Mediterranean-Atlantic water exchange until their tectonic closure at about 7 Ma. Afterwards, only limited water exchange through a narrow proto-Gibraltar Strait was possible (Fig. 1.1; Capella et al., 2019, 2018; Krijgsman et al., 2018).

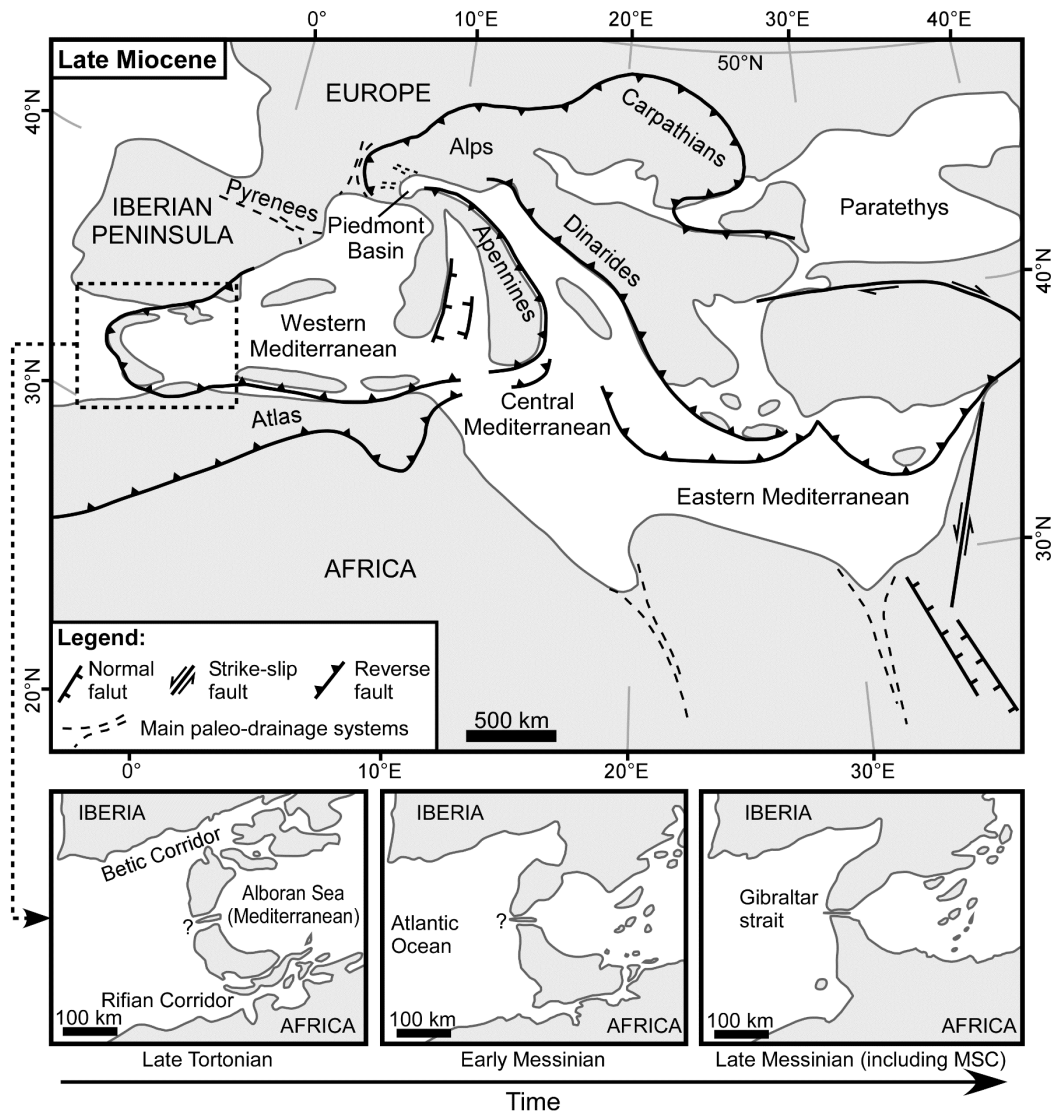


Figure 1.1 – Paleogeographic reconstruction of the Mediterranean Basin in late Miocene time according to Jolivet et al. (2006) and Popov et al. (2006). Below, the tectonic evolution of the Atlantic-Mediterranean gateways during the late Miocene according to Krijgsman et al. (2018). MSC: Messinian salinity crisis.

The progressive tectonic isolation of the paleo-Mediterranean Sea possibly amplified the global cooling and aridification trend characterizing the late Miocene (e.g., Capella et al., 2019; Flecker et al., 2015; Ivanovic et al., 2014). Such a trend was testified by decreasing seawater temperature, ephemeral glaciations in the Northern Hemisphere, enhanced seasonality, aridification of large continental areas at tropical and sub-tropical latitudes, and a major turnover in terrestrial

biomes (Herbert et al., 2016; Holbourn et al., 2018; Pound et al., 2012, 2011; Schuster et al., 2006; Zachos et al., 2001; Zhang et al., 2014). The climate of the Mediterranean area overall followed the global trend (Bertini and Martinetto, 2011; Favre et al., 2007; Jiménez-Moreno et al., 2010; Vasiliev et al., 2020, 2019). However, the progressive tectonic restriction made the basin highly sensitive to climate and hydrologic fluctuations controlled by changes in the orbital parameters of the Earth (Kouwenhoven et al., 2006; Krijgsman et al., 2001; Mayser et al., 2017; Sierro et al., 2003, 1999; Tzanova et al., 2015). Climate fluctuations were chiefly controlled by changes in the orientation of the axis of the Planet (precession), with a periodicity of about 21 kyr (Griffin, 2002; Marzocchi et al., 2015; Simon et al., 2017). Changes in the shape of the orbit (eccentricity) and the inclination of the axis (obliquity) contributed to a lesser extent, modulating precession-driven climate and hydrologic fluctuations (Bosmans et al., 2015; Marzocchi et al., 2015). At precession minima, the amount of solar radiation (insolation) received by the Northern Hemisphere maximized, enhancing the seasonality over the Mediterranean. Concurrently, the influence of the North African monsoon on the freshwater budget of the basin was intensified by the northward shift of the Intertropical Convergence Zone. This resulted in bringing higher precipitations over continental Africa up to about 20 °N latitude. Under these conditions, the Mediterranean Basin experienced a warmer and more humid climate, which favored a high fluvial discharge and consequently enhanced primary productivity in superficial waters (Marzocchi et al., 2015; Simon et al., 2017). Increased freshwater input, together with progressive tectonic restriction, promoted the development of thermohaline stratification, scarcely oxygenated bottom waters, and the deposition of organic-rich shales (Rohling et al., 2015). Conversely, precession maxima coincided with minimum insolation on the Northern Hemisphere, weakening the seasonality. Concurrently, the Intertropical Convergence Zone migrated southward below 10 °N latitude, shifting meteoric precipitations over the Atlantic Ocean. Such conditions favored an overall cooler and drier climate and the decrease of freshwater input into the paleo-Mediterranean Basin (Marzocchi et al., 2015; Simon et al., 2017). Therefore, the thermohaline circulation was restored, leading to renewed seafloor ventilation, as testified by the deposition of organic-lean, bioturbated marls (Rohling et al., 2015).

Tectonic restriction starting at about 7 Ma (closure of the Rifian and Betic Corridors; Fig. 1.1) made the basin progressively more sensitive to climate variability, leading to the deterioration of the environmental conditions of the paleo-Mediterranean Sea during the early Messinian (7.25–5.97 Ma). The diversity and abundance of benthonic foraminifera assemblages progressively decreased, suggesting scarce deep-water ventilation and increased bottom water salinity related to enhanced thermohaline stratification (Gennari et al., 2018; Kouwenhoven et al., 2006, 1999). An analogous trend was observed for planktonic foraminifera assemblages and related to increasing upper water column salinity (Bellanca et al., 2001; Blanc-Valleron et al., 2002; Kouwenhoven et al., 2006; Sierro et al., 2003, 2001, 1999). Ultimately, it was claimed that stable hypersaline conditions developed throughout the entire paleo-Mediterranean Basin about 6 Ma ago. Compelling evidence was the precipitation of evaporites (gypsum and carbonates) at the margins of the basin and the alleged disappearance of marine biota from the stratigraphic record, heralding the Messinian salinity crisis (MSC,

5.97–5.33 Ma; Camerlenghi and Aloisi, 2020; Hsü et al., 1973b, 1973a; Krijgsman et al., 1999; Manzi et al., 2013; Rouchy and Caruso, 2006; Roveri et al., 2014a).

## **1.2. The Messinian salinity crisis: state of the art and open problems**

The concept of ‘*Messinian salinity crisis*’ was developed in the 1960s, following studies on onshore successions exposed in the circum-Mediterranean region (Ruggeri, 1967; Selli, 1960). The studies showed that the Messinian stage was typified by the deposition of rocks under “anomalous” salinity conditions, both hypersaline (gypsum, anhydrite and halite) and hyposaline (brackish water sediments observed at the top of the Messinian succession). However, the extent of this event only became clear during the 1970s (among others: Hsü, 1972; Hsü et al., 1973b, 1973a; Ryan, 1976; Ryan and Cita, 1978). At that time, the geophysical exploration of the Mediterranean abyssal plains revealed the presence of thick (up to 2 km) salt bodies buried beneath Pliocene-Quaternary sediments. In particular, the salt body in the Western Mediterranean was found to have a tripartite seismic internal structure, which was readily correlated with the supposedly tripartite (gypsum, halite, gypsum) onshore evaporitic Messinian succession from Sicily (Roveri et al., 2014a and references therein). The recovery of evaporitic rocks from the topmost part of the buried salt bodies during the Deep Sea Drilling Project, Leg 13, confirmed that during the Messinian the Mediterranean Sea was turned into the youngest Salt Giant on Earth history (Hsü et al., 1973a). The deposition of the Mediterranean Salt Giant was explained with the theory of the ‘*desiccation of the Mediterranean*’ (Hsü et al., 1973b). The theory suggested that during the Messinian the Mediterranean Sea was completely isolated from the Atlantic Ocean, drying out and becoming a hot, dry giant salt pan. However, only the uppermost part of the buried salt bodies was drilled. Therefore, a great uncertainty remained about the timing, duration, and mechanisms that led to the deposition of the Mediterranean Salt Giant. Such uncertainty promoted a vigorous scientific debate and the introduction of alternative interpretations in the following years (Butler et al., 1995; Camerlenghi and Aloisi, 2020; Clauzon et al., 1996; Krijgsman et al., 1999; Nesteroff, 1973; Riding et al., 1998; Rouchy and Caruso, 2006; Roveri et al., 2014a, 2014b, 2001; Selli, 1973).

The great improvements in investigation techniques during the last 50 years helped to solve some major problems related to the salinity crisis. The deposition of the Mediterranean Salt Giant in a deep basin at least intermittently connected to the Atlantic Ocean is now widely accepted (Roveri et al., 2014a). The same applies to the onset of the event, which is considered synchronous throughout the Mediterranean Basin at about 5.97 Ma (Gennari et al., 2018; Hilgen and Krijgsman, 1999; Krijgsman et al., 2002, 2001, 1999; Lozar et al., 2018; Lozar and Negri, 2019; Manzi et al., 2018, 2013). The MSC event is now framed in a well-constrained chrono-stratigraphic model (Fig. 1.2; CIESM, 2008; Manzi et al., 2018; Roveri et al., 2014a). The model suggests a first stage (5.97–5.60 Ma) during which gypsum started to precipitate at 5.97 Ma only in shallow-water (< 200 m) marginal Mediterranean sub-basins (Fig. 1.2; Lugli et al., 2010). Gypsum precipitation alternated to deposition of shales, forming up to 16 lithological cycles

consisting in gypsum/shale couplets grouped in the Primary Lower Gypsum (PLG) unit (Lugli et al., 2010). As for the pre-MSC sediments, the deposition of the shale/gypsum couplets was suggested to be controlled by precession-paced climate fluctuations, with shales representing precession minima and gypsum precession maxima (Krijgsman et al., 1999; Lugli et al., 2010). In deeper settings (> 200 m), however, gypsum precipitation at the seafloor was progressively delayed, while in the depocentral zones no gypsum was deposited during this stage (Fig. 1.2; Dela Pierre et al., 2016, 2011; Manzi et al., 2018, 2007). The delay in gypsum precipitation and its absence in deeper settings has been tentatively explained with the absence of a sill, trapping brines in sub-basins (Lugli et al., 2010). Alternatively, it was proposed that in deeper settings reduction of sulfate – used as electron acceptor during organic matter remineralization – outpaced sulfate replenishment, resulting in gypsum undersaturation at the seafloor and hence no deposition/preservation (de Lange and Krijgsman, 2010; García-Veigas et al., 2018). A carbonate unit, known as ‘*Calcare di Base*’, is also widespread in the central Mediterranean (Sicily and Calabria), although its attribution to the first stage is still debated (Fig. 1.2; Caruso et al., 2015; Manzi et al., 2016a, 2011; Rouchy and Caruso, 2006). The second stage (5.60–5.54 Ma) was characterized by the subaerial exposure of the PLG unit, that consequently underwent partial dismantling. The products of erosion were deposited in the depocentral zones of the Mediterranean Basin by various types of gravity flows (Fig. 1.2; Roveri et al., 2014a). Concurrently, halite and K- and Mg-salts precipitated in the depocentral zones of the Mediterranean Basin (Fig. 1.2; Lugli et al., 1999; Manzi et al., 2018, 2012). The sediments deposited during the second stage of the MSC were grouped in the Resedimented Lower Gypsum unit (Fig. 1.2; Roveri et al., 2008a, 2008c). The third stage (5.54–5.33 Ma) was typified by the deposition in a brackish environment of fine-to-coarse grained siliciclastic deposits in the northern and western Mediterranean and a new sulfate evaporite-bearing unit (Upper Gypsum) in the central and eastern Mediterranean (Fig. 1.2; Manzi et al., 2016b, 2009; Rouchy and Caruso, 2006; Roveri et al., 2014a, 2001). The latest part of this stage (Lago-Mare phase; 5.42–5.33 Ma) was characterized by a strong influence from the Paratethys Basin, indicated by the occurrence of Paratethyan faunal assemblages (e.g., ostracods and mollusks) in Mediterranean sediments (Fig. 1.2; Manzi et al., 2016b; Orszag-Sperber, 2006; Rouchy and Caruso, 2006).

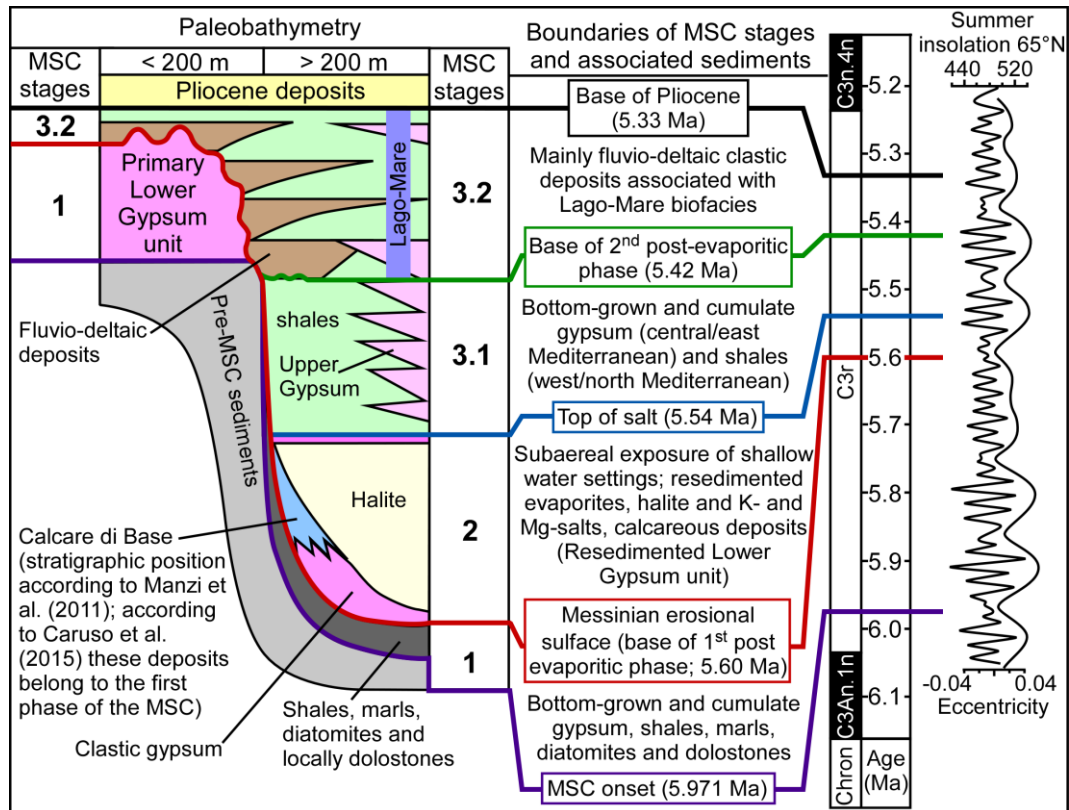


Figure 1.2 – Chrono-stratigraphic model of the Messinian salinity crisis (MSC; modified from Roveri et al., 2016) correlated with the summer insolation curve for the Northern Hemisphere (65 °N) and the eccentricity curve proposed by Laskar et al. (2004). Ma: million years.

Despite the advancements in the knowledge on the MSC event, it remains poorly understood how the climate and hydrology of the Mediterranean Basin changed at the onset of the crisis. Similarly, the impact of such a change on the physical and chemical properties of the paleo-Mediterranean Sea is still uncertain. For instance, the precipitation of evaporites was assumed to indicate the aridification of the entire Mediterranean region (Hsü et al., 1973b). Nonetheless, evidence from later studies based on paleovegetation proxies suggested no substantial climate change or strengthening of climate gradients throughout the Mediterranean Basin across the MSC onset (Bertini, 2006; Bertini and Martinetto, 2011; Fauquette et al., 2006; Favre et al., 2007; Suc and Bessais, 1990). These studies, however, focused exclusively on shales from the PLG unit, therefore not providing a full picture of the climate and hydrologic variability accompanying the advent of the crisis and the deposition of evaporites. The inception of evaporite precipitation was also taken as the evidence for the development of hypersaline conditions throughout the basin (Hsü et al., 1973a), corroborated by the scarcity or lack of marine microfossils in the MSC stratigraphic record (Bellanca et al., 2001; Blanc-Valleron et al., 2002). However, the recent reassessment of the Mediterranean Messinian (micro)paleontological record suggests that normal marine conditions persisted, at least locally, after the MSC onset (Carnevale et al., 2019 and references therein). Even more remarkable is the evidence that the PLG gypsum entraps fossils of stenohaline organisms (diatoms; Dela Pierre et al., 2015) and that paleosalinity data from fluid inclusions and hydration water reveal that the gypsum could have

precipitated from fluids with an even lower salinity than that of modern seawater (Evans et al., 2015; Natalicchio et al., 2014). Ultimately, recent re-analyses of abyssal evaporites and hydrological models suggest that the MSC sediments did not necessarily deposit in hypersaline ponds (Hsü et al., 1973b), but in deep-water environments characterized by strong thermohaline stratification (de Lange and Krijgsman, 2010; García-Veigas et al., 2018; Hardie and Lowenstein, 2004; Lugli et al., 2015; Simon and Meijer, 2017).

### **1.3. Lipid biomarkers: a tool for unraveling the geological past**

In deep geological time (i.e. the Precambrian) and during the Phanerozoic environmental and ecological crises such as the MSC, body fossils are scarce or lack from the stratigraphic record. Under these circumstances, organic geochemical investigations targeting lipid biomarkers and their carbon and hydrogen stable isotope compositions represent a possible alternative tool for unraveling paleoenvironmental conditions (e.g., Brassell, 1992; Killops and Killops, 2005; Luo et al., 2019).

Lipid biological markers or shorter *lipid biomarkers* are organic compounds enclosed in geological materials (e.g., sedimentary rocks) whose structures can be linked to biological precursor compounds (e.g., Brassell, 1992; Killops and Killops, 2005). They are composed principally of carbon and hydrogen atoms (hydrocarbon backbone, arranged either in open or closed chains), plus additional heteroatoms, the most common of which are oxygen, sulfur, and nitrogen (Brassell, 1992; Killops and Killops, 2005). Lipid biomarkers represent the 'organic-solvent extractable' fraction (bitumen) of the organic matter preserved in sediments and sedimentary rocks. To a certain extent, preservation can potentially last for billions of years (e.g., Brocks et al., 2005; French et al., 2015a; Mycke et al., 1988) if catagenetic processes do not exceed the oil window (about 100–150 °C and 2.5–4.5 km depth; Killops and Killops, 2005). Commonly used solvents for extraction of biomarkers from the geological matrix are *n*-hexane, toluene, and dichloromethane, possibly mixed with more polar solvents (e.g., methanol) to enhance the effectiveness of the extraction process. Extraction is typically achieved using a Soxhlet apparatus or ultrasonication (Brassell, 1992). Upon extraction, biomarkers are commonly separated in fractions with different polarity via chromatographic techniques (e.g., column chromatography) or with different size and shape (e.g., molecular sieves; Fig. 1.3). Following fractionation, lipids are analyzed through gas chromatography (GC), mass spectrometry (MS) and high-pressure liquid chromatography (HPLC; Fig. 1.3; Bianchi and Canuel, 2011; Brassell, 1992; Killops and Killops, 2005). Coupled GC–MS systems are nowadays routinely used to quantify (GC) and identify (MS) lipids which volatilize at temperatures up to 325 °C, while for involatile and labile compounds HPLC–MS systems are used. The analysis of compound specific stable isotopes is achieved using a GC coupled to an isotope ratio mass spectrometer (IRMS), which allows measuring isotopic abundances (Bianchi and Canuel, 2011). Examples for the above-mentioned extraction procedures and settings of the analytical systems can be found in Sections 2.4.3 and 3.4.4, as well as in Appendix D2 (Fig. 1.3).



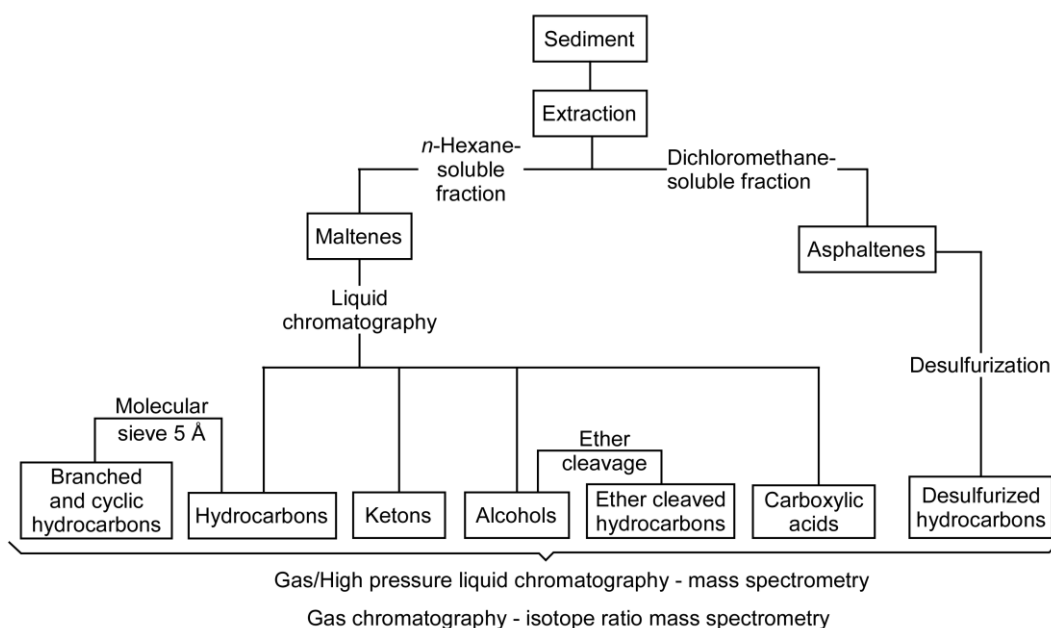


Figure 1.3 – Simplified representation of an extraction and fractionation scheme for biomarker separations and analyses (the scheme adheres to the procedure followed in this thesis).

Fossil lipids are at best equal to or at least similar to the original lipids, which are synthesized by the living representatives of the three major kingdoms of the tree of life, Archaea, Bacteria, and Eukarya (Fig. 1.4; Gaines et al., 2009; Killops and Killops, 2005). Many lipid biomarkers are building blocks of cell membranes, such as isoprenoid glycerol ethers for Archaea or *n*-alkyl glycerol esters for Bacteria and Eukarya (Fig. 1.4). Others are membrane rigidifiers, for instance sterols for Eukarya (and few Bacteria) and hopanoids for Bacteria (Fig. 1.4). Besides them, other important sources of lipid biomarkers are epicuticular waxes from terrestrial plant leaves (long chain *n*-alkanes) and pigments (chlorophylls and carotenoids; Fig. 1.4; e.g., Brassell, 1992; Diefendorf et al., 2011; Eglinton and Hamilton, 1967; Eglinton and Eglinton, 2008; French et al., 2015b; Gaines et al., 2009; Killops and Killops, 2005; Luo et al., 2019). The identification of lipid biomarkers in the geological record may therefore provide insights on the source organism(s) and consequently on the predominating environmental conditions in which the latter lived at the time of sediment deposition (e.g., Luo et al., 2019). In fact, environmental factors, mostly governed by climate fluctuations, exert a primary control on abundance and diversity of organisms. Therefore, the identification of specific lipid biomarkers, their distribution, and their carbon ( $\delta^{13}\text{C}$ ) and hydrogen ( $\delta^2\text{H}$ ) stable isotopes can be used in ‘*molecular stratigraphy*’ (Brassell et al., 1986) to reconstruct paleoenvironmental parameters and the carbon and hydrologic cycles (e.g., Collister et al., 1994; Diefendorf and Freimuth, 2017; Kenig et al., 1995; Kuypers et al., 2001; Pancost and Boot, 2004; Pancost and Sinninghe Damsté, 2003; Pearson et al., 2016; Sachse et al., 2012; Schefuß et al., 2005; Schouten et al., 1998b, 2013; Wakeham et al., 2003). Multiple molecular proxy indices were developed to constrain, for example, paleo-sea-surface temperatures (e.g.,  $\text{U}^{\text{K}}_{37}$ , Brassell et al., 1986; tetraether index of compounds with 86 carbon atoms ( $\text{TEX}_{86}$ ), Schouten et al., 2002) and paleoredox conditions (e.g., lycopane/*n*-

C<sub>31</sub> alkane ratio, Sinninghe Damsté et al., 2003). Enhanced/reduced terrestrial input in basins – directly dependent on the climate and hydrologic regime – can be traced as well with molecular proxies (e.g., branched and isoprenoid tetraether index (BIT), Hopmans et al., 2004). Insights on the climate and the hydrologic cycle can also be acquired from δ<sup>2</sup>H and δ<sup>13</sup>C stable isotopes of long chain *n*-alkanes, with δ<sup>13</sup>C values further helping in constraining the dominant vegetation (C<sub>3</sub> vs. C<sub>4</sub> plants; e.g., Schefuß et al., 2005). Lipid biomarkers were further suggested as potential tool for tracing perturbations in the carbon cycle through their δ<sup>13</sup>C isotopic signature, as in the case of archaeal membrane lipids (e.g., Kuypers et al., 2001; Schoon et al., 2013). Despite the great potential of lipid biomarkers as paleoenvironmental proxies, major limitations in their application are preservational issues, uncertainty on their source organisms, and the limited extension back in the geological past of some well-constrained source organisms (Luo et al., 2019). A possible solution to overcome some of these problems is the application of a multiproxy approach, integrating multiple organic geochemistry proxies with other independent proxies (e.g., major and trace elements, Calvert and Pedersen, 2007).

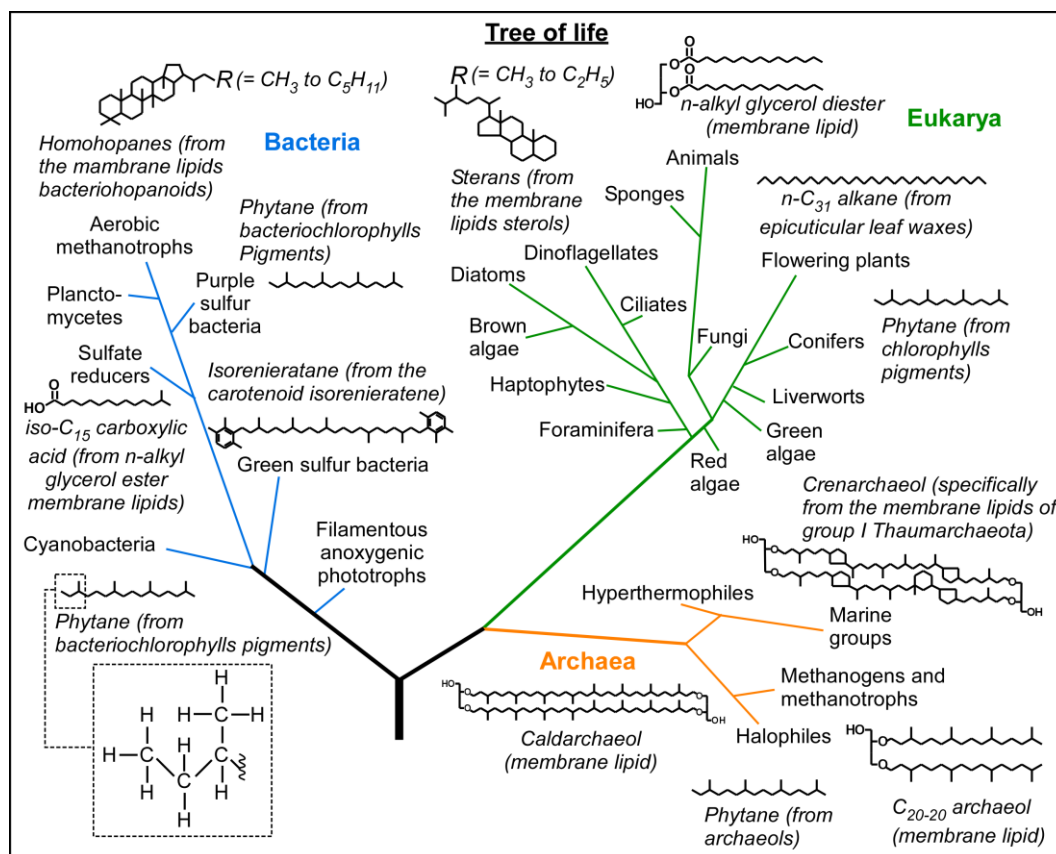


Figure 1.4 – Simplified tree of life showing the three kingdoms of life, as reconstructed from nucleotide sequences of small-subunit ribosomal-RNA. Characteristic lipid biomarkers, including cell membrane derivatives of the three kingdoms and lipid biomarkers from pigments of phototropic Eukarya and Bacteria, as well as epicuticular waxes of terrestrial plant leaves are shown. Part of the structural formula of the lipid biomarker phytane is shown in detail in the dashed box. Figure modified from Luo et al. (2019).

### 1.3.1. Molecular fossils applied to the unresolved MSC problems

In the early 1990s, pioneering organic geochemical studies were conducted on shales from the PLG unit, revealing deposition in a stratified water column. Sulfidic conditions extending up into the photic zone (photic zone euxinia) were identified, as evidenced by the abundant occurrence of the carotenoid isorenieratane, derived from green sulfur bacteria (Kenig et al., 1995; Sinninghe Damsté et al., 1995b, 1995a). However, the environmental conditions characterizing the precession maxima hemicycles remained unassessed. More recently, organic geochemistry investigations targeting MSC sediments started over. The  $\delta^2\text{H}$  isotopic signature of lipids from terrestrial plants and marine algae were used to reconstruct the hydrologic cycle of the Mediterranean area during the MSC (Andersen et al., 2001; Vasiliev et al., 2017, 2015, 2013). Insights on terrestrial vegetation (dominance of  $\text{C}_3$  vs.  $\text{C}_4$  plants) and climate conditions were obtained investigating the  $\delta^{13}\text{C}$  isotopic signature of leaf-wax derived *n*-alkane lipids (Vasiliev et al., 2015; Natalicchio et al., 2019). Evidence of stratified water column conditions has been documented for sediments deposited during all three stages of the crisis (Christeleit et al., 2015; Isaji et al., 2019b, 2019a; Natalicchio et al., 2017). Furthermore, archaea, virtually widespread in all kind of environments (Dawson et al., 2012; Robertson et al., 2005; Schouten et al., 2013; Turich et al., 2007; Wakeham et al., 2003), have received little attention so far, although evidence suggests that they rose during the early phase of the MSC (Birgel et al., 2014; Natalicchio et al., 2017; Turich and Freeman, 2011). Despite the advancements, neither the dawn of the MSC event nor the sediments deposited at precession maxima during the first stage of the crisis have been studied in detail for lipid biomarkers, leading to incomplete reconstructions. Additionally, sediments deposited at paleobathymetries between 200 m and 1000 m in ‘*intermediate onshore basins*’ (*sensu* Roveri et al., 2014a) were often neglected. However, intermediate paleobathymetric settings were suggested as possible keys in solving the riddle of the enigmatic environmental and biological changes accompanying the onset of the MSC (Roveri et al., 2014a). In fact, intermediate paleobathymetric settings represent the link to the still inaccessible early MSC sediments deposited in the depocentral areas of the late Miocene Mediterranean.

### 1.4. Thesis overview, research questions, and synthesis of the key findings

This thesis aims to contribute to the clarification of the environmental change that occurred in the Mediterranean area across the onset of the MSC from an intermediate paleobathymetric perspective. The Piedmont Basin (NW Italy) was selected as a case study. This basin represents the northernmost offshoot of the late Miocene Mediterranean Basin (Dela Pierre et al., 2016, 2011). In the Piedmont Basin, the pre-MSC and earliest MSC sediments from intermediate paleobathymetric settings are exposed in outcrops along the tectonically uplifted southern margin. These sediments are represented by shale/marl couplets, whose deposition was influenced by climate fluctuations paced by precession (Natalicchio et al., 2019). This project focused chiefly on the Govone section, which is located in the southern margin of the Piedmont Basin along a riverbank (44°48'08" N;

8°07'34" E; Dela Pierre et al., 2016; Gennari et al., 2020). Data from the neighboring Pollenzo section were also integrated. The Pollenzo section is located about 20 km south-westward from the Govone section, in a more proximal position in respect to the paleomargin of the Piedmont Basin (44°41'08" N, 7°55'33" E; Dela Pierre et al., 2016, 2011). Organic geochemical (lipid biomarkers distribution; compound-specific hydrogen ( $\delta^2\text{H}$ ) and carbon ( $\delta^{13}\text{C}$ ) stable isotopes), inorganic geochemical (major and trace elements; bulk rock carbon and oxygen stable isotopes), stratigraphic, petrographic, and mineralogical analyses were applied.

The thesis is structured in five Chapters. **Chapter one** sets the stage for the thesis, with an introduction on the late Miocene Mediterranean Basin, the state of the art regarding the Messinian salinity crisis (MSC) and an overview on lipid biomarkers as paleoenvironmental proxies and tools for tackling some of the open MSC problems.

Following this introduction, the **second Chapter** addresses the scientific question (SQ1): *how did climate and hydrology varied in the northern Mediterranean across the MSC onset?* Our findings indicate a strong precessional forcing on climate and hydrologic variability, evidenced by periodical fluctuations in abundance and  $\delta^2\text{H}$  values of terrestrial plant waxes and element/Al ratios in the investigated sediments. The same proxies indicate a long-term trend towards moister conditions due to enhanced supply of Mediterranean-derived moisture.  $\delta^{13}\text{C}$  values of terrestrial plant waxes point to no expansion of vegetation adapted to arid climate conditions, indicating only modest climate fluctuations.

In the **third Chapter** we posed ourselves the scientific question, SQ2: *how were the water column and sedimentary environments impacted by the advent of the MSC in the Piedmont Basin?* Distribution of archaeal lipids in MSC sediments suggests persisting normal marine conditions in the upper water column after the MSC onset. Concurrently, the distribution of lipid biomarkers (principally tetrahymanol and lycopane) and petrographic evidence from MSC sediments indicate intensified thermohaline stratification. The fluctuation of the surface separating the upper and the lower parts of the water column, i.e. the chemocline, influenced the distribution of the MSC sediments.

In the **fourth Chapter** the following scientific question, SQ3, was addressed: *How did the onset of the MSC affect the carbon cycle in the northernmost Mediterranean sub-basin?* The  $\delta^{13}\text{C}$  signature of tricyclic biphytane, derived from crenarchaeol sourced by marine Thaumarchaeota, has revealed the development of a  $^{13}\text{C}$ -depleted relatively deep-water body and a  $^{13}\text{C}$ -enriched upper water layer across the onset of the MSC. Thermohaline stratification and export to the seafloor of organic carbon controlled perturbations in the carbon cycle.

Finally, in **Chapter five**, a synthesis is provided and implications of this study and possible future developments are discussed.



# Chapter 2

## CLIMATIC AND HYDROLOGIC VARIABILITY IN THE NORTHERN MEDITERRANEAN ACROSS THE ONSET OF THE MESSINIAN SALINITY CRISIS

---

*The second Chapter of the thesis has been published in Palaeogeography, Palaeoclimatology and Palaeoecology as: Sabino, M., Schefuß, E., Natalicchio, M., Dela Pierre, F., Birgel, D., Bortels, D., Schnetger, B., Peckmann, J., 2020. Climatic and hydrologic variability in the northern Mediterranean across the onset of the Messinian salinity crisis. Palaeogeography, Palaeoclimatology, Palaeoecology 545, article 109632.*

### 2.1. Abstract

The youngest and one of the largest saline deposits of Earth history formed in the Mediterranean during the Messinian salinity crisis (MSC; 5.97–5.33 Ma, Late Miocene), when global climate was experiencing a trend of cooling and aridification. However, recent paleoclimate reconstructions indicate strong climate gradients across the Mediterranean Basin and the persistence of humid conditions in the northern Mediterranean during the earliest phase of the MSC. To characterize climatic and hydrologic variability across the onset of the MSC, we studied inorganic geochemical proxies, comprising Si, Ti, and Zr element distributions and organic geochemical proxies, such as sedimentary plant wax contents and their carbon ( $\delta^{13}\text{C}_{n\text{-alk}}$ ) and hydrogen ( $\delta^2\text{H}_{n\text{-alk}}$ ) stable isotope compositions in deep-water (> 200 m), alternating shale and marl deposits of the Piedmont Basin (Govone section; NW Italy). Our results suggest that deposition was controlled by precession-driven climate fluctuations before and after the onset of the MSC, with shales deposited under moister conditions (lower element/Al ratios and  $\delta^2\text{H}_{n\text{-alk}}$  values) and marls when drier conditions prevailed (higher element/Al ratios and  $\delta^2\text{H}_{n\text{-alk}}$  values). The observed  $\delta^2\text{H}_{n\text{-alk}}$  pattern further suggests changes in the relative contributions of the sources of moisture for precipitation. At precession minima, shales were deposited and moisture was mainly sourced from the North Atlantic, as reflected by lower  $\delta^2\text{H}_{n\text{-alk}}$  values. At precession maxima, marls were deposited and higher  $\delta^2\text{H}_{n\text{-alk}}$  values point to a – probably western – Mediterranean source of moisture. The decrease of element/Al ratios as well as the coeval increase of plant wax abundances after the onset of the MSC indicate enhanced humidity and increased net precipitation over the northern Mediterranean. These changes coincided with a restriction of the Atlantic-Mediterranean gateways and resulted from an enhanced contribution of deuterium-enriched moisture sourced from seawater evaporation in the Mediterranean, evidenced by an increase of  $\delta^2\text{H}_{n\text{-alk}}$  values.

## 2.2. Introduction

Following the Mid-Miocene Climatic Optimum, the global climate experienced a trend of cooling and aridification, coinciding with evidence for transient glaciations in the Northern Hemisphere and the establishment of a marked seasonality (e.g., Herbert et al., 2016; Pound et al., 2012; Tzanova et al., 2015; Zachos et al., 2001). This trend culminated in the Late Miocene (between 7 and 5.3 Ma) in the decrease of ocean temperatures to modern values (Herbert et al., 2016) and was accompanied by changes in terrestrial ecosystems. One prominent change was the expansion of C<sub>4</sub>-dominated grasses at the expenses of C<sub>3</sub> grasslands (Cerling et al., 1997; Hötzel et al., 2013; Strömberg, 2011). In the Mediterranean area, the Late Miocene cooling coincided in part with the so-called Messinian salinity crisis (MSC, 5.97–5.33 Ma; Manzi et al., 2013). The MSC represents an environmental crisis during which the Mediterranean was transformed into the youngest salt giant in Earth history (Cita et al., 1978; Flecker et al., 2015; Hsü et al., 1973b; Roveri et al., 2014a). This event is thought to have been driven by the progressive restriction of the Atlantic-Mediterranean gateways (e.g., Flecker et al., 2015; Krijgsman et al., 2018), superimposed on long (eccentricity) and short (precession) orbitally-controlled climate fluctuations (Roveri et al., 2014a), modulating the hydrological budget of the basin (Meijer and Tuenter, 2007; Simon et al., 2017). Part of the pre-MSC stratigraphic record is typified by a precession-paced cyclic succession of shales, diatomites, and marls, with shales recording humid conditions at precession minima and insolation maxima and marls recording more arid conditions at precession maxima and insolation minima (Bellanca et al., 2001; Blanc-Valleron et al., 2002; Gennari et al., 2018; Hilgen and Krijgsman, 1999; Kouwenhoven et al., 2006; Lozar et al., 2018; Manzi et al., 2007; Sierro et al., 1999). During the first phase of the MSC, shale and gypsum couplets of the Primary Lower Gypsum unit (PLG; Roveri et al., 2008c) were deposited in shallow peripheral basins (< 200 m), changing laterally to shale and marl cycles similar to their pre-MSC counterparts in basins of intermediate to great water depths (> 200 m; e.g., Dela Pierre et al., 2011; Manzi et al., 2007; Natalicchio et al., 2019). The evaporite cycles and their lateral equivalents reflect precession-controlled fluctuations of the Mediterranean climate (Krijgsman et al., 1999; Natalicchio et al., 2019), with gypsum depositing in marginal settings and marls in intermediate to deep settings. The deposition of gypsum and marls corresponds to precession maxima and periods of more arid conditions, reflecting a reduced net hydrological budget of the basin (Roveri et al., 2014a).

The widespread deposition of evaporites during the MSC was originally taken as the main argument for aridification of the whole Mediterranean area (Hsü et al., 1973b). However, later reconstructions indicated no substantial climate change across the onset of the MSC and revealed that strong latitudinal gradients persisted in the Mediterranean with a wet northern region and an arid southern region (Bertini, 2006; Bertini and Martinetto, 2011, 2008; Fauquette et al., 2006; Favre et al., 2007; Jiménez-Moreno et al., 2013, 2010; Suc and Bessais, 1990). Such reconstructions were mostly based on pollen and plant remains, which are, however, scarce and poorly preserved within evaporites (Bertini, 2006; Bertini and Martinetto, 2011; Fauquette et al., 2006). An alternative approach to reconstruct climate variability involves the application of inorganic and organic geochemical proxies such as major and trace elements (Calvert and Pedersen, 2007; Schnetger

et al., 2000; Tribovillard et al., 2006; Wehausen and Brumsack, 2000, 1999) and sedimentary long chain *n*-alkanes and their carbon and hydrogen stable isotopic compositions (Eglinton and Eglinton, 2008; Naafs et al., 2012; Pancost and Boot, 2004; Pedentchouk and Zhou, 2018; Schefuß et al., 2005, 2003; Tipple and Pagani, 2010; Vasiliev et al., 2017, 2015). Long-chain *n*-alkanes are common constituents of epicuticular waxes of terrestrial higher plants (e.g. Diefendorf et al., 2011; Eglinton and Hamilton, 1967). Due to their refractory nature, they are excellent recorders of climate-induced change in terrestrial vegetation and input of terrestrial organic matter (TOM) to ocean basins (e.g., Pancost and Boot, 2004; Schefuß et al., 2003). Here, we use geochemical proxies to study the onset of the MSC archived in the Govone section (Piedmont Basin, NW Italy), aiming for the reconstruction of changes in climate, terrestrial vegetation C<sub>3</sub> vs. C<sub>4</sub> plants, and hydrology at the northernmost offshoot of the Mediterranean Basin. The MSC is reflected at this location by a cyclic succession of shales and marls, representing the deep-water equivalent of the PLG unit (Bernardi, 2013; Dela Pierre et al., 2016). Our study documents the presence of humid climate conditions in the northern sectors of the Mediterranean during the earliest phase of the MSC. Moreover, the new data complement climate and few hydrological reconstructions from other Mediterranean regions (Andersen et al., 2001; Vasiliev et al., 2017, 2015, 2013), confirming the presence of strong climate gradients across the Mediterranean during the MSC.

## **2.3. Geological and stratigraphic setting**

### **2.3.1. The Piedmont Basin**

The Piedmont Basin is a wedge-top basin filled with upper Eocene to Messinian sediments that developed in the Alpine retroforeland and became eventually involved in the Apennine orogeny (Fig. 2.1A; Mosca et al., 2010; Rossi, 2017; Rossi and Craig, 2016). The Messinian sediments, mostly buried beneath Pliocene to Quaternary deposits of the Savigliano and Alessandria sub-basins (Irace et al., 2005), are exposed along the uplifted southern and northern basin margins (Fig. 2.1A; Dela Pierre et al., 2011). The succession starts with alternating organic-rich shales and marls deposited in an outer shelf to slope environment (Sant'Agata Fossili Marls, Tortonian – lower Messinian; Sturani, 1973; Fig. 2.1B), forming 2 to 3 m thick lithological cycles. Abundance fluctuations of calcareous microfossil assemblages demonstrated that lithological cyclicity was controlled by precession-controlled climate change, with shales recording moister climate at precession minima and insolation maxima and marls reflecting drier climate at precession maxima and insolation minima (Lozar et al., 2018; Violanti et al., 2013). At the southern and northern basin margins, the Sant'Agata Fossili Marls are overlain by sulfate evaporites of the PLG unit deposited during the first stage of the MSC (Fig. 2.1B; Dela Pierre et al., 2011). Basinward, the gypsum layers of the PLG unit laterally pass into marls alternated with organic-rich shales (Fig. 2.1B; Dela Pierre et al., 2011; Natalicchio et al., 2019, 2017). The PLG unit and its lateral, deeper equivalents are unconformably overlain by resedimented and chaotic evaporites (Valle Versa chaotic complex; Dela Pierre et al., 2007; Irace et al., 2005), equivalent to the Resedimented Lower Gypsum unit deposited in many Mediterranean sub-basins during the second stage of the MSC (5.60–5.55 Ma; Roveri et al., 2014a).



The Messinian succession ends with fluvio-deltaic and lacustrine deposits, characterized by brackish water fauna of the Lago-Mare biofacies (Cassano Spinola Conglomerates; Sturani, 1976; Dela Pierre et al., 2011; Fig. 2.1B), recording the third stage of the MSC (5.55–5.33 Ma; Roveri et al., 2014a).

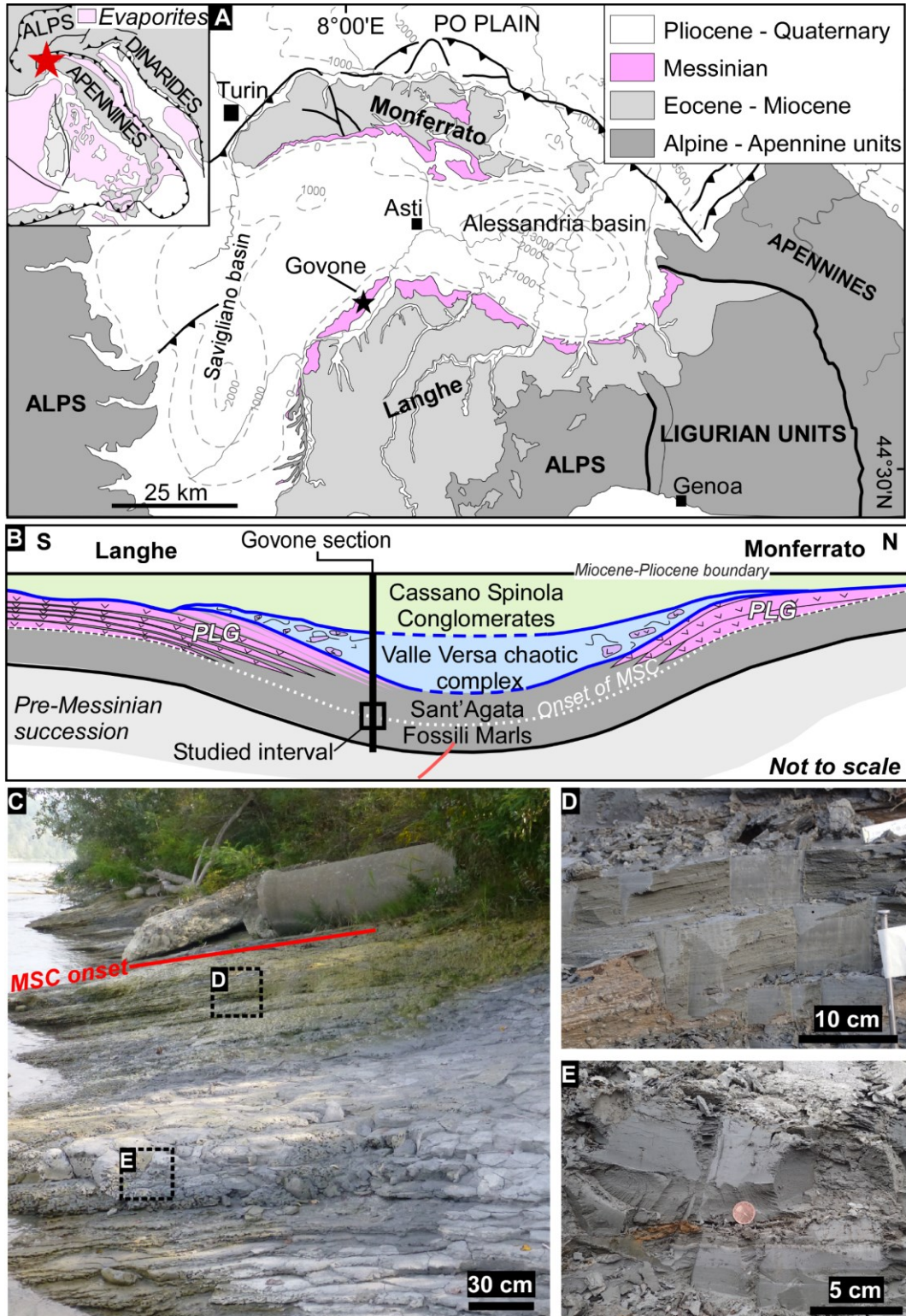


Figure 2.1 [previous page] – (A) Structural sketch map of the Piedmont Basin indicating the location of the Govone section (modified from Bigi et al., 1990). Inset in the top left corner: Piedmont Basin position (star) and distribution of the Messinian evaporites on the Italian peninsula and in the Western Mediterranean (modified from Natalicchio et al., 2019). Gray dotted lines indicate the isobaths of the base of the Pliocene. (B) Stratigraphic relationships among the Messinian deposits of the Piedmont Basin along a N–S profile, with the position of the Govone section (modified from Dela Pierre et al., 2011). (C) Overview of the Govone lithological cycles deposited across the Messinian salinity crisis onset (red line). The insets indicate the position of Figures 2.1D and 2.1E. (D) Laminated pre-MSC shale. Note lamination. (E) Homogenous pre-MSC marl. MSC: Messinian salinity crisis; PLG: Primary Lower Gypsum unit.

---

### 2.3.1.1. The Govone section

The Govone section (44°48'08" N; 8°07'34" E) is located at the southwestern margin of the Piedmont Basin (Fig. 2.1A, B) and comprises the entire Messinian succession (Bernardi, 2013; Dela Pierre et al., 2016, 2012). Here, the Sant'Agata Fossili Marls comprise 35 lithological cycles (Gm1–Gm35; Fig. 2.2) composed of shale and marl couplets with up to 2 m thickness (Fig. 2.1C, D, E). The upper cycles (Gm33 to Gm35) are disturbed to some extent by slumping. The Sant'Agata Fossili Marls are conformably overlain by the PLG unit, which is composed of nine lithological cycles (Gg1–Gg9; Fig. 2.2). Gypsum beds are up to 3 m thick and are made up of laminar gypsum, consisting of alternating clay-rich and gypsum-rich laminae. In some layers, flattened conical structures, composed of mm to cm-sized selenite crystals are present. They are interpreted as poorly developed branching selenite (*sensu* Lugli et al., 2010), whose growth was hampered by clay deposition (Dela Pierre et al., 2016). The PLG unit is overlain by clastic gypsum layers interbedded to laminated shales (Valle Versa chaotic complex; Dela Pierre et al., 2016). The Messinian succession terminates with fluvio-deltaic deposits (Cassano Spinola Conglomerates; Dela Pierre et al., 2016).

### 2.3.1.2. The MSC onset in the Govone section

The age model for the Govone section (Bernardi, 2013) is based on the identification of several age-diagnostic planktonic foraminifer bioevents correlated with the astronomically tuned Perales reference section (Manzi et al., 2013; Sierro et al., 2003, 2001). The most diagnostic bioevents identified by Bernardi (2013) and used for astrochronological correlations are: (1) the first abundant occurrence of *Turborotalita multiloba* in cycle Gm12, which is dated 6.415 Ma in the Perales section (Sierro et al., 2001); (2) the left/right coiling change of *Neogloboquadrina acostaensis* in cycle Gm14, recorded in cycle UA17 at Perales and dated at 6.36 Ma (Sierro et al., 2001); (3) the 1<sup>st</sup> influx of *Globorotalia scitula* in cycle Gm17, dated at 6.29 Ma in Perales (Sierro et al., 2001). A hiatus of about 50 kyr (approximately three precessional cycles), corresponding to a slump scar, was identified in the marls of cycle Gm17, immediately above this last bioevent (Bernardi, 2013); (4) a 2<sup>nd</sup> influx of *G. scitula* in cycle Gm24, which occurs within an acme interval of *T. multiloba*. This acme interval was reported in Perales between cycles UA23 and UA30 (Sierro et al., 2001). Consequently, the 2<sup>nd</sup> influx of *G. scitula* in cycle Gm24 is correlated with that recognized in Perales in cycle UA29 and dated at 6.10 Ma

(Sierro et al., 2001). Accordingly, the onset of the MSC – corresponding to the timeline at 5.97 Ma – was placed in the Govone section at the base of the marls of cycle Gm30, i.e. six precession cycles above the 2<sup>nd</sup> influx of *G. scitula* (Bernardi, 2013). Correlation with the Perales reference section indicates that the marls of cycle Gm30 correspond to the first gypsum bed of Perales (cycle PLG1, Manzi et al., 2013), which appears six cycles above the 2<sup>nd</sup> influx of *G. scitula* (Fig. 2.2A). In the Govone section, calcareous microfossils disappear in the marls of cycle Gm27, probably because of diagenetic processes favoring dissolution of calcareous tests (Bernardi, 2013). The disappearance of calcareous tests prevents the recognition of the calcareous nannofossil bioevents (abundance peak of *Sphenolithus abies*, followed by minor peaks of *Helicosphaera carteri* and *Umbilicosphaera rotula*) that were used to approximate the onset of the MSC in the absence of evaporites in different Mediterranean sub-basins (Gennari et al., 2018; Lozar and Negri, 2019) including the Piedmont Basin (Pollenzo section; Lozar et al., 2018). The position proposed by Bernardi (2013) and herein for the onset of the MSC does not correspond to the position reported by Dela Pierre et al. (2016), who placed the MSC onset one cycle below, i.e. cycle Gm29. The latter misplacement reflected an error in the bed by bed correlation of the upper part of the Govone section with the Perales section. Consequently, the work of Dela Pierre et al. (2016) should not be used as a reference for the age model of the Govone section. In the topmost part of the Sant'Agata Fossili Marls, the presence of slumps makes the identification of the cyclostratigraphic pattern problematic. However, it is still possible to recognize undeformed layers of organic-rich shales that correspond to the lower part of the three lithological cycles (Gm33, Gm34 and Gm35) immediately below the gypsum-bearing cycles of the PLG unit (Fig. 2.2A). To sum up, in the Govone section the onset of the MSC was identified in the upper part of the Sant'Agata Fossili Marls (Fig. 2.2A). The studied section includes four pre-MSC cycles (Gm26–Gm29) and four MSC cycles (Gm30–Gm33; Fig. 2.2B), the latter corresponding to the deep-water counterparts of the lower four PLG cycles exposed in the marginal part of the basin, with marls interpreted as lateral equivalents of gypsum (cf. Bernardi, 2013).

## 2.4. Materials and methods

Thirty-three excavated samples (four samples per cycle on average) were collected from cycles Gm26 to Gm33. For each sample an aliquot was dried and homogenized with an agate mortar. The obtained powders were divided in sub-aliquots to perform the analyses described below.

### 2.4.1. X-ray fluorescence (XRF) analyses

All samples were analyzed by X-ray fluorescence (XRF) for major and trace element contents at the Institute of Chemistry and Biology of the Marine (ICBM) Environment of the University of Oldenburg using an Axios plus, Analytical spectrometer. Di-lithium tetraborate (4.2 g) and ammonium nitrate (1 g) for preoxidation were added to 0.7 g of samples and then fused to glass beads. An in-house black shale reference material and international standard were used to check analytical accuracy, which was  $\leq 0.3\%$  for major (Al, Si, Ti) and  $\leq 4\%$  for trace (Zr) elements. Silicon, Ti and Zr were plotted against Al to assess relative enrichment or depletion with respect to the background aluminosilicates of the investigated

marls and shales (Calvert and Pedersen, 2007; Tribovillard et al., 2006). Ratios were calculated from wt%/wt% for Si/Al and Ti/Al and from (mg/kg)/wt% for Zr/Al.

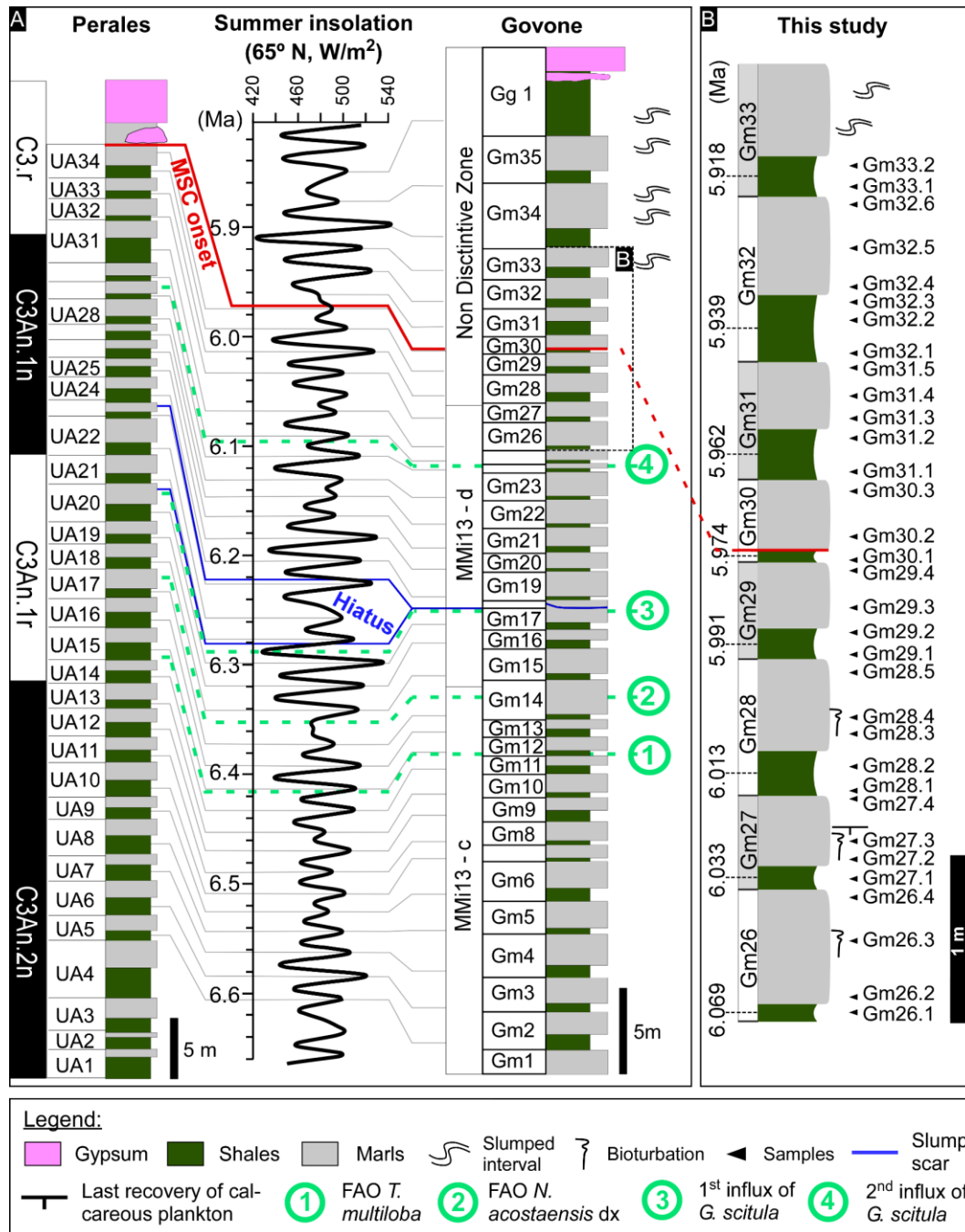


Figure 2.2 – (A) Govone section (Bernardi, 2013) tuned with astronomical solution (65° N summer insolation; Laskar et al., 2004) and correlated with the Perales section (Spain; Manzi et al., 2013; Sierro et al., 2001). (B) The investigated interval (cycles Gm26–Gm33). FAO: first abundant occurrence; MSC: Messinian salinity crisis.

### 2.4.2. Total organic and inorganic carbon contents

The total inorganic (TIC) and organic (TOC) carbon contents were measured at the Institute for Geology of the University of Hamburg. The sub-aliquots were further split into two fractions. One fraction was used to determine total carbon (TC) contents using a LECO SC-144DR Carbon Analyzer equipped with an infrared detector, heating the sample to 1350 °C. The other fraction was heated to 550 °C for 5 h to combust the organic carbon (OC) fraction, before temperature was raised to 1350 °C to determine total inorganic carbon (TIC) contents. Prior and after sample analysis, a Synthetic Carbon Leco 502-029 ( $1.01 \pm 0.02$  carbon%) standard was measured. TOC contents were determined with the formula  $TOC = TC - TIC$ .

### 2.4.3. Lipid biomarker analyses

Twenty-one samples were selected for lipid biomarker analyses (at least 2 samples per cycle) following the procedure described in Birgel et al. (2006). The total lipids were extracted by saponification with 6% potassium hydroxide in methanol in an ultrasonic bath (80 °C/2 h), followed by repeated ultrasonication with dichloromethane(DCM):methanol (3:1, v:v) until the organic solvent phase became colorless. To transfer also the released fatty acids after saponification (not further discussed in this study) to the organic solvent phase, extracts were treated with pure water and 10% hydrochloric acids to reach pH 2. The organic solvent phase with the extracts was reduced through a rotary evaporator, transferred into vials with DCM and dried. To prepare the extracts for gas chromatography (GC) analyses, a cleaning procedure was applied: the vials containing the total lipid extracts were washed with *n*-hexane to separate the *n*-hexane-soluble fraction (collected in a separate vial) from the dichloromethane-soluble fraction. The former was further split in four sub-fractions of increasing polarity (hydrocarbons, ketones, alcohols, and carboxylic acids) via solid phase extraction using a Supelco glass cartridge (6 ml, 500 mg, DSC-NH2). The hydrocarbon fraction was eluted with *n*-hexane and finally dried. For GC analysis, *n*-hexane was used as eluent. Compounds were identified with a Thermo Scientific Trace GC Ultra coupled to a Thermo Scientific DSQ II mass spectrometer (GC-MS) through comparison of retention times and published mass spectral data. A Fisons Instruments GC 8000 series equipped with a flame-ionization detector (GC-FID) was used for compound quantification. For the hydrocarbon fraction, 5 $\alpha$ -cholestane was used as internal standard for quantification. Helium was used as carrier gas for GC-MS runs, while for GC-FID analyses hydrogen was used. An Agilent HP-5MS UI fused silica column with a length of 30 m, a diameter of 0.25 mm, and a film thickness of 0.25  $\mu$ m was used for all analyses. The GC temperature program was: 50 °C (3 min); from 50 °C to 230 °C (held 2 min) at 25 °C/min; from 230 °C to 320 °C (held 20 min) at 6 °C/min.

#### 2.4.3.1. Compound-specific hydrogen and carbon stable isotopes

Compound-specific stable hydrogen ( $\delta^2\text{H}$ ; 16 samples) and carbon ( $\delta^{13}\text{C}$ ; 21 samples) isotope analyses of long-chain *n*-alkanes were performed at MARUM – Center for Marine Environmental Sciences, University of Bremen and Institute for Geology at Hamburg University, respectively.

Hydrogen isotopes were measured using a ThermoFisher Scientific Trace GC coupled via a pyrolysis reactor (operated at 1420 °C) to a ThermoFisher Scientific MAT 253 isotope mass spectrometer (GC–IRMS). The GC temperature program was: 120 °C held for 3 min, heating up to 320 °C with a rate of 5 °C/min and then held for 15 min.  $\delta^2\text{H}$  values were calibrated against  $\text{H}_2$  external reference gas and are reported in ‰ *vs.* Vienna Standard Mean Ocean Water (V–SMOW). The  $\text{H}^3+$ -factor varied from 5.05 to 5.14 during the measurement period. After every six runs an externally calibrated standard mixture of 16 *n*-alkanes was measured. Its long-term precision and accuracy were 3‰ and < 1‰, respectively. Analyses were conducted in duplicate when *n*-alkane concentrations were high enough. Average reproducibility in replicate analyses of the *n*-C<sub>31</sub> and *n*-C<sub>33</sub> alkanes was 1.1‰ and 1.8‰, respectively. Measurement of *n*-C<sub>29</sub> alkane  $\delta^2\text{H}$  values was impossible due to coelution with the internal standard (5 $\alpha$ -cholestane). Carbon isotopes were measured using an Agilent 6890 GC coupled via a Thermo Finnigan Combustion III to a Thermo Finnigan Delta Plus XL isotope mass spectrometer (GC–IRMS). The temperature program was: 50 °C held for 2 min, heating up to 320 °C with a rate of 12 °C/min and held for 35 min.  $\delta^{13}\text{C}$  values are reported in ‰ *vs.* Vienna Pee Dee Belemnite (V–PDB). After every 3 to 4 samples, an externally calibrated standard mixture of 15 *n*-alkanes was measured. Analyses were conducted at least in duplicates when *n*-alkanes concentrations were high enough. Average reproducibility in replicate analyses of the *n*-C<sub>31</sub> and *n*-C<sub>33</sub> alkanes was 0.3‰ and 0.4‰, respectively.  $\delta^{13}\text{C}$  values of *n*-C<sub>29</sub> alkane were not considered because of coelution with the internal standard.

#### 2.4.3.2. Carbon Preference Index

The odd-over-even predominance of higher plants derived *n*-alkanes was calculated through the Carbon Preference Index (CPI), according to the formula from Bray and Evans (1961):

$$\text{CPI} = 0.5 \times \left( \frac{\text{C}_{25} + \text{C}_{27} + \text{C}_{29} + \text{C}_{31} + \text{C}_{33}}{\text{C}_{24} + \text{C}_{26} + \text{C}_{28} + \text{C}_{30} + \text{C}_{32}} + \frac{\text{C}_{25} + \text{C}_{27} + \text{C}_{29} + \text{C}_{31} + \text{C}_{33}}{\text{C}_{26} + \text{C}_{28} + \text{C}_{30} + \text{C}_{32} + \text{C}_{34}} \right) \quad (2.1)$$

where  $\text{C}_n$  indicates the relative concentrations of C<sub>24</sub> to C<sub>34</sub> *n*-alkanes. CPI values in sediments can be used to trace the level of degradation and/or contamination of the terrestrial organic matter, with low values (CPI ≤ 2) indicating diagenetic/catagenetic degradation (e.g., Maysers et al., 2017; Pancost and Boot, 2004) and/or contamination from recycled and degraded organic matter from older sediments (Cortina et al., 2016).

## 2.5. Results

### 2.5.1. Lithological cycles, major and trace element distribution, and total organic carbon

The studied section consists of lithological cycles of shale and marl couplets ranging in thickness from 50 cm to 1 m (Fig. 2.1C, D, E, 2.3). The laminated shales are dark gray to olive (Fig. 2.1D), while marls are light gray and homogeneous (Fig.

2.1E); in the pre-MSC cycles (except for cycle Gm29) marls are bioturbated. Estimates on sedimentation rates are obtained by dividing the thickness of each cycle by the time of deposition and vary between 2.3 cm/kyr and 4.9 cm/kyr, with slightly higher average sedimentation rates in the MSC interval (4.1 cm/kyr) than in the pre-MSC cycles (3.1 cm/kyr; see Appendix B). No sedimentation rates are assessed for cycle Gm33 because of a slumped interval at its top. The Ti/Al, Si/Al, and Zr/Al ratios display a distinct cyclic pattern with a narrow amplitude. Lower values are found for shales and higher values for marls (Fig. 2.3; see Appendix B), although locally this pattern is partially blurred, particularly for the Si/Al ratio (Gm31–Gm32 cycles; see Section 2.6.1. for a discussion). Overall, the ratios slightly decrease from the pre-MSC to the MSC intervals (Fig. 2.3). The total organic carbon (TOC) contents vary in accord with lithological cyclicality, with higher contents (up to 3.1%) found for shales and lower contents (as low as 1.0%) obtained for marls (Appendix B).

### 2.5.2. *n*-Alkanes distribution and Carbon Preference Index (CPI)

The *n*-alkanes found in the Govone samples range from C<sub>18</sub> to C<sub>37</sub> with a strong odd-over-even predominance (Fig. 2.4). The most abundant homologues are the *n*-C<sub>31</sub> and *n*-C<sub>29</sub> alkanes, followed by *n*-C<sub>27</sub> and *n*-C<sub>33</sub> (Fig. 2.4; Appendix B). Longer homologues, i.e. *n*-C<sub>35</sub> and *n*-C<sub>37</sub>, were also detected. However, *n*-C<sub>35</sub> coelutes with lycopane (Fig. 2.4), a compound whose source is still uncertain (Sinninghe Damsté et al., 2003; Wakeham et al., 1993), while *n*-C<sub>37</sub> occurs only in trace amounts. Short chain *n*-alkanes (*n*-C<sub>18–23</sub>) show commonly very low abundances (< 1.5 µg/g TOC). The contents of long chain *n*-alkanes (C<sub>27</sub>, C<sub>29</sub>, C<sub>31</sub> and C<sub>33</sub>) mirror the lithological cyclicality, with highest contents in shales (up to 156 µg/g TOC) and lowest contents in marls (as low as 10 µg/g TOC). After the MSC onset, contents of long-chain *n*-alkanes increase (Fig. 2.3), reflected by an almost doubling of average contents from the pre-MSC (34 µg/g TOC) to the MSC cycles (58 µg/g TOC). The CPI ranges from 4.3 to 7.7 with highest values in shales (Fig. 2.3; Appendix B). Lower average CPI values are found after the onset of the MSC (for the pre-MSC: 6.2; MSC: 5.4; Fig. 2.3; Appendix B). The CPI values are persistently > 4 and show that sedimentary TOM is largely unaffected by recycled organic matter. The pronounced cyclicality reflected in proxy patterns suggests that aging of leaf waxes in soils is negligible (e.g., Aichner et al., 2018; Eglinton et al., 1997), indicating that possible temporal biases are smaller than the temporal spacing of sample intervals (minimum temporal spacing for biomarker analyses of ~2 kyr and ~3 kyr for pre-MSC and MSC, respectively).

### 2.5.3. *n*-Alkanes – carbon and hydrogen isotopes ( $\delta^{13}\text{C}$ and $\delta^2\text{H}$ values)

The  $\delta^{13}\text{C}$  values of *n*-C<sub>31</sub> and *n*-C<sub>33</sub> alkanes vary from –33.7‰ to –30.2‰, without a pattern depending on lithology (Fig. 2.3; Appendix B). On average,  $\delta^{13}\text{C}$  values slightly decrease in MSC sediments ( $\delta^{13}\text{C}_{31\text{-alk}}$ : –32.4‰;  $\delta^{13}\text{C}_{33\text{-alk}}$ : –32.3‰) compared to pre-MSC sediments ( $\delta^{13}\text{C}_{31\text{-alk}}$ : –31.7‰;  $\delta^{13}\text{C}_{33\text{-alk}}$ : –31.3‰; Fig. 2.3; Appendix B). The  $\delta^2\text{H}$  values of the *n*-C<sub>31</sub> and *n*-C<sub>33</sub> alkanes range from –191‰ to –140‰, yielding a cyclic pattern in phase with lithology. Shales are characterized

by  $^2\text{H}$ -depletion compared to marls (Fig. 2.3; Appendix B). Moreover, a shift toward higher  $\delta^2\text{H}$  values is observed in the MSC interval, mainly caused by stronger  $^2\text{H}$ -enrichment in shales (Fig. 2.3).

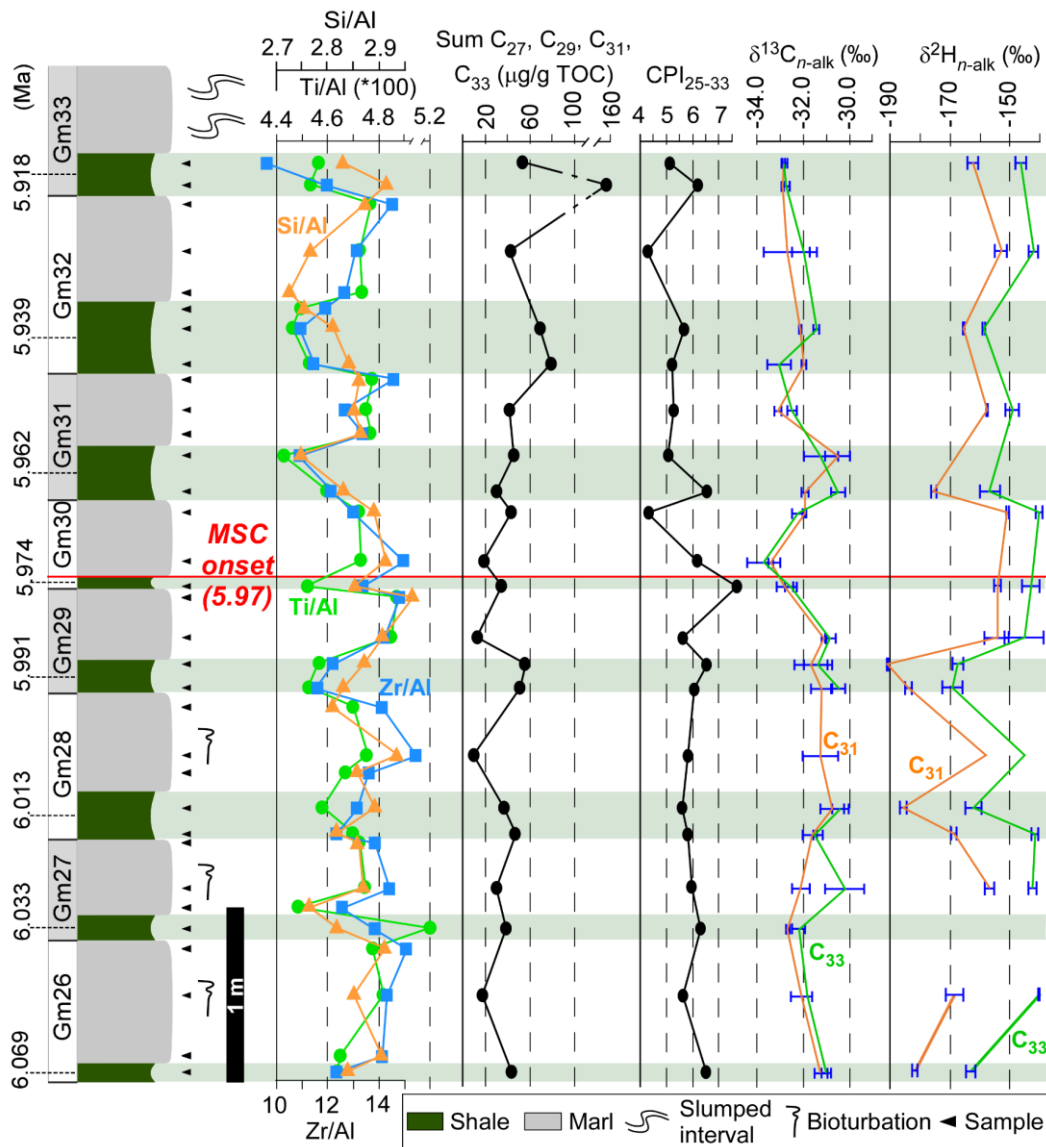


Figure 2.3 – From left to right of the Govone section: Si/Al, Ti/Al and Zr/Al ratios; sum of the odd-numbered C<sub>27</sub>-C<sub>33</sub> n-alkanes; Carbon Preference Index (CPI); compound-specific carbon ( $\delta^{13}\text{C}_{n\text{-alk}}$ ) and hydrogen ( $\delta^2\text{H}_{n\text{-alk}}$ ) stable isotope compositions. Error bars are indicated where measurements have been conducted at least in duplicate. Shaded pale green areas indicate shales. Ages reflecting the midpoint of shale layers (far left) are from Manzi et al. (2013).



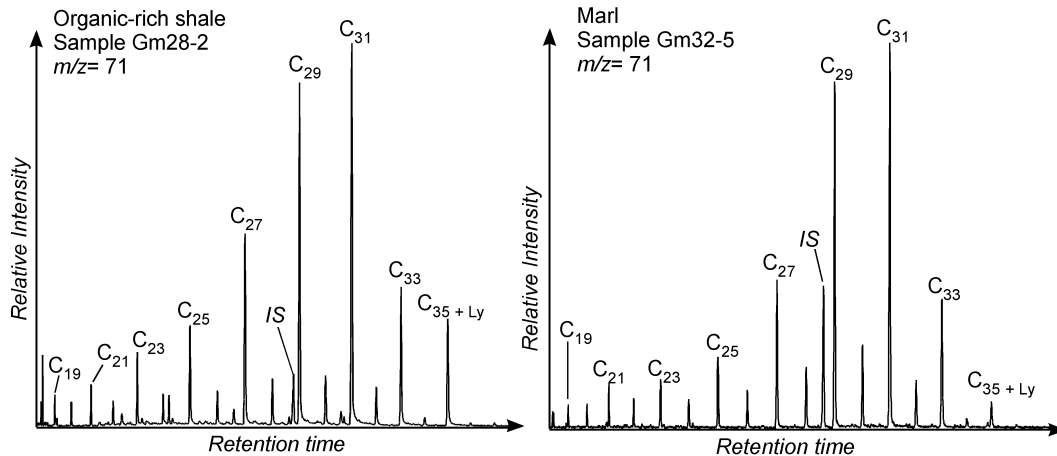


Figure 2.4 – Partial GC–MS chromatograms ( $m/z$  71) of sedimentary  $n$ -alkanes of two representative samples of shale (left) and marl (right). The  $n$ -C<sub>35</sub> alkane coelutes with lycopane (Ly). Note the relative intensity of the internal standard (IS) compared to the  $n$ -alkanes, indicating the higher content of lipids in shales compared to marls.

## 2.6. Discussion

### 2.6.1. Implications of changing elemental abundances

Fluctuations of Ti/Al, Si/Al, and Zr/Al ratios in marine sediments are commonly used as climate proxies. These element patterns allow to distinguish between arid phases, where aeolian input prevails, and humid phases characterized by dominant fluvial input (Calvert and Fontugne, 2001; Calvert and Pedersen, 2007; Martinez-Ruiz et al., 2015; Moller et al., 2012; Natalicchio et al., 2019; Schnetger et al., 2000; Wehausen and Brumsack, 2000, 1999). During arid phases, Ti is transported by wind in the detrital silt-sized fraction in the form of heavy minerals such as rutile, sphene, and ilmenite, resulting in an increase of the Ti/Al ratio in marine sediments (Moller et al., 2012; Schnetger et al., 2000; van der Laan et al., 2012). During humid climate phases, the Ti/Al ratio in marine sediments decreases due to higher fluvial input of clay minerals containing Al and a denser terrestrial vegetation cover, favoring chemical weathering – sink of Ti minerals – and lowering the deflation potential of the land surface (Moller et al., 2012; Schnetger et al., 2000). Similarly, Si/Al and Zr/Al ratios can be used to trace increased aeolian input, since wind derived material like loess is enriched in quartz and zircon, which are resistant to chemical and physical weathering (Schnetger, 1992; Wehausen and Brumsack, 1999). In the Govone section, fluctuation of element abundances follows lithological cyclicity (Fig. 2.3), although in places this pattern is partially blurred, particularly the Si/Al ratio (Gm31–Gm32 cycles). The most likely reason for the latter is enrichment of biogenic silica (e.g., Calvert and Pedersen, 2007) or authigenic minerals derived from dissolution and reprecipitation of biogenic silica (Badaut and Risacher, 1983; Schieber, 1996), which can bias climate reconstructions. Therefore, when using the Si/Al ratio as paleoclimate proxy, this approach must be validated by other proxies such as Ti/Al and Zr/Al ratios or the distribution of land-derived lipids (e.g.,  $n$ -alkanes). Despite some variability, the lower Ti/Al, Zr/Al, and Si/Al ratios of shales agree with more humid conditions, whereas the higher element/Al ratios in marls suggest increased aeolian transport

during more arid phases. Interestingly, a trend to lower ratios after the MSC onset suggests that the supply of heavy minerals and quartz, representing sources of Ti, Zr, and Si, weakened and input of clay minerals, representing a source of Al, apparently increased. Both scenarios agree with an increase of humidity during the early phase of the MSC, in line with recent reconstructions for northern, marginal sectors of the Mediterranean (Natalicchio et al., 2019). Humid to arid climate oscillations have already been recognized in the pre-MSC cycles of Govone (Bernardi, 2013) and other parts of the Mediterranean (e.g., Blanc-Valleron et al., 2002; Gennari et al., 2018; Kouwenhoven et al., 2006; Lozar et al., 2018; Sierro et al., 2003) based on changes in calcareous plankton assemblages attributed to precessional forcing. The cyclic element patterns described above confirm that the deposition of the microfossil deprived (pre-MSC) and apparently microfossil free (MSC) Govone strata was controlled by precession, with shales reflecting more humid phases at precession minima (insolation maxima) and marls reflecting more arid phases at precession maxima (insolation minima; see also Natalicchio et al., 2019 for the neighboring Pollenzo section).

### **2.6.2. Controls of climate on input of terrestrial organic matter (TOM)**

Long-chain *n*-alkanes (C<sub>27-33</sub>) are lipid biomarkers predominantly sourced by epicuticular leaf waxes of terrestrial vascular plants (Eglinton and Hamilton, 1967; Eglinton and Eglinton, 2008). Their highly refractory nature to degradation in the water column and sediments (Diefendorf and Freimuth, 2017) makes them excellent proxies for tracing the input of terrestrial organic matter (TOM) to the sediment (Diefendorf and Freimuth, 2017; Mayser et al., 2017; Pancost and Boot, 2004; Pedentchouk and Zhou, 2018; Schefuß et al., 2003; Vasiliev et al., 2019, 2017). Higher contents of long-chain *n*-alkanes in the shales than in marls of the Govone section suggest that TOM input was controlled by precession. The high CPI values (> 4) and the observed *n*-alkanes distribution confirm that plant waxes were mostly sourced by coeval terrestrial vegetation of the Piedmont Basin hinterland through fluvial transport, while aeolian transport was apparently of only minor importance (cf. Natalicchio et al., 2019). Taken together, such patterns confirm that TOM input was higher during humid phases at insolation maxima, corresponding to times of shale deposition and low element/Al ratios. Moister conditions favored the growth of vegetation in the hinterland and triggered more intense riverine runoff (Natalicchio et al., 2019), resulting in higher contents of long chain *n*-alkanes in shales. At times of marl deposition during more arid phases dominated by aeolian transport, the input of TOM and river discharge were significantly reduced (cf. Natalicchio et al., 2019). Apart from the variability between the different lithologies, a general increase of long chain *n*-alkane contents occurred after the onset of the MSC (Fig. 2.3). Such increase may reflect progressive shallowing of the basin along with a displacement of the coastline toward the basin depocenter or an increase of humidity, resulting in denser vegetation and more transport of TOM to the basin. Since neither sedimentological characteristics, nor geological regional reconstructions (e.g., Dela Pierre et al., 2011) indicate abrupt shallowing, the increase of *n*-alkane contents and the lowering of CPI values rather point to a shift toward more humid conditions after

the advent of the crisis. Such change toward moister conditions enhanced (1) soil weathering and the associated degradation of plant waxes in soils (Luo et al., 2012) and (2) riverine runoff and transport of TOM to the basin. This scenario is consistent with the observed increase of sedimentation rates from the pre-MSC (3.1 cm/kyr on average) to the MSC interval (4.1 cm/kyr on average).

### 2.6.3 Source of terrestrial organic matter: insights from compound-specific carbon isotopes

The  $\delta^{13}\text{C}_{31-33\text{-alk}}$  values obtained for the Govone section ranging from  $-33.7\text{‰}$  to  $-30.2\text{‰}$  indicate the predominance of  $\text{C}_3$  vegetation in the hinterland of the Piedmont Basin.  $\text{C}_3$  plants, mostly trees and shrubs adapted to cooler and humid conditions, use the Calvin-Benson-Bassham cycle and synthesize  $^{13}\text{C}$ -depleted long chain  $n$ -alkanes ( $\delta^{13}\text{C}_{n\text{-alk}} \sim -34\text{‰}$ ). Conversely,  $\text{C}_4$  plants, mostly grasses adapted to warm and arid conditions, use the Hatch-Slack pathway and produce less  $^{13}\text{C}$ -depleted lipids ( $\delta^{13}\text{C}_{n\text{-alk}} \sim -21\text{‰}$ ; Collister et al., 1994; Naafs et al., 2012; Tipple and Pagani, 2010). The predominance of  $\text{C}_3$  plants in the Messinian of the working area was already recorded using lipid biomarkers (Pollenzo section; Natalicchio et al., 2019), paleobotanical data (pollen and macrofossils), and paleovegetation models (Bertini, 2006; Bertini and Martinetto, 2011, 2008; Fauquette et al., 2006; Favre et al., 2007). All proxies indicate the predominance of arboreal  $\text{C}_3$  plants, whereas herbs were very scarce at least during insolation maxima. According to Bertini and Martinetto (2011), land plants were mostly represented by subtropical humid taxa in lowlands and conifers in uplands. However, only the subtropical-humid taxa are likely sources of  $n$ -alkanes in the studied section; otherwise the chain distribution pattern of  $n$ -alkanes would be different. The two main conifer families reported for the Piedmont Basin are *Pinaceae* and *Cupressaceae* (Bertini and Martinetto, 2011, 2008). *Pinaceae* produce very low amounts of plant waxes or even none (Diefendorf et al., 2015), whereas *Cupressaceae* produce abundant  $\text{C}_{33}$  to  $\text{C}_{37}$  odd-numbered  $n$ -alkanes (Diefendorf et al., 2015; Diefendorf and Freimuth, 2017). These  $n$ -alkanes are minor constituents in the Govone sediments, therefore conifers are at best a minor source of  $n$ -alkanes. The almost identical  $\delta^{13}\text{C}_{n\text{-alk}}$  values in the marls relative to shales further suggest that subtropical  $\text{C}_3$  plants still dominated at precession maxima even after the MSC onset. Since the MSC marls in intermediate to deep basins are considered as time equivalents of the marginal gypsum deposits (i.e. the PLG unit; Manzi et al., 2007; Dela Pierre et al., 2011; Natalicchio et al., 2019), our new data provide information on the type of vegetation at insolation minima during the first stage of the MSC; information that was not available before due to the absence of pollen and plant fossils in evaporites (cf. Bertini, 2006). To sum up, little variability of  $\delta^{13}\text{C}$  values of long chain  $n$ -alkanes in the Govone section point to the persistence of subtropical forests dominated by  $\text{C}_3$  plants throughout the investigated interval (i.e. between 6.07 and 5.92 Ma). Furthermore, slightly lower  $\delta^{13}\text{C}$  values in the upper part of the section probably reflect reduced water stress for  $\text{C}_3$  plants caused by an increased humidity after the MSC onset. Reduced water stress decreased water use efficiency of plants, leading to enhanced isotope fractionation upon uptake of carbon dioxide and hence lower  $\delta^{13}\text{C}$  values of leaf waxes (e.g., Diefendorf and Freimuth, 2017; Madhavan et al., 1991). Such pattern suggests that during the earliest phase of the MSC, the

precession-paced climate in the northern Mediterranean never became arid as seen for the central or southern parts of the Mediterranean, which were instead dominated by an open, xeric vegetation (Bertini et al., 1998; Bertini and Martinetto, 2011, 2008; Fauquette et al., 2006; Favre et al., 2007; Suc and Bessais, 1990).

#### **2.6.4. Hydrological changes across the onset of the MSC: insights from compound-specific hydrogen isotopes**

The  $\delta^2\text{H}$  values of terrestrial plant *n*-alkanes ( $\delta^2\text{H}_{n\text{-alk}}$ ) preserved in sediments represent a powerful tool for unravelling paleohydrological and paleoclimatic changes on continents (e.g., Andersen et al., 2001; Vasiliev et al., 2017, 2015). The hydrogen isotopic signature of plant *n*-alkanes mainly depends on the  $\delta^2\text{H}$  value of meteoric water, the main hydrogen source for terrestrial plants (Sachse et al., 2012), and, to a lesser extent, on isotope enrichment due to evapotranspiration and water-use efficiency of the respective plant (Kahmen et al., 2013b, 2013a; Sachse et al., 2012; Tipple and Pagani, 2010). In particular,  $^2\text{H}$ -enrichment in waxes can result from (1) reduced rainfall, (2) increased evapotranspiration, (3) a high condensation temperature under warmer climate, (4) replacement of  $\text{C}_3$  grasses by  $\text{C}_4$  grasses, (5) downslope movements of vegetation belts, or (6) a change toward a  $^2\text{H}$ -enriched moisture source (Collins et al., 2013; Dansgaard, 1964; Herrmann et al., 2017; Hou et al., 2008; Jaeschke et al., 2018; Kahmen et al., 2013b, 2013a; Risi et al., 2008; Rozanski et al., 1993; Sachse et al., 2012; Tipple and Pagani, 2010). In the Govone section,  $\delta^2\text{H}_{n\text{-alk}}$  values show a cyclic pattern in phase with lithological cyclicity (with more negative  $\delta^2\text{H}_{n\text{-alk}}$  values in shales) and other paleoclimatic proxies such as element/Al ratios and *n*-alkane contents (Fig. 2.3). Such a pattern suggests that  $\delta^2\text{H}$  variability was influenced by climate change at precession scale. Because  $\delta^{13}\text{C}_{n\text{-alk}}$  values indicate persistent  $\text{C}_3$  plant dominance, a change of vegetation can be excluded. Similarly, downslope and upslope vegetation shifts are unlikely to have caused such oscillations, although some minor effects cannot be excluded. In fact, to produce the observed differences in  $\delta^2\text{H}_{n\text{-alk}}$  values between precession maxima and minima, altitudinal shifts of about 1000 m are needed; for modern environments, gradients of 15–20‰/1000 m have been reported (Jaeschke et al., 2018 and references therein). In the modern and Messinian alpine environments, characterized by strong vegetation zonation, it is unlikely that shifts of such high magnitude may have occurred without a change in  $\text{C}_3$  vegetation (e.g., conifer expansion). Such a severe shift is not recorded in the Govone data set. Therefore, the main cause of  $\delta^2\text{H}_{n\text{-alk}}$  fluctuations must have been climate change driven by precession, including changes in (1) the amount and intensity of rainfall, (2) evapotranspiration, (3) temperature, and (4) relative moisture sources. In the present-day northern Mediterranean south of the Alps, moisture is mainly sourced from the Western Mediterranean, the North Atlantic and, to a lesser extent, from Central Europe (e.g., Celle-Jeanton et al., 2001; Drumond et al., 2011; Gómez-Hernández et al., 2013; Sodemann and Zubler, 2010). The resulting precipitation is typified by mixed  $\delta^2\text{H}$  signatures, with the North Atlantic supplying  $^2\text{H}$ -depleted rainfall compared to the Mediterranean. Unfortunately, no data are available for moisture sourced from central Europe (Celle-Jeanton et al., 2001). Interestingly,

climate models indicate that at least until the Pleistocene, the Western and northern Mediterranean were affected by precession-driven changes in the intensity of the Mediterranean storm track (Kutzbach et al., 2014; Toucanne et al., 2015). The Mediterranean storm track is related to the extension of North Atlantic depressions toward the Mediterranean, bringing additional precipitation from the North Atlantic during insolation maxima (Meijer and Tuenter, 2007; Toucanne et al., 2015). Assuming similar moisture sources for the northern Mediterranean during the Late Messinian and considering that the Piedmont Basin was influenced by precession-controlled climate oscillations (Natalicchio et al., 2019), we suggest that the lower  $\delta^2\text{H}_{n\text{-alk}}$  values in shales reflect a higher contribution of moisture from the North Atlantic during insolation maxima when the Mediterranean storm track was more intense (Fig. 2.5A). The resulting increased rainfall and lower evapotranspiration contributed to  $^2\text{H}$ -depletion of long chain  $n$ -alkanes. As insolation maxima are expected to coincide with higher temperatures, the temperature effect cannot explain our observations. Conversely, the higher  $\delta^2\text{H}_{n\text{-alk}}$  values in marls would indicate a weakening of the Mediterranean storm track at insolation minima (cf. Kutzbach et al., 2014; Toucanne et al., 2015), resulting in (1) relatively increased  $^2\text{H}$ -enriched moisture from Mediterranean sources, (2) decreased precipitation, and (3) higher evapotranspiration rates (Fig. 2.5B). Expected lower temperatures had apparently not a major effect on the  $^2\text{H}$  isotope patterns. The increase of  $\delta^2\text{H}_{n\text{-alk}}$  values across the MSC onset is mostly due to higher values in shales. Such a pattern would suggest an overall shift toward more arid conditions at first glance. However, this interpretation would be in conflict with the other proxies (lower element/Al ratios, increased contents of long chain  $n$ -alkanes, their lower CPI and lower  $\delta^{13}\text{C}$ -values) and the paleovegetation reconstructions for the northern Mediterranean (e.g., Bertini and Martinetto, 2011), all pointing to an increase of humidity after the MSC onset. We consequently put forward the scenario that the observed  $^2\text{H}$ -enrichment was caused by a progressively increasing moisture contribution from the Mediterranean. The observed increase of  $\delta^2\text{H}_{n\text{-alk}}$  values coincided with a reduction of the Atlantic-Mediterranean connection at the onset of the MSC (cf. Flecker et al., 2015; Krijgsman et al., 2018; Roveri et al., 2014a). Indeed, climate simulations for the Mediterranean area in the Late Miocene predict that the net hydrological budget, especially in the Western Mediterranean, was smaller than today because of basin restriction (Gladstone et al., 2007; Marzocchi et al., 2016; Meijer and Tuenter, 2007; Simon et al., 2017). It is consequently likely that evaporation was enhanced, resulting in an increased supply of  $^2\text{H}$ -rich moisture from the Mediterranean (Fig. 2.5C). Due to these changes (1)  $^2\text{H}$  became enriched in Mediterranean seawater (2) as well as in Mediterranean-derived moisture, and (3) Mediterranean-sourced ( $^2\text{H}$ -enriched) precipitation increased, causing an increase of humidity in the northern Mediterranean across the onset of the MSC.

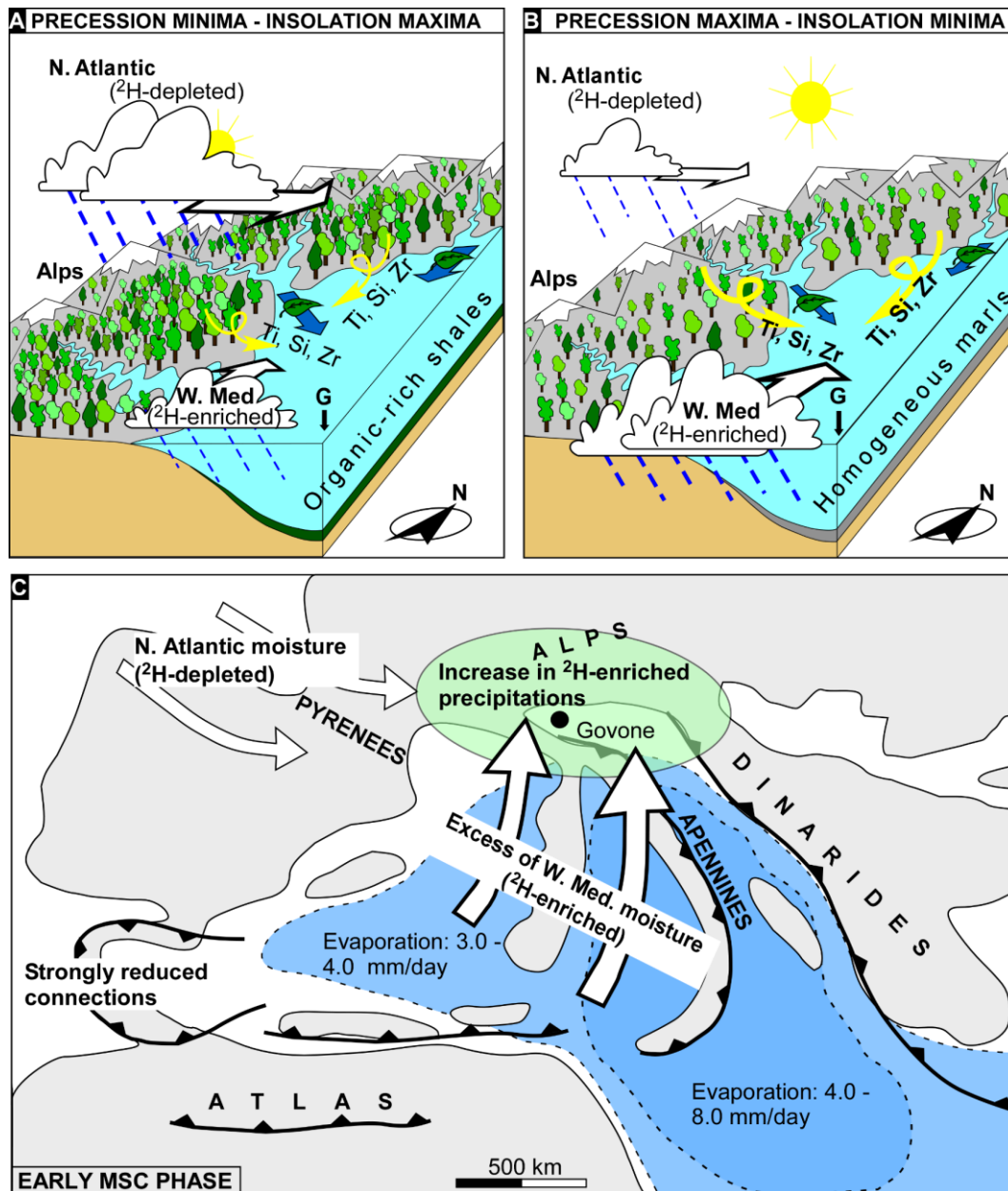


Figure 2.5 – Paleoclimatic and paleohydrological reconstruction of the Piedmont Basin at precession minima/insolation maxima (A) and precession maxima/insolation minima (B) across the onset of the MSC. (C) Reconstruction of the northern Mediterranean hydrological pattern during the early MSC. Areas of major evaporation (according to Gladstone et al., 2007) are indicated in shades of blue. Green shaded area indicates the northern Mediterranean. Paleogeography modified from Popov et al. (2006). G: Govone section; MSC: Messinian salinity crisis; N. Atlantic: North Atlantic; W. Med.: Western Mediterranean.

## 2.7. Conclusions

The distribution of major elements and plant-wax derived long chain *n*-alkanes, as well as their  $\delta^{13}\text{C}_{n\text{-alk}}$  and  $\delta^2\text{H}_{n\text{-alk}}$  values, allowed tracing climate variability and hydrological changes in the northern Mediterranean basin across the onset of the Messinian salinity crisis (MSC). In the studied Govone section, fluctuations of major and trace elements (Ti/Al, Si/Al, Zr/Al ratios) and of long chain *n*-alkane contents are in phase with lithological cyclicity, confirming the control of precession-paced climate change on the deposition of pre-MSC and MSC strata. The observed cyclic pattern is mirrored by the  $\delta^2\text{H}$  values of long chain *n*-alkanes, indicating the same precession-controlled driving forces had induced hydrological change. Shales, characterized by lower element/Al ratios and lower  $\delta^2\text{H}_{n\text{-alk}}$  values as well as higher long chain *n*-alkane contents, were deposited under more humid conditions and higher riverine runoff at precession minima. Moister climate was favored by an intensified Mediterranean storm track, supplying  $^2\text{H}$ -depleted moisture from the North Atlantic. Conversely, marls with their higher element/Al ratios, higher  $\delta^2\text{H}_{n\text{-alk}}$  values, and lower long chain *n*-alkane contents reflect drier climate and reduced continental input at precession maxima and times of a weakened Mediterranean storm track. The  $\delta^{13}\text{C}_{n\text{-alk}}$  values indicate that  $\text{C}_3$  plants were the dominant source of terrestrial organic matter, agreeing with a persistently humid climate in the northern Mediterranean. Moreover, an increase of humidity, which is superimposed on the precession-controlled climate fluctuations, is inferred for the early phase of the MSC in the study area. This shift most likely reflects a hydrological change in the Mediterranean triggered by further restriction of the Atlantic-Mediterranean connection, which enhanced evaporation of Mediterranean seawater. Such evaporation produced  $^2\text{H}$ -enriched moisture, which led to progressively  $^2\text{H}$ -enriched precipitation in the study area after the onset of the MSC.

## 2.8. Acknowledgments

We thank S. Beckmann (Universität Hamburg) for technical support during organic geochemical analyses, E. Grundken and C. Lehnert (Universität Oldenburg) for XRF analysis, J. Richarz (Universität Hamburg) for the analysis of TOC contents, R. Gennari (University of Turin) for help with the age model, and N. Burdanowitz (Universität Hamburg) for support in the application of molecular proxies. This project has received funding from the European Union's Horizon 2020 research and innovation program under the Marie Skłodowska-Curie grant agreement No. 658252 to M. Natalicchio and from University of Torino grant to F. Dela Pierre. M. Sabino was funded by a doctoral scholarship provided by the Landesgraduiertenförderung of the state of Hamburg. E. Schefuß is funded and the hydrogen isotope analyses are supported by MARUM – Centre for Marine Environmental Sciences, University of Bremen. The article is further based upon work from COST Action “Uncovering the Mediterranean salt giant” (MEDSALT) supported by COST (European Cooperation in Science and Technology). Insightful comments of two anonymous reviewers helped to improve the manuscript.





# Chapter 3

## **THE RESPONSE OF WATER COLUMN AND SEDIMENTARY ENVIRONMENTS TO THE ADVENT OF THE MESSINIAN SALINITY CRISIS: INSIGHTS FROM AN ONSHORE DEEP-WATER SECTION (GOVONE, NW ITALY)**

---

*The third Chapter of the thesis has been published in Geological Magazine as: Sabino, M., Dela Pierre, F., Natalicchio, M., Birgel, D., Gier, S., Peckmann, J., 2020. The response of water column and sedimentary environments to the advent of the Messinian salinity crisis: insights from an onshore deep-water section (Govone, NW Italy). Geological Magazine, 1–17. Article reproduced with permission, not for further re-distribution or re-use.*

### **3.1. Abstract**

During Messinian time, the Mediterranean underwent hydrological modifications culminating 5.97 Ma ago with the Messinian salinity crisis (MSC). Evaporite deposition and alleged annihilation of most marine eukaryotes were taken as evidence of the establishment of basin-wide hypersalinity followed by desiccation. However, the paleoenvironmental conditions during the MSC are still a matter of debate, chiefly because most of its sedimentary record is buried below the abyssal plains of the present-day Mediterranean Sea. To shed light on environmental change at the advent and during the early phase of the MSC, we investigated the Govone section from the Piedmont Basin (NW Italy) using a multidisciplinary approach (organic geochemical, petrographic, and carbon and oxygen stable isotope analyses). The Govone section archives the onset of the crisis in a succession of organic-rich shales and dolomite-rich marls. The MSC part of the succession represents the deep-water equivalent of sulphate evaporites deposited at the basin margins during the first phase of the crisis. Our study reveals that the onset of the MSC was marked by the intensification of water-column stratification, rather than the establishment of widespread hypersaline conditions. A chemocline divided the water column into an oxygen-depleted, denser and more saline bottom layer and an oxygenated, upper seawater layer influenced by freshwater inflow. Vertical oscillations of the chemocline controlled the stratigraphic architecture of the sediments pertaining to the first stage of the MSC. Accordingly, temporal and spatial changes of water masses with different redox chemistries must be considered when interpreting the MSC event.

### **3.2. Introduction**

During Messinian time (7.25–5.33 Ma) the Mediterranean area underwent progressive environmental and hydrological changes, which culminated c. 5.97 Ma ago with the Messinian salinity crisis (MSC; Camerlenghi and Aloisi, 2020; Hsü et al., 1973b; Roveri et al., 2014a). During this event, the Mediterranean Sea turned into the youngest Salt Giant of Earth history (Warren, 2010) as a response of its

isolation from the global ocean caused by the restriction of the Mediterranean–Atlantic gateways (Capella et al., 2019; Flecker et al., 2015; Krijgsman et al., 2018). One of the most striking effects of the hydrological changes that affected the basin was the intensification of water-column stratification and consequent development of bottom-water anoxia starting at c. 6.7 Ma (Roveri et al., 2014a). The deterioration of paleoenvironmental conditions was recorded by the deposition of precession-paced alternations of organic-rich shales, diatomites, and marls (Hilgen and Krijgsman, 1999; Krijgsman et al., 2002; Sierro et al., 1999). Starting from 5.97 Ma (Manzi et al., 2013), the shale-diatomite-marl successions were replaced at the basin margins by couplets of sulphate evaporites and organic-rich shales of the Primary Lower Gypsum unit (PLG; Roveri et al., 2008b), marking the first stage of the MSC (5.97–5.60 Ma; Roveri et al., 2014a). The deposition of evaporites has been considered as compelling evidence of the development of hypersaline conditions, which resulted in the demise of most marine eukaryotes (e.g., Bellanca et al., 2001), but promoted the rise of halophilic prokaryotes (Birgel et al., 2014; Turich and Freeman, 2011). The PLG unit passes laterally in intermediate to deep-water settings (> 200 m depth) into evaporite-free successions, composed of shales alternating with carbonates and/or dolomite-rich marls barren of calcareous microfossils (Dela Pierre et al., 2011; Manzi et al., 2011, 2007; Natalicchio et al., 2019; Roveri et al., 2014a). After the formulation of the ‘deep desiccated basin model’ in the 1970s (Hsü et al., 1973b), the paleoenvironmental conditions of the Mediterranean water column and seafloor during the MSC are still a matter of debate. The scarcity or lack of body fossils in MSC sediments, the lack of modern analogues for the Messinian evaporites, and the inaccessibility of the offshore evaporites have hampered the development of a widely accepted scenario (Camerlenghi and Aloisi, 2020; Rouchy and Caruso, 2006; Roveri et al., 2014a; Ryan, 2009).

The analysis of molecular fossils (lipid biomarkers) preserved in Messinian evaporites and their intermediate- to deep-water lateral equivalents provides fundamental information for the reconstruction of the Mediterranean hydrological cycle and paleoenvironments (Natalicchio et al., 2019; Sabino et al., 2020b; Vasiliev et al., 2017). This approach is a valuable tool to unveil the conditions in the water column during the MSC. Organic geochemical investigations targeting abyssal evaporites (Christeleit et al., 2015) and Messinian salts (Isaji et al., 2019b) revealed that evaporites were deposited under a stratified water column during the latest MSC phases. These results agree with recent hydrological models (de Lange and Krijgsman, 2010; García-Veigas et al., 2018; Simon and Meijer, 2017). In contrast, only a few geochemical data are available for the sediments deposited during the early stages of the MSC (Isaji et al., 2019a; Kenig et al., 1995; Sinninghe Damsté et al., 1995b). These studies all describe organic-rich shales of the PLG unit, depicting a stratified basin that received freshwater from rivers (Natalicchio et al., 2019, 2017; Sabino et al., 2020b) and/or low-salinity water from the Paratethys (Grothe et al., 2020). To shed new light on the response of the water column and sediments to the advent of the MSC, we studied sedimentary strata exposed in the Govone section (Piedmont Basin, NW Italy). In this section, the onset of the crisis is archived in a sequence of organic-rich shales and marls, representing the deep-water equivalents of primary sulphate evaporites deposited at the basin margins (Gennari et al., 2020; Sabino et al., 2020b). These sediments

have recently been investigated to reconstruct the paleoclimate and paleohydrologic variability in the northern Mediterranean across the onset of the MSC (Sabino et al., 2020b). This previous study, which was based on inorganic geochemical proxies and on carbon and hydrogen stable isotope composition of lipids from terrestrial plant waxes, revealed fluctuations between more humid (shales) and more arid (marls) climates and an evolution towards moister conditions after the onset of the MSC (Sabino et al., 2020b). Here, we focus on the same succession studied by Sabino et al. (2020b), integrating stratigraphic, petrographic, carbon and oxygen stable isotope analyses, and the study of molecular fossils to reconstruct the paleoenvironments. This approach allows us to reconstruct the environmental changes across the onset of the MSC and reveals how these changes influenced the stratigraphic architecture of the sediments deposited during times of change in the Mediterranean realm.

### **3.3. Geological setting**

#### **3.3.1. The Messinian succession in the Piedmont Basin**

The Piedmont Basin (NW Italy; Fig. 3.1A) is a wedge-top basin located on the inner side of the SW Alpine arc filled with upper Eocene – Messinian sediments (Mosca et al., 2010; Rossi et al., 2009). The Messinian succession is exposed on the uplifted southern and northern margins of the basin and starts with outer shelf to slope marls and shales (Sant’Agata Fossili Marls; Tortonian – lower Messinian; Sturani and Sampò, 1973). These deposits, characterized by the repetition of shale and marl couplets, record progressively more restricted conditions heralding the onset of the MSC (Sturani, 1973; Sturani and Sampò, 1973). The lithological cyclicity was controlled by climate fluctuations driven by precession, with shales representing more humid conditions at precession minima and marls recording more arid conditions at precession maxima (Natalicchio et al., 2019; Sabino et al., 2020b). At the basin margins, this unit is overlain by shale and gypsum couplets belonging to the PLG unit (Fig. 3.1B). In settings of intermediate water depth, the gypsum beds of the lowermost PLG cycles are transitional to carbonate-rich layers and marls hosting fossilized microbial mats of putative sulfide-oxidizing bacteria, in turn passing in deeper-water settings into dolomite-rich marls (Fig. 3.1C; Dela Pierre et al., 2016, 2012; Natalicchio et al., 2019, 2017; Sabino et al., 2020b). In the basin depocenter, only shales and marls are found (Irace et al., 2009). The PLG unit and its deeper-water equivalents are overlain by chaotic and clastic gypsum facies (Valle Versa chaotic complex; Dela Pierre et al., 2007; Irace et al., 2005), which are correlated to the Resedimented Lower Gypsum unit deposited during the second stage of the MSC (5.60–5.55 Ma; Roveri et al., 2014a). The Messinian succession is completed by fluvio-deltaic and lacustrine sediments, referred to as the Cassano Spinola Conglomerates (Fig. 3.1C; Dela Pierre et al., 2016, 2011; Sturani, 1976), recording the third stage of the MSC (5.55–5.33 Ma; Roveri et al., 2014a).

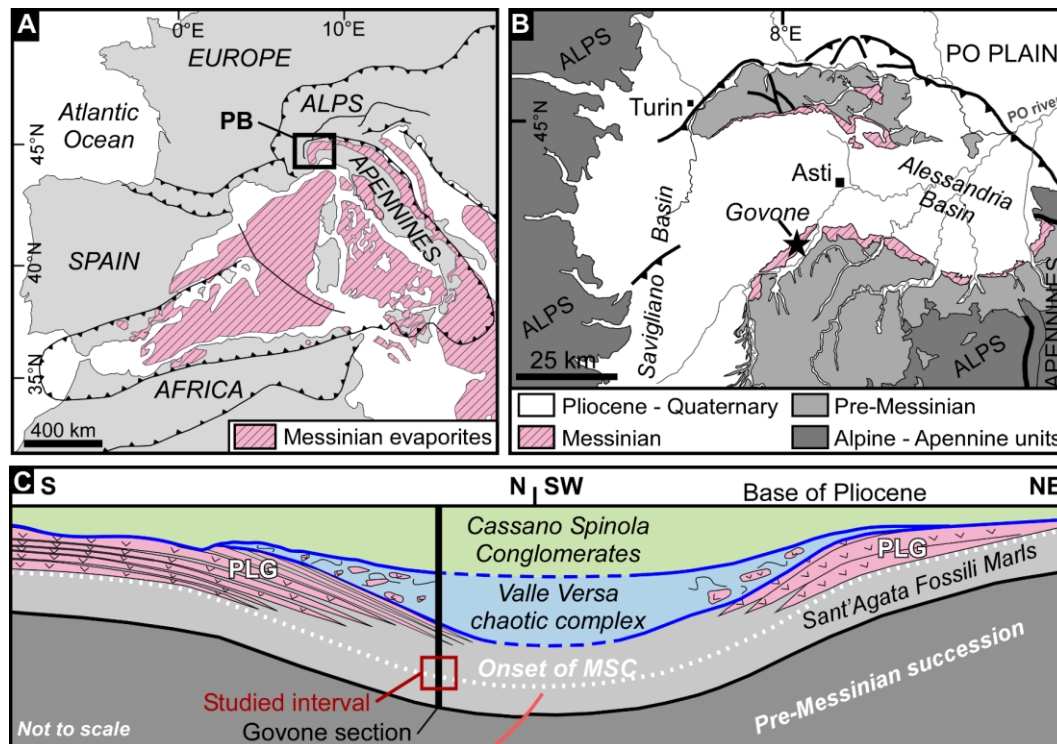


Figure 3.1 – (A) Distribution of the Messinian evaporites (pink) in the Western Mediterranean Basin and location of the Piedmont Basin (black box; modified from Manzi et al., 2013). (B) Structural sketch map of the Piedmont Basin (modified from Bigi et al., 1990); the star indicates the location of the Govone section. (C) Schematic profile of the Piedmont Basin, showing the stratigraphic architecture of the Messinian succession; the Govone section (vertical black bar) and the studied interval (red box) are indicated. Note that the gypsum beds are progressively younger towards the depocenter. MSC: Messinian salinity crisis; PB: Piedmont Basin; PLG: Primary Lower Gypsum (modified from Dela Pierre et al., 2011).

### 3.3.2. The Govone section and the position of the MSC onset

In the Govone section, located at the southern margin of the Piedmont Basin (44°48'08" N; 8°07'34" E; Fig. 3.1B), the whole Messinian succession is exposed, starting with 35 lithologic cycles up to 2 m in thickness (Gm1–Gm35; Fig. 3.2; Bernardi, 2013; Bernardi et al., 2012; Dela Pierre et al., 2016; Gennari et al., 2020; Sabino et al., 2020b). These cycles consist of shale/marl couplets and belong to the Sant'Agata Fossili Marls. This unit is conformably overlain by the PLG unit (Fig. 3.1B), made up of nine cycles (Gg1–Gg9) of shales and gypsum-rich layers; the latter consist of flattened conical structures formed by millimeter-sized gypsum crystals enclosed in laminated gypsiferous silty mudstones (Bernardi, 2013). The PLG is in turn overlain by shales and clastic evaporites belonging to the Valle Versa chaotic complex, finally followed by fluvio-deltaic deposits of the Cassano Spinola Conglomerates (Fig. 3.1B; Bernardi, 2013; Dela Pierre et al., 2016; Sabino et al., 2020b). The age model for the Govone section (Gennari et al., 2020) had already been adopted by Sabino et al. (2020b). The position of the MSC onset (5.97 Ma; Manzi et al., 2013) was defined through the identification of diagnostic planktonic foraminifer bioevents, the ages of which were calibrated through the correlation with the astronomically tuned Perales section (Fig. 3.2; Manzi et al., 2013; Sierro

et al., 2003, 2001). The main bioevents identified by Gennari et al. (2020) are: (1) the first abundant occurrence (FAO) of *Turborotalita multiloba* in cycle Gm12, occurring in cycle UA15 in Perales and dated 6.415 Ma (Sierro et al., 2001); (2) the left/right coiling change of *Neogloboquadrina acostaensis* in cycle Gm14, identified in Perales at cycle UA17 and dated 6.36 Ma (Sierro et al., 2001); (3) the first influx of *Globorotalia scitula* in cycle Gm17, dated 6.29 Ma in the Perales section (cycle UA20; Sierro et al., 2001); and (4) a second influx of *Globorotalia scitula* in cycle Gm24, which falls within an acme interval of *T. multiloba*. For the Perales section, Sierro et al. (2001) reported this acme between cycles UA23 and UA30, allowing Gennari et al. (2020) to correlate the second influx of *G. scitula* in the Govone section with the second influx recognized in cycle UA29 in the Perales section and dated at 6.10 Ma. Since the second influx of *G. scitula* occurs six precession cycles below the onset of the crisis in the Perales section (Sierro et al., 2001), the MSC onset in Govone was placed at the base of the marls of cycle Gm30 (Fig. 3.2; Gennari et al., 2020; Sabino et al., 2020b), which accordingly correspond to the gypsum bed in cycle PLG1 of Perales (Fig. 3.2; Manzi et al., 2013). According to the adopted model, the uppermost six Sant'Agata Fossili Marls cycles below the first local gypsum bed (Gg1 cycle) represent the deep-water counterparts of the lowermost PLG cycles (Fig. 3.2), with marls representing the time equivalents of the shallow-water marginal gypsum (Gennari et al., 2020; Sabino et al., 2020b). In this study we investigate four pre-MS (Gm26–Gm29) and four MS (Gm30–Gm33) cycles, representing a time interval of c. 150 ka. Younger strata of the Govone section containing gypsum (Fig. 3.1C) are not studied here.

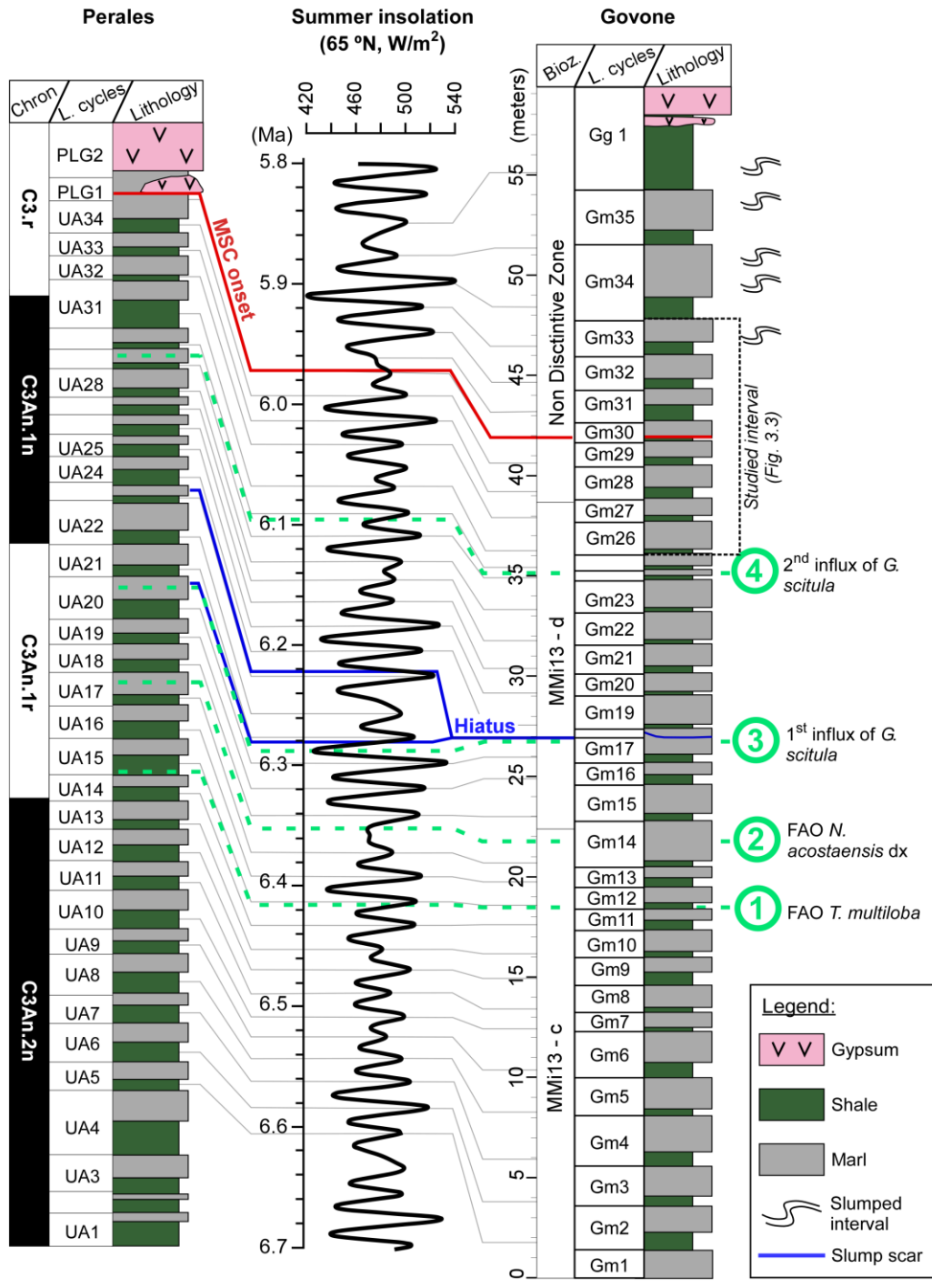


Figure 3.2 – Tuning of the Govone section with the astronomical solution (65° N summer insolation; Laskar et al., 2004) and correlation with the Perales section (Spain; Manzi et al., 2013; Sierro et al., 2001). Numbers in circles on the right represent the main bioevents reported in the main text. Bioz.: biozones; FAO: first abundant occurrence (modified from Gennari et al., 2020; Sabino et al., 2020b).

## **3.4. Materials and methods**

### **3.4.1. Petrography and mineralogy**

A total of 33 fresh, unweathered samples were excavated from cycles Gm26 to Gm33 (on average, 4 samples per cycle); the Govone sedimentary rocks tend to be well preserved and continuously exposed due to ongoing erosion in the river bed. A total of 18 slabs and thin-sections were obtained from representative samples (10 from pre-MSC cycles and 8 from MSC cycles) and studied at the Department of Earth Sciences, University of Turin by optical (transmitted, reflected, and UV light) and scanning electron microscopy (SEM). SEM analyses were performed on carbon-coated stubs for morphological analyses and on carbon-coated, polished thin-sections for semi-quantitative elemental analysis and backscattered electron imagery, using a JEOL JSM IT300LV scanning electron microscope equipped with an energy-dispersive EDS Oxford Instrument Link System microprobe (University of Turin).

X-ray diffraction (XRD) analyses were performed on all 33 samples using a Panalytical X'Pert PRO diffractometer (CuK $\alpha$  radiation, 40 kV, 40 mA, step size 0.0167, 5 s per step) at the Department of Geodynamics and Sedimentology, University of Vienna. The samples were loaded in the sample holders as oriented powders. The X-ray diffraction patterns were interpreted using the Panalytical software 'X'Pert High score plus' to determine the carbonate phase mineralogy.

### **3.4.2. Carbon and oxygen stable isotopes**

Carbon ( $\delta^{13}\text{C}$ ) and oxygen ( $\delta^{18}\text{O}$ ) bulk-rock stable isotope analyses were performed on 9 samples (pre-MSC cycles, 1 sample; MSC cycles, 8 samples). These analyses add to those of Bernardi (2013) who analyzed 20 samples, 12 from pre-MSC cycles and 8 from MSC cycles. Analyses were performed at the MARUM stable isotope laboratory (University of Bremen). The 9 new samples were measured at 75 °C on a Finnigan MAT 252 gas isotope ratio mass spectrometer connected to a Kiel III automated carbonate preparation device. The instrument was calibrated against an inhouse standard (ground Solnhofen limestone), which in turn was calibrated against the NBS 19 calcite standard. Over the measurement period, the standard deviations of the in-house standard were 0.04‰ for  $\delta^{13}\text{C}$  and 0.06‰ for  $\delta^{18}\text{O}$  values. Data are reported in delta-notation *vs.* V-PDB. When dolomite was the only carbonate phase, the  $\delta^{18}\text{O}$  values were corrected for -0.8‰ for measurements from Bernardi (2013; analyses performed at 50 °C; Sharma and Clayton, 1965) and -1.2‰ for the new measurements (analyses performed at 75 °C; Kim et al., 2007; Rosenbaum and Sheppard, 1986). The correction was necessary to account for the fractionation effect during the phosphoric acid reaction (Appendix C).

### **3.4.3. Total inorganic and organic carbon contents**

Total inorganic (TIC) and organic (TOC) carbon contents were measured at the Institute for Geology of the University of Hamburg. After drying (at 50 °C for 24 h), the samples were manually ground with an agate mortar. The powders were split in two aliquots: one fraction was heated to 1350 °C and total carbon (TC) contents were measured using a LECO SC-144DR Carbon Analyser equipped with

an infrared detector. The second fraction was first heated to 550 °C for 5 h to remove organic carbon (OC) and then heated to 1350 °C to measure TIC contents. Prior to and after sample analyses, a Synthetic Carbon Leco 502-029 (1.01 ± 0.02 carbon%) standard was measured. TOC contents were determined using the formula  $TOC = TC - TIC$ .

#### 3.4.4. Lipid biomarker analyses

Lipid biomarker analyses were performed on 21 samples (at least 2 samples per cycle) using the procedure described in Sabino et al. (2020b). Briefly, after a modified Bligh and Dyer extraction, samples were separated in an *n*-hexane-soluble and a dichloromethane-soluble fraction. The former was further separated into four sub-fractions: (a) hydrocarbons, (b) ketones, (c) alcohols and (d) carboxylic acids. The alcohol fraction was derivatized for 1 h at 70 °C by adding pyridine and N,O-bis(trimethylsilyl)trifluoroacetamide (BSTFA) (1:1; *v/v*). The ketones and carboxylic acids did not contain any indigenous compounds and are not discussed further. Alcohol and hydrocarbon fractions were dried and re-dissolved in *n*-hexane for analyses. Compounds were identified using a Thermo Scientific Trace gas chromatograph (GC) Ultra coupled to a Thermo Scientific DSQ II mass spectrometer (MS) through comparison of retention times and published mass spectra. Quantification was achieved with a Fisons Instruments GC 8000 series equipped with a flame-ionization detector (FID). Internal standards used for quantification were 5 $\alpha$ -cholestane for the hydrocarbon fraction and 1-nonadecanol and DAGE C<sub>18-18</sub> for the alcohol fraction. The carrier gases were helium and hydrogen for the GC–MS and GC–FID analyses, respectively. Both devices were equipped with an Agilent HP–5MS UI fused silica column with a length of 30 m, a diameter of 0.25 mm and a film thickness of 0.25  $\mu$ m. The GC temperature program was: 50 °C (3 min); from 50 °C to 230 °C (held 2 min) at 25 °C/min; then from 230 °C to 320 °C (held 20 min) at 6 °C/min. An aliquot of the hydrocarbon fraction was used to isolate branched and cyclic compounds from the *n*-alkanes. The aliquot was treated with 300 mg of 5 Å molecular sieve and 2 mL cyclohexane, was shaken well, then extracted by ultrasonication for 2 h. The extract was filtered, and the mole sieve was repeatedly washed with cyclohexane and filtered once again to release all branched and cyclic compounds. After drying with molecular nitrogen, the extract was re-dissolved in *n*-hexane for compound identification and quantification. The GC temperature program was: 50 °C (3 min); from 50 °C to 230 °C (held 2 min) at 25 °C/min; then from 230 °C to 325 °C (held 25 min) at 6 °C/min.

##### 3.4.4.1. Desulfurization with nickel boride

Desulphurization was performed for the dichloromethane-soluble fractions (asphaltenes), applying a procedure slightly modified from Schouten et al. (1993) and Blumenberg et al. (2010). Briefly, the asphaltenes were dissolved in 8 mL tetrahydrofuran/methanol (1:1, *v/v*), then 200 mg of each anhydrous nickel chloride and sodium borohydride were added. After 1 h reaction time, the samples were centrifuged, and the supernatant was collected. The solid residue was extracted twice with dichloromethane/methanol (1:1, *v/v*), then centrifuged again



and the supernatant was combined with the previous extract. An aqueous solution was added, and the organic layer collected and dried with a rotary evaporator. The residual organic phase was filtered through dry sodium sulphate to completely remove water. Column chromatography was performed using a silica gel column and 2.5 mL of *n*-hexane/dichloromethane (9:1, *v/v*) as eluent to separate the released hydrocarbons after desulphurization from the polar compounds. The desulfurized hydrocarbon fraction was re-dissolved in *n*-hexane and the compounds identified through GC–MS analyses using the following program: from 60 °C (1 min) to 150 °C at 15 °C/min and then up to 320 °C (held 40 min) at 4 °C/min. Due to low contents, the desulfurized hydrocarbon fractions were also run in single ion mode (SIM) with the masses *m/z* 133 and 546, specific masses of di-aromatic carotenoids and isorenieratane, respectively.

#### 3.4.4.2. Glycerol dibiphytanyl glycerol tetraether analyses

Glycerol dibiphytanyl glycerol tetraethers (GDGTs) were obtained from 10% vol. of the total lipid extract (TLE) according to the method of Hopmans et al. (2000) and modified by Baumann et al. (2018). The aliquot was dissolved in *n*-hexane and an internal standard (C<sub>46</sub> GDGT; 12 mg/L) was added. The analyses were performed using a Varian MS Workstation 6.91 high-performance liquid chromatography (HPLC) system coupled to a Varian 1200 L triple quadrupole mass spectrometer. The compounds were separated on a Grace Prevail Cyano column (150 × 2.1 mm; 3 μm particle size) and a guard column, held at 30 °C. The following gradient was applied: linear change from 97.5% A (100% *n*-hexane) and 2.5% B (90% *n*-hexane: 10% 2-propanol; *v/v*) to 75% A and 25% B from 0 to 35 min; then linearly to 100% B in 5 min and held for 8 min; and thereafter, back to 97.5% A and 2.5% B to re-equilibrate the column for 12 min. The total run time was 60 min and the solvent flow was kept constant at 0.3 mL/min during the entire run time. The identification of GDGTs was achieved using a mass spectrometer equipped with an atmospheric pressure chemical ionization (APCI) interface operated in positive ion mode. The APCI parameters were: molecular nitrogen as nebulizing gas with a pressure of 60 psi; temperature fluctuating between 35 °C and 40 °C; 50 °C as API housing temperature; 200 °C for the drying gas of the API with a pressure of 12 psi; and 400 °C and 18 psi for the APCI auxiliary gas temperature and pressure, respectively. The injection volume was 10 μL. The scanned spectral range was set at *m/z* 500 to 750 and 950 to 1500. The response factors were evaluated after every 4 to 5 samples using a standard mixture containing synthetic archaeol (1,2-Di-O-phytanyl-*sn*-glycerol; CAS 99341-19-2), DAGE C<sub>18:18</sub> (CAS 6076-38-6), DAGE C<sub>18:18-4ene</sub> (1,3- Dilinoleoyl-rac-glycerol; CAS 15818-46-9) and synthetic C<sub>46</sub> GDGT (CAS 138456-87-8). The response factors between synthetic archaeol and C<sub>46</sub> GDGT were usually around 1.5:1. Relative lipid abundances were determined by selecting individual base peaks with the target mass *m/z*, including ions symmetrically with ±1.0 of target *m/z*.

### 3.5. Results

#### 3.5.1. Petrography and mineralogy

The studied interval is characterized by 8 lithological cycles of shales and argillaceous marls (referred to as marls) up to 1 m thick (Fig. 3.3A, B). The inorganic carbon contents range from 0.4% to 6.0%, with higher contents in marls (Fig. 3.3A). XRD analyses indicate that the inorganic carbon in the Govone section is composed of calcite and dolomite (Appendix C). Dolomite coexists with calcite in cycles Gm26 and Gm27, while it represents the only carbonate phase in cycle Gm28 (except for sample Gm28.1) and above (Fig. 3.3A).

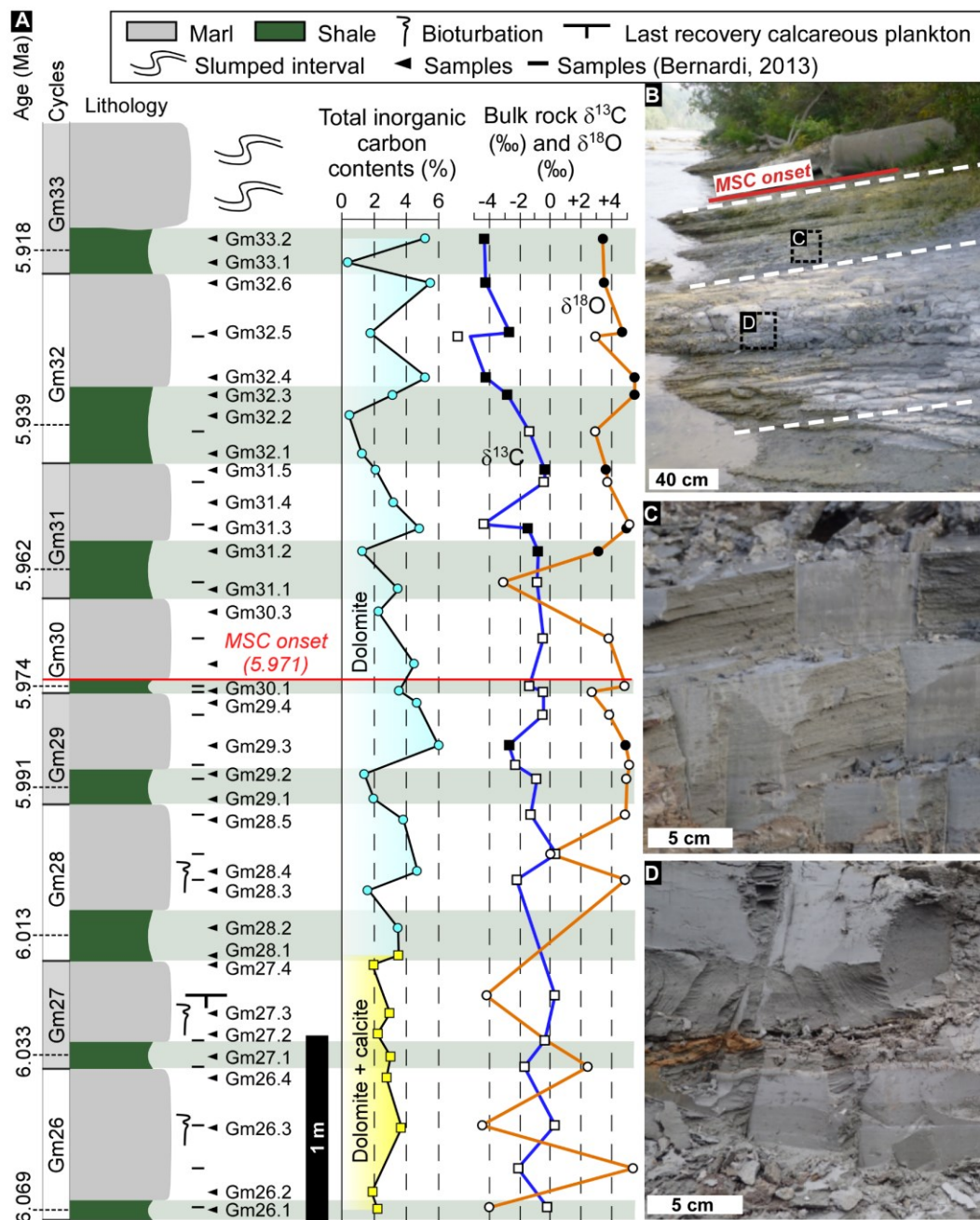


Figure 3.3 [previous page] – (A) The Govone section with sample locations, total inorganic carbon contents, carbonate mineralogy and bulk-rock carbon ( $\delta^{13}\text{C}$ ) and oxygen ( $\delta^{18}\text{O}$ ) stable isotope values. White squares and circles refer to  $\delta^{13}\text{C}$  and  $\delta^{18}\text{O}$  values from Bernardi (2013), whereas black squares and circles refer to values from this study. (B) Outcrop view of the Govone section. The red line corresponds to the onset of the Messinian salinity crisis (MSC); the white dashed lines indicate the top of marl beds; insets indicate the position of Figures 3.3C and 3.3D. (C) Close-up of pre-MSC laminated organic-rich shales. (D) Close-up of pre-MSC homogenous marls.

---

### 3.5.1.1. Shales

Shales are laminated, dark-green-colored (Fig. 3.3C) and rich in organic matter (TOC > 2%). They are characterized by an alternation of discontinuous, sub-millimetric, cream-colored (type A) and dark-grey-colored (type B) laminae, irregularly interrupted by layers up to 1.5 cm thick composed of terrigenous silt- to sand-sized grains (Fig. 3.4A). These layers are considered to represent the products of more intense fluvial discharge to the basin (Dela Pierre et al., 2014). Type A laminae show a distinct bulbous to pinch-and-swell type character (Fig. 3.4A; *sensu* Pilskaln and Pike, 2001). They are formed of two varieties of fluorescent peloids: (1) flattened to lens-shaped peloids up to 0.5 mm across with well-defined boundaries; and (2) irregular aggregates, up to 1 mm across, with irregular, diffused boundaries (Fig. 3.4A–C). In cycles Gm26 and Gm27, the peloids are composed of scattered silt-sized siliciclastic grains (quartz, mica flakes, and feldspars), black organic matter particles, and coccoliths, very abundant in the lens-shaped peloids (Fig. 3.4D). In cycles Gm28 to Gm33, peloids are barren of coccoliths and mostly formed of dolomite microcrystals up to 10  $\mu\text{m}$  across, scattered pyrite framboids, and accessory silt-sized siliciclastic grains (Fig. 3.4E). Dolomite microcrystals show prevalently globular, hemispherical or cauliflower-like (*sensu* Warthmann et al., 2000) habits (Fig. 3.4E–G), and sometimes exhibit a central hollow (Fig. 3.4G). Type B laminae are only a few microns thick, laterally discontinuous (Fig. 3.4A), and composed of silt- to clay-sized terrigenous grains (mainly quartz, feldspars, and mica flakes), black amorphous organic matter debris enriched in sulfur (as revealed by EDS analyses), and abundant pyrite framboids, up to 10  $\mu\text{m}$  across. These laminae are interpreted to represent the product of enhanced terrigenous input into the basin, under the control of short-term, probably seasonal, climate change (Dela Pierre et al., 2014). Both types of laminae contain scattered planktonic foraminifer tests (only in cycles Gm26 and Gm27; Fig. 3.4H, I), fish scales, and vertebrae. Tiny (< 10  $\mu\text{m}$ ) pyrite framboids (Fig. 3.4F–H), locally filling foraminifer tests (Fig. 3.4I), are abundant.

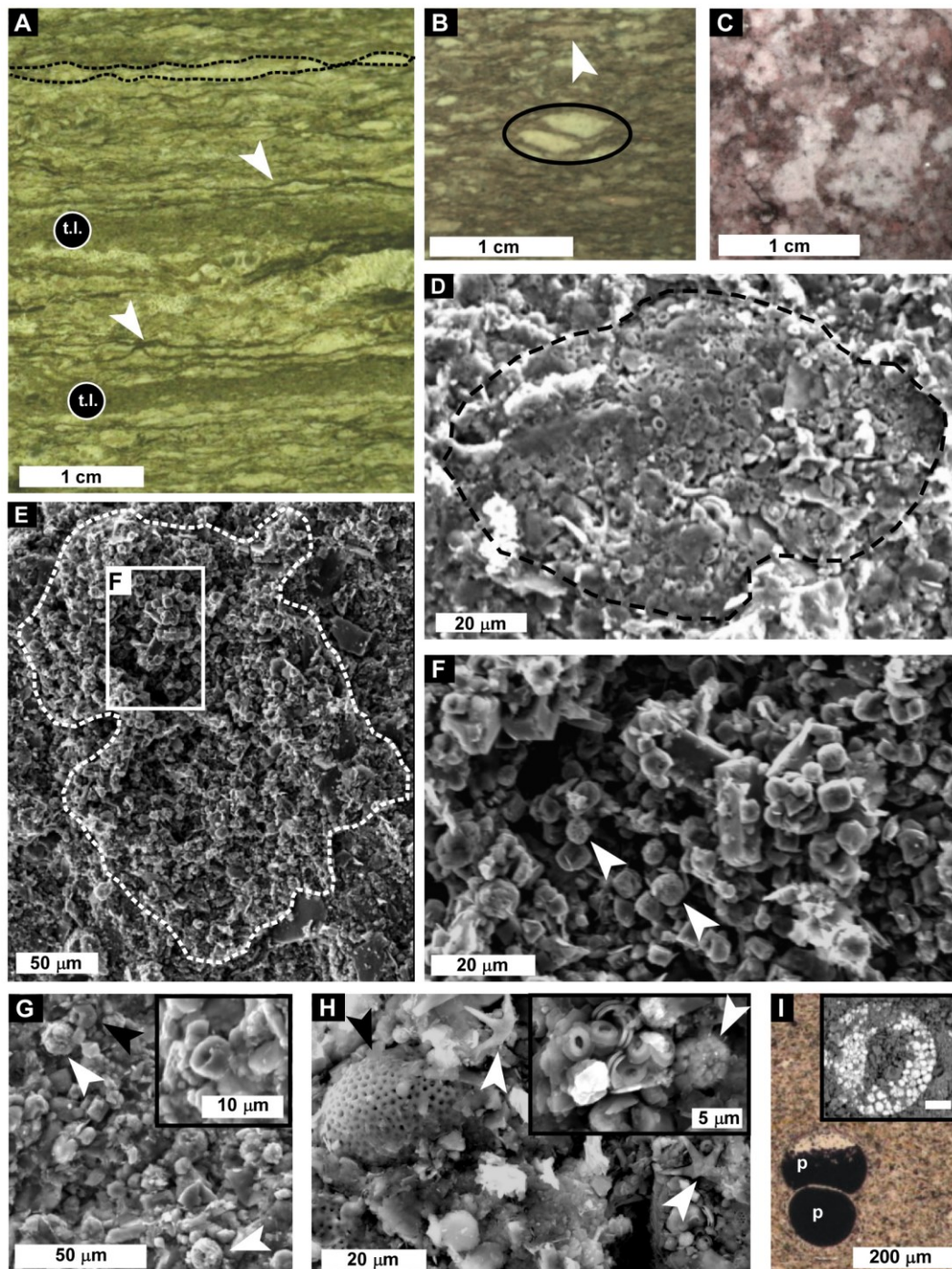


Figure 3.4 – Organic-rich shales. (A) Polished slab cut perpendicular to bedding. Type A and B laminae separated by coarser terrigenous layers (t.l.). The black dashed lines envelope a type A lamina, the white arrows indicate two type B laminae. (B) Fluorescent, lens-shaped faecal pellets (black oval) and flattened, faintly fluorescent aggregate (white arrow); UV-fluorescence image. (C) Irregular aggregates cut parallel to bedding; UV-fluorescence image. (D) Faecal pellet (dashed line) composed of coccoliths; SEM micrograph. (E) Irregular aggregate (dashed line) mostly composed of dolomite microcrystals from the MSC part of the section. The white box indicates the position of (F); SEM micrograph. (F) Globular dolomite microcrystals and scattered pyrite framboids (white arrows); SEM micrograph. (G) Hollow dolomite microcrystals (black arrow and inset) and scattered pyrite framboids (white arrows); SEM micrograph. (H) Hollow dolomite microcrystals (black arrow) and scattered pyrite framboids (white arrows); SEM micrograph. (I) Pyrite framboids (p) and an inset showing a circular aggregate of pyrite framboids. [continued in the next page]

[Figure 3.4 – continuation] (H) Planktonic foraminifer test (black arrow) surrounded by coccoliths (white arrows). The inset shows a detail with coccoliths and a small pyrite framboid (arrow); SEM micrograph. (I) Foraminifer test partially filled with pyrite (p); plane-polarized light. The inset is a backscattered electron image of a pyrite infilling, consisting of an aggregate of tiny pyrite framboids. Scale bar in the inset is 20  $\mu\text{m}$ .

### 3.5.1.2. Marls

Marls are grey-colored (Fig. 3.3D) with bioturbation only present in the pre-MSC cycles (Fig. 3.5A). Marls are rich in silt-sized terrigenous grains (mainly quartz, feldspar, and mica flakes), and contain finely dispersed pyrite grains up to 10  $\mu\text{m}$  across (framboids and octahedral crystals; Fig. 3.5B, C). Dolomite is common in the MSC cycles, consisting of globular and cauliflower-like (Fig. 3.5D–F) microcrystals, up to 20  $\mu\text{m}$  across, often typified by a central hollow (Fig. 3.5E, F). Dumbbell-shaped crystals also occur (Fig. 3.5F).

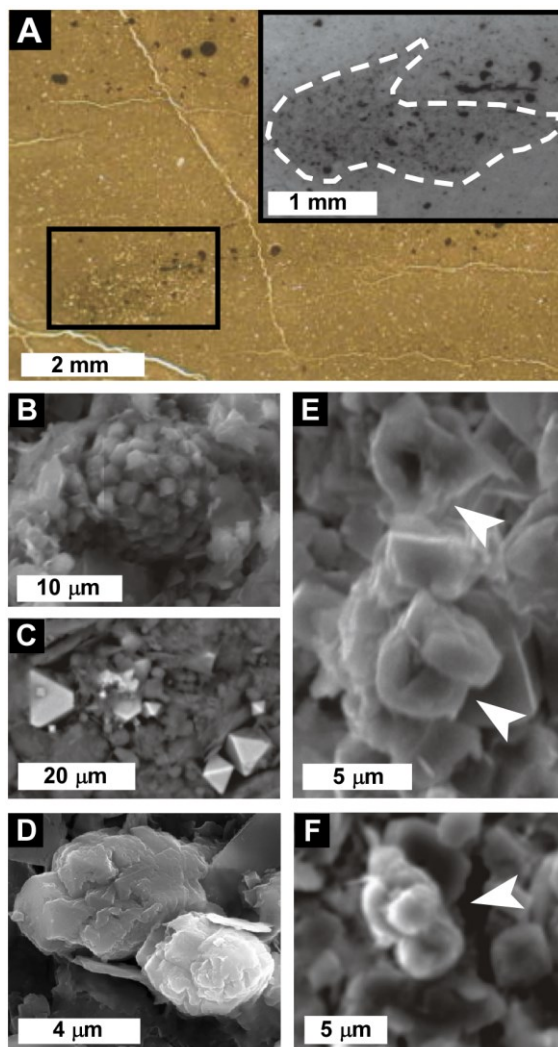


Figure 3.5 – (A) Photomicrographs and (B–F) SEM images of marls. (A) Bioturbation traces in pre-MSC marl (black box); the inset is a close-up image in UV light of the bioturbation traces, highlighted by dashed line. Pyrite: (B) framboid, (C) octahedral crystals. Dolomite microcrystals with (D) cauliflower, (E) globular and (F, arrow) dumbbell-like shapes. The arrows in (E) indicate central hollows in dolomite microcrystals.

### 3.5.2. Carbon and oxygen stable isotopes

The bulk-rock  $\delta^{13}\text{C}$  values range from  $-5.2\text{‰}$  to  $+0.3\text{‰}$ , lacking an obvious relationship with lithology (Fig. 3.3; Appendix C). However, a general trend towards more negative  $\delta^{13}\text{C}$  values is observed across the MSC onset, evidenced by overall more pronounced  $^{13}\text{C}$ -depletion in MSC cycles (average  $\delta^{13}\text{C} = -2.4\text{‰}$ ) than in pre-MSC cycles (average  $\delta^{13}\text{C} = -1.0\text{‰}$ ). A moderate negative correlation was found when plotting the bulk-rock  $\delta^{13}\text{C}$  values of shales ( $n = 6$ ) and marls ( $n = 7$ ) against the TIC contents, where dolomite was the only carbonate phase detected (shales,  $r = -0.7$ ; marls,  $r = -0.6$ ; Appendix C). The  $\delta^{18}\text{O}$  bulk-rock values vary from  $-4.5\text{‰}$  to  $+5.5\text{‰}$ . As for  $\delta^{13}\text{C}$  values, a correlation with lithology was not observed (Fig. 3.3). The largest fluctuations were found in the pre-MSC cycles ( $+5.4\text{‰} \geq \delta^{18}\text{O} \geq -4.5\text{‰}$ ), while the MSC cycles show less variable, positive  $\delta^{18}\text{O}$  values (average  $+3.5\text{‰}$ ; Fig. 3.3).

### 3.5.3. Total organic carbon contents and lipid biomarkers

The TOC contents vary from 1.0% to 3.1% (Fig. 3.6; Appendix C) and follow lithological cyclicity, with higher contents in shales (average 2.4%) and lower contents in marls (average 1.6%), particularly in pre-MSC cycles (as low as 1.0%).

	Max (%)	Min (%)	Average pre-MSC (%)	Average MSC (%)
GDGT-0	31.2	18.0	25.2	27.9
GDGT-1	11.9	5.4	9.0	8.2
GDGT-2	14.5	5.6	11.0	8.9
GDGT-3	3.1	1.0	2.5	1.9
GDGT-5	32.9	18.3	24.8	24.8
GDGT-5' (regio isomer)	4.2	1.8	3.2	3.1
C <sub>20-20</sub> archaeol	42.9	7.8	24.4	25.1
	Max ( $\mu\text{g/g}$ TOC)	Min ( $\mu\text{g/g}$ TOC)	Average Pre-MSC ( $\mu\text{g/g}$ TOC)	Average MSC ( $\mu\text{g/g}$ TOC)
Lycopane				
Shales	25.0	0.1	9.7	6.6
Marls			0.1	0.3
Tetrahymanol				
Shales	26.5	1.1	10.6	4.6
Marls			1.7	2.3

Table 3.1 – Archaeol, GDGTs (both in % relative to all GDGTs plus archaeol), lycopane and tetrahymanol abundances in pre-MSC and MSC Govone sediments. Max: maximum content; Min: minimum content; GDGT-0: caldarchaeol; GDGT-5: crenarchaeol.

#### 3.5.3.1. Archaeol and GDGT distribution and caldarchaeol/crenarchaeol ratio

GDGTs and C<sub>20-20</sub> archaeol (archaeol) were detected in the Govone samples. The former are mainly represented by GDGT-0 (caldarchaeol) and GDGT-5 (crenarchaeol), with relative contents ranging from 18.0% to 31.2% and 18.3% to

32.9% of the total GDGTs plus archaeol assemblage, respectively (Fig. 3.6, Tab. 3.1; Appendix C). GDGTs with 1–3 cyclopentane rings and GDGT-5' (crenarchaeol isomer) yielded relative contents of  $\leq 11.0\%$  on average (Fig. 3.6, Tab. 3.1). Archaeol revealed relative contents between 7.8% and 42.9% of the total GDGTs plus archaeol inventory (Fig. 3.6, Tab. 3.1, Appendix C). The distribution of GDGTs and archaeol did not vary across the MSC onset (Fig. 3.6, Tab. 3.1). The caldarchaeol/crenarchaeol ratio varies between 0.8 and 1.5, with an average of 1.1 (Fig. 3.6; Appendix C).

### 3.5.3.2. *Acyclic and cyclic triterpenoids and the lycopane/ $n$ -C<sub>31</sub> alkane ratio*

The hydrocarbon and alcohol fractions contain, among other compounds ( $n$ -alkanes and  $n$ -alkanols, steranes and sterols, hopanes and hopanols, long-chain diols and keto-ols, thiolanes, thianes and thiophenes; data not shown), the acyclic triterpenoid lycopane and the pentacyclic triterpenoid tetrahymanol. Lycopane, isolated with a molecular sieve from the  $n$ -alkanes, was found in most of the 18 samples (except for marls in cycle Gm26), yielding varying contents (up to 25.0  $\mu\text{g/g}$  TOC). In general, shales revealed much higher contents than marls (Fig. 3.6, Tab. 3.1; Appendix C). Lycopane contents increase upwards, especially above the MSC onset (Fig. 3.6). The lycopane/ $n$ -C<sub>31</sub> alkane ratio, a paleo-oxicity proxy introduced by Sinninghe Damsté et al. (2003), ranges from 0.01 to 1.2 (Appendix C) with most ratios  $< 0.3$ ; such values suggest that the seafloor was constantly oxygenated (cf. Sinninghe Damsté et al., 2003), although petrographic and other organic geochemical evidence suggests the opposite (see Section 3.6.3. below). This inconsistency most likely results from the high flux of leaf-wax-derived long-chain  $n$ -alkanes relative to lycopane, which can significantly affect the ratio and make the use of its absolute values unreliable (cf. Sinninghe Damsté et al., 2003). We therefore decided not to apply the absolute values of the ratio, as suggested by Sinninghe Damsté et al. (2003), but refer to trends between the lithologies to infer relative variations in paleo-oxicity. Tetrahymanol occurs in all samples with contents ranging from 1.1 to 26.5  $\mu\text{g/g}$  TOC (Fig. 3.6; Appendix C). Tetrahymanol is more abundant in shales than in marls, although the difference between the two lithologies is less pronounced in the MSC interval than in the pre-MSC part of the section (Fig. 3.6, Tab. 3.1; Appendix C).

### 3.5.3.3. *Hydrocarbons liberated after desulphurization*

The desulphurization of asphaltenes released mostly  $n$ -alkanes (C<sub>14</sub> to C<sub>40</sub>), a pentacyclic C<sub>30</sub> sulfide (cf. Poinot et al., 1998) and, especially in shales, phytane. As well as these compounds, we identified C<sub>27</sub> to C<sub>29</sub> steranes, C<sub>31</sub> to C<sub>35</sub> hopanes, and, only in samples from cycles Gm28 to Gm30, the diaromatic carotenoid isorenieratane. In most cases (with the exception of sample Gm30), isorenieratane was identified in single ion mode (SIM) only ( $m/z$  133 and 546). This is in accordance with very low contents, rendering quantification impossible.

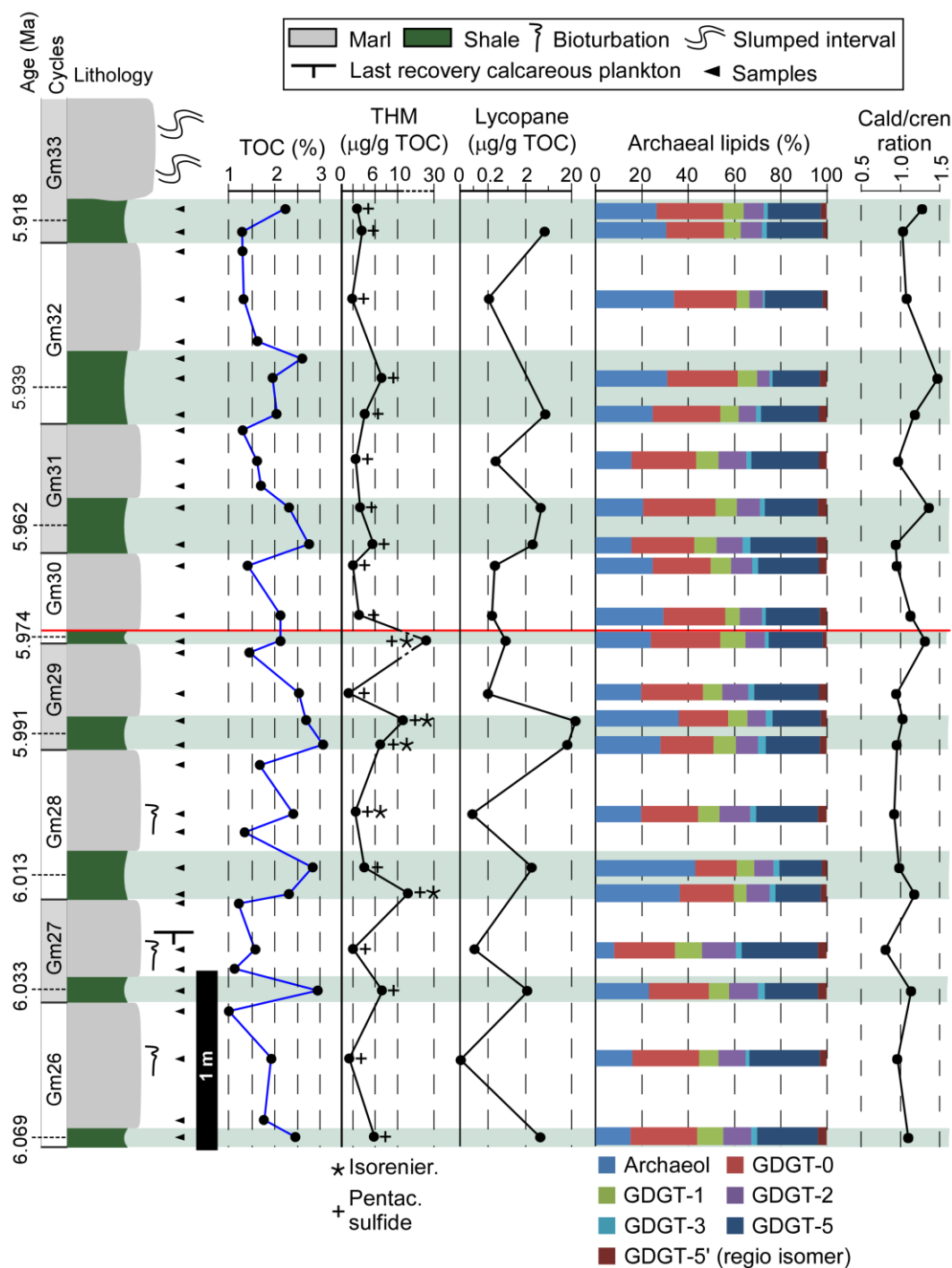


Figure 3.6 – TOC contents, lipid biomarker distributions and caldarchaeol/crenarchaeol ratio (cald/cren ratio) across the onset of the Messinian salinity crisis in the Govone section. Note pentacyclic C<sub>30</sub> sulfide (Pentac. sulfide) and isorenieratane (isorenier.) in the tetrahymanol distribution profile and the non-metric scale in the lycopane distribution profile. The red line at the base of the marls in cycle Gm30 indicates the onset of the Messinian salinity crisis. GDGT: glycerol dibiphytanyl glycerol tetraethers; Ly: lycopane; THM: tetrahymanol; GDGT-0: caldarchaeol; GDGT-5: crenarchaeol.



### **3.6. Discussion**

#### **3.6.1. Water-column stratification and euxinia across the onset of the MSC**

The restriction of the Mediterranean leading to the MSC was associated with an intensification of water-column stratification (Roveri et al., 2014a) that persisted during the entire MSC event (Christeleit et al., 2015; García-Veigas et al., 2018; Simon and Meijer, 2017). The same evolution has been reconstructed for the Piedmont Basin (Bernardi, 2013; Dela Pierre et al., 2011; Lozar et al., 2018; Violanti et al., 2013), especially by the study of the Pollenzo section, a section about 20 km SW from the Govone section (Natalicchio et al., 2019, 2017). For the Pollenzo section, the most compelling evidence of increasing water-column stratification after the MSC onset is the appearance of tetrahymanol. This compound is produced by organisms commonly thriving at chemoclines (Wakeham et al., 2012), namely bacterivorous ciliates, anoxygenic phototrophic bacteria and aerobic methanotrophic bacteria (Banta et al., 2015; Cordova-Gonzalez et al., 2020; Eickhoff et al., 2013; Harvey and McManus, 1991; Kleemann et al., 1990; Rashby et al., 2007); tetrahymanol is therefore considered a robust indicator of water-column stratification (e.g., Sinninghe Damsté et al., 1995b). Tetrahymanol was found throughout the section at Govone, suggesting that, in the more distal settings of the Piedmont Basin, stratified conditions had already been established before the onset of the MSC. The higher tetrahymanol contents in shales suggest that stratification was more intense at precession minima, most likely in response of enhanced riverine runoff (cf. Natalicchio et al., 2019; Sabino et al., 2020b). Enhanced riverine runoff in turn promoted episodes of high productivity and phytoplankton blooms. The latter are testified by the very abundant lens-shaped peloids and irregular aggregates, which have been interpreted as faecal pellets and marine snow-flakes, respectively (cf. Dela Pierre et al., 2014), both main components of so-called marine snow (e.g., Alldredge et al., 2002; Alldredge and Silver, 1988). Interestingly, in the shales of the uppermost pre-MSC cycles (Gm28–30), tetrahymanol is accompanied by isorenieratane, derived from the degradation of isorenieratene sourced by green sulfur bacteria (Repeta et al., 1989; Van Gemerden and Mas, 1995). These phototrophic bacteria require hydrogen sulfide to perform anoxygenic photosynthesis (e.g., Van Gemerden and Mas, 1995) and are found in modern stratified basins when sulfidic conditions extend into the photic zone (e.g., Black Sea, Sinninghe Damsté et al., 1993; Wakeham et al., 2007; Cariaco Basin, Wakeham et al., 2012), making isorenieratene and its derivatives biomarkers for photic zone euxinia (e.g., Kuypers et al., 2002; Repeta and Simpson, 1991). The co-occurrence of tetrahymanol and isorenieratane in shales therefore supports pronounced water-column stratification at precession minima already before the onset of the MSC, occasionally accompanied by photic zone euxinia. The lower contents of tetrahymanol and the lack of isorenieratane in the MSC shales apparently suggest the weakening of stratification, which is however in contrast with evidence from the neighboring Pollenzo section (Natalicchio et al., 2019, 2017). This inconsistency could reflect unfavorable environmental conditions at precession minima for the producers of isorenieratene and tetrahymanol after the MSC onset in the distal part of the basin (Govone), rather than the weakening of water-column

stratification. Interestingly, in modern stratified basins, ciliates are found to feed, among other organisms, on green sulfur bacteria (Wakeham et al., 2012, 2007). The trophic relationship between autotrophic green sulfur bacteria and heterotrophic ciliates, already inferred for the MSC sediments of the Northern Apennines (Vena del Gesso Basin, Sinninghe Damsté et al., 1995a), can potentially explain the trend of compound contents in the Govone section, where tetrahymanol peaks coincide with the presence of isorenieratane. Adverse conditions for green sulfur bacteria were most likely related to an intensified input of terrigenous material by rivers after the MSC onset, as evidenced by increasing contents of terrestrial plant waxes (Natalicchio et al., 2019; Sabino et al., 2020b). Enhanced riverine runoff might have increased turbidity and input of oxygen in the upper water column, both deleterious factors for phototrophic green sulfur bacteria (Van Gernerden and Mas, 1995), in turn causing a decrease of the ciliate population. Evidence of persistent stratification and sulfidic conditions in the water column at precession minima after the MSC onset, although not extending into the photic zone, is provided by the occurrence of small pyrite framboids and sulfur-enriched organic matter. The small size of the super-abundant pyrite framboids (< 10 µm) may suggest that they formed within an euxinic water column (cf. Bond and Wignall, 2010; Passier et al., 1997; Tagliavento et al., 2020; Wilkin et al., 1996). Organic sulfur compounds, such as the pentacyclic C<sub>30</sub> sulfide, are believed to form during a very early diagenetic stage, possibly already in the water column when reduced-sulfur species (e.g., hydrogen sulfide) exceed reduced iron and consequently bind to settling organic matter (Poinsot et al., 1998; Sinninghe Damsté and de Leeuw, 1990; Wakeham et al., 1995). Compared with shales, marls reveal lower contents of tetrahymanol. Such a pattern reflects the weakening of stratification at precession maxima in response to more efficient mixing of the water column (e.g., Sierro et al., 2001; Violanti et al., 2013). Mixing was promoted by drier climate conditions and reduced fluvial discharge, in accordance with higher element/Al ratios and a decrease of contents in the sediments of terrestrial plant waxes, which show deuterium enrichment (Sabino et al., 2020b). However, water-column stratification never completely ceased to exist, since the occurrence of small pyrite framboids and sulfur organic compounds suggests that sulfidic conditions were intermittently present in the water column. The trend to slightly higher tetrahymanol contents in MSC marls compared with pre-MSC marls suggests that water-column stratification was more intense at precession maxima after the onset of the MSC compared with precession maxima during the pre-MSC, in agreement with the appearance of tetrahymanol in time-equivalent more marginal sediments (Pollenzo section; Natalicchio et al., 2017). This was possibly due to the establishment of a wetter climate in the northern Mediterranean (cf. Natalicchio et al., 2019; Sabino et al., 2020b).

### **3.6.2. Persistence of marine conditions in surface waters after the onset of the MSC**

The Govone section is characterized by the progressive decline and final disappearance of calcareous plankton approaching the MSC onset (Bernardi, 2013). Such ecological change is recorded in other sections across the Mediterranean and was taken as evidence of progressively harsher conditions in

surface waters, with fluctuations of salinity up to high levels not tolerated by most marine biota (e.g., Blanc-Valleron et al., 2002; Manzi et al., 2007; Sierra et al., 1999). The establishment of hypersaline conditions during the MSC is also reflected by the archaeal di- and tetraether lipid assemblages of MSC carbonates from Sicily and Calabria (the so-called '*Calcarea di Base*'); in these deposits, C<sub>20-20</sub> archaeol, C<sub>20-25</sub> archaeol (extended archaeol), and caldarchaeol dominate the isoprenoid diphytanyl glycerol diether (DGD) and GDGT inventories (Birgel et al., 2014; Turich and Freeman, 2011). In contrast, the isoprenoid DGD and GDGT distribution found for the Govone section is significantly different from that of the *Calcarea di Base* and does not agree with widespread hypersalinity after the onset of the MSC. In fact, archaeol does not dominate over the total GDGTs (c. 25% of the total GDGT and DGD lipid inventory) and is never accompanied by extended archaeol, allowing the exclusion of a significant contribution from halophilic archaea (cf. Dawson et al., 2012; Teixidor et al., 1993). Possible alternative sources for archaeol are non-halophilic archaea, such as methanogens, methanotrophs and marine Euryarchaeota thriving in epi- to mesopelagic zones (Blumenberg et al., 2004; De Rosa and Gambacorta, 1988; Sollai et al., 2019; Turich et al., 2007). Methanogenic and methanotrophic archaea, on the other hand, can be excluded for the Govone section, since the distribution of isoprenoidal di- and tetraether lipids varies from those observed in methane-seep environments, the latter typified by the dominance of archaeol, hydroxyarchaeol, and GDGT-1 and 2 over the other dibiphytanyl tetraethers (Blumenberg et al., 2004; De Rosa and Gambacorta, 1988; Turich et al., 2007). Consequently, marine Euryarchaeota thriving in the epi- to mesopelagic zones of a normal marine water column are the most likely source of archaeol (cf. Elling et al., 2015; Schouten et al., 2008; Sollai et al., 2019; Turich et al., 2007). Interestingly, it has been suggested that mesopelagic marine Euryarchaeota from the group III (MGIII) are important producers of archaeol, especially in oxygen-deficient zones where they can even dominate the archaeal community (Belmar et al., 2011; Sollai et al., 2019). Since episodic oxygen deficiency seems to have characterized the water column of the Piedmont Basin during the MSC, mesopelagic marine Euryarchaeota are the most likely source of archaeol in the Govone section, indicating the persistence of marine rather than hypersaline conditions across the onset of the MSC. Marine conditions are in accordance with the distribution of the GDGTs and the caldarchaeol/crenarchaeol ratio (c. 1), which mirror the distribution and the ratios reported for open-ocean settings (e.g., Kim et al., 2010; Pearson and Ingalls, 2013; Schouten et al., 2013; Turich et al., 2007). Under such conditions, the main contributors to the GDGT pool are planktonic marine Euryarchaeota of the group II (MGII) and Thaumarchaeota (marine group I, MGI), dwelling in the epi- to mesopelagic zones (Santoro et al., 2019; Schouten et al., 2013). Despite some controversy (Lincoln et al., 2014; Schouten et al., 2014), MGII archaea are thought to source mostly acyclic GDGTs (caldarchaeol), whereas MGI archaea synthesize both acyclic and polycyclic GDGTs, especially crenarchaeol (Elling et al., 2017; Zeng et al., 2019). This pattern results in the dominance of caldarchaeol and crenarchaeol over the other GDGTs and a caldarchaeol/crenarchaeol ratio of c. 1 (Schouten et al., 2013 for a review; Sinninghe Damsté et al., 2002), which closely mirror the tetraether archaeal lipid distribution and the ratio of marine planktonic Thaumarchaeota growing in cultures at normal salinity (c. 35‰ salinity; Elling et al., 2015). The

persistence of marine conditions in surface waters challenges the idea of an establishment of a completely hypersaline water mass early on during the MSC (e.g., Bellanca et al., 2001). The lack of pervasive hypersaline conditions agrees with (1) the presence of marine fossils (foraminifers, calcareous nannoplankton, diatoms, fishes) above the MSC onset in more marginal sections of the Piedmont Basin (Carnevale et al., 2019; Dela Pierre et al., 2014; Lozar et al., 2018; Violanti et al., 2013) and (2) paleosalinity estimates from gypsum fluid inclusions, indicating that the parent brine had a salinity possibly even lower than seawater (Natalicchio et al., 2014). In this light, the disappearance of calcareous plankton in the Govone section two cycles below the onset of the MSC most likely reflects diagenetic dissolution of calcareous skeletons rather than harsh environmental conditions in superficial waters (Dela Pierre et al., 2014).

### **3.6.3. Fluctuations in oxygen concentration of bottom waters across the onset of the MSC**

Intensification of water-column stratification in the Mediterranean Basin shortly before the onset of the MSC was associated with widespread depletion of oxygen in bottom waters, which is recorded by the precession-driven deposition of organic-rich sediments (Hilgen and Krijgsman, 1999; Krijgsman et al., 2002, 2001) and by the replacement of oxyphilic benthic foraminifera with stress-tolerant taxa (e.g., Blanc-Valleron et al., 2002; Gennari et al., 2018; Kouwenhoven et al., 1999). Such a trend was confirmed for the Piedmont Basin by changes in the assemblages of benthic foraminifers in the pre-MSC sediments (Bernardi, 2013; Violanti et al., 2013). However, very little information is available for the microfossil-poor or microfossil-barren MSC strata. The Govone section archives the fluctuation of oxygen contents at the seafloor driven by precessional forcing. Humid climate and enhanced riverine runoff at precession minima (Natalicchio et al., 2019; Sabino et al., 2020b) favored intense water-column stratification and bottom anoxia, which is witnessed by the deposition of laminated, organic-rich shales (TOC > 2%). Evidence of bottom-water anoxia during the deposition of shales includes their high contents of lycopane. Studies of modern (Sinninghe Damsté et al., 2003; Wakeham et al., 1993) and ancient sediments (e.g., Behrooz et al., 2018; Freeman et al., 1990; Kenig et al., 1995; Löhr et al., 2018) have shown that preservation of lycopane is highest when bottom waters are anoxic. Lower TOC contents (mostly < 2%) and the sharp drop of lycopane contents ( $\leq 0.4 \mu\text{g/g TOC}$ ) in marls indicate higher oxygen levels at the seafloor than at times of shale deposition, reflecting precession-driven climate change (Sabino et al., 2020b). However, changes can be observed across the onset of the MSC, possibly recording different degrees of bottom-water ventilation before and after the advent of the crisis. In particular, pre-MSC marls show bioturbation traces and contain few stress-tolerant benthic foraminifers (Bernardi, 2013; Dela Pierre et al., 2016), suggesting that the seafloor was at least episodically oxygenated. In contrast, the absence of bioturbation and the slight increase of lycopane contents in MSC marls compared with pre-MSC marls indicate that bottom waters became progressively oxygen depleted, agreeing with an intensification of water-column stratification at precession maxima during the MSC relative to precession maxima in pre-MSC times (Section 3.6.1. above). Despite such a trend to lower oxygen levels, the only low lycopane contents at

precession maxima compared with precession minima (shale deposition) suggest that bottom waters were not fully anoxic during the deposition of marls (cf. Sinninghe Damsté et al., 2003).

### **3.6.4. Primary Lower Gypsum: implications on depositional environments and stratigraphic architecture**

The integration of geochemical, sedimentological, and petrographic data indicates that during the early phase of the MSC the water column in the Piedmont Basin was stratified and comprised (1) an oxygenated upper layer, typified by mostly marine conditions and receiving input of freshwater from rivers (Natalicchio et al., 2019; Sabino et al., 2020b) and/or low-salinity water from the Paratethys (Grothe et al., 2020); and (2) an anoxic to euxinic lower layer, formed by denser, more saline waters (Dela Pierre et al., 2014; Natalicchio et al., 2017), the latter agreeing with more positive  $\delta^{18}\text{O}$  values (average +3.5‰) of MSC sediments. The two water masses were separated by a pycnocline, at which chemical gradients established with time and a chemocline developed, as observed for modern basins (Wakeham et al., 2012, 2007) and reconstructed for ancient basins with stratified water masses (e.g., the Badenian basin of Eastern Europe; Babel, 2004; Babel and Bogucki, 2007). Stratigraphic data reveal a lateral facies change in the PLG unit from the margin to the depocenter of the Piedmont Basin for sediments deposited during precession maxima (Dela Pierre et al., 2011). Bottom-grown selenite gypsum is observed only in the shallow, marginal part of the basin (Arnulfi section; Fig. 3.7). Moving towards the depocenter, gypsum makes lateral transition to marls and carbonates with filamentous fossils (Pollenzo section; Fig. 3.7) – interpreted to represent chemotrophic microbial mats (Dela Pierre et al., 2012) – and finally to dolomite-rich marls (Govone section; Fig. 3.7). Conversely, at precession minima, organic-rich shales were deposited across the entire Piedmont Basin (Dela Pierre et al., 2011, 2016; Fig. 3.7). We suggest that these stratigraphic patterns reflect vertical chemocline oscillations controlled by precession (Fig. 3.7). The widespread seafloor anoxia recorded by shales indicates that the chemocline was located above the sea bottom across most of the basin during precession minima. These conditions favored organic matter preservation in the water column and led to an increased sedimentation of organic matter, which, in turn, favored heterotrophic, bacterial sulphate reduction and promoted bacterially mediated precipitation of early diagenetic dolomite in anoxic, organic-rich sediments (Fig. 3.7A). This inference agrees with (1) the negative bulk-rock  $\delta^{13}\text{C}$  values (cf. Petrash et al., 2017); (2) the moderate negative correlation ( $r = -0.7$ ) between TIC contents, represented by dolomite, and bulk-rock  $\delta^{13}\text{C}$  values (high TIC contents coincide with low  $\delta^{13}\text{C}$  values); and (3) dolomite crystal habits (Figs 3.4F, G, 3.5D–F; cf. Bontognali et al., 2010; Han et al., 2016; Sanz-Montero et al., 2008; van Lith et al., 2003; Warthmann et al., 2000). The change towards a less humid climate at precession maxima (Sabino et al., 2020b) resulted in the deepening of the chemocline and the thinning of the anoxic zone (Fig. 3.7B). Under these circumstances, selenite grew only in the shallower part of the basin (Arnulfi section, Fig. 3.7B), where low-salinity waters enriched in calcium and sulphate ions, possibly derived from leaching of former evaporites (Natalicchio et al., 2014), occurred above an oxygenated sea bottom (e.g., García-Veigas et al., 2018). In

more distal settings, the absence of gypsum was possibly related to low-oxygen conditions, which favored bacterial sulphate reduction and resultant gypsum undersaturation (Fig. 3.7B; cf. Babel, 2004; de Lange and Krijgsman, 2010; García-Veigas et al., 2018). The parts of the basin where the chemocline impinged on the seafloor (Pollenzo section, Fig. 3.7B; Natalicchio et al., 2017) were covered by microbial mats of putative sulfide-oxidizing bacteria (Natalicchio et al., 2017). In modern settings, these bacteria thrive under hypoxic conditions where the chemocline intercepts the seafloor and steep gradients between electron acceptors and hydrogen sulfide occur (e.g., the Black Sea; Jessen et al., 2016). In contrast, in deeper parts of the basin (Govone section; Fig. 3.7B) the sea bottom was in contact with more reducing waters. These conditions favored the preservation of organic matter in the water column, enhanced the deposition of organic matter at the seafloor and led to an increase in bacterial sulphate reduction in the sediments, which triggered the widespread precipitation of early diagenetic microbial dolomite (Fig. 3.7B).

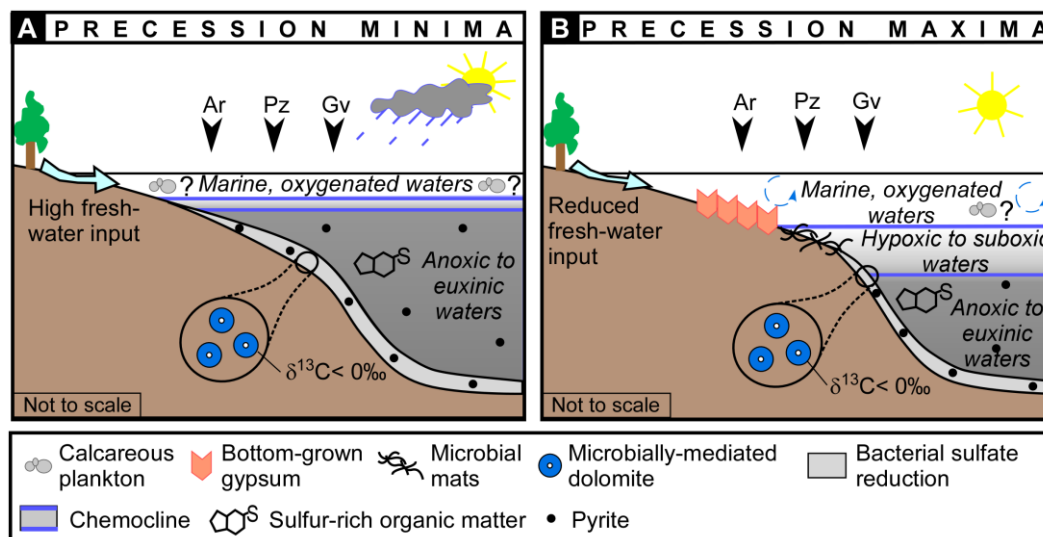


Figure 3.7 – Reconstruction of the water-column structure of the Piedmont Basin at (A) precession minima, insolation maxima and shale deposition and (B) precession maxima, insolation minima and marl deposition during the earliest phase of the Messinian salinity crisis. The black arrows indicate the positions of sections (Ar: Arnulfi; Pz: Pollenzo; Gv: Govone). The thickness of the chemocline is emphasized in (B) to highlight the different conditions described in the text.

### **3.7. Conclusions**

Hydrological change affecting the Piedmont Basin during the early stages of the Messinian salinity crisis (MSC) led to an intensification of water-column stratification. The water column was divided into denser, more saline and oxygen-depleted bottom waters separated by a chemocline from an upper water layer consisting of oxic seawater influenced by freshwater inflow. No evidence of a sharp increase of salinity across the MSC onset was found. Vertical oscillations of the chemocline exerted control over the stratigraphic architecture of the Primary Lower Gypsum unit and its deeper-water equivalents deposited during the first stage of the MSC. This study documents how temporal and spatial changes of water masses with different redox chemistries must be carefully considered when interpreting the MSC event.

### **3.8. Acknowledgments**

We thank S. Beckmann (Universität Hamburg) for technical support during organic geochemical analyses, L. Baumann (Universität Hamburg) for support in the application of the GDGTs proxies, D. Bortels (Universität Hamburg) for help with lipid biomarker extraction, J. Richarz (Universität Hamburg) for the analysis of TOC contents and H. Kuhnert (University of Bremen) for the bulk-rock carbon and oxygen stable isotopes analyses and help with data processing. S. Cavagna (University of Torino) is thanked for support with SEM-EDS analyses. This project received funding from University of Torino grants (ex 60% 2017 and 2019) to F. Dela Pierre. M. Sabino is funded by a doctoral scholarship provided by the Landesgraduiertenförderung of the state of Hamburg. The article is based upon work towards COST (European Cooperation in Science and Technology) Action 'Uncovering the Mediterranean salt giant' (MEDSALT). Comments by Iuliana Vasiliev and an anonymous reviewer helped to improve the manuscript.





# Chapter 4

## MARINE THAUMARCHAEOTA RECORD CARBON ISOTOPE EXCURSIONS IN THE NORTHERNMOST OFFSHOOT OF THE LATE MIOCENE MEDITERRANEAN BASIN

---

*The fourth Chapter of the thesis is based on the content of the scientific article submitted to the peer-reviewed journal Geology as: Sabino, M., Birgel, D., Natalicchio, M., Dela Pierre, F., Peckmann, J. Marine Thaumarchaeota record carbon isotope excursions in the northernmost offshoot of the late Miocene Mediterranean Basin.*

### 4.1. Abstract

Group I mesophilic Thaumarchaeota fix carbon by taking up dissolved inorganic carbon (DIC). Accordingly,  $\delta^{13}\text{C}$  values of crenarchaeol – a biomarker of Thaumarchaeota – can be used to reconstruct  $\delta^{13}\text{C}_{\text{DIC}}$  of seawater if inputs from soil Thaumarchaeota are negligible. Semi-enclosed basins are very sensitive to carbon cycle perturbations since they tend to develop thermohaline stratification. Therefore, ancient semi-enclosed basins represent promising settings to assess the potential of thaumarchaeal lipids for  $\delta^{13}\text{C}_{\text{DIC}}$  reconstruction. We analyzed shale/marl couplets deposited about 6 Ma ago in the Piedmont Basin (NW Italy), the northernmost sub-basin of the semi-enclosed late Miocene Mediterranean. At that time, thermohaline stratification typified the Piedmont Basin due to progressive isolation of the Mediterranean Sea from the global ocean, climaxing with the Messinian salinity crisis (5.97–5.33 Ma). Before the onset of the crisis, the permanently stratified distal part of the basin hosted a  $^{13}\text{C}$  depleted ( $\delta^{13}\text{C}_{\text{DIC}}$  of about  $-6\text{‰}$ ) water mass below the chemocline. The advent of the crisis was marked by basinwide  $^{13}\text{C}$  enrichment of the DIC pool, with positive  $\delta^{13}\text{C}_{\text{DIC}}$  excursions up to  $+5\text{‰}$ . Such positive shift was caused by preferential export of  $^{12}\text{C}$  to the seafloor after phytoplankton blooms and limited replenishment of remineralized carbon due to the basinwide stabilization of thermohaline stratification. This study confirms that the carbon stable isotope composition of crenarchaeol has great potential to trace carbon cycle perturbations.

### 4.2. Introduction

Marine group I (MGI) mesophilic Thaumarchaeota are among the dominant archaea in marine environments (Santoro et al., 2019). Their occurrence can be traced by crenarchaeol, a source-specific pentacyclic glycerol dibiphytanyl glycerol tetraether (GDGT; Besseling et al., 2020; Schouten et al., 2013). Different communities of MGI Thaumarchaeota were identified, with the upper water column community typified by lower GDGT-2/GDGT-3 ratios than the deeper-water community (Kim et al., 2015). In modern marine settings, the  $\delta^{13}\text{C}$  values of crenarchaeol – measured as the cyclohexane ring-containing tricyclic biphytane (Bp-3) derived from ether cleavage – typically fall between  $-22\text{‰}$  and  $-19\text{‰}$

(Schouten et al., 2013). These values depend on autotrophic fixation of dissolved bicarbonate, with a biosynthetic fractionation factor ( $\epsilon$ ) of approximately 20‰ (Könneke et al., 2012). Therefore,  $\delta^{13}\text{C}_{\text{BP-3}}$  values were considered as potential proxy for tracing the carbon isotope composition of the dissolved inorganic carbon pool ( $\delta^{13}\text{C}_{\text{DIC}}$ ) and hence perturbations of the carbon cycle (Schouten et al., 2013). Semi-enclosed basins are sensitive to environmental change since they tend to develop thermohaline stratification, which impacts the  $\delta^{13}\text{C}_{\text{DIC}}$  of the water column (e.g., Fry et al., 1991). Water masses below the chemocline commonly become enriched in  $^{12}\text{C}$  due to pronounced organic matter remineralization, resulting in  $\delta^{13}\text{C}_{\text{DIC}}$  values as low as  $-19\text{‰}$  (e.g., van Breugel et al., 2005). Conversely, seasonal eutrophication and  $^{12}\text{CO}_2$  degassing in surface waters can produce  $^{13}\text{C}$  enrichment (Schmittner et al., 2013), with  $\delta^{13}\text{C}_{\text{DIC}}$  values as high as  $+16.5\text{‰}$  in lacustrine environments (e.g., Oren et al., 1995; Stiller et al., 1985). In ancient marine sediments, crenarchaeol exhibits  $\delta^{13}\text{C}$  signatures close to modern values (cf. Schouten et al., 2013). Ancient MGI Thaumarchaeota are thought to have had the same metabolism as modern representatives of this group, thus  $\delta^{13}\text{C}_{\text{BP-3}}$  values can potentially be used as paleo- $\delta^{13}\text{C}_{\text{DIC}}$  proxy (e.g., Kuypers et al., 2001; Schoon et al., 2013). Despite the potential of thaumarchaeal lipids as  $\delta^{13}\text{C}_{\text{DIC}}$  proxy, it has recently been suggested that growth rate and carbon dioxide concentration can influence the  $\epsilon$  values of MGI Thaumarchaeota, resulting in a maximum deviation of approximately 2‰ (Hurley et al., 2019; Pearson et al., 2019). However, whether such deviation recorded in modern seawater is actually exported and preserved to the sediment needs further exploration (Hurley et al., 2019). Other possible bias for  $\delta^{13}\text{C}_{\text{DIC}}$  reconstruction can derive from the assimilation of organic carbon and input of lipids of heterotrophic marine Euryarchaeota or group I mesophilic soil Thaumarchaeota (Pearson et al., 2016). Recent studies discarded the capabilities of Thaumarchaeota to assimilate organic carbon (cf. Pearson et al., 2019) and of marine Euryarchaeota to synthesize cyclic GDGTs (cf. Besseling et al., 2020). However, high input of terrestrial material – and hence soil-derived thaumarchaeal lipids – to semi-enclosed basins needs to be carefully considered in  $\delta^{13}\text{C}_{\text{DIC}}$  reconstructions.

To assess the potential of the  $\delta^{13}\text{C}$  values of thaumarchaeal lipids as  $\delta^{13}\text{C}_{\text{DIC}}$  proxies, we conducted a case study on the Piedmont Basin (NW Italy), the northernmost sub-basin of the late Miocene Mediterranean Basin (Dela Pierre et al., 2011). Tectonic isolation from the global ocean in the late Miocene caused the development of thermohaline stratification, bottom-water anoxia, and finally hypersalinity during the Messinian salinity crisis (MSC, 5.97-5.33 Ma; García-Veigas et al., 2018; Roveri et al., 2014a). These conditions favored the rise of prokaryotes in the Messinian Mediterranean Sea (Birgel et al., 2014; Christeleit et al., 2015). Reconstruction of marine archaeal communities of the Piedmont Basin indicated that MGI Thaumarchaeota represented the main group of planktonic archaea at the MSC onset (Natalicchio et al., 2017; Sabino et al., 2020a). After assessing possible bias induced by input of lipids of soil archaea, we reconstruct the  $\delta^{13}\text{C}_{\text{DIC}}$  of a stratified water body along a transect from proximal to distal parts of the southern margin of the Piedmont Basin using the  $\delta^{13}\text{C}$  values of thaumarchaeal lipids. This approach shows great promise to depict carbon cycle perturbations in ancient marine environments.

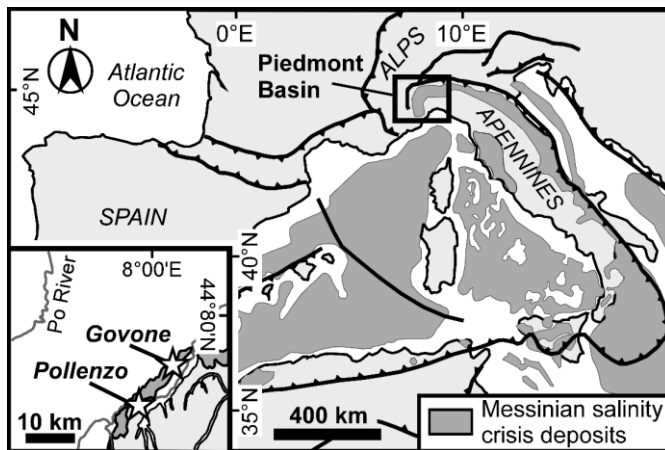


Figure 4.1 – Distribution of the deposits of the Messinian salinity crisis in the Mediterranean Basin; the inset indicates the locations of the proximal Pollenzo (44°41'08" N, 7°55'33" E) and distal Govone (44°48'08" N, 8°07'34" E) sections in the southern part of the Piedmont Basin (modified from Sabino et al., 2020a).

### 4.3. Materials and methods

We analyzed five lithologic cycles (shale/marl couplets) deposited across the MSC onset (5.97 Ma) at a water depth greater than 200 m in more proximal (Pollenzo; 43 samples) and distal areas (Govone; 14 samples) along the southern margin of the Piedmont Basin (Fig. 4.1, 4.2; for details, see Appendix D). These cycles belong to the Sant'Agata Fossili Marls Formation (Dela Pierre et al., 2011) and reflect astronomically-driven humid (shales) and arid (marls) climate oscillations (cf. Natalicchio et al., 2019; Sabino et al., 2020b). In the studied sections (Fig. 4.2), the MSC onset was placed at the base of marls of cycles Pm5 (Pollenzo; Natalicchio et al., 2019) and Gm30 (Govone; Gennari et al., 2020). An aliquot of the total lipid extract of the 57 samples was used to obtain isoprenoid and branched GDGTs, analyzed through high performance liquid chromatography – mass spectrometry (HPLC–MS). The branched and isoprenoid tetraether (BIT) index and the GDGT-2/GDGT-3 ratio were calculated to evaluate terrestrial input and the relative contribution of upper water column *vs.* deeper water column thaumarchaeal communities, respectively (Hopmans et al., 2004; Kim et al., 2015). Ether-bound isoprenoids were released from GDGTs by treating another aliquot of the extracts with HI/LiAlH<sub>4</sub>, while the asphaltene fraction of 18 samples (Pollenzo: 4 samples; Govone: 14 samples) was desulfurized to release sulfur-bound compounds from macromolecules. The hydrocarbon fractions obtained from ether-cleavage and desulfurization were analyzed through gas chromatography – mass spectrometry (GC–MS).  $\delta^{13}\text{C}$  analyses of ether-cleaved biphytanes (Bp), phytane (Ph, from ether cleavage and desulfurization), desulfurized C<sub>27</sub> to C<sub>29</sub> steranes, and C<sub>20-20</sub> and C<sub>20-25</sub> archaeols (from the free alcohol fraction) were performed on 38 samples (Pollenzo: 24 samples; Govone: 14 samples).  $\delta^{13}\text{C}$  values are reported in ‰ *vs.* the Vienna Pee Dee Belemnite (V–PDB) standard. For details, see Appendix D.

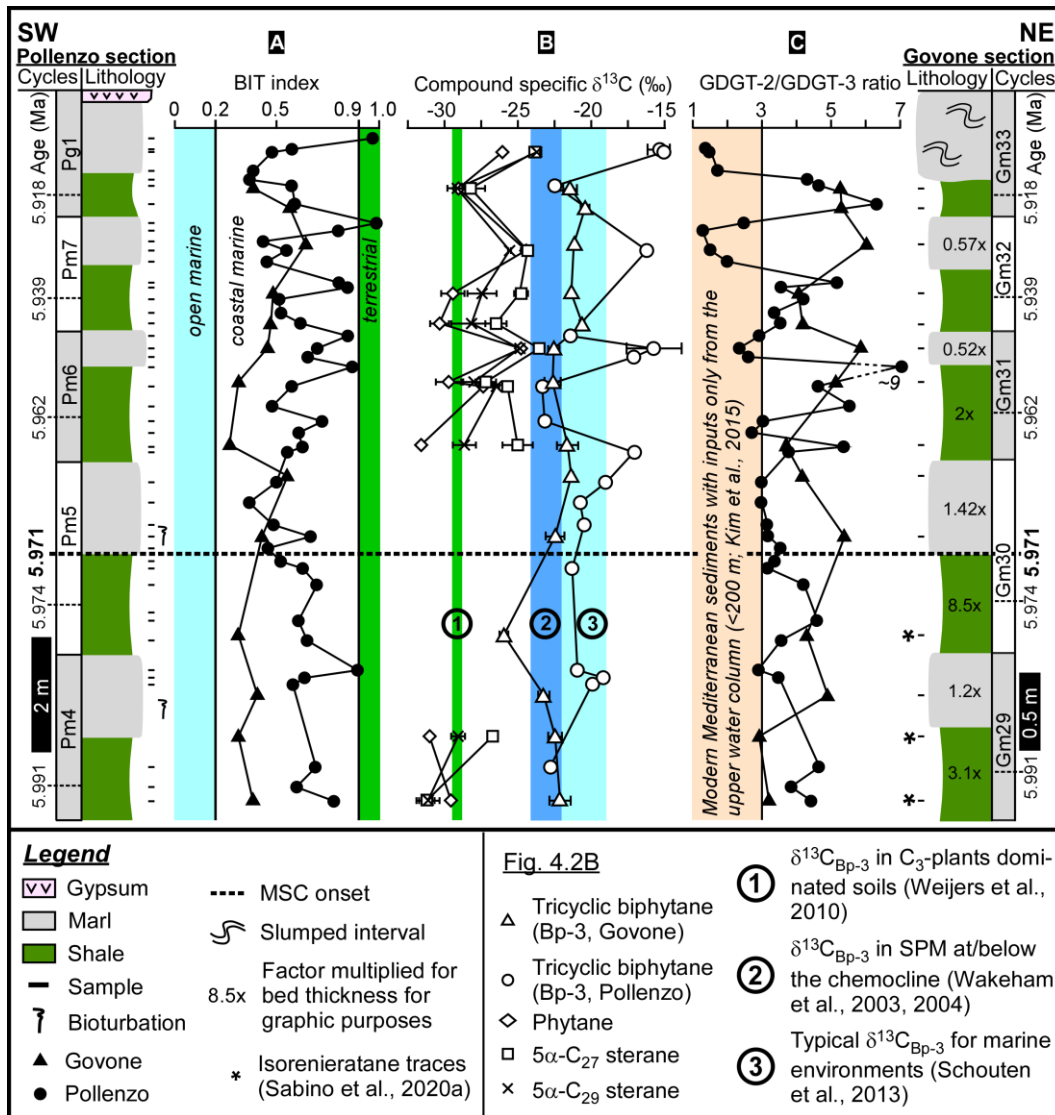


Figure 4.2 – (A) Branched and isoprenoid tetraether (BIT) index, (B) compound specific carbon ( $\delta^{13}C$ ) stable isotopes, and (C) GDGT-2/GDGT-3 ratio in the Pollenzo and Govone sections. GDGT: glycerol dibiphytanyl glycerol tetraether; MSC: Messinian salinity crisis; SPM: suspended particulate matter. Stratigraphic sections after Natalicchio et al. (2019; Pollenzo) and Sabino et al. (2020a; Govone).

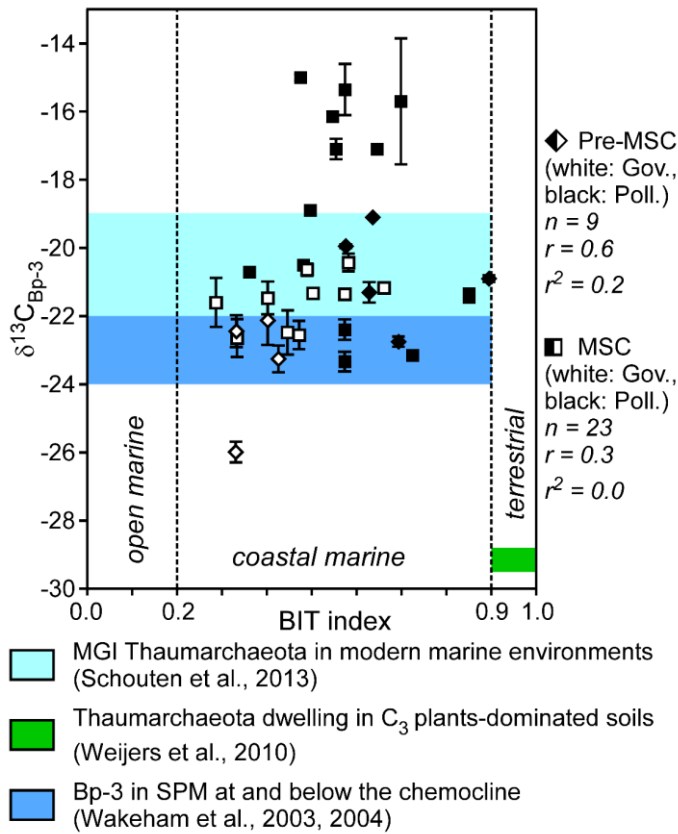


Figure 4.3 – Branched and isoprenoid tetraether (BIT) index vs. carbon stable isotope composition of tricyclic biphytane ( $\delta^{13}\text{C}_{\text{Bp-3}}$ ). Gov.: Govone; MGI: marine group I; MSC: Messinian salinity crisis; Poll.: Pollenzo; SPM: suspended particulate matter.

## 4.4. Results and discussion

### 4.4.1. Are $\delta^{13}\text{C}_{\text{Bp-3}}$ values a robust $\delta^{13}\text{C}_{\text{DIC}}$ proxy?

The BIT index between 0.3 and 1.0 (Fig. 4.2A) indicates moderate to high soil-derived organic matter input into the Piedmont Basin at the advent of the MSC, which is in agreement with abundant terrestrial plant remains and wax components reported for this basin (Bertini and Martinetto, 2011; Natalicchio et al., 2019; Sabino et al., 2020b). High terrestrial input, however, may bias a marine archaeal signal due to contributions from soil archaea, dominated by group I mesophilic soil Thaumarchaeota (Bates et al., 2011; Weijers et al., 2006). Their GDGT inventory comprises crenarchaeol, its isomer, and GDGT-0 to -4 (Sinninghe Damsté et al., 2012), the same lipids produced by MGI Thaumarchaeota (Schouten et al., 2013). The  $\delta^{13}\text{C}$  signature of lipids produced by Thaumarchaeota is best traced by Bp-3, exclusively derived from crenarchaeol (Schouten et al., 2013). The  $\delta^{13}\text{C}_{\text{Bp-3}}$  values from MGI Thaumarchaeota typically fall between  $-22\text{‰}$  and  $-19\text{‰}$  (Schouten et al., 2013). In contrast, the  $\delta^{13}\text{C}_{\text{Bp-3}}$  values of soil Thaumarchaeota are around  $-30\text{‰}$  in case of a dominance of C<sub>3</sub> vegetation, and are less <sup>12</sup>C depleted ( $-23\text{‰}$ ) if C<sub>4</sub> vegetation prevails (Weijers et al., 2010). It has been reported that C<sub>3</sub> plants dominated the Piedmont Basin hinterland in the late Messinian (Bertini and Martinetto, 2011). In case of a bias from soil archaea, a positive correlation between the highest BIT values and the lowest  $\delta^{13}\text{C}_{\text{Bp-3}}$  values is to be expected. However, the lowest  $\delta^{13}\text{C}_{\text{Bp-3}}$  values correlate with the lowest BIT values (Fig. 4.3), suggesting negligible input of soil thaumarchaeal lipids in the studied sediments (data on acyclic, mono-, and bicyclic biphytanes are provided in Appendix D).

Therefore, the measured  $\delta^{13}\text{C}_{\text{BP-3}}$  values apparently reflect a signature of MGI Thaumarchaeota and can therefore be used as  $\delta^{13}\text{C}_{\text{DIC}}$  proxy, assuming  $\varepsilon$  of approximately 20‰ (Könneke et al., 2012) and a possible  $\pm 2\%$  deviation (cf. Hurley et al., 2019).

#### 4.4.2. Impact of water column stratification on the $\delta^{13}\text{C}_{\text{DIC}}$ pool

During the late Miocene, thermohaline stratification developed in the water column of the Mediterranean Sea (Roveri et al., 2014a) including in the peripheral Piedmont Basin (Natalicchio et al., 2017). Before the MSC onset, the water column was periodically mixed toward the more proximal parts of the Piedmont Basin margin (Pollenzo; Natalicchio et al., 2017), while persistent stratification and episodic photic zone euxinia typified distal areas (Govone; Sabino et al., 2020a). This relationship is reflected by the  $\delta^{13}\text{C}_{\text{BP-3}}$  values of the pre-MSC sediments along the studied transect. In proximal settings, mixing probably promoted the redistribution of remineralized carbon in the water column, maintaining a  $\delta^{13}\text{C}_{\text{DIC}}$  signature close to that of modern seawater ( $-1\% < \delta^{13}\text{C}_{\text{DIC}} < +2\%$ ; Schmittner et al., 2013). This is testified by  $\delta^{13}\text{C}_{\text{BP-3}}$  values falling in the range of values found in modern marine settings ( $-22\% < \delta^{13}\text{C}_{\text{BP-3}} < -19\%$ ; Fig. 4.2B, 4.3; Schouten et al., 2013). Conversely, towards the depocenter (Govone), persistent thermohaline stratification resulted in an overall more  $^{13}\text{C}$  depleted DIC pool, reflected by  $\delta^{13}\text{C}_{\text{BP-3}}$  values typical of suspended particulate matter of modern permanently stratified basins at and below the chemocline ( $-22\% < \delta^{13}\text{C}_{\text{BP-3}} < -24\%$ ; Fig. 4.2B, 4.3; Wakeham et al., 2003, 2004). Applying the assumed  $\varepsilon$  of approximately  $20\% \pm 2\%$  of MGI Thaumarchaeota, the  $\delta^{13}\text{C}_{\text{DIC}}$  value in distal areas is estimated to have been  $-2\% \pm 2\%$ . To estimate the  $\delta^{13}\text{C}_{\text{DIC}}$  of the stagnant water mass below the chemocline during Messinian times, the sediments of cycle Gm30 (Govone) are used as an example. These sediments record a negative  $\delta^{13}\text{C}_{\text{BP-3}}$  excursion ( $-26\%$ ) and were deposited under photic zone euxinia, with a relatively shallow chemocline (Fig. 4.2B, C; Sabino et al., 2020a). Therefore, the DIC from the stagnant water mass was probably the main carbon source for the thaumarchaeal communities, with an estimated  $\delta^{13}\text{C}_{\text{DIC}}$  value of  $-6\% \pm 2\%$ .

The MSC onset coincided with severe restriction and intensified water column stratification in the Mediterranean Basin (García-Veigas et al., 2018; Roveri et al., 2014a), in case of the Piedmont Basin favored by increased riverine input (Natalicchio et al., 2019). Trends in the  $\delta^{13}\text{C}$  signatures of thaumarchaeal lipids – as well as of algal steranes and phytane, see Appendix D – reflect progressive  $^{13}\text{C}$  enrichment in seawater DIC (Fig. 4.2B). Remarkably, excursions toward  $\delta^{13}\text{C}_{\text{BP-3}}$  values as high as  $-15\%$  coincide with GDGT-2/GDGT-3 ratios lower than 3 (Fig. 4.2B, C). Such low ratios are found in sediments of today's Mediterranean Sea whose thaumarchaeal lipids derive only from the community thriving in the upper water column ( $< 200$  m; cf. Kim et al., 2015). Similarly, the patterns recorded in the more proximal settings (Pollenzo) are likely due to lipids sourced from the thaumarchaeal community dwelling in the upper water column. Overall, the data suggest that  $\delta^{13}\text{C}_{\text{DIC}}$  values were as high as  $+5\% \pm 2\%$  in the upper water column during the earliest phase of the MSC. Drier climate in the Mediterranean during the MSC (Roveri et al., 2014a) makes preferred  $^{12}\text{CO}_2$  degassing via enhanced

seawater evaporation a possible explanation for  $^{13}\text{C}$  enrichment in the DIC pool (e.g., Horton et al., 2016). This mechanism, however, contradicts with the reconstructed persistence of humid conditions in the northern Mediterranean after the MSC onset (cf. Sabino et al., 2020b). Interestingly, precession-paced climate change inducing periodic increase of riverine runoff and nutrient input into the basin was shown to have led to phytoplankton blooms (Natalicchio et al., 2019). We suggest that enhanced primary production and massive export of  $^{12}\text{C}$  to the seafloor resulted in  $^{13}\text{C}$  enrichment in the DIC pool of the upper water column (Fig. 4.4). Concurrently, stabilization of thermohaline stratification limited the replenishment of remineralized carbon to the upper water column, agreeing with the coinciding  $^{13}\text{C}$  enrichment in algal lipids (Fig. 4.2B). In contrast, the MSC sediments of the distal Govone section lack the abnormally high  $\delta^{13}\text{C}_{\text{BP-3}}$  values and show GDGT-2/GDGT-3 ratios higher than 3 (Fig. 4.2C), indicating input of lipids also from MGI Thaumarchaeota dwelling in deeper waters (Kim et al., 2015). Assimilation of  $^{12}\text{C}$  enriched DIC from the water column below the chemocline resulted in lower  $\delta^{13}\text{C}_{\text{BP-3}}$  values (around  $-21\text{‰}$ ). Periodically enhanced input of  $^{12}\text{C}$  enriched DIC into the upper water column is possibly suggested by lowering of the  $\delta^{13}\text{C}$  values of algal lipids (Fig. 4.2B). Given that mixing was suppressed by the stable thermohaline stratification (García-Veigas et al., 2018; Sabino et al., 2020a), enhanced input of  $^{12}\text{C}$  enriched DIC was probably caused by increased riverine runoff. In fact,  $\delta^{13}\text{C}_{\text{DIC}}$  values as low as  $-11\text{‰}$  have been reported for today's rivers draining the former catchment area of the Piedmont Basin (Marchina et al., 2016). To sum up, permanent stratification of the water column after the onset of the MSC promoted the development of strong vertical chemical gradients, establishing a  $^{13}\text{C}$  enriched upper water column overlaying a  $^{12}\text{C}$  enriched water mass in the Piedmont Basin.

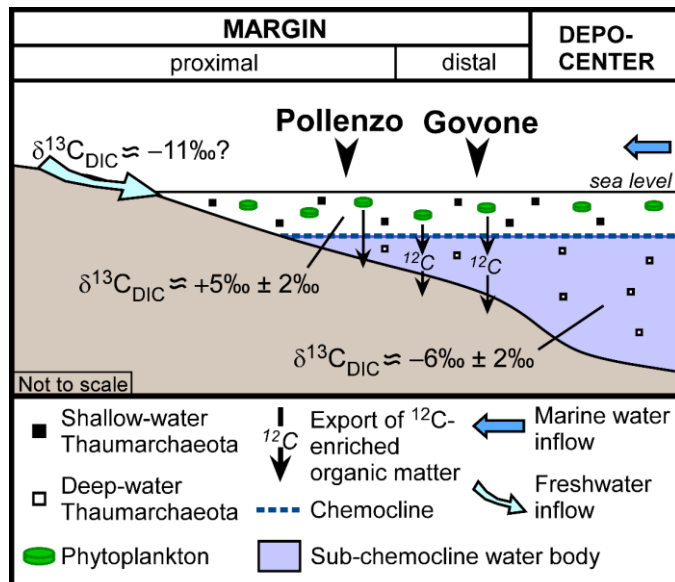


Figure 4.4 –  $\delta^{13}\text{C}_{\text{DIC}}$  values in the stratified water mass of the Piedmont Basin at the advent of the Messinian salinity crisis. DIC: dissolved inorganic carbon.

## 4.5. Summary and implications

The carbon stable isotope signature of tricyclic biphytane ( $\delta^{13}\text{C}_{\text{Bp-3}}$ ), resulting from ether cleavage of crenarchaeol produced by marine Thaumarchaeota, allowed to trace for the first time the composition of the pool of dissolved inorganic carbon (DIC) at the advent of the late Miocene Messinian salinity crisis in the northernmost offshoot of the semi-enclosed Mediterranean Sea, the Piedmont Basin. A  $^{12}\text{C}$  enriched ( $\delta^{13}\text{C}_{\text{DIC}}$  of about  $-6\text{‰}$ ) stagnant water body existed before the onset of the crisis toward the basin depocenter. The advent of the crisis was marked by  $^{13}\text{C}$  enrichment of the DIC pool in the upper water column ( $\delta^{13}\text{C}_{\text{DIC}}$  as high as about  $+5\text{‰}$ ) due to the basinwide stabilization of thermohaline stratification. The  $^{13}\text{C}$  enrichment of the upper water column is interpreted to reflect preferential export of  $^{12}\text{C}$  to the seafloor after phytoplankton blooms and limited replenishment of remineralized DIC. This study highlights the potential of tricyclic biphytane to trace the isotope composition of seawater DIC in stratified water bodies of ancient oceanic basins.

## 4.6. Acknowledgments

We thank S. Beckmann (Universität Hamburg) for technical support during organic geochemical analyses. M. Sabino is funded by a doctoral scholarship provided by the Landesgraduiertenförderung of the state of Hamburg. The article is further based upon work from COST Action ‘Uncovering the Mediterranean salt giant’ (MEDSALT) supported by COST (European Cooperation in Science and Technology).





# Chapter 5

## SYNTHESIS AND FUTURE PERSPECTIVES

The outcome of the organic and inorganic geochemical, stratigraphic, and petrographic investigations has allowed answering the scientific questions (SQ1, 2, 3) posed in the opening of the thesis (Chapter 1). Accordingly, the environmental change across the onset of the late Miocene Messinian salinity crisis (MSC; 5.97–5.33 Ma) in the northernmost Mediterranean sub-basin, the Piedmont Basin (NW Italy), was traced (Fig. 5.1).

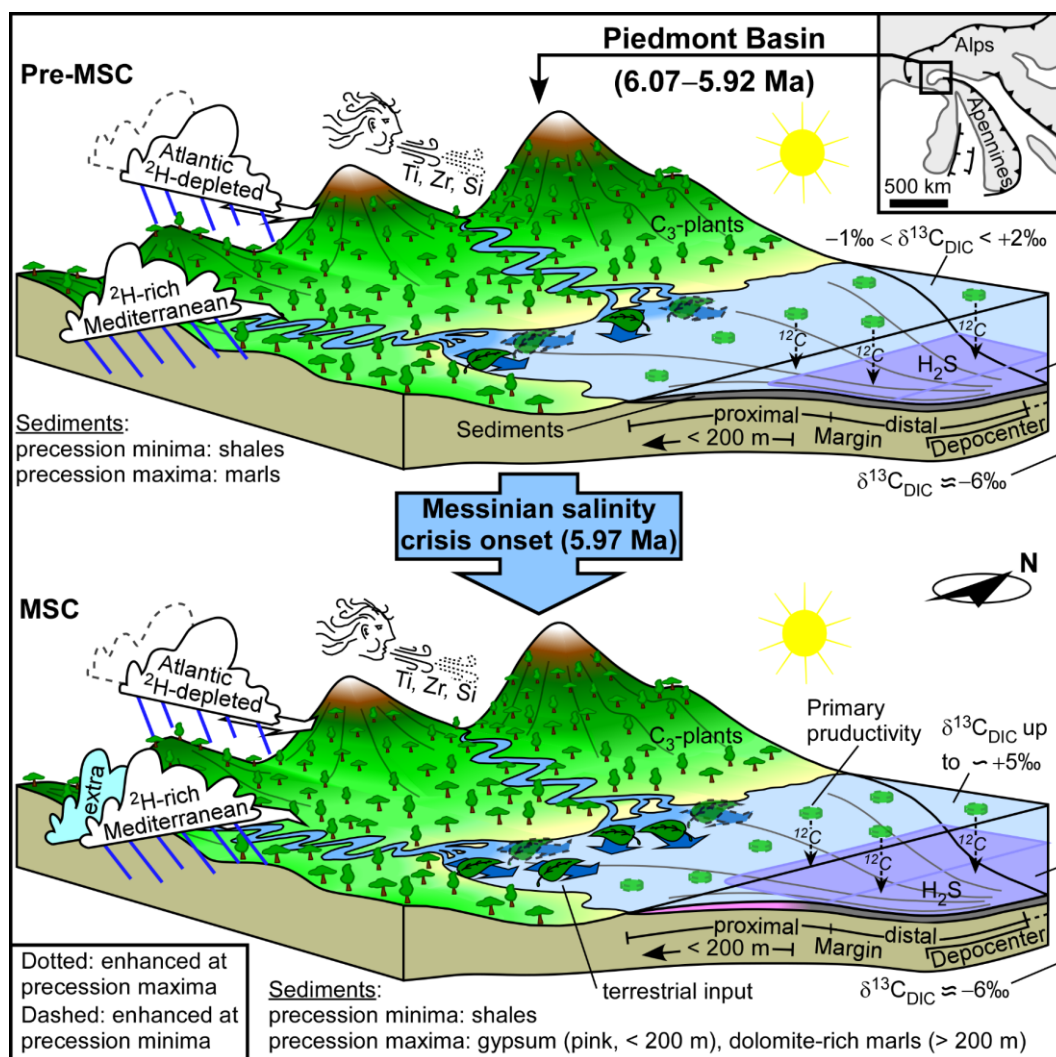


Figure 5.1 – Scenario for the Piedmont Basin across the onset of the Messinian salinity crisis (the time interval 6.07 – 5.92 Ma) according to the outcome of this study.

SQ1: *How did climate and hydrology varied in the northern Mediterranean across the MSC onset?*

No strong aridification in the northern Mediterranean Basin across the MSC onset has been detected. Rather, an overall increase in humidity has been found, caused by enhanced contribution of moisture with Mediterranean origin to the northern Mediterranean rainfall (Fig. 5.1). Superimposed on the long-term trend, the cyclic change in parameters of Earth's orbit (precession, with a periodicity of about 21 kyr) drove climate and hydrologic fluctuations in the Piedmont Basin. Moister conditions and higher fluvial discharge prevailed at precession minima, due to enhanced contribution of moisture with North Atlantic origin to the northern Mediterranean rainfall (Fig. 5.1). Conversely, a relatively drier climate dominated the precession maxima hemicycles, since the influence of North Atlantic perturbations was attenuated (Fig. 5.1). Most importantly, the outcome of this study indicates that during the deposition of marls – and hence the corresponding time-equivalent gypsum – no substantial climate change towards arid conditions occurred. Therefore, strong aridity does not appear as the *conditio sine qua non* gypsum could precipitate in the Mediterranean realm, as already suggested by studies targeting gypsum fluid inclusions and hydration water (Evans et al., 2015; Natalicchio et al., 2014). These results fully expose our poor knowledge of the climate and hydrologic conditions accompanying deposition of evaporites during the MSC. Accordingly, it appears urgent to extend multiproxy investigations to other late Miocene Mediterranean sub-basins, targeting specifically sediments representing precession maxima (possibly also gypsum) to better perceive and unravel the climate and hydrologic conditions at that time.

SQ2: *How were the water column and sedimentary environments impacted by the advent of the MSC in the Piedmont Basin?*

SQ3: *How did the onset of the MSC affect the carbon cycle in the northernmost Mediterranean sub-basin?*

The MSC onset was further marked in the Piedmont Basin by the persistence of normal marine conditions in the upper water column and an intensification of thermohaline stratification (Fig. 5.1). This feature was already rather persistent prior to the advent of the MSC, yet only close to the depocenter of the Piedmont Basin. Thermohaline stratification promoted the occurrence of a relatively deep, oxygen-depleted and sulfidic water body overlaid by an upper, normal marine water body (Fig. 5.1). The stagnant, deep-water mass was estimated to have developed a  $^{12}\text{C}$ -enriched dissolved organic carbon (DIC) pool with a  $\delta^{13}\text{C}$  value of about  $-6\text{‰}$  (Fig. 5.1). Towards the margin, however, thermohaline stratification was periodically disrupted (precession maxima), maintaining a  $\delta^{13}\text{C}_{\text{DIC}}$  between  $-1\text{‰}$  and  $+2\text{‰}$  (Fig. 5.1). Only after the MSC onset thermohaline stratification became stable also towards the margin. This promoted the development of a progressively more  $^{13}\text{C}$  enriched DIC pool in the upper water column, periodically reaching  $\delta^{13}\text{C}_{\text{DIC}}$  values as high as  $+5\text{‰}$  (Fig. 5.1). The  $^{13}\text{C}$  enrichment was linked to phytoplankton blooms and the following export of  $^{12}\text{C}$  rich organic matter to the seafloor. Concurrently, the stabilization of thermohaline stratification led to a limited replenishment of remineralized DIC back to the upper water column. For the first time, this thesis records the perturbation of the late Miocene Mediterranean carbon cycle in relation to the massive export of organic matter to the seafloor and thermohaline stratification. Remarkably, the MSC event has been suggested to have been

characterized by strong water column stratification at the Mediterranean scale (e.g., García-Veigas et al., 2018; Hardie and Lowenstein, 2004; Simon and Meijer, 2017). Furthermore, the MSC event possibly impacted the global carbon cycle and hence the climate of the late Miocene (Capella et al., 2019; Flecker et al., 2015; Ivanovic et al., 2014). Therefore, it appears critical to evaluate the local *vs.* regional significance in the identified carbon cycle perturbations, both temporally and spatially extending the applied investigations. This will potentially have implications for global scale climate models of the late Miocene, but also beyond this time period. In fact, the late Miocene represents the time in which the Modern climate and oceanic circulation started to develop.

**SQ2: *How were the water column and sedimentary environments impacted by the advent of the MSC in the Piedmont Basin?***

The distribution of the early MSC sediments was controlled by the depth of the chemocline, i.e. the water volume encompassing strong chemical gradients, which separated a deeper water body from

an upper water body (Fig. 5.1). At precession minima, the chemocline was located relatively high above the seafloor, promoting strong oxygen-deprived conditions at the seafloor and deposition of organic-rich shales throughout the basin. At precession maxima the chemocline deepened. In intermediate paleobathymetric settings (> 200 m), where the chemocline intercepted or was above the seafloor, dolomite-rich marls were deposited (Fig. 5.1). In this scenario, oxygen-depleted conditions prevailed at the seafloor, favoring organoclastic sulfate reduction and precipitation of bacterially mediated dolomite. The rate of sulfate reduction apparently outpaced sulfate replenishment, resulting in gypsum undersaturation and hence no precipitation/preservation of sulfate evaporites occurred (Fig. 5.1). Conversely, gypsum precipitated since 5.97 Ma in shallower areas, where the thermohaline stratification was disrupted, the seafloor oxygenated, and organoclastic sulfate reduction suppressed (Fig. 5.1). These results highlight that sediment deposition during the MSC was controlled by fluctuations in the position of the chemocline and the resultant redox chemistry of the water masses. Thermohaline stratification was apparently a prominent feature of the late Miocene Mediterranean Sea during the MSC (see above). Therefore, when interpreting the MSC event, a careful evaluation of spatial and temporal changes of the physicochemical parameters of water masses is needed. A possible opportunity to better constrain redox conditions at the seafloor and in the water column could be the investigation of redox sensitive elements and element speciations (e.g., Algeo and Li, 2020; Bennett and Canfield, 2020), approaches still largely unexplored for the MSC that may be instrumental for better constraining redox conditions at the seafloor and in the water column. Further insights for a better understanding of the biogeochemical cycle of the late Miocene Mediterranean Sea is to be expected, possibly elucidating the still unclear trigger for gypsum precipitation.



## REFERENCE LIST

---

- Aichner, B., Ott, F., Słowiński, M., Noryśkiewicz, A.M., Brauer, A., Sachse, D., 2018. Leaf wax *n*-alkane distributions record ecological changes during the Younger Dryas at Trzechowskie paleolake (northern Poland) without temporal delay. *Clim. Past* 14, 1607–1624. <https://doi.org/10.5194/cp-14-1607-2018>
- Algeo, T.J., Li, C., 2020. Redox classification and calibration of redox thresholds in sedimentary systems. *Geochim. Cosmochim. Acta* 287, 8–26. <https://doi.org/10.1016/j.gca.2020.01.055>
- Allredge, A.L., Cowles, T.J., MacIntyre, S., Rines, J.E.B., Donaghay, P.L., Greenlaw, C.F., Holliday, D. V., Deksheniaks, M.M., Sullivan, J.M., Zaneveld, J.R. V., 2002. Occurrence and mechanisms of formation of a dramatic thin layer of marine snow in a shallow Pacific fjord. *Mar. Ecol. Prog. Ser.* 233, 1–12. <https://doi.org/10.3354/meps233001>
- Allredge, A.L., Silver, M.W., 1988. Characteristics, dynamics and significance of marine snow. *Prog. Oceanogr.* 20, 41–82. [https://doi.org/10.1016/0079-6611\(88\)90053-5](https://doi.org/10.1016/0079-6611(88)90053-5)
- Andersen, N., Paul, H.A., Bernasconi, S.M., McKenzie, J.A., Pasteur, L., Albrecht, P., 2001. Large and rapid climate variability during the Messinian salinity crisis: evidence from deuterium concentrations of individual biomarkers. *Geology* 29, 799–802. [https://doi.org/10.1130/0091-7613\(2001\)029<0799:LARCVD>2.0.CO;2](https://doi.org/10.1130/0091-7613(2001)029<0799:LARCVD>2.0.CO;2)
- Bąbel, M., 2004. Models for evaporite, selenite and gypsum microbialite deposition in ancient saline basins. *Acta Geol. Pol.* 54, 219–249.
- Bąbel, M., Bogucki, A., 2007. The Badenian evaporite basin of the northern Carpathian Foredeep as a model of a meromictic selenite basin. *Geol. Soc. Spec. Publ.* 285, 219–246. <https://doi.org/10.1144/SP285.13>
- Badaut, D., Risacher, F., 1983. Authigenic smectite on diatom frustules in Bolivian saline lakes. *Geochim. Cosmochim. Acta* 47, 363–375. [https://doi.org/10.1016/0016-7037\(83\)90259-4](https://doi.org/10.1016/0016-7037(83)90259-4)
- Banta, A.B., Wei, J.H., Welander, P.V., 2015. A distinct pathway for tetrahymanol synthesis in bacteria. *Proc. Natl. Acad. Sci.* 112, 13478–13483. <https://doi.org/10.1073/pnas.1511482112>
- Bates, S.T., Berg-Lyons, D., Caporaso, J.G., Walters, W.A., Knight, R., Fierer, N., 2011. Examining the global distribution of dominant archaeal populations in soil. *ISME J.* 5, 908–917. <https://doi.org/10.1038/ismej.2010.171>
- Baumann, L.M.F., Taubner, R.S., Bauersachs, T., Steiner, M., Schleper, C., Peckmann, J., Rittmann, S.K.M.R., Birgel, D., 2018. Intact polar lipid and core lipid inventory of the hydrothermal vent methanogens *Methanocaldococcus villosus* and *Methanothermococcus okinawensis*. *Org. Geochem.* 126, 33–42. <https://doi.org/10.1016/j.orggeochem.2018.10.006>
- Behrooz, L., Naafs, B.D.A., Dickson, A.J., Love, G.D., Batenburg, S.J., Pancost, R.D., 2018. Astronomically driven variations in depositional environments in the South Atlantic during the Early Cretaceous. *Paleoceanogr. Paleoclimatology* 33, 894–912. <https://doi.org/10.1029/2018PA003338>
- Bellanca, A., Caruso, A., Ferruzza, G., Neri, R., Rouchy, J.-M., Sprovieri, M., Blanc-Valleron, M.-M., 2001. Transition from marine to hypersaline conditions in the Messinian Tripoli Formation from the marginal areas of the central Sicilian Basin. *Sediment. Geol.* 140, 87–105. [https://doi.org/10.1016/S0037-0738\(00\)00173-1](https://doi.org/10.1016/S0037-0738(00)00173-1)
- Belmar, L., Molina, V., Ulloa, O., 2011. Abundance and phylogenetic identity of archaeoplankton in the permanent oxygen minimum zone of the eastern tropical South Pacific. *FEMS Microbiol. Ecol.* 78, 314–326. <https://doi.org/10.1111/j.1574-6941.2011.01159.x>
- Bennett, W.W., Canfield, D.E., 2020. Redox-sensitive trace metals as paleoredox proxies: a review and analysis of data from modern sediments. *Earth-Science Rev.* 204, 103175. <https://doi.org/10.1016/j.earscirev.2020.103175>
- Bernardi, E., 2013. Integrated stratigraphy of the northernmost record of the Messinian salinity crisis: new insights from the Tertiary Piedmont Basin. PhD thesis, University of Torino.
- Bernardi, E., Dela Pierre, F., Gennari, R., Lozar, F., Violanti, D., 2012. Astrochronological calibration and paleoenvironmental reconstruction of the Messinian events at the Northern edge of the Mediterranean: The Govone section (Tertiary Piedmont Basin). *Rend. Online Soc. Geol. Ital.* 20, 10–11.

- Bertini, A., 2006. The Northern Apennines palynological record as a contribute for the reconstruction of the Messinian palaeoenvironments. *Sediment. Geol.* 188–189, 235–258. <https://doi.org/10.1016/j.sedgeo.2006.03.007>
- Bertini, A., Londeix, L., Maniscalco, R., Di Stefano, A., Suc, J.-P., Clauzon, G., Gautier, F., Grasso, M., 1998. Paleobiological evidence of depositional conditions in the Salt Member, Gessoso-Solfifera Formation (Messinian, Upper Miocene) of Sicily. *Micropaleontology* 44, 413–433. <https://doi.org/10.2307/1486042>
- Bertini, A., Martinetto, E., 2011. Reconstruction of vegetation transects for the Messinian-Piacenzian of Italy by means of comparative analysis of pollen, leaf and carpological records. *Palaeogeogr. Palaeoclimatol. Palaeoecol.* 304, 230–246. <https://doi.org/10.1016/j.palaeo.2010.09.005>
- Bertini, A., Martinetto, E., 2008. Messinian to Zanclean vegetation and climate of Northern and Central Italy. *Boll. della Soc. Paleontol. Ital.* 47, 105–121. <https://doi.org/10.1080/10292389409380483>
- Besseling, M.A., Hopmans, E.C., Bale, N.J., Schouten, S., Sinninghe Damsté, J.S., Villanueva, L., 2020. The absence of intact polar lipid-derived GDGTs in marine waters dominated by Marine Group II: implications for lipid biosynthesis in Archaea. *Sci. Rep.* 10, 1–10. <https://doi.org/10.1038/s41598-019-57035-0>
- Bialik, O.M., Frank, M., Betzler, C., Zammit, R., Waldmann, N.D., 2019. Two-step closure of the Miocene Indian Ocean Gateway to the Mediterranean. *Sci. Rep.* 9, 1–10. <https://doi.org/10.1038/s41598-019-45308-7>
- Bianchi, T.S., Canuel, E.A., 2011. Analytical chemical methods and instrumentation, in: *Chemical biomarkers in aquatic ecosystems*. Princeton University press, Princeton, USA, pp. 49–78. <https://doi.org/10.1515/9781400839100.49>
- Bigi, G., Cosentino, D., Parotto, M., Sartori, R., Scandone, P., 1990. Structural model of Italy: Geodynamic Project. Consiglio Nazionale delle Ricerche (S.EL.CA, scale 1:500,000, sheet 1).
- Birgel, D., Guido, A., Liu, X., Hinrichs, K.-U., Gier, S., Peckmann, J., 2014. Hypersaline conditions during deposition of the Calcare di Base revealed from archaeal di- and tetraether inventories. *Org. Geochem.* 77, 11–21. <https://doi.org/10.1016/j.orggeochem.2014.09.002>
- Birgel, D., Thiel, V., Hinrichs, K.-U., Elvert, M., Campbell, K.A., Reitner, J., Farmer, J.D., Peckmann, J., 2006. Lipid biomarker patterns of methane-seep microbialites from the Mesozoic convergent margin of California. *Org. Geochem.* 37, 1289–1302. <https://doi.org/10.1016/j.orggeochem.2006.02.004>
- Blanc-Valleron, M.-M., Pierre, C., Caulet, J.P., Caruso, A., Rouchy, J.-M., Cespuglio, G., Sprovieri, R., Pestrea, S., Di Stefano, E., 2002. Sedimentary, stable isotope and micropaleontological records of paleoceanographic change in the Messinian Tripoli Formation (Sicily, Italy). *Palaeogeogr. Palaeoclimatol. Palaeoecol.* 185, 255–286. [https://doi.org/10.1016/S0031-0182\(02\)00302-4](https://doi.org/10.1016/S0031-0182(02)00302-4)
- Blumenberg, M., Mollenhauer, G., Zabel, M., Reimer, A., Thiel, V., 2010. Decoupling of bio- and geohopanoids in sediments of the Benguela Upwelling System (BUS). *Org. Geochem.* 41, 1119–1129. <https://doi.org/10.1016/j.orggeochem.2010.06.005>
- Blumenberg, M., Seifert, R., Reitner, J., Pape, T., Michaelis, W., 2004. Membrane lipid patterns typify distinct anaerobic methanotrophic consortia. *Proc. Natl. Acad. Sci.* 101, 11111–11116. <https://doi.org/10.1073/pnas.0401188101>
- Bond, D.P.G., Wignall, P.B., 2010. Pyrite framboid study of marine Permian-Triassic boundary sections: a complex anoxic event and its relationship to contemporaneous mass extinction. *Bull. Geol. Soc. Am.* 122, 1265–1279. <https://doi.org/10.1130/B30042.1>
- Bontognali, T.R.R., Vasconcelos, C., Warthmann, R.J., Bernasconi, S.M., Dupraz, C., Strohmenger, C.J., Mckenzie, J.A., 2010. Dolomite formation within microbial mats in the coastal sabkha of Abu Dhabi (United Arab Emirates). *Sedimentology* 57, 824–844. <https://doi.org/10.1111/j.1365-3091.2009.01121.x>
- Bosmans, J.H.C., Drijfhout, S.S., Tuenter, E., Hilgen, F.J., Lourens, L.J., Rohling, E.J., 2015. Precession and obliquity forcing of the freshwater budget over the Mediterranean. *Quat. Sci. Rev.* 123, 16–30. <https://doi.org/10.1016/j.quascirev.2015.06.008>
- Brassell, S.C., 1992. Biomarkers in sediments, sedimentary rocks and petroleum: biological origins, geological fate and applications, in: Pratt, L.M., Comer, J.B., Brassell, S.C. (Eds.), *Geochemistry of organic matter in sediments and sedimentary rocks*. SEPM, Oklahoma, USA, pp. 29–72. <https://doi.org/10.2110/scn.92.27.0029>

- Brassell, S.C., Eglinton, G., Marlowe, I.T., Pflaumann, U., Sarnthein, M., 1986. Molecular stratigraphy: a new tool for climatic assessment. *Nature* 320, 129–133. <https://doi.org/10.1038/320129a0>
- Bray, E.E., Evans, E.D., 1961. Distribution of *n*-paraffins as a clue to recognition of source beds. *Geochim. Cosmochim. Acta* 22, 2–15. [https://doi.org/10.1016/0016-7037\(61\)90069-2](https://doi.org/10.1016/0016-7037(61)90069-2)
- Brocks, J.J., Love, G.D., Summons, R.E., Knoll, A.H., Logan, G.A., Bowden, S.A., 2005. Biomarker evidence for green and purple sulphur bacteria in a stratified Palaeoproterozoic sea. *Nature* 437, 866–870. <https://doi.org/10.1038/nature04068>
- Butler, R.W.H., Lickorish, W.H., Grasso, M., Pedley, H.M., Ramberti, L., 1995. Tectonics and sequence stratigraphy in Messinian basins, Sicily: constraints on the initiation and termination of the Mediterranean salinity crisis. *Geol. Soc. Am.* 107, 425–439. [https://doi.org/10.1130/0016-7606\(1995\)107<0425:TASSIM>2.3.CO;2](https://doi.org/10.1130/0016-7606(1995)107<0425:TASSIM>2.3.CO;2)
- Calvert, S.E., Fontugne, M.R., 2001. On the late Pleistocene-Holocene sapropel record of climatic and oceanographic variability in the Eastern Mediterranean. *Paleoceanography* 16, 78–94. <https://doi.org/10.1029/1999PA000488>
- Calvert, S.E., Pedersen, T.F., 2007. Elemental proxies for palaeoclimatic and palaeoceanographic variability in marine sediments: interpretation and application, in: Hillaire-Marcel, C., De Vernal, A. (Eds.), *Proxies in Late Cenozoic paleoceanography, developments in marine geology*. Elsevier, pp. 567–644. [https://doi.org/10.1016/S1572-5480\(07\)01019-6](https://doi.org/10.1016/S1572-5480(07)01019-6)
- Camerlenghi, A., Aloisi, V., 2020. Uncovering the Mediterranean Salt Giant (MEDSALT) – Scientific networking as incubator of cross-disciplinary research in Earth Sciences. *Eur. Rev.* 28, 40–61. <https://doi.org/doi:10.1017/S1062798719000255>
- Capella, W., Barhoun, N., Flecker, R., Hilgen, F.J., Kouwenhoven, T., Matenco, L.C., Sierro, F.J., Tubbure, M.A., Yousfi, M.Z., Krijgsman, W., 2018. Palaeogeographic evolution of the late Miocene Rifian Corridor (Morocco): reconstructions from surface and subsurface data. *Earth-Science Rev.* 180, 37–59. <https://doi.org/10.1016/j.earscirev.2018.02.017>
- Capella, W., Flecker, R., Hernández-Molina, F.J., Simon, D., Meijer, P.T., Rogerson, M., Sierro, F.J., Krijgsman, W., 2019. Mediterranean isolation preconditioning the Earth System for late Miocene climate cooling. *Sci. Rep.* 9, 1–8. <https://doi.org/10.1038/s41598-019-40208-2>
- Capella, W., Matenco, L., Dmitrieva, E., Roest, W.M.J., Hessels, S., Hssain, M., Chakor-Alami, A., Sierro, F.J., Krijgsman, W., 2017. Thick-skinned tectonics closing the Rifian Corridor. *Tectonophysics* 710–711, 249–265. <https://doi.org/10.1016/j.tecto.2016.09.028>
- Carnevale, G., Gennari, R., Lozar, F., Natalicchio, M., Pellegrino, L., Dela Pierre, F., 2019. Living in a deep desiccated Mediterranean Sea: an overview of the Italian fossil record of the Messinian salinity crisis. *Boll. della Soc. Paleontol. Ital.* 58, 109–140. <https://doi.org/10.4435/BSPL.2019.04>
- Caruso, A., Pierre, C., Blanc-Valleron, M.-M., Rouchy, J.-M., 2015. Carbonate deposition and diagenesis in evaporitic environments: the evaporative and sulphur-bearing limestones during the settlement of the Messinian Salinity Crisis in Sicily and Calabria. *Palaeogeogr. Palaeoclimatol. Palaeoecol.* 429, 136–162. <https://doi.org/10.1016/j.palaeo.2015.03.035>
- Celle-Jeanton, H., Travi, Y., Blavoux, B., 2001. Isotopic typology of the precipitation in the Western Mediterranean region at the three different time scales. *Geophys. Res. Lett.* 28, 1215–1218. <https://doi.org/10.1029/2000GL012407>
- Cerling, T.E., Harris, J.M., MacFadden, B.J., Leakey, M.G., Quade, J., Eisenmann, V., Ehleringer, J.R., 1997. Global vegetation change through the Miocene/Pliocene boundary. *Nature* 389, 153–158. <https://doi.org/10.1038/38229>
- Christeleit, E.C., Brandon, M.T., Zhuang, G., 2015. Evidence for deep-water deposition of abyssal Mediterranean evaporites during the Messinian salinity crisis. *Earth Planet. Sci. Lett.* 427, 226–235. <https://doi.org/10.1016/j.epsl.2015.06.060>
- CIESM, 2008. The Messinian Salinity Crisis from mega-deposits to microbiology - A consensus report, CIESM Work. ed. F. Briand, Monaco. 168 pp.
- Cita, M.B., Wright, R.C., Ryan, W.B.F., Longinelli, A., 1978. Messinian paleoenvironments. Initial reports Deep Sea Drill. Proj. 42 Pt. 1 42, 1003–1035. <https://doi.org/10.2973/dsdp.proc.42-1.153.1978>
- Clauzon, G., Suc, J.-P., Gautier, F., Berger, A., Loutre, M.-F., 1996. Alternate interpretation



- of the Messinian salinity crisis: controversy resolved? *Geology* 24, 363–366. [https://doi.org/10.1130/0091-7613\(1996\)024<0363:AIOTMS>2.3.CO;2](https://doi.org/10.1130/0091-7613(1996)024<0363:AIOTMS>2.3.CO;2)
- Collins, J.A., Schefuß, E., Mulitza, S., Prange, M., Werner, M., Tharammal, T., Paul, A., Wefer, G., 2013. Estimating the hydrogen isotopic composition of past precipitation using leaf-waxes from western Africa. *Quat. Sci. Rev.* 65, 88–101. <https://doi.org/10.1016/j.quascirev.2013.01.007>
- Collister, J.W., Rieley, G., Stern, B., Eglinton, G., Fry, B., 1994. Compound-specific  $\delta^{13}\text{C}$  analyses of leaf lipids from plants with differing carbon dioxide metabolisms. *Org. Geochem.* 21, 619–627. [https://doi.org/10.1016/0146-6380\(94\)90008-6](https://doi.org/10.1016/0146-6380(94)90008-6)
- Cordova-Gonzalez, A., Birgel, D., Kappler, A., Peckmann, J., 2020. Carbon stable isotope patterns of cyclic terpenoids: a comparison of cultured alkaliphilic aerobic methanotrophic bacteria and methane-seep environments. *Org. Geochem.* 139, 103940. <https://doi.org/10.1016/j.orggeochem.2019.103940>
- Cortina, A., Grimalt, J.O., Rigual-Hernández, A., Ballegeer, A.-M., Martrat, B., Sierro, F.J., Flores, J.A., 2016. The impact of ice-sheet dynamics in western Mediterranean environmental conditions during Terminations. An approach based on terrestrial long chain *n*-alkanes deposited in the upper slope of the Gulf of Lions. *Chem. Geol.* 430, 21–33. <https://doi.org/10.1016/j.chemgeo.2016.03.015>
- Dansgaard, W., 1964. Stable isotopes in precipitation. *Tellus* 16, 436–468. <https://doi.org/10.3402/tellusa.v16i4.8993>
- Dawson, K.S., Freeman, K.H., Macalady, J.L., 2012. Molecular characterization of core lipids from halophilic archaea grown under different salinity conditions. *Org. Geochem.* 48, 1–8. <https://doi.org/10.1016/j.orggeochem.2012.04.003>
- de Lange, G.J., Krijgsman, W., 2010. Messinian salinity crisis: A novel unifying shallow gypsum/deep dolomite formation mechanism. *Mar. Geol.* 275, 273–277. <https://doi.org/10.1016/j.margeo.2010.05.003>
- De Rosa, M., Gambacorta, A., 1988. The lipids of archaeobacteria. *Prog. Lipid Res.* 27, 153–175. [https://doi.org/10.1016/0163-7827\(88\)90011-2](https://doi.org/10.1016/0163-7827(88)90011-2)
- Dela Pierre, F., Bernardi, E., Cavagna, S., Clari, P., Gennari, R., Irace, A., Lozar, F., Lugli, S., Manzi, V., Natalicchio, M., Roveri, M., Violanti, D., 2011. The record of the Messinian salinity crisis in the Tertiary Piedmont Basin (NW Italy): The Alba section revisited. *Palaeogeogr. Palaeoclimatol. Palaeoecol.* 310, 238–255. <https://doi.org/10.1016/j.palaeo.2011.07.017>
- Dela Pierre, F., Clari, P., Bernardi, E., Natalicchio, M., Costa, E., Cavagna, S., Lozar, F., Lugli, S., Manzi, V., Roveri, M., Violanti, D., 2012. Messinian carbonate-rich beds of the Tertiary Piedmont Basin (NW Italy): Microbially-mediated products straddling the onset of the salinity crisis. *Palaeogeogr. Palaeoclimatol. Palaeoecol.* 344–345, 78–93. <https://doi.org/10.1016/j.palaeo.2012.05.022>
- Dela Pierre, F., Clari, P., Natalicchio, M., Ferrando, S., Giustetto, R., Lozar, F., Lugli, S., Manzi, V., Roveri, M., Violanti, D., 2014. Flocculent layers and bacterial mats in the mudstone interbeds of the Primary Lower Gypsum unit (Tertiary Piedmont basin, NW Italy): Archives of palaeoenvironmental changes during the Messinian salinity crisis. *Mar. Geol.* 355, 71–87. <https://doi.org/10.1016/j.margeo.2014.05.010>
- Dela Pierre, F., Festa, A., Irace, A., 2007. Interaction of tectonic, sedimentary, and diapiric processes in the origin of chaotic sediments: An example from the Messinian of Torino Hill (Tertiary Piedmont Basin, northwestern Italy). *Bull. Geol. Soc. Am.* 119, 1107–1119. <https://doi.org/10.1130/B26072.1>
- Dela Pierre, F., Natalicchio, M., Ferrando, S., Giustetto, R., Birgel, D., Carnevale, G., Gier, S., Lozar, F., Marabello, D., Peckmann, J., 2015. Are the large filamentous microfossils preserved in messinian gypsum colorless sulfide-oxidizing bacteria? *Geology* 43, 855–858. <https://doi.org/10.1130/G37018.1>
- Dela Pierre, F., Natalicchio, M., Lozar, F., Bonetto, S., Carnevale, G., Cavagna, S., Colombero, S., Sabino, M., Violanti, D., 2016. The northernmost record of the Messinian salinity crisis (Piedmont basin, Italy). *Geol. F. Trips* 8(2.1), 1–58. <https://doi.org/10.3301/GFT.2016.03>
- Diefendorf, A.F., Freeman, K.H., Wing, S.L., Graham, H.V., 2011. Production of *n*-alkyl lipids in living plants and implications for the geologic past. *Geochim. Cosmochim. Acta* 75, 7472–7485. <https://doi.org/10.1016/j.gca.2011.09.028>
- Diefendorf, A.F., Freimuth, E.J., 2017. Extracting the most from terrestrial plant-derived *n*-alkyl lipids and their carbon isotopes from the sedimentary record: a review. *Org. Geochem.* 103, 1–21. <https://doi.org/10.1016/j.orggeochem.2016.10.016>

- Diefendorf, A.F., Leslie, A.B., Wing, S.L., 2015. Leaf wax composition and carbon isotopes vary among major conifer groups. *Geochim. Cosmochim. Acta* 170, 145–156. <https://doi.org/10.1016/j.gca.2015.08.018>
- Drumond, A., Nieto, R., Hernandez, E., Gimeno, L., 2011. A Lagrangian analysis of the variation in moisture sources related to drier and wetter conditions in regions around the Mediterranean Basin. *Nat. Hazards Earth Syst. Sci.* 11, 2307–2320. <https://doi.org/10.5194/nhess-11-2307-2011>
- Eglinton, G., Hamilton, R.J., 1967. Leaf epicuticular waxes. *Science* 156, 1322–1335. <https://doi.org/10.1126/science.156.3780.1322>
- Eglinton, T.I., Benitez-Nelson, B.C., Pearson, A., McNichol, A.P., Bauer, J.E., Druffel, E.R.M., 1997. Variability in radiocarbon ages of individual organic compounds from marine sediments. *Science* 277, 796–799. <https://doi.org/10.1126/science.277.5327.796>
- Eglinton, T.I., Eglinton, G., 2008. Molecular proxies for paleoclimatology. *Earth Planet. Sci. Lett.* 275, 1–16. <https://doi.org/10.1016/j.epsl.2008.07.012>
- Eickhoff, M., Birgel, D., Talbot, H.M., Peckmann, J., Kappler, A., 2013. Oxidation of Fe(II) leads to increased C-2 methylation of pentacyclic triterpenoids in the anoxygenic phototrophic bacterium *Rhodopseudomonas palustris* strain TIE-1. *Geobiology* 11, 268–278. <https://doi.org/10.1111/gbi.12033>
- Elling, F.J., Könneke, M., Mußmann, M., Greve, A., Hinrichs, K.-U., 2015. Influence of temperature, pH, and salinity on membrane lipid composition and TEX<sub>86</sub> of marine planktonic thaumarchaeal isolates. *Geochim. Cosmochim. Acta* 171, 238–255. <https://doi.org/10.1016/j.gca.2015.09.004>
- Elling, F.J., Könneke, M., Nicol, G.W., Stieglmeier, M., Bayer, B., Spieck, E., de la Torre, J.R., Becker, K.W., Thomm, M., Prosser, J.I., Herndl, G.J., Schleper, C., Hinrichs, K.-U., 2017. Chemotaxonomic characterisation of the thaumarchaeal lipidome. *Environ. Microbiol.* 19, 2681–2700. <https://doi.org/10.1111/1462-2920.13759>
- Evans, N.P., Turchyn, A.V., Gázquez, F., Bontognali, T.R.R., Chapman, H.J., Hodell, D.A., 2015. Coupled measurements of  $\delta^{18}\text{O}$  and  $\delta\text{D}$  of hydration water and salinity of fluid inclusions in gypsum from the Messinian Yesares Member, Sorbas Basin (SE Spain). *Earth Planet. Sci. Lett.* 430, 499–510. <https://doi.org/10.1016/j.epsl.2015.07.071>
- Fauquette, S., Suc, J.-P., Bertini, A., Popescu, S.-M., Warny, S., Bachiri Taoufiq, N., Perez Villa, M.J., Chikhi, H., Feddi, N., Subally, D., Clauzon, G., Ferrier, J., 2006. How much did climate force the Messinian salinity crisis? Quantified climatic conditions from pollen records in the Mediterranean region. *Palaeogeogr. Palaeoclimatol. Palaeoecol.* 238, 281–301. <https://doi.org/10.1016/j.palaeo.2006.03.029>
- Favre, E., François, L., Fluteau, F., Cheddadi, R., Thévenod, L., Suc, J.-P., 2007. Messinian vegetation maps of the Mediterranean region using models and interpolated pollen data. *Geobios* 40, 433–443. <https://doi.org/10.1016/j.geobios.2006.12.002>
- Flecker, R., Krijgsman, W., Capella, W., de Castro Martins, C., Dmitrieva, E., Mayser, J.P., Marzocchi, A., Modestu, S., Ochoa, D., Simon, D., Tulbure, M., van den Berg, B., van der Schee, M., de Lange, G., Ellam, R., Govers, R., Gutjahr, M., Hilgen, F., Kouwenhoven, T., Lofi, J., Meijer, P., Sierro, F.J., Bachiri, N., Barhoun, N., Alami, A.C., Chacon, B., Flores, J.A., Gregory, J., Howard, J., Lunt, D., Ochoa, M., Pancost, R., Vincent, S., Yousfi, M.Z., 2015. Evolution of the Late Miocene Mediterranean-Atlantic gateways and their impact on regional and global environmental change. *Earth-Science Rev.* 150, 365–392. <https://doi.org/10.1016/j.earscirev.2015.08.007>
- Freeman, K.H., Hayes, J.M., Trendel, J.-M., Albrecht, P., 1990. Evidence from carbon isotope measurements for diverse origins of sedimentary hydrocarbons. *Nature* 343, 254–256. <https://doi.org/10.1038/343254a0>
- French, K.L., Hallmann, C., Hope, J.M., Schoon, P.L., Zumberge, J.A., Hoshino, Y., Peters, C.A., George, S.C., Love, G.D., Brocks, J.J., Buick, R., Summons, R.E., 2015a. Reappraisal of hydrocarbon biomarkers in Archean rocks. *Proc. Natl. Acad. Sci.* 112, 5915–5920. <https://doi.org/10.1073/pnas.1419563112>
- French, K.L., Rocher, D., Zumberge, J.E., Summons, R.E., 2015b. Assessing the distribution of sedimentary C<sub>40</sub> carotenoids through time. *Geobiology* 13, 139–151. <https://doi.org/10.1111/gbi.12126>
- Fry, B., Jannasch, H.W., Molyneaux, S.J., Wirsén, C.O., Muramoto, J.A., King, S., 1991. Stable isotope studies of the carbon, nitrogen and sulfur cycles in the Black Sea and the Cariaco Trench. *Deep. Res. Part A* 38, S1003–S1019. [https://doi.org/10.1016/s0198-0149\(10\)80021-4](https://doi.org/10.1016/s0198-0149(10)80021-4)

- Gaines, S.M., Eglinton, G., Rullkötter, J., 2009. *Echoes of life: what fossil molecules reveal about earth history*. Oxford University Press, New York. 355 pp.
- García-Veigas, J., Cendón, D.I., Gibert, L., Lowenstein, T.K., Artiaga, D., 2018. Geochemical indicators in Western Mediterranean Messinian evaporites: implications for the salinity crisis. *Mar. Geol.* 403, 197–214. <https://doi.org/10.1016/j.margeo.2018.06.005>
- Gennari, R., Lozar, F., Natalicchio, M., Zanella, E., Carnevale, G., Dela Pierre, F., 2020. Chronology of the Messinian Events in the northernmost part of the Mediterranean: the Govone section (Piedmont Basin, NW Italy). *Riv. Ital. di Paleontol. e Stratigr.* 126, 541–560. <http://hdl.handle.net/2318/1743913>
- Gennari, R., Lozar, F., Turco, E., Dela Pierre, F., Lugli, S., Manzi, V., Natalicchio, M., Roveri, M., Schreiber, B.C., Taviani, M., 2018. Integrated stratigraphy and paleoceanographic evolution of the pre-evaporitic phase of the Messinian salinity crisis in the Eastern Mediterranean as recorded in the Tokhni section (Cyprus island). *Newsletters Stratigr.* 51, 33–55. <https://doi.org/10.1127/nos/2017/0350>
- Gladstone, R., Flecker, R., Valdes, P., Lunt, D., Markwick, P., 2007. The Mediterranean hydrologic budget from a Late Miocene global climate simulation. *Palaeogeogr. Palaeoclimatol. Palaeoecol.* 251, 254–267. <https://doi.org/10.1016/j.palaeo.2007.03.050>
- Gómez-Hernández, M., Drumond, A., Gimeno, L., Garcia-Herrera, R., 2013. Variability of moisture sources in the Mediterranean region during the period 1980–2000. *Water Resour. Res.* 49, 6781–6794. <https://doi.org/10.1002/wrcr.20538>
- Griffin, D.L., 2002. Aridity and humidity: two aspects of the late Miocene climate of North Africa and the Mediterranean. *Palaeogeogr. Palaeoclimatol. Palaeoecol.* 182, 65–91. [https://doi.org/10.1016/S0031-0182\(01\)00453-9](https://doi.org/10.1016/S0031-0182(01)00453-9)
- Grothe, A., Andreetto, F., Reichart, G.-J., Wolthers, M., Van Baak, C.G.C., Vasiliev, I., Stoica, M., Sangiorgi, F., Middelburg, J.J., Davies, G.R., Krijgsman, W., 2020. Paratethys pacing of the Messinian Salinity Crisis: Low salinity waters contributing to gypsum precipitation? *Earth Planet. Sci. Lett.* 532, 116029. <https://doi.org/10.1016/j.epsl.2019.116029>
- Han, X., Schultz, L., Zhang, W., Zhu, J., Meng, F., Geesey, G.G., 2016. Mineral formation during bacterial sulfate reduction in the presence of different electron donors and carbon sources. *Chem. Geol.* 435, 49–59. <https://doi.org/10.1016/j.chemgeo.2016.04.022>
- Hardie, L.A., Lowenstein, T.K., 2004. Did the Mediterranean Sea dry out during the Miocene? A reassessment of the evaporite evidence from DSDP Legs 13 and 42A cores. *J. Sediment. Res.* 74, 453–461. <https://doi.org/10.1306/112003740453>
- Harvey, H.R., McManus, G.B., 1991. Marine ciliates as a widespread source of tetrahymanol and hopan-3 $\beta$ -ol in sediments. *Geochem. et Cosmochim. Acta* 55, 3387–3390. [https://doi.org/10.1016/0016-7037\(91\)90496-R](https://doi.org/10.1016/0016-7037(91)90496-R)
- Herbert, T.D., Lawrence, K.T., Tzanova, A., Peterson, L.C., Caballero-Gill, R., Kelly, C.S., 2016. Late Miocene global cooling and the rise of modern ecosystems. *Nat. Geosci.* 9, 843–847. <https://doi.org/10.1038/ngeo2813>
- Herrmann, N., Boom, A., Carr, A.S., Chase, B.M., West, A.G., Zabel, M., Schefuß, E., 2017. Hydrogen isotope fractionation of leaf wax *n*-alkanes in southern African soils. *Org. Geochem.* 109, 1–13. <https://doi.org/10.1016/j.orggeochem.2017.03.008>
- Hilgen, F.J., Bissoli, L., Iaccarino, S., Krijgsman, W., Meijer, R., Negri, A., Villa, G., 2000. Integrated stratigraphy and astrochronology of the Messinian GSSP at Oued Akrech (Atlantic Morocco). *Earth Planet. Sci. Lett.* 182, 237–251. [https://doi.org/10.1016/S0012-821X\(00\)00247-8](https://doi.org/10.1016/S0012-821X(00)00247-8)
- Hilgen, F.J., Krijgsman, W., 1999. Cyclostratigraphy and astrochronology of the Tripoli diatomite formation (pre-evaporite Messinian, Sicily, Italy). *Terra Nov.* 11, 16–22. <https://doi.org/10.1046/j.1365-3121.1999.00221.x>
- Hilgen, F.J., Krijgsman, W., Langereis, C.G., Lourens, L.J., Santarelli, A., Zachariasse, W.J., 1995. Extending the astronomical (polarity) time scale into the Miocene. *Earth Planet. Sci. Lett.* 136, 495–510. [https://doi.org/10.1016/0012-821X\(95\)00207-S](https://doi.org/10.1016/0012-821X(95)00207-S)
- Holbourn, A.E., Kuhnt, W., Clemens, S.C., Kochhann, K.G.D., Jöhnck, J., Lübbers, J., Andersen, N., 2018. Late Miocene climate cooling and intensification of southeast Asian winter monsoon. *Nat. Commun.* 9, 1584. <https://doi.org/10.1038/s41467-018-03950-1>
- Hopmans, E.C., Schouten, S., Pancost, R.D., van der Meer, M.T.J., Sinninghe Damsté, J.S.,

2000. Analysis of intact tetraether lipids in archaeal cell material and sediments by high performance liquid chromatography/atmospheric pressure chemical ionization mass spectrometry. *Rapid Commun. Mass Spectrom.* 14, 585–589. [https://doi.org/10.1002/\(SICI\)1097-0231\(20000415\)14:7<585::AID-RCM913>3.0.CO;2-N](https://doi.org/10.1002/(SICI)1097-0231(20000415)14:7<585::AID-RCM913>3.0.CO;2-N)
- Hopmans, E.C., Weijers, J.W.H., Schefuß, E., Herfort, L., Sinninghe Damsté, J.S., Schouten, S., 2004. A novel proxy for terrestrial organic matter in sediments based on branched and isoprenoid tetraether lipids. *Earth Planet. Sci. Lett.* 224, 107–116. <https://doi.org/10.1016/j.epsl.2004.05.012>
- Horton, T.W., Defliese, W.F., Tripathi, A.K., Oze, C., 2016. Evaporation induced <sup>18</sup>O and <sup>13</sup>C enrichment in lake systems: a global perspective on hydrologic balance effects. *Quat. Sci. Rev.* 131, 365–379. <https://doi.org/10.1016/j.quascirev.2015.06.030>
- Hötzel, S., Dupont, L., Schefuß, E., Rommerskirchen, F., Wefer, G., 2013. The role of fire in Miocene to Pliocene C<sub>4</sub> grassland and ecosystem evolution. *Nat. Geosci.* 6, 1027–1030. <https://doi.org/10.1038/ngeo1984>
- Hou, J., D'Andrea, W.J., Huang, Y., 2008. Can sedimentary leaf waxes record D/H ratios of continental precipitation? Field, model, and experimental assessments. *Geochim. Cosmochim. Acta* 72, 3503–3517. <https://doi.org/10.1016/j.gca.2008.04.030>
- Hsü, K.J., 1972. Origin of saline giants: a critical review after the discovery of the Mediterranean Evaporite. *Earth Sci. Rev.* 8, 371–396. [https://doi.org/10.1016/0012-8252\(72\)90062-1](https://doi.org/10.1016/0012-8252(72)90062-1)
- Hsü, K.J., Cita, M.B., Ryan, W.B.F., 1973a. The Origin of the Mediterranean Evaporite, in: Ryan, W.B.F., Hsü, K.J., Cita, M.B. (Eds.), *Initial Reports of the Deep Sea Drilling Project 13, Part 2*. U.S. Government Printing Office, Washington, DC, pp. 1203–1231. <https://doi.org/10.2973/dsdp.proc.13.143.1973>
- Hsü, K.J., Ryan, W.B.F., Cita, M.B., 1973b. Late Miocene desiccation of the Mediterranean. *Nature* 242, 240–244. <https://doi.org/10.1038/242240a0>
- Hurley, S.J., Close, H.G., Elling, F.J., Jasper, C.E., Gospodinova, K., McNichol, A.P., Pearson, A., 2019. CO<sub>2</sub>-dependent carbon isotope fractionation in Archaea, Part II: the marine water column. *Geochim. Cosmochim. Acta* 261, 383–395. <https://doi.org/10.1016/j.gca.2019.06.043>
- Irace, A., Clemente, P., Natalicchio, M., Ossella, L., Trenkwald, S., De Luca, D.A., Mosca, P., Piana, F., Polino, R., Violanti, D., 2009. *Geologia e idrostratigrafia profonda della Pianura Padana Occidentale*. La Nuova Lito Firenze. 110 pp.
- Irace, A., Dela Pierre, F., Clari, P., 2005. «Normal» and «chaotic» deposits in the Messinian Gessoso-solfifera Fm. at the north-eastern border of the Langhe domain (Tertiary Piedmont basin). *Boll. della Soc. Geol. Ital. Suppl.* 4, 77–85.
- Isaji, Y., Kawahata, H., Takano, Y., Ogawa, N.O., Kuroda, J., Yoshimura, T., Lugli, S., Manzi, V., Roveri, M., Ohkouchi, N., 2019a. Diazotrophy drives primary production in the organic-rich shales deposited under a stratified environment during the Messinian salinity crisis (Vena Del Gesso, Italy). *Front. Earth Sci.* 7, 1–13. <https://doi.org/10.3389/feart.2019.00085>
- Isaji, Y., Yoshimura, T., Kuroda, J., Tamenori, Y., Jiménez-Espejo, F.J., Lugli, S., Manzi, V., Roveri, M., Kawahata, H., Ohkouchi, N., 2019b. Biomarker records and mineral compositions of the Messinian halite and K–Mg salts from Sicily. *Prog. Earth Planet. Sci.* 6, 60. <https://doi.org/10.1186/s40645-019-0306-x>
- Ivanovic, R.F., Valdes, P.J., Flecker, R., Gutjahr, M., 2014. Modelling global-scale climate impacts of the late Miocene Messinian Salinity Crisis. *Clim. Past* 10, 607–622. <https://doi.org/10.5194/cp-10-607-2014>
- Jaeschke, A., Rethemeyer, J., Lappé, M., Schouten, S., Boeckx, P., Schefuß, E., 2018. Influence of land use on distribution of soil *n*-alkane  $\delta$ D and brGDGTs along an altitudinal transect in Ethiopia: implications for (paleo)environmental studies. *Org. Geochem.* 124, 77–87. <https://doi.org/10.1016/j.orggeochem.2018.06.006>
- Jessen, G.L., Lichtschlag, A., Struck, U., Boetius, A., 2016. Distribution and composition of thiotrophic mats in the hypoxic zone of the Black Sea (150–170 m water depth, Crimea margin). *Front. Microbiol.* 7, 1–14. <https://doi.org/10.3389/fmicb.2016.01011>
- Jiménez-Moreno, G., Fauquette, S., Suc, J.-P., 2010. Miocene to Pliocene vegetation reconstruction and climate estimates in the Iberian Peninsula from pollen data. *Rev. Palaeobot. Palynol.* 162, 403–415. <https://doi.org/10.1016/j.revpalbo.2009.08.001>
- Jiménez-Moreno, G., Pérez-Asensio, J.N., Larrasoana, J.C., Aguirre, J., Civis, J., Rivas-Carballo, M.R., Valle-Hernández, M.F., González-Delgado, J.A., 2013. Vegetation, sea-

- level, and climate changes during the Messinian salinity crisis. *Bull. Geol. Soc. Am.* 125, 432–444. <https://doi.org/10.1130/B30663.1>
- Jolivet, L., Augier, R., Robin, C., Suc, J.-P., Rouchy, J.-M., 2006. Lithospheric-scale geodynamic context of the Messinian salinity crisis. *Sediment. Geol.* 188–189, 9–33. <https://doi.org/10.1016/j.sedgeo.2006.02.004>
- Kahmen, A., Hoffmann, B., Schefuß, E., Arndt, S.K., Cernusak, L.A., West, J.B., Sachse, D., 2013a. Leaf water deuterium enrichment shapes leaf wax *n*-alkane  $\delta D$  values of angiosperm plants II: observational evidence and global implications. *Geochim. Cosmochim. Acta* 111, 50–63. <https://doi.org/10.1016/j.gca.2012.09.004>
- Kahmen, A., Schefuß, E., Sachse, D., 2013b. Leaf water deuterium enrichment shapes leaf wax *n*-alkane  $\delta D$  values of angiosperm plants I: experimental evidence and mechanistic insights. *Geochim. Cosmochim. Acta* 111, 39–49. <https://doi.org/10.1016/j.gca.2012.09.003>
- Kenig, F., Sinninghe Damsté, J.S., Frewin, N.L., Hayes, J.M., de Leeuw, J.W., 1995. Molecular indicators for palaeoenvironmental change in a Messinian evaporitic sequence (Vena del Gesso, Italy). II: high-resolution variations in abundances and  $^{13}C$  contents of free and sulphur-bound carbon skeletons in a single marl bed. *Org. Geochem.* 23, 485–526. [https://doi.org/10.1016/0146-6380\(95\)00049-K](https://doi.org/10.1016/0146-6380(95)00049-K)
- Killops, S., Killops, V., 2005. *Introduction to Organic Geochemistry*, 2nd ed. Blackwell Publishing, Oxford, UK. 393 pp.
- Kim, J.-H., Schouten, S., Rodrigo-Gámiz, M., Rampen, S., Marino, G., Huguet, C., Helmke, P., Buscail, R., Hopmans, E.C., Pross, J., Sangiorgi, F., Middelburg, J.B.M., Sinninghe Damsté, J.S., 2015. Influence of deep-water derived isoprenoid tetraether lipids on the TEX<sub>86</sub><sup>H</sup> paleothermometer in the Mediterranean Sea. *Geochim. Cosmochim. Acta* 150, 125–141. <https://doi.org/10.1016/j.gca.2014.11.017>
- Kim, J.-H., van der Meer, J., Schouten, S., Helmke, P., Willmott, V., Sangiorgi, F., Koç, N., Hopmans, E.C., Sinninghe Damsté, J.S., 2010. New indices and calibrations derived from the distribution of crenarchaeal isoprenoid tetraether lipids: implications for past sea surface temperature reconstructions. *Geochim. Cosmochim. Acta* 74, 4639–4654. <https://doi.org/10.1016/j.gca.2010.05.027>
- Kim, S.-T., Mucci, A., Taylor, B.E., 2007. Phosphoric acid fractionation factors for calcite and aragonite between 25 and 75 °C: Revisited. *Chem. Geol.* 246, 135–146. <https://doi.org/10.1016/j.chemgeo.2007.08.005>
- Kleemann, G., Poralla, K., Englert, G., Kjösen, H., Liaaen-Jensen, S., Neunlist, S., Rohmer, M., 1990. Tetrahymanol from the phototrophic bacterium *Rhodospseudomonas palustris*: first report of a gammacerane triterpene from a prokaryote. *J. Gen. Microbiol.* 136, 2551–2553. <https://doi.org/10.1099/00221287-136-12-2551>
- Knoll, A.H., Summons, R.E., Waldbauer, J.R., Zumberge, J.E., 2007. The geological succession of primary producers in the oceans, in: Falkowski, P., Knoll, A.H. (Eds.), *The evolution of primary producers in the sea*. Elsevier, Burlington, MA, pp. 133–163. <https://doi.org/10.1016/B978-012370518-1/50009-6>
- Könneke, M., Lipp, J.S., Hinrichs, K.-U., 2012. Carbon isotope fractionation by the marine ammonia-oxidizing archaeon *Nitrosopumilus maritimus*. *Org. Geochem.* 48, 21–24. <https://doi.org/10.1016/j.orggeochem.2012.04.007>
- Kouwenhoven, T.J., Morigi, C., Negri, A., Giunta, S., Krijgsman, W., Rouchy, J.-M., 2006. Palaeoenvironmental evolution of the eastern Mediterranean during the Messinian: constraints from integrated microfossil data of the Pissouri Basin (Cyprus). *Mar. Micropaleontol.* 60, 17–44. <https://doi.org/10.1016/j.marmicro.2006.02.005>
- Kouwenhoven, T.J., Seidenkrantz, M.-S., van der Zwaan, G.J., 1999. Deep-water changes: the near-synchronous disappearance of a group of benthic foraminifera from the Late Miocene Mediterranean. *Palaeogeogr. Palaeoclimatol. Palaeoecol.* 152, 259–281. [https://doi.org/10.1016/S0031-0182\(99\)00065-6](https://doi.org/10.1016/S0031-0182(99)00065-6)
- Krijgsman, W., Blanc-Valleron, M.-M., Flecker, R., Hilgen, F.J., Kouwenhoven, T.J., Merle, D., Orszag-Sperber, F., Rouchy, J.-M., 2002. The onset of the Messinian salinity crisis in the Eastern Mediterranean (Pissouri Basin, Cyprus). *Earth Planet. Sci. Lett.* 194, 299–310. [https://doi.org/10.1016/S0012-821X\(01\)00574-X](https://doi.org/10.1016/S0012-821X(01)00574-X)
- Krijgsman, W., Capella, W., Simon, D., Hilgen, F.J., Kouwenhoven, T.J., Meijer, P.T., Sierro, F.J., Tubbure, M.A., van den Berg, B.C.J., van der Schee, M., Flecker, R., 2018. The Gibraltar Corridor: watergate of the Messinian Salinity Crisis. *Mar. Geol.* 403, 238–246. <https://doi.org/10.1016/j.margeo.2018.06.008>
- Krijgsman, W., Fortuin, A.R., Hilgen, F.J., Sierro, F.J., 2001. Astrochronology for the

- Messinian Sorbas basin (SE Spain) and orbital (precessional) forcing for evaporite cyclicity. *Sediment. Geol.* 140, 43–60. [https://doi.org/10.1016/S0037-0738\(00\)00171-8](https://doi.org/10.1016/S0037-0738(00)00171-8)
- Krijgsman, W., Hilgen, F.J., Raffi, I., Sierro, F.J., Wilson, D.S., 1999. Chronology, causes and progression of the Messinian salinity crisis. *Nature* 400, 652–655. <https://doi.org/10.1038/23231>
- Kutzbach, J.E., Chen, G., Cheng, H., Edwards, R.L., Liu, Z., 2014. Potential role of winter rainfall in explaining increased moisture in the Mediterranean and Middle East during periods of maximum orbitally-forced insolation seasonality. *Clim. Dyn.* 42, 1079–1095. <https://doi.org/10.1007/s00382-013-1692-1>
- Kuypers, M.M.M., Blokker, P., Erbacher, J., Kinkel, H., Pancost, R.D., Schouten, S., Sinninghe Damsté, J.S., 2001. Massive expansion of marine archaea during a mid-Cretaceous oceanic anoxic event. *Science*. 293, 92–94. <https://doi.org/10.1126/science.1058424>
- Kuypers, M.M.M., Pancost, R.D., Nijenhuis, I.A., Sinninghe Damsté, J.S., 2002. Enhanced productivity led to increased organic carbon burial in the euxinic North Atlantic basin during the late Cenomanian oceanic anoxic event. *Paleoceanography* 17, 3-1–3-13. <https://doi.org/10.1029/2000PA000569>
- Laskar, J., Robutel, P., Joutel, F., Gastineau, M., Correia, A.C.M., Levrard, B., 2004. A long-term numerical solution for the insolation quantities of the Earth. *Astron. Astrophys.* 428, 261–285. <https://doi.org/10.1051/0004-6361:20041335>
- Li, P., Tanhua, T., 2020. Recent changes in deep ventilation of the Mediterranean Sea; evidence from long-term transient tracer observations. *Front. Mar. Sci.* 7, 594. <https://doi.org/10.3389/fmars.2020.00594>
- Lincoln, S.A., Wai, B., Eppley, J.M., Church, M.J., Summons, R.E., DeLong, E.F., 2014. Planktonic Euryarchaeota are a significant source of archaeal tetraether lipids in the ocean. *Proc. Natl. Acad. Sci.* 111, 9858–9863. <https://doi.org/10.1073/pnas.1409439111>
- Lionello, P., Abrantes, F., Congedi, L., Dulac, F., Gacic, M., Gomis, D., Goodess, C., Hoff, H., Kutiel, H., Luterbacher, J., Planton, S., Reale, M., Schröder, K., Vittoria Struglia, M., Toreti, A., Tsimplis, M., Ulbrich, U., Xoplaki, E., 2012. Introduction: mediterranean climate-background information, in: Lionello, P. (Ed.), *The climate of the mediterranean region: from the past to the future*. Elsevier Inc., Waltham, MA, pp. xxxv–xc. <https://doi.org/10.1016/B978-0-12-416042-2.00012-4>
- Löhr, S.C., Kennedy, M.J., George, S.C., Williamson, R.J., Xu, H., 2018. Sediment microfabric records mass sedimentation of colonial cyanobacteria and extensive syndepositional metazoan reworking in Pliocene sapropels. *Depos. Rec.* 4, 293–317. <https://doi.org/10.1002/dep2.49>
- Lozar, F., Negri, A., 2019. A review of basin-wide calcareous nannofossil bioevents in the Mediterranean at the onset of the Messinian salinity crisis. *Mar. Micropaleontol.* 151, 101752. <https://doi.org/10.1016/J.MARMICRO.2019.101752>
- Lozar, F., Violanti, D., Bernardi, E., Dela Pierre, F., Natalicchio, M., 2018. Identifying the onset of the Messinian salinity crisis: a reassessment of the biochronostratigraphic tools (Piedmont Basin, NW Italy). *Newsletters Stratigr.* 51, 11–31. <https://doi.org/10.1127/nos/2017/0354>
- Lugli, S., Manzi, V., Roveri, M., Schreiber, B.C., 2015. The deep record of the Messinian salinity crisis: evidence of a non-desiccated Mediterranean Sea. *Palaeogeogr. Palaeoclimatol. Palaeoecol.* 433, 201–218. <https://doi.org/10.1016/j.palaeo.2015.05.017>
- Lugli, S., Manzi, V., Roveri, M., Schreiber, B.C., 2010. The Primary Lower Gypsum in the Mediterranean: a new facies interpretation for the first stage of the Messinian salinity crisis. *Palaeogeogr. Palaeoclimatol. Palaeoecol.* 297, 83–99. <https://doi.org/10.1016/j.palaeo.2010.07.017>
- Lugli, S., Schreiber, B.C., Triberti, B., 1999. Giant polygons in the Realmonte mine (Agrigento, Sicily): evidence for the desiccation of a messinian halite basin. *J. Sediment. Res.* 69, 764–771. <https://doi.org/10.1306/D4268A86-2B26-11D7-8648000102C1865D>
- Luo, G., Yang, H., Algeo, T.J., Hallmann, C., Xie, S., 2019. Lipid biomarkers for the reconstruction of deep-time environmental conditions. *Earth-Science Rev.* 189, 99–124. <https://doi.org/10.1016/j.earscirev.2018.03.005>
- Luo, P., Peng, P.A., Lü, H.Y., Zheng, Z., Wang, X., 2012. Latitudinal variations of CPI values

- of long-chain *n*-alkanes in surface soils: evidence for CPI as a proxy of aridity. *Sci. China Earth Sci.* 55, 1134–1146. <https://doi.org/10.1007/s11430-012-4401-8>
- Madhavan, S., Treichel, I., O'Leary, M.H., 1991. Effects of relative humidity on carbon isotope fractionation in plants. *Bot. Acta* 104, 292–294. <https://doi.org/10.1111/j.1438-8677.1991.tb00232.x>
- Manzi, V., Gennari, R., Hilgen, F., Krijgsman, W., Lugli, S., Roveri, M., Sierro, F.J., 2013. Age refinement of the Messinian salinity crisis onset in the Mediterranean. *Terra Nov.* 25, 315–322. <https://doi.org/10.1111/ter.12038>
- Manzi, V., Gennari, R., Lugli, S., Minelli, N., Reghizzi, M., Roveri, M., Schreiber, B.C., 2016a. Comment on “Carbonate deposition and diagenesis in evaporitic environments: the evaporative and sulphur-bearing limestones during the settlement of the Messinian Salinity Crisis in Sicily and Calabria” by Caruso et al., 2015. *Palaeo3*, 429, 136–162. *Palaeogeogr. Palaeoclimatol. Palaeoecol.* 459, 585–596. <https://doi.org/10.1016/j.palaeo.2016.01.037>
- Manzi, V., Gennari, R., Lugli, S., Persico, D., Reghizzi, M., Roveri, M., Schreiber, B.C., Calvo, R., Gavrieli, I., Gvirtzman, Z., 2018. The onset of the Messinian salinity crisis in the deep Eastern Mediterranean basin. *Terra Nov.* 30, 189–198. <https://doi.org/10.1111/ter.12325>
- Manzi, V., Gennari, R., Lugli, S., Roveri, M., Scafetta, N., Schreiber, B.C., 2012. High-frequency cyclicity in the Mediterranean Messinian evaporites: evidence for solar-lunar climate forcing. *J. Sediment. Res.* 82, 991–1005. <https://doi.org/10.2110/jsr.2012.81>
- Manzi, V., Lugli, S., Roveri, M., Dela Pierre, F., Gennari, R., Lozar, F., Natalicchio, M., Schreiber, B.C., Taviani, M., Turco, E., 2016b. The Messinian salinity crisis in Cyprus: a further step towards a new stratigraphic framework for Eastern Mediterranean. *Basin Res.* 28, 207–236. <https://doi.org/10.1111/bre.12107>
- Manzi, V., Lugli, S., Roveri, M., Schreiber, B.C., 2009. A new facies model for the Upper Gypsum of Sicily (Italy): chronological and palaeoenvironmental constraints for the Messinian salinity crisis in the Mediterranean. *Sedimentology* 56, 1937–1960. <https://doi.org/10.1111/j.1365-3091.2009.01063.x>
- Manzi, V., Lugli, S., Roveri, M., Schreiber, B.C., Gennari, R., 2011. The Messinian “Calcare di Base” (Sicily, Italy) revisited. *Bull. Geol. Soc. Am.* 123, 347–370. <https://doi.org/10.1130/B30262.1>
- Manzi, V., Roveri, M., Gennari, R., Bertini, A., Biffi, U., Giunta, S., Iaccarino, S.M., Lanci, L., Lugli, S., Negri, A., Riva, A., Rossi, M.E., Taviani, M., 2007. The deep-water counterpart of the Messinian Lower Evaporites in the Apennine foredeep: the Fanantello section (Northern Apennines, Italy). *Palaeogeogr. Palaeoclimatol. Palaeoecol.* 251, 470–499. <https://doi.org/10.1016/j.palaeo.2007.04.012>
- Marchina, C., Bianchini, G., Knoeller, K., Natali, C., Pennisi, M., Colombani, N., 2016. Natural and anthropogenic variations in the Po river waters (northern Italy): insights from a multi-isotope approach. *Isotopes Environ. Health Stud.* 52, 649–672. <https://doi.org/10.1080/10256016.2016.1152965>
- Martinez-Ruiz, F., Kastner, M., Gallego-Torres, D., Rodrigo-Gámiz, M., Nieto-Moreno, V., Ortega-Huertas, M., 2015. Paleoclimate and paleoceanography over the past 20,000 yr in the Mediterranean Sea Basins as indicated by sediment elemental proxies. *Quat. Sci. Rev.* 107, 25–46. <https://doi.org/10.1016/j.quascirev.2014.09.018>
- Marzocchi, A., Flecker, R., van Baak, C.G.C., Lunt, D.J., Krijgsman, W., 2016. Mediterranean outflow pump: an alternative mechanism for the Lago-mare and the end of the Messinian Salinity Crisis. *Geology* 44, 523–526. <https://doi.org/10.1130/G37646.1>
- Marzocchi, A., Lunt, D.J., Flecker, R., Bradshaw, C.D., Farnsworth, A., Hilgen, F.J., 2015. Orbital control on late Miocene climate and the North African monsoon: insight from an ensemble of sub-precessional simulations. *Clim. Past* 11, 1271–1295. <https://doi.org/10.5194/cp-11-1271-2015>
- Mayser, J.P., Flecker, R., Marzocchi, A., Kouwenhoven, T.J., Lunt, D.J., Pancost, R.D., 2017. Precession driven changes in terrestrial organic matter input to the Eastern Mediterranean leading up to the Messinian Salinity Crisis. *Earth Planet. Sci. Lett.* 462, 199–211. <https://doi.org/10.1016/j.epsl.2017.01.029>
- Meijer, P.T., Tuentner, E., 2007. The effect of precession-induced changes in the Mediterranean freshwater budget on circulation at shallow and intermediate depth. *J. Mar. Syst.* 68, 349–365. <https://doi.org/10.1016/j.jmarsys.2007.01.006>
- Moller, T., Schulz, H., Hamann, Y., Dellwig, O., Kucera, M., 2012. Sedimentology and

- geochemistry of an exceptionally preserved last interglacial sapropel S5 in the Levantine Basin (Mediterranean Sea). *Mar. Geol.* 291–294, 34–48. <https://doi.org/10.1016/j.margeo.2011.10.011>
- Mosca, P., Polino, R., Rogledi, S., Rossi, M., 2010. New data for the kinematic interpretation of the Alps-Apennines junction (Northwestern Italy). *Int. J. Earth Sci.* 99, 833–849. <https://doi.org/10.1007/s00531-009-0428-2>
- Mycke, B., Michaelis, W., Degens, E.T., 1988. Biomarkers in sedimentary sulfides of precambrian age. *Org. Geochem.* 13, 619–625. [https://doi.org/10.1016/0146-6380\(88\)90081-2](https://doi.org/10.1016/0146-6380(88)90081-2)
- Naafs, B.D.A., Hefter, J., Acton, G., Haug, G.H., Martínez-García, A., Pancost, R., Stein, R., 2012. Strengthening of North American dust sources during the late Pliocene (2.7 Ma). *Earth Planet. Sci. Lett.* 317–318, 8–19. <https://doi.org/10.1016/j.epsl.2011.11.026>
- Natalicchio, M., Birgel, D., Peckmann, J., Lozar, F., Carnevale, G., Liu, X., Hinrichs, K.-U., Dela Pierre, F., 2017. An archaeal biomarker record of paleoenvironmental change across the onset of the Messinian salinity crisis in the absence of evaporites (Piedmont Basin, Italy). *Org. Geochem.* 113, 242–253. <https://doi.org/10.1016/j.orggeochem.2017.08.014>
- Natalicchio, M., Dela Pierre, F., Birgel, D., Brumsack, H., Carnevale, G., Gennari, R., Gier, S., Lozar, F., Pellegrino, L., Sabino, M., Schnetger, B., Peckmann, J., 2019. Paleoenvironmental change in a precession-paced succession across the onset of the Messinian salinity crisis: insight from element geochemistry and molecular fossils. *Palaeogeogr. Palaeoclimatol. Palaeoecol.* 518, 45–61. <https://doi.org/10.1016/j.palaeo.2019.01.009>
- Natalicchio, M., Dela Pierre, F., Lugli, S., Lowenstein, T.K., Feiner, S.J., Ferrando, S., Manzi, V., Roveri, M., Clari, P., 2014. Did Late Miocene (Messinian) gypsum precipitate from evaporated marine brines? Insights from the Piedmont Basin (Italy). *Geology* 42, 179–182. <https://doi.org/10.1130/G34986.1>
- Nesteroff, W.D., 1973. Un modèle pour les évaporites messiniennes en Méditerranée, des bassins peu profonds avec des dépôts d'évaporites lagunaires, in: *Messinian Events in the Mediterranean*, Geodynamics Scientific Report No. 7.
- Oppermann, B.I., Michaelis, W., Blumenberg, M., Frerichs, J., Schulz, H.M., Schippers, A., Beaubien, S.E., Krüger, M., 2010. Soil microbial community changes as a result of long-term exposure to a natural CO<sub>2</sub> vent. *Geochim. Cosmochim. Acta* 74, 2697–2716. <https://doi.org/10.1016/j.gca.2010.02.006>
- Oren, A., Gurevich, P., Anati, D.A., Barkan, E., Luz, B., 1995. A bloom of *Dunaliella parva* in the Dead Sea in 1992: biological and biogeochemical aspects. *Hydrobiologia* 297, 173–185. <https://doi.org/10.1007/BF00019283>
- Orszag-Sperber, F., 2006. Changing perspectives in the concept of “Lago-Mare” in Mediterranean Late Miocene evolution. *Sediment. Geol.* 188–189, 259–277. <https://doi.org/10.1016/j.sedgeo.2006.03.008>
- Pancost, R.D., Boot, C.S., 2004. The palaeoclimatic utility of terrestrial biomarkers in marine sediments. *Mar. Chem.* 92, 239–261. <https://doi.org/10.1016/j.marchem.2004.06.029>
- Pancost, R.D., Sinninghe Damsté, J.S., 2003. Carbon isotopic compositions of prokaryotic lipids as tracers of carbon cycling in diverse settings. *Chem. Geol.* 195, 29–58. [https://doi.org/10.1016/S0009-2541\(02\)00387-X](https://doi.org/10.1016/S0009-2541(02)00387-X)
- Pancost, R.D., van Geel, B., Baas, M., Sinninghe Damsté, J.S., 2000.  $\delta^{13}\text{C}$  values and radiocarbon dates of microbial biomarkers as tracers for carbon recycling in peat deposits. *Geology* 28, 663–666. [https://doi.org/10.1130/0091-7613\(2000\)28<663:CVARDO>2.0.CO;2](https://doi.org/10.1130/0091-7613(2000)28<663:CVARDO>2.0.CO;2)
- Passier, H.F., Middelburg, J.J., de Lange, G.J., Böttcher, M.E., 1997. Pyrite contents, microtextures, and sulfur isotopes in relation to formation of the youngest eastern Mediterranean sapropel. *Geology* 25, 519–522. [https://doi.org/10.1130/0091-7613\(1997\)025<0519:PCMASI>2.3.CO;2](https://doi.org/10.1130/0091-7613(1997)025<0519:PCMASI>2.3.CO;2)
- Pearson, A., Hurley, S.J., Elling, F.J., Wilkes, E.B., 2019. CO<sub>2</sub>-dependent carbon isotope fractionation in Archaea, Part I: modeling the 3HP/4HB pathway. *Geochim. Cosmochim. Acta* 261, 368–382. <https://doi.org/10.1016/j.gca.2019.06.042>
- Pearson, A., Hurley, S.J., Walter, S.R.S., Kusch, S., Lichtin, S., Zhang, Y.G., 2016. Stable carbon isotope ratios of intact GDGTs indicate heterogeneous sources to marine sediments. *Geochim. Cosmochim. Acta* 181, 18–35. <https://doi.org/10.1016/j.gca.2016.02.034>



- Pearson, A., Ingalls, A.E., 2013. Assessing the use of archaeal lipids as marine environmental proxies. *Annu. Rev. Earth Planet. Sci.* 41, 359–384. <https://doi.org/10.1146/annurev-earth-050212-123947>
- Pedentchouk, N., Zhou, Y., 2018. Factors controlling carbon and hydrogen isotope fractionation during biosynthesis of lipids by phototrophic organisms, in: Wilkes, H. (Ed.), *Hydrocarbons, oils and lipids: diversity, origin, chemistry and fate. Handbook of hydrocarbon and lipid microbiology.* Springer International Publishing, pp. 1–24. [https://doi.org/10.1007/978-3-319-54529-5\\_37-1](https://doi.org/10.1007/978-3-319-54529-5_37-1)
- Petrash, D.A., Bialik, O.M., Bontognali, T.R.R., Vasconcelos, C., Roberts, J.A., McKenzie, J.A., Konhauser, K.O., 2017. Microbially catalyzed dolomite formation: from near-surface to burial. *Earth-Science Rev.* 171, 558–582. <https://doi.org/10.1016/j.earscirev.2017.06.015>
- Pilskaln, C.H., Pike, J., 2001. Formation of Holocene sedimentary laminae in the Black Sea and the role of the benthic flocculent layer. *Paleoceanography* 16, 1–19. <https://doi.org/10.1029/1999PA000469>
- Poinsot, J., Schneckenburger, P., Adam, P., Schaeffer, P., Trendel, J.M., Riva, A., Albrecht, P., 1998. Novel polycyclic sulfides derived from regular polyprenoids in sediments: characterization, distribution, and geochemical significance. *Geochim. Cosmochim. Acta* 62, 805–814. [https://doi.org/10.1016/S0016-7037\(98\)00022-2](https://doi.org/10.1016/S0016-7037(98)00022-2)
- Popov, S.V., Shcherba, I.G., Ilyina, L.B., Nevesskaya, L.A., Paramonova, N.P., Khondkarian, S.O., Magyar, I., 2006. Late Miocene to Pliocene palaeogeography of the Paratethys and its relation to the Mediterranean. *Palaeogeogr. Palaeoclimatol. Palaeoecol.* 238, 91–106. <https://doi.org/10.1016/j.palaeo.2006.03.020>
- Pound, M.J., Haywood, A.M., Salzmann, U., Riding, J.B., 2012. Global vegetation dynamics and latitudinal temperature gradients during the Mid to Late Miocene (15.97–5.33 Ma). *Earth-Science Rev.* 112, 1–22. <https://doi.org/10.1016/j.earscirev.2012.02.005>
- Pound, M.J., Haywood, A.M., Salzmann, U., Riding, J.B., Lunt, D.J., Hunter, S.J., 2011. A Tortonian (Late Miocene, 11.61–7.25Ma) global vegetation reconstruction. *Palaeogeogr. Palaeoclimatol. Palaeoecol.* 300, 29–45. <https://doi.org/10.1016/j.palaeo.2010.11.029>
- Rashby, S.E., Sessions, A.L., Summons, R.E., Newman, D.K., 2007. Biosynthesis of 2-methylbacteriohopanepolyols by an anoxygenic phototroph. *Proc. Natl. Acad. Sci.* 104, 15099–15104. <https://doi.org/10.1073/pnas.0704912104>
- Repeta, D.J., Simpson, D.J., 1991. The distribution and recycling of chlorophyll, bacteriochlorophyll and carotenoids in the Black Sea. *Deep. Res. Part A. Oceanogr. Res. Pap.* 38, S969–S984. [https://doi.org/10.1016/S0198-0149\(10\)80019-6](https://doi.org/10.1016/S0198-0149(10)80019-6)
- Repeta, D.J., Simpson, D.J., Jorgensen, B.B., Jannasch, H.W., 1989. Evidence for anoxygenic photosynthesis from the distribution of bacterio-chlorophylls in the Black Sea. *Nature* 342, 69–72. <https://doi.org/10.1038/342069a0>
- Riding, R., Braga, J.C., Martín, J.M., Sánchez-Almazo, I.M., 1998. Mediterranean Messinian salinity crisis: constraints from a coeval marginal basin, Sorbas, southeastern Spain. *Mar. Geol.* 146, 1–20. [https://doi.org/10.1016/S0025-3227\(97\)00136-9](https://doi.org/10.1016/S0025-3227(97)00136-9)
- Risi, C., Bony, S., Vimeux, F., 2008. Influence of convective processes on the isotopic composition ( $\delta^{18}\text{O}$  and  $\delta\text{D}$ ) of precipitation and water vapor in the tropics: 2. Physical interpretation of the amount effect. *J. Geophys. Res. Atmos.* 113, 1–12. <https://doi.org/10.1029/2008JD009943>
- Robertson, C.E., Harris, J.K., Spear, J.R., Pace, N.R., 2005. Phylogenetic diversity and ecology of environmental Archaea. *Curr. Opin. Microbiol.* 8, 638–642. <https://doi.org/10.1016/j.mib.2005.10.003>
- Rohling, E.J., Marino, G., Grant, K.M., 2015. Mediterranean climate and oceanography, and the periodic development of anoxic events (sapropels). *Earth-Science Rev.* 143, 62–97. <https://doi.org/10.1016/j.earscirev.2015.01.008>
- Rosenbaum, J., Sheppard, S.M.F., 1986. An isotopic study of siderites, dolomites and ankerites at high temperatures. *Geochim. Cosmochim. Acta* 50, 1147–1150. [https://doi.org/10.1016/0016-7037\(86\)90396-0](https://doi.org/10.1016/0016-7037(86)90396-0)
- Rossi, M., 2017. Outcrop and seismic expression of stratigraphic patterns driven by accommodation and sediment supply turnarounds: implications on the meaning and variability of unconformities in syn-orogenic basins. *Mar. Pet. Geol.* 87, 112–127. <https://doi.org/10.1016/j.marpetgeo.2017.03.032>
- Rossi, M., Craig, J., 2016. A new perspective on sequence stratigraphy of syn-orogenic basins: insights from the Tertiary Piedmont Basin (Italy) and implications for play

- concepts and reservoir heterogeneity. *Geol. Soc. Spec. Publ.* 436, 93–133. <https://doi.org/10.1144/SP436.10>
- Rossi, M., Mosca, P., Polino, R., Rogledi, S., Biffi, U., 2009. New outcrop and subsurface data in the Tertiary Piedmont Basin (NW-Italy): unconformity-bounded stratigraphic units and their relationships with basin-modification phases. *Riv. Ital. di Paleontol. e Stratigr.* 115, 305–335. <https://doi.org/10.13130/2039-4942/6386>
- Rouchy, J.-M., Caruso, A., 2006. The Messinian salinity crisis in the Mediterranean basin: a reassessment of the data and an integrated scenario. *Sediment. Geol.* 188–189, 35–67. <https://doi.org/10.1016/j.sedgeo.2006.02.005>
- Roveri, M., Bassetti, M.A., Ricci Lucchi, F., 2001. The mediterranean Messinian salinity crisis: an Apennine foredeep perspective. *Sediment. Geol.* 140, 201–214. [https://doi.org/10.1016/S0037-0738\(00\)00183-4](https://doi.org/10.1016/S0037-0738(00)00183-4)
- Roveri, M., Bertini, A., Di Stefano, A., Gennari, R., Gliozzi, E., Grossi, F., Iaccarino, S.M., Lugli, S., Manzi, V., Taviani, M., 2008a. A high-resolution stratigraphic framework for the latest Messinian events in the Mediterranean area. *Stratigraphy* 5, 323–342.
- Roveri, M., Flecker, R., Krijgsman, W., Lofi, J., Lugli, S., Manzi, V., Sierro, F.J., Bertini, A., Camerlenghi, A., De Lange, G., Govers, R., Hilgen, F.J., Hübscher, C., Meijer, P.T., Stoica, M., 2014a. The Messinian Salinity Crisis: past and future of a great challenge for marine sciences. *Mar. Geol.* 352, 25–58. <https://doi.org/10.1016/j.margeo.2014.02.002>
- Roveri, M., Gennari, R., Lugli, S., Manzi, V., Minelli, N., Reghizzi, M., Riva, A., Rossi, M.E., Schreiber, B.C., 2016. The Messinian salinity crisis: open problems and possible implications for Mediterranean petroleum systems. *Pet. Geosci.* 22, 283–290. <https://doi.org/10.1144/petgeo2015-089>
- Roveri, M., Lugli, S., Manzi, V., Schreiber, B., 2008b. The Messinian salinity crisis: a sequence-stratigraphic approach. *GeoActa* 1, 169–190.
- Roveri, M., Lugli, S., Manzi, V., Schreiber, B.C., 2008c. The Messinian Sicilian stratigraphy revisited: new insights for the Messinian salinity crisis. *Terra Nov.* 20, 483–488. <https://doi.org/10.1111/j.1365-3121.2008.00842.x>
- Roveri, M., Manzi, V., Bergamasco, A., Falcieri, F.M., Gennari, R., Lugli, S., Schreiber, B.C., 2014b. Dense shelf water cascading and Messinian Canyons: a new scenario for the Mediterranean salinity crisis. *Am. J. Sci.* 314, 751–784. <https://doi.org/10.2475/05.2014.03>
- Rozanski, K., Araguás-Araguás, L., Gonfiantini, R., 1993. Isotopic patterns in modern global precipitation. *Clim. Chang. Cont. Isot. Rec.* 78, 1–36. <https://doi.org/10.1029/gm078p0001>
- Ruggeri, G., 1967. The Miocene and later evolution of the Mediterranean Sea, in: Adams, C.G., Ager, A.V. (Eds.), *Aspects of Tethyan biogeography*. London, pp. 283–290.
- Ryan, W.B.F., 2009. Decoding the mediterranean salinity crisis. *Sedimentology* 56, 95–136. <https://doi.org/10.1111/j.1365-3091.2008.01031.x>
- Ryan, W.B.F., 1976. Quantitative evaluation of the depth of the western Mediterranean before, during and after the Late Miocene salinity crisis. *Sedimentology* 23, 791–813. <https://doi.org/10.1111/j.1365-3091.1976.tb00109.x>
- Ryan, W.B.F., Cita, M.B., 1978. The nature and distribution of Messinian erosional surfaces – Indicators of a several-kilometer-deep Mediterranean in the Miocene. *Mar. Geol.* 27, 193–230. [https://doi.org/10.1016/0025-3227\(78\)90032-4](https://doi.org/10.1016/0025-3227(78)90032-4)
- Sabino, M., Dela Pierre, F., Natalicchio, M., Birgel, D., Gier, S., Peckmann, J., 2020a. The response of water column and sedimentary environments to the advent of the Messinian salinity crisis: insights from an onshore deep-water section (Govone, NW Italy). *Geol. Mag.* 1–17. <https://doi.org/10.1017/S0016756820000874>
- Sabino, M., Schefuß, E., Natalicchio, M., Dela Pierre, F., Birgel, D., Bortels, D., Schnetger, B., Peckmann, J., 2020b. Climatic and hydrologic variability in the northern Mediterranean across the onset of the Messinian salinity crisis. *Palaeogeogr. Palaeoclimatol. Palaeoecol.* 545, 109632. <https://doi.org/10.1016/j.palaeo.2020.109632>
- Sachse, D., Billault, I., Bowen, G.J., Chikaraishi, Y., Dawson, T.E., Feakins, S.J., Freeman, K.H., Magill, C.R., McInerney, F.A., van der Meer, M.T.J., Polissar, P., Robins, R.J., Sachs, J.P., Schmidt, H.-L., Sessions, A.L., White, J.W.C., West, J.B., Kahmen, A., 2012. Molecular paleohydrology: interpreting the hydrogen-isotopic composition of lipid biomarkers from photosynthesizing organisms. *Annu. Rev. Earth Planet. Sci.* 40, 221–249. <https://doi.org/10.1146/annurev-earth-042711-105535>

- Santoro, A.E., Richter, R.A., Dupont, C.L., 2019. Planktonic marine Archaea. *Ann. Rev. Mar. Sci.* 11, 131–158. <https://doi.org/10.1146/annurev-marine-121916-063141>
- Sanz-Montero, M.E., Rodríguez-Aranda, J.P., García Del Cura, M.A.A., 2008. Dolomite-silica stromatolites in Miocene lacustrine deposits from the Duero Basin, Spain: the role of organotemplates in the precipitation of dolomite. *Sedimentology* 55, 729–750. <https://doi.org/10.1111/j.1365-3091.2007.00919.x>
- Schefuß, E., Ratmeyer, V., Stuut, J.-B.W., Jansen, J.H.F., Sinninghe Damsté, J.S., 2003. Carbon isotope analyses of *n*-alkanes in dust from the lower atmosphere over the central eastern Atlantic. *Geochim. Cosmochim. Acta* 67, 1757–1767. [https://doi.org/10.1016/S0016-7037\(02\)01414-X](https://doi.org/10.1016/S0016-7037(02)01414-X)
- Schefuß, E., Schouten, S., Schneider, R.R., 2005. Climatic controls on central African hydrology during the past 20,000 years. *Nature* 437, 1003–1006. <https://doi.org/10.1038/nature03945>
- Schieber, J., 1996. Early diagenetic silica deposition in algal cysts and spores; a source of sand in black shales? *J. Sediment. Res.* 66, 175–183. <https://doi.org/10.1306/D42682ED-2B26-11D7-8648000102C1865D>
- Schmittner, A., Gruber, N., Mix, A.C., Key, R.M., Tagliabue, A., Westberry, T.K., 2013. Biology and air-sea gas exchange controls on the distribution of carbon isotope ratios ( $\delta^{13}\text{C}$ ) in the ocean. *Biogeosciences* 10, 5793–5816. <https://doi.org/10.5194/bg-10-5793-2013>
- Schnetger, B., 1992. Chemical-composition of loess from a local and worldwide view. *Neues Jahrb. Miner. Monatshefte* 1, 29–47.
- Schnetger, B., Brumsack, H.-J., Schale, H., Hinrichs, J., Dittert, L., 2000. Geochemical characteristics of deep-sea sediments from the Arabian Sea: a high-resolution study. *Deep. Res. Part II Top. Stud. Oceanogr.* 47, 2735–2768. [https://doi.org/10.1016/S0967-0645\(00\)00047-3](https://doi.org/10.1016/S0967-0645(00)00047-3)
- Schoon, P.L., Heilmann-Clausen, C., Pagh Schultz, B., Sluijs, A., Sinninghe Damsté, J.S., Schouten, S., 2013. Recognition of Early Eocene global carbon isotope excursions using lipids of marine Thaumarchaeota. *Earth Planet. Sci. Lett.* 373, 160–168. <https://doi.org/10.1016/j.epsl.2013.04.037>
- Schouten, S., Hoefs, M.J.L., Koopmans, M.P., Bosch, H.-J., Sinninghe Damsté, J.S., 1998a. Structural characterization, occurrence and fate of archaeal ether-bound acyclic and cyclic biphytanes and corresponding diols in sediments. *Org. Geochem.* 29, 1305–1319. [https://doi.org/10.1016/S0146-6380\(98\)00131-4](https://doi.org/10.1016/S0146-6380(98)00131-4)
- Schouten, S., Hopmans, E.C., Baas, M., Boumann, H., Standfest, S., Könneke, M., Stahl, D.A., Sinninghe Damsté, J.S., 2008. Intact membrane lipids of “*Candidatus Nitrosopumilus maritimus*,” a cultivated representative of the cosmopolitan mesophilic group I crenarchaeota. *Appl. Environ. Microbiol.* 74, 2433–2440. <https://doi.org/10.1128/AEM.01709-07>
- Schouten, S., Hopmans, E.C., Schefuß, E., Sinninghe Damsté, J.S., 2002. Distributional variations in marine crenarchaeotal membrane lipids: a new tool for reconstructing ancient sea water temperatures? *Earth Planet. Sci. Lett.* 204, 265–274. [https://doi.org/10.1016/S0012-821X\(02\)00979-2](https://doi.org/10.1016/S0012-821X(02)00979-2)
- Schouten, S., Hopmans, E.C., Sinninghe Damsté, J.S., 2013. The organic geochemistry of glycerol dialkyl glycerol tetraether lipids: a review. *Org. Geochem.* 54, 19–61. <https://doi.org/10.1016/j.orggeochem.2012.09.006>
- Schouten, S., Klein Breteler, W.C.M., Blokker, P., Schogt, N., Rijpstra, W.I.C., Grice, K., Baas, M., Sinninghe Damsté, J.S., 1998b. Biosynthetic effects on the stable carbon isotopic compositions of algal lipids: implications for deciphering the carbon isotopic biomarker record. *Geochim. Cosmochim. Acta* 62, 1397–1406. [https://doi.org/10.1016/S0016-7037\(98\)00076-3](https://doi.org/10.1016/S0016-7037(98)00076-3)
- Schouten, S., Pavlović, D., Sinninghe Damsté, J.S., de Leeuw, J.W., 1993. Nickel boride: an improved desulphurizing agent for sulphur-rich geomacromolecules in polar and asphaltene fractions. *Org. Geochem.* 20, 901–909. [https://doi.org/10.1016/0146-6380\(93\)90101-G](https://doi.org/10.1016/0146-6380(93)90101-G)
- Schouten, S., Villanueva, L., Hopmans, E.C., van der Meer, M.T.J., Sinninghe Damsté, J.S., 2014. Are Marine Group II Euryarchaeota significant contributors to tetraether lipids in the ocean? *Proc. Natl. Acad. Sci.* 111, E4285. <https://doi.org/10.1073/pnas.1416176111>
- Schuster, M., Düringer, P., Ghienne, J.-F., Vignaud, P., Mackaye, H.T., Likius, A., Brunet, M., 2006. The age of the Sahara desert. *Science*. 311, 821.

- <https://doi.org/10.1126/science.1120161>
- Selli, R., 1973. An outline of the Italian Messinian. *Messin. Events Mediterr.* 7, 150–171.
- Selli, R., 1960. Il Messiniano Mayer-Eymar 1867. Proposta di un neostratotipo. *G. di Geol.* 28, 1–33.
- Sharma, T., Clayton, R.N., 1965. Measurement of O<sup>18</sup>/O<sup>16</sup> ratios of total oxygen of carbonates. *Geochim. Cosmochim. Acta* 29, 1347–1353. [https://doi.org/10.1016/0016-7037\(65\)90011-6](https://doi.org/10.1016/0016-7037(65)90011-6)
- Sierro, F.J., Flores, J.A., Francés, G., Vazquez, A., Utrilla, R., Zamarreño, I., Erlenkeuser, H., Barcena, M.A., 2003. Orbitally-controlled oscillations in planktic communities and cyclic changes in western Mediterranean hydrography during the Messinian. *Palaeogeogr. Palaeoclimatol. Palaeoecol.* 190, 289–316. [https://doi.org/10.1016/S0031-0182\(02\)00611-9](https://doi.org/10.1016/S0031-0182(02)00611-9)
- Sierro, F.J., Flores, J.A., Zamarreño, I., Vázquez, A., Utrilla, R., Francés, G., Hilgen, F.J., Krijgsman, W., 1999. Messinian pre-evaporite sapropels and procession-induced oscillations in western Mediterranean climate. *Mar. Geol.* 153, 137–146. [https://doi.org/10.1016/S0025-3227\(98\)00085-1](https://doi.org/10.1016/S0025-3227(98)00085-1)
- Sierro, F.J., Hilgen, F.J., Krijgsman, W., Flores, J.A., 2001. The Abad composite (SE Spain): a Messinian reference section for the Mediterranean and the APTS. *Palaeogeogr. Palaeoclimatol. Palaeoecol.* 168, 141–169. [https://doi.org/10.1016/S0031-0182\(00\)00253-4](https://doi.org/10.1016/S0031-0182(00)00253-4)
- Simon, D., Marzocchi, A., Flecker, R., Lunt, D.J., Hilgen, F.J., Meijer, P.T., 2017. Quantifying the Mediterranean freshwater budget throughout the late Miocene: new implications for sapropel formation and the Messinian Salinity Crisis. *Earth Planet. Sci. Lett.* 472, 25–37. <https://doi.org/10.1016/j.epsl.2017.05.013>
- Simon, D., Meijer, P.T., 2017. Salinity stratification of the Mediterranean Sea during the Messinian crisis: a first model analysis. *Earth Planet. Sci. Lett.* 479, 366–376. <https://doi.org/10.1016/j.epsl.2017.09.045>
- Sinninghe Damsté, J.S., de Leeuw, J.W., 1990. Analysis, structure and geochemical significance of organically bound sulfur in the geosphere: state of the art and future research. *Org. Geochem.* 16, 1077–1101. [https://doi.org/10.1016/0146-6380\(90\)90145-P](https://doi.org/10.1016/0146-6380(90)90145-P)
- Sinninghe Damsté, J.S., Frewin, N.L., Kenig, F., de Leeuw, J.W., 1995a. Molecular indicators for palaeoenvironmental change in a Messinian evaporitic sequence (Vena del Gesso, Italy). I: variations in extractable organic matter of ten cyclically deposited marl beds. *Org. Geochem.* 23, 471–483. [https://doi.org/10.1016/0146-6380\(95\)00040-L](https://doi.org/10.1016/0146-6380(95)00040-L)
- Sinninghe Damsté, J.S., Kenig, F., Koopmans, M.P., Köster, J., Schouten, S., Hayes, J.M., de Leeuw, J.W., 1995b. Evidence for gammacerane as an indicator of water column stratification. *Geochim. Cosmochim. Acta* 59, 1895–1900. [https://doi.org/10.1016/0016-7037\(95\)00073-9](https://doi.org/10.1016/0016-7037(95)00073-9)
- Sinninghe Damsté, J.S., Kuypers, M.M.M., Schouten, S., Schulte, S., Rullkötter, J., 2003. The lycopane/C<sub>31</sub> *n*-alkane ratio as a proxy to assess palaeoacidity during sediment deposition. *Earth Planet. Sci. Lett.* 209, 215–226. [https://doi.org/10.1016/S0012-821X\(03\)00066-9](https://doi.org/10.1016/S0012-821X(03)00066-9)
- Sinninghe Damsté, J.S., Rijpstra, W.I.C., Hopmans, E.C., Jung, M.Y., Kim, J.G., Rhee, S.K., Stieglmeier, M., Schleper, C., 2012. Intact polar and core glycerol dibiphytanyl glycerol tetraether lipids of group I.1a and I.1b *Thaumarchaeota* in soil. *Appl. Environ. Microbiol.* 78, 6866–6874. <https://doi.org/10.1128/AEM.01681-12>
- Sinninghe Damsté, J.S., Schouten, S., Hopmans, E.C., van Duin, A.C.T., Genevasen, J.A.J., 2002. Crenarchaeol: the characteristic core glycerol dibiphytanyl glycerol tetraether membrane lipid of cosmopolitan pelagic crenarchaeota. *J. Lipid Res.* 43, 1641–1651. <https://doi.org/10.1194/jlr.M200148-JLR200>
- Sinninghe Damsté, J.S., Wakeham, S.G., Kohlen, M.E.L., Hayes, J.M., de Leeuw, J.W., 1993. A 6,000-year sedimentary molecular record of chemocline excursions in the Black Sea. *Lett. To Nat.* 362, 827–829. <https://doi.org/10.1038/362827a0>
- Sodemann, H., Zubler, E., 2010. Seasonal and inter-annual variability of the moisture sources for Alpine precipitation during 1995–2002. *Int. J. Climatol.* 30, 947–961. <https://doi.org/10.1002/joc.1932>
- Sollai, M., Villanueva, L., Hopmans, E.C., Keil, R.G., Sinninghe Damsté, J.S., 2019. Archaeal sources of intact membrane lipid biomarkers in the oxygen deficient zone of the eastern tropical South Pacific. *Front. Microbiol.* 10, 765.

- <https://doi.org/10.3389/fmicb.2019.00765>
- Stiller, M., Rounick, J.S., Shasha, S., 1985. Extreme carbon-isotope enrichments in evaporating brines. *Nature* 316, 434–435. <https://doi.org/10.1038/316434a0>
- Strömberg, C.A.E., 2011. Evolution of grasses and grassland ecosystems. *Annu. Rev. Earth Planet. Sci.* 39, 517–544. <https://doi.org/10.1146/annurev-earth-040809-152402>
- Sturani, C., 1976. Messinian facies in the Piedmont Basin. *Mem. Soc. Geol. Ital.* 16, 11–25.
- Sturani, C., 1973. A fossil eel (*Anguilla sp.*) from the Messinian of Alba (Tertiary Piedmont Basin). Palaeoenvironmental and palaeogeographic implications, in: Drooger, C.W. (Ed.), *Messinian Events in the Mediterranean*. K. Nederl. Akad. Wetensch. Amsterdam, pp. 243–255.
- Sturani, C., Sampò, M., 1973. Il Messiniano inferiore in facies diatomitica nel Bacino Terziario Piemontese. *Mem. Soc. Geol. Ital.* 12, 335–338.
- Suc, J.-P., Bessais, E., 1990. Pérennité d'un climat thermo-xérique en Sicile avant, pendant, après la crise de salinité messinienne. *Comptes rendus l'Académie des Sci. Série 2, Mécanique, Phys. Chim. Sci. l'univers, Sci. la Terre* 310, 1701–1707.
- Tagliavento, M., Lauridsen, B.W., Stemmerik, L., 2020. Episodic dysoxia during Late Cretaceous cyclic chalk-marl deposition – Evidence from framboidal pyrite distribution in the upper Maastrichtian Rørdal Mb., Danish Basin. *Cretac. Res.* 106, 104223. <https://doi.org/10.1016/j.cretres.2019.104223>
- Teixidor, P., Grimait, J.O., Pueyo, J.J., Rodriguez-Valera, F., 1993. Isopranylglycerol diethers in non-alkaline evaporitic environments. *Geochim. Cosmochim. Acta* 57, 4479–4489. [https://doi.org/10.1016/0016-7037\(93\)90497-K](https://doi.org/10.1016/0016-7037(93)90497-K)
- Tipple, B.J., Pagani, M., 2010. A 35 Myr North American leaf-wax compound-specific carbon and hydrogen isotope record: implications for C<sub>4</sub> grasslands and hydrologic cycle dynamics. *Earth Planet. Sci. Lett.* 299, 250–262. <https://doi.org/10.1016/j.epsl.2010.09.006>
- Toucanne, S., Angue Minto'o, C.M., Fontanier, C., Bassetti, M.-A., Jorry, S.J., Jouet, G., 2015. Tracking rainfall in the northern Mediterranean borderlands during sapropel deposition. *Quat. Sci. Rev.* 129, 178–195. <https://doi.org/10.1016/j.quascirev.2015.10.016>
- Tribouillard, N., Algeo, T.J., Lyons, T., Riboulleau, A., 2006. Trace metals as paleoredox and paleoproductivity proxies: an update. *Chem. Geol.* 232, 12–32. <https://doi.org/10.1016/j.chemgeo.2006.02.012>
- Tulbure, M.A., Capella, W., Barhoun, N., Flores, J.A., Hilgen, F.J., Krijgsman, W., Kouwenhoven, T., Sierro, F.J., Yousfi, M.Z., 2017. Age refinement and basin evolution of the North Rifian Corridor (Morocco): no evidence for a marine connection during the Messinian Salinity Crisis. *Palaeogeogr. Palaeoclimatol. Palaeoecol.* 485, 416–432. <https://doi.org/10.1016/j.palaeo.2017.06.031>
- Turich, C., Freeman, K.H., 2011. Archaeal lipids record paleosalinity in hypersaline systems. *Org. Geochem.* 42, 1147–1157. <https://doi.org/10.1016/j.orggeochem.2011.06.002>
- Turich, C., Freeman, K.H., Bruns, M.A., Conte, M., Jones, A.D., Wakeham, S.G., 2007. Lipids of marine Archaea: patterns and provenance in the water-column and sediments. *Geochim. Cosmochim. Acta* 71, 3272–3291. <https://doi.org/10.1016/j.gca.2007.04.013>
- Tzanova, A., Herbert, T.D., Peterson, L., 2015. Cooling Mediterranean Sea surface temperatures during the Late Miocene provide a climate context for evolutionary transitions in Africa and Eurasia. *Earth Planet. Sci. Lett.* 419, 71–80. <https://doi.org/10.1016/j.epsl.2015.03.016>
- van Breugel, Y., Schouten, S., Paetzel, M., Nordeide, R., Sinninghe Damsté, J.S., 2005. The impact of recycling of organic carbon on the stable carbon isotopic composition of dissolved inorganic carbon in a stratified marine system (Kyllaren fjord, Norway). *Org. Geochem.* 36, 1163–1173. <https://doi.org/10.1016/j.orggeochem.2005.03.003>
- van der Laan, E., Hilgen, F.J., Lourens, L.J., de Kaenel, E., Gaboardi, S., Iaccarino, S., 2012. Astronomical forcing of Northwest African climate and glacial history during the late Messinian (6.5–5.5Ma). *Palaeogeogr. Palaeoclimatol. Palaeoecol.* 313, 107–126. <https://doi.org/10.1016/j.palaeo.2011.10.013>
- Van Gernerden, H., Mas, J., 1995. Ecology of phototrophic sulfur bacteria, in: Blankenship, R.E., Madigan, M.T., Bauer, C.E. (Eds.), *Anoxygenic photosynthetic bacteria*. Springer, Dordrecht, pp. 49–85. [https://link.springer.com/chapter/10.1007/0-306-47954-0\\_4](https://link.springer.com/chapter/10.1007/0-306-47954-0_4)
- van Lith, Y., Warthmann, R., Vasconcelos, C., Mckenzie, J.A., 2003. Sulphate-reducing

- bacteria induce low-temperature Ca-dolomite and high Mg-calcite formation. *Geobiology* 1, 71–79. <https://doi.org/10.1046/j.1472-4669.2003.00003.x>
- Vasiliev, I., Feurdean, A., Reichart, G.-J., Mulch, A., 2020. Late Miocene intensification of continentality in the Black Sea region. *Int. J. Earth Sci.* 109, 831–846. <https://doi.org/10.1007/s00531-020-01832-w>
- Vasiliev, I., Karakitsios, V., Bouloubassi, I., Agiadi, K., Kontakiotis, G., Antonarakou, A., Triantaphyllou, M., Gogou, A., Kafousia, N., de Rafélis, M., Zarkogiannis, S., Kaczmar, F., Parinos, C., Pasadakis, N., 2019. Large sea surface temperature, salinity, and productivity preservation changes preceding the onset of the Messinian Salinity Crisis in the eastern Mediterranean Sea. *Paleoceanogr. Paleoclimatology* 34, 182–202. <https://doi.org/10.1029/2018PA003438>
- Vasiliev, I., Mezger, E.M., Lugli, S., Reichart, G.-J., Manzi, V., Roveri, M., 2017. How dry was the Mediterranean during the Messinian salinity crisis? *Palaeogeogr. Palaeoclimatol. Palaeoecol.* 471, 120–133. <https://doi.org/10.1016/j.palaeo.2017.01.032>
- Vasiliev, I., Reichart, G.-J., Grothe, A., Sinninghe Damsté, J.S., Krijgsman, W., Sangiorgi, F., Weijers, J.W.H., van Røij, L., 2015. Recurrent phases of drought in the upper Miocene of the Black Sea region. *Palaeogeogr. Palaeoclimatol. Palaeoecol.* 423, 18–31. <https://doi.org/10.1016/j.palaeo.2015.01.020>
- Vasiliev, I., Reichart, G.-J., Krijgsman, W., 2013. Impact of the Messinian salinity crisis on Black Sea hydrology – Insights from hydrogen isotopes analysis on biomarkers. *Earth Planet. Sci. Lett.* 272–282. <https://doi.org/10.1016/j.epsl.2012.11.038>
- Violanti, D., Lozar, F., Natalicchio, M., Dela Pierre, F., Bernardi, E., Clari, P., Cavagna, S., 2013. Stress-tolerant microfossils of a Messinian succession from the Northern Mediterranean basin (Pollenzo section, Piedmont, northwestern Italy). *Boll. della Soc. Paleontol. Ital.* 52, 45–54. <https://doi.org/10.4435/BSPI.2013.09>
- Volkman, J.K., 2003. Sterols in microorganisms. *Appl. Microbiol. Biotechnol.* 60, 495–506. <https://doi.org/10.1007/s00253-002-1172-8>
- Wakeham, S.G., Amann, R., Freeman, K.H., Hopmans, E.C., Jørgensen, B.B., Putnam, I.F., Schouten, S., Sinninghe Damsté, J.S., Talbot, H.M., Woebken, D., 2007. Microbial ecology of the stratified water column of the Black Sea as revealed by a comprehensive biomarker study. *Org. Geochem.* 38, 2070–2097. <https://doi.org/10.1016/j.orggeochem.2007.08.003>
- Wakeham, S.G., Freeman, K.H., Pease, T.K., Hayes, J.M., 1993. A photoautotrophic source for lycopane in marine water columns. *Geochimica Cosmochim. Acta* 57, 159–165. [https://doi.org/10.1016/0016-7037\(93\)90476-D](https://doi.org/10.1016/0016-7037(93)90476-D)
- Wakeham, S.G., Hopmans, E.C., Schouten, S., Sinninghe Damsté, J.S., 2004. Archaeal lipids and anaerobic oxidation of methane in euxinic water columns: a comparative study of the Black Sea and Cariaco Basin. *Chem. Geol.* 205, 427–442. <https://doi.org/10.1016/j.chemgeo.2003.12.024>
- Wakeham, S.G., Lewis, C.M., Hopmans, E.C., Schouten, S., Sinninghe Damsté, J.S., 2003. Archaea mediate anaerobic oxidation of methane in deep euxinic waters of the Black Sea. *Geochim. Cosmochim. Acta* 67, 1359–1374. [https://doi.org/10.1016/S0016-7037\(02\)01220-6](https://doi.org/10.1016/S0016-7037(02)01220-6)
- Wakeham, S.G., Sinninghe Damsté, J.S., Kohnen, M.E.L., de Leeuw, J.W., 1995. Organic sulfur compounds formed during early diagenesis in Black Sea sediments. *Geochim. Cosmochim. Acta* 59, 521–533. [https://doi.org/10.1016/0016-7037\(94\)00361-O](https://doi.org/10.1016/0016-7037(94)00361-O)
- Wakeham, S.G., Turich, C., Schubotz, F., Podlaska, A., Li, X.N., Varela, R., Astor, Y., Sáenz, J.P., Rush, D., Sinninghe Damsté, J.S., Summons, R.E., Scranton, M.I., Taylor, G.T., Hinrichs, K.-U., 2012. Biomarkers, chemistry and microbiology show chemoautotrophy in a multilayer chemocline in the Cariaco Basin. *Deep. Res. Part I Oceanogr. Res. Pap.* 63, 133–156. <https://doi.org/10.1016/j.dsr.2012.01.005>
- Warren, J.K., 2010. Evaporites through time: tectonic, climatic and eustatic controls in marine and nonmarine deposits. *Earth-Science Rev.* 98, 217–268. <https://doi.org/10.1016/j.earscirev.2009.11.004>
- Warthmann, R., van Lith, Y., Vasconcelos, C., McKenzie, J.A., Karpoff, A.M., 2000. Bacterially induced dolomite precipitation in anoxic culture experiments. *Geology* 28, 1091–1094. [https://doi.org/10.1130/0091-7613\(2000\)28<1091:BIDPIA>2.0.CO;2](https://doi.org/10.1130/0091-7613(2000)28<1091:BIDPIA>2.0.CO;2)
- Wehausen, R., Brumsack, H.-J., 2000. Chemical cycles in Pliocene sapropel-bearing and sapropel-barren eastern Mediterranean sediments. *Palaeogeogr. Palaeoclimatol. Palaeoecol.* 158, 325–352. [https://doi.org/10.1016/S0031-0182\(00\)00057-2](https://doi.org/10.1016/S0031-0182(00)00057-2)

- Wehausen, R., Brumsack, H.-J., 1999. Cyclic variations in the chemical composition of eastern Mediterranean Pliocene sediments: a key for understanding sapropel formation. *Mar. Geol.* 153, 161–176. [https://doi.org/10.1016/S0025-3227\(98\)00083-8](https://doi.org/10.1016/S0025-3227(98)00083-8)
- Weijers, J.W.H., Schouten, S., Spaargaren, O.C., Sinninghe Damsté, J.S., 2006. Occurrence and distribution of tetraether membrane lipids in soils: implications for the use of the TEX<sub>86</sub> proxy and the BIT index. *Org. Geochem.* 37, 1680–1693. <https://doi.org/10.1016/j.orggeochem.2006.07.018>
- Weijers, J.W.H., Wiersenberg, G.L.B., Bol, R., Hopmans, E.C., Pancost, R.D., 2010. Carbon isotopic composition of branched tetraether membrane lipids in soils suggest a rapid turnover and a heterotrophic life style of their source organism(s). *Biogeosciences Discuss.* 7, 3691–3734. <https://doi.org/10.5194/bgd-7-3691-2010>
- Wilkin, R.T., Barnes, H.L., Brantley, S.L., 1996. The size distribution of framboidal pyrite in modern sediments: an indicator of redox conditions. *Geochim. Cosmochim. Acta* 60, 3897–3912. [https://doi.org/10.1016/0016-7037\(96\)00209-8](https://doi.org/10.1016/0016-7037(96)00209-8)
- Zachos, J., Pagani, H., Sloan, L., Thomas, E., Billups, K., 2001. Trends, rhythms, and aberrations in global climate 65 Ma to present. *Science.* 292, 686–693. <https://doi.org/10.1126/science.1059412>
- Zeng, Z., Liu, X.-L., Farley, K.R., Wei, J.H., Metcalf, W.W., Summons, R.E., Welander, P.V., 2019. GDGT cyclization proteins identify the dominant archaeal sources of tetraether lipids in the ocean. *Proc. Natl. Acad. Sci.* 116, 22505–22511. <https://doi.org/10.1073/pnas.1909306116>
- Zhang, Z., Ramstein, G., Schuster, M., Li, C., Contoux, C., Yan, Q., 2014. Aridification of the Sahara desert caused by Tethys Sea shrinkage during the Late Miocene. *Nature* 513, 401–404. <https://doi.org/10.1038/nature13705>





## APPENDIX A

---

Appendix A provides details on contributions from the author of the thesis to the articles representing Chapters 2 to 4 and to other publications not included in this thesis. It has to be acknowledged that all co-authors contributed constructively to the discussion of the data of the scientific articles.

### Chapters of the thesis:

**Sabino, M.**, Schefuß, E., Natalicchio, M., Dela Pierre, F., Birgel, D., Bortels, D., Schnetger, B., Peckmann, J., 2020. Climatic and hydrologic variability in the northern Mediterranean across the onset of the Messinian salinity crisis. *Palaeogeography, Palaeoclimatology, Palaeoecology* 545, article 109632. 10.1016/j.palaeo.2020.109632. (Chapter 2)

*Author's contribution: preparation, analysis, and interpretation of organic geochemical data. Major contribution in designing, formatting, and writing the article.*

**Sabino, M.**, Dela Pierre, F., Natalicchio, M., Birgel, D., Gier, S., Peckmann, J., 2020. The response of water column and sedimentary environments to the advent of the Messinian salinity crisis: insights from an onshore deep-water section (Govone, NW Italy). *Geological Magazine*, 1 – 17. 10.1017/S0016756820000874. (Chapter 3)

*Author's contribution: preparation, analysis, and interpretation of organic geochemical data and petrographic data. Major contribution in designing, formatting, and writing the article.*

**Sabino, M.**, Birgel, D., Natalicchio, M., Dela Pierre, F., Peckmann, J. (submitted). Marine Thaumarchaeota record carbon isotope excursions in the northernmost offshoot of the late Miocene Mediterranean Basin. (Chapter 4)

*Author's contribution: preparation, analysis, and interpretation of organic geochemical data for the Govone section and partially for the data for the Pollenzo section (carbon stable isotope ratios of the desulfurized fractions). Major contribution in designing, formatting, and writing the article.*

### Data sets published into the open access library PANGAEA:

**Sabino, M.**, Schefuß, E., Natalicchio, M., Dela Pierre, F., Birgel, D., Bortels, D., Schnetger, B., Peckmann, J., 2020. Climate variability in the northern Mediterranean across the onset of the Messinian salinity crisis: insights from inorganic and organic geochemical proxies. PANGAEA. 10.1594/PANGAEA.918497

*Author's contribution: re-adaptation and brief description of the data set for publication purposes.*

**Sabino, M.**, Dela Pierre, F., Natalicchio, M., Birgel, D., Gier, S., Peckmann, J., 2021. Changes in water column and sedimentary environments at the onset of the Messinian salinity crisis: insights from an onshore deep-water section (Govone, NW Italy). PANGAEA. DOI: 10.1594/PANGAEA.927059

*Author's contribution: re-adaptation and brief description of the data set for publication purposes.*

Additional publications:

Natalicchio, M., Dela Pierre, F., Birgel, D., Brumsack, H., Carnevale, G., Gennari, R., Gier, S., Lozar, F., Pellegrino, L., **Sabino, M.**, Schnetger, B., Peckmann, J., 2019. Paleoenvironmental change in a precession-paced succession across the onset of the Messinian salinity crisis: insight from element geochemistry and molecular fossils. *Palaeogeography, Palaeoclimatology, Palaeoecology* 518, 45–61. 10.1016/j.palaeo.2019.01.009 (not included)

*Author's contribution: preparation, analysis, and interpretation of parts of the geochemical data and contribution to the discussion.*



## APPENDIX B

---

Appendix B contains inorganic and organic geochemical proxies discussed in Chapter 2. Moreover, sedimentation rates for the lithological cycles of the Govone section are listed (Appendix B.4). Details on references mentioned in this Appendix can be found in the Reference list.

### Appendix B.1

Contents of major and trace elements (silicon, titanium, aluminum, and zirconium) derived from their oxides and element/aluminum ratios.

Samples	SiO <sub>2</sub> (%wt)	Si (%wt)	TiO <sub>2</sub> (%wt)	Ti (%wt)	Al <sub>2</sub> O <sub>3</sub> (%wt)	Al (%wt)	Zr (mg/kg)	Ti/Al*100	Si/Al	Zr/Al
Gm33.2	26.7	12.5	0.3	0.2	8.5	4.5	43	4.57	2.78	9.58
Gm33.1	53.4	25.0	0.7	0.4	16.5	8.7	104	4.53	2.87	11.94
Gm32.6	27.6	12.9	0.4	0.2	8.6	4.6	66	4.77	2.82	14.47
Gm32.5	45.0	21.0	0.6	0.4	14.6	7.7	101	4.73	2.72	13.06
Gm32.4	27.6	12.9	0.4	0.2	9.1	4.8	61	4.73	2.68	12.68
Gm32.3	35.6	16.6	0.5	0.3	11.6	6.1	73	4.49	2.71	11.89
Gm32.2	50.3	23.5	0.6	0.4	16.1	8.5	93	4.46	2.76	10.92
Gm32.1	45.8	21.4	0.6	0.3	14.5	7.7	88	4.53	2.79	11.48
Gm31.5	45.3	21.2	0.6	0.4	14.2	7.5	110	4.78	2.81	14.61
Gm31.4	38.0	17.8	0.5	0.3	12.0	6.3	80	4.75	2.80	12.63
Gm31.3	30.6	14.3	0.4	0.2	9.6	5.1	68	4.77	2.82	13.42
Gm31.2	45.6	21.3	0.6	0.4	14.9	7.9	86	4.43	2.70	10.88
Gm31.1	31.7	14.8	0.4	0.2	10.1	5.3	65	4.60	2.78	12.22
Gm30.3	42.6	19.9	0.6	0.3	13.2	7.0	91	4.72	2.84	12.99
Gm30.2	29.5	13.8	0.4	0.2	9.1	4.8	72	4.73	2.86	14.95
Gm30.1	35.5	16.6	0.4	0.3	11.2	5.9	79	4.51	2.80	13.34
Gm29.4	32.5	15.2	0.4	0.3	9.8	5.2	77	4.87	2.92	14.80
Gm29.3	22.8	10.7	0.3	0.2	7.1	3.7	53	4.85	2.86	14.20
Gm29.2	43.6	20.4	0.5	0.3	13.6	7.2	88	4.56	2.82	12.20
Gm29.1	39.3	18.4	0.5	0.3	12.5	6.6	76	4.52	2.78	11.51
Gm28.5	38.0	17.8	0.5	0.3	12.2	6.4	91	4.70	2.76	14.13
Gm28.4	30.1	14.1	0.4	0.2	9.2	4.9	75	4.76	2.89	15.42
Gm28.3	43.4	20.3	0.6	0.3	13.6	7.2	98	4.67	2.81	13.58
Gm28.2	32.8	15.3	0.4	0.2	10.2	5.4	71	4.58	2.84	13.16
Gm28.1	32.7	15.3	0.4	0.3	10.4	5.5	68	4.70	2.77	12.34
Gm27.4	44.7	20.9	0.6	0.4	14.0	7.4	103	4.73	2.81	13.86
Gm27.3	38.9	18.2	0.5	0.3	12.2	6.5	93	4.75	2.82	14.41
Gm27.2	44.0	20.5	0.6	0.3	14.3	7.6	95	4.48	2.72	12.56
Gm27.1	29.1	13.6	0.4	0.3	9.3	4.9	68	5.16	2.77	13.86
Gm26.4	41.5	19.4	0.5	0.3	12.8	6.8	102	4.78	2.86	15.08
Gm26.3	34.8	16.2	0.5	0.3	11.0	5.8	83	4.82	2.80	14.32
Gm26.2	44.5	20.8	0.6	0.3	13.8	7.3	103	4.65	2.86	14.14
Gm26.1	36.8	17.2	0.5	0.3	11.7	6.2	76	4.64	2.79	12.32

**Appendix B.2**

Total organic carbon (TOC) and *n*-alkane (C<sub>18</sub> to C<sub>37</sub>) contents in Govone sediments.  
d.n.a.: data non available; tr.: traces.

Samples	TOC (%)	<i>n</i> -alkanes (µg/g TOC)									
		C <sub>18</sub>	C <sub>19</sub>	C <sub>20</sub>	C <sub>21</sub>	C <sub>22</sub>	C <sub>23</sub>	C <sub>24</sub>	C <sub>25</sub>	C <sub>26</sub>	C <sub>27</sub>
Gm33.2	2.2	d.n.a.	0.31	0.50	1.06	0.80	2.68	1.37	5.30	1.70	9.03
Gm33.1	1.3	0.51	1.20	1.02	1.94	1.47	5.97	2.94	12.56	4.78	28.47
Gm32.5	1.3	0.15	0.76	0.97	0.39	0.72	1.45	0.94	2.16	1.38	6.09
Gm32.2	2.0	0.46	1.10	0.67	1.38	1.20	3.30	2.17	6.01	2.24	12.32
Gm32.1	2.0	0.54	1.04	0.76	1.63	1.19	3.69	2.45	7.14	2.88	14.87
Gm31.4	1.6	0.17	0.38	0.41	0.70	0.68	1.53	1.00	2.44	1.30	5.87
Gm31.2	2.3	0.38	0.70	0.49	1.46	0.71	2.30	1.20	3.74	1.67	7.98
Gm31.1	2.7	0.10	0.39	0.29	0.75	0.46	1.65	0.63	2.94	0.96	5.62
Gm30.3	1.4	0.28	0.49	0.48	0.98	0.77	1.57	1.32	3.11	1.71	6.38
Gm30.2	2.1	0.20	0.41	0.38	0.75	0.46	0.81	0.71	1.32	0.61	2.77
Gm30.1	2.1	0.17	0.42	0.43	d.n.a.	d.n.a.	1.27	0.76	1.86	0.77	5.46
Gm29.3	2.5	tr.	0.10	0.19	0.48	0.23	0.48	0.33	0.76	0.39	1.74
Gm29.2	2.7	d.n.a.	d.n.a.	d.n.a.	d.n.a.	d.n.a.	2.52	1.02	3.75	1.37	8.63
Gm29.1	3.1	0.63	0.56	0.83	1.51	0.83	2.63	1.67	4.29	1.54	9.31
Gm28.4	2.4	tr.	tr.	tr.	0.58	0.24	0.51	0.32	0.78	0.39	1.55
Gm28.2	2.8	0.12	0.53	0.55	0.80	0.88	1.71	1.16	2.70	1.05	5.89
Gm28.1	2.3	0.24	0.41	0.47	0.62	0.51	1.63	0.87	3.00	1.27	7.89
Gm27.3	1.6	0.25	0.51	0.60	0.47	0.56	1.71	2.77	3.31	0.87	3.92
Gm27.1	2.9	0.25	0.48	0.44	0.83	0.50	1.92	0.87	3.08	0.99	6.43
Gm26.3	1.9	tr.	0.35	0.68	1.01	0.55	0.86	0.59	1.20	0.58	2.59
Gm26.1	2.4	0.16	0.28	0.34	0.77	0.50	1.64	0.78	3.03	1.16	7.39

Samples	TOC (%)	<i>n</i> -alkanes (µg/g TOC)									
		C <sub>28</sub>	C <sub>29</sub>	C <sub>30</sub>	C <sub>31</sub>	C <sub>32</sub>	C <sub>33</sub>	C <sub>34</sub>	C <sub>35</sub>	C <sub>37</sub>	
Gm33.2	2.2	2.84	17.55	3.76	20.31	2.51	7.61	0.40	11.10	tr.	
Gm33.1	1.3	7.41	51.19	8.17	56.91	4.94	19.29	0.90	13.11	tr.	
Gm32.5	1.3	2.60	13.58	3.55	16.14	2.08	6.03	0.48	1.39	tr.	
Gm32.2	2.0	3.27	22.29	3.72	24.95	2.73	9.78	0.51	10.17	tr.	
Gm32.1	2.0	4.03	25.59	4.86	27.87	3.20	10.81	0.81	11.96	tr.	
Gm31.4	1.6	2.01	13.03	2.57	16.27	1.70	6.30	0.46	1.74	tr.	
Gm31.2	2.3	2.53	14.80	2.86	16.73	1.93	6.39	0.50	1.67	tr.	
Gm31.1	2.7	1.36	9.69	1.33	10.62	0.96	4.11	0.24	6.06	tr.	
Gm30.3	1.4	2.82	13.82	3.41	16.80	2.10	6.54	0.49	1.96	tr.	
Gm30.2	2.1	0.78	6.29	0.78	6.51	0.54	2.55	0.19	1.14	tr.	
Gm30.1	2.1	1.28	11.67	1.20	12.47	0.96	4.77	0.26	1.16	tr.	
Gm29.3	2.5	0.59	3.49	0.63	4.76	0.41	1.87	0.16	0.58	tr.	
Gm29.2	2.7	2.26	17.93	2.15	20.90	2.45	8.44	0.70	1.70	tr.	
Gm29.1	3.1	2.24	15.25	2.29	19.02	2.09	7.94	0.50	1.71	tr.	
Gm28.4	2.4	0.47	2.98	0.47	3.81	0.27	1.46	0.14	0.49	tr.	
Gm28.2	2.8	1.66	11.33	1.74	13.73	1.70	5.43	0.47	1.26	tr.	
Gm28.1	2.3	3.13	15.57	1.96	17.95	1.69	6.62	0.57	1.61	tr.	
Gm27.3	1.6	1.19	10.00	1.27	11.59	0.95	4.64	0.35	1.40	tr.	
Gm27.1	2.9	1.60	12.38	2.00	14.63	1.41	5.49	0.43	1.36	tr.	
Gm26.3	1.9	0.76	5.20	0.78	6.50	0.61	2.63	0.39	0.85	tr.	
Gm26.1	2.4	1.94	14.01	1.89	15.61	1.44	6.23	0.52	6.18	tr.	

**Appendix B.3**

Carbon Preference Index (CPI), sum ( $\Sigma$ ) of C<sub>27-33</sub> odd *n*-alkanes, and compound-specific hydrogen ( $\delta^2\text{H}$ ) and carbon ( $\delta^{13}\text{C}$ ) stable isotopes. d.n.a.: data non available; MSC: Messinian salinity crisis; SD: standard deviation; TOC: total organic carbon.

Samples	CPI	$\Sigma_{\text{C27-C33}}$	$\delta^{13}\text{C}_{\text{alkane}}$ (‰)				$\delta^2\text{H}_{\text{alkane}}$ (‰)				
		( $\mu\text{g/g}$ TOC)	<i>n</i> -C <sub>31</sub>		<i>n</i> -C <sub>33</sub>		<i>n</i> -C <sub>31</sub>		<i>n</i> -C <sub>33</sub>		
			SD		SD		SD		SD		
Gm33.2	5.1	54.5	-32.9	0.15	-32.9	0.05	-162	1.9	-146	1.7	
Gm33.1	6.2	155.9	-32.9	0.07	-32.8	0.13	d.n.a.	d.n.a.	d.n.a.	d.n.a.	
Gm32.5	4.3	41.8	-32.7	1.00	-32.0	0.53	-153	1.9	-142	1.6	
Gm32.2	5.7	69.3	-32.2	0.07	-31.5	0.12	-166	0.0	-159	0.5	
Gm32.1	5.2	79.1	-32.0	0.12	-33.1	0.53	d.n.a.	d.n.a.	d.n.a.	d.n.a.	
Gm31.4	5.3	41.5	-33.2	0.16	-32.5	0.20	-158	0.4	-149	2.4	
Gm31.2	5.1	45.9	-30.5	0.55	-31.3	0.74	d.n.a.	d.n.a.	d.n.a.	d.n.a.	
Gm31.1	6.5	30.0	-32.0	0.15	-30.5	0.30	-176	0.9	-157	3.4	
Gm30.3	4.3	43.5	-31.9	0.00	-32.3	0.23	-151	0.5	-140	1.1	
Gm30.2	6.2	18.1	-33.5	0.10	-33.7	0.73	d.n.a.	d.n.a.	d.n.a.	d.n.a.	
Gm30.1	7.7	34.4	-32.8	0.37	-32.6	0.25	-154	1.1	-143	3.0	
Gm29.3	5.6	11.9	-31.1	0.09	-30.9	0.23	-154	4.0	-145	6.6	
Gm29.2	6.6	55.9	-31.7	0.71	-31.4	0.60	-191	0.1	-167	1.7	
Gm29.1	6.1	51.5	-31.3	0.42	-30.5	0.29	-184	1.2	-169	3.4	
Gm28.4	5.8	9.8	-31.3	0.76	d.n.a.	d.n.a.	-158	d.n.a.	-145	0.0	
Gm28.2	5.6	36.4	-30.8	0.50	-30.4	0.35	-186	1.1	-162	2.6	
Gm28.1	5.8	48.0	-31.6	0.43	-31.5	0.08	-169	1.0	-142	1.2	
Gm27.3	6.0	30.2	-32.1	0.37	-30.2	0.84	-157	1.4	-142	1.4	
Gm27.1	6.3	38.9	-32.7	0.08	-32.2	0.29	d.n.a.	d.n.a.	d.n.a.	d.n.a.	
Gm26.3	5.6	16.9	-32.1	0.47	-31.9	d.n.a.	-169	3.0	-140	0.2	
Gm26.1	6.5	43.2	-31.3	0.29	-31.0	0.22	-182	0.9	-163	1.5	
		CPI	$\Sigma_{\text{C27-C33}}$ ( $\mu\text{g/g}$ TOC)	$\delta^{13}\text{C}_{n-}$ C <sub>31</sub> (‰)	$\delta^{13}\text{C}_{n-}$ C <sub>33</sub> (‰)	$\delta^2\text{H}_{n-}$ C <sub>31</sub> (‰)	$\delta^2\text{H}_{n-}$ C <sub>33</sub> (‰)				
Average Pre-MS		6.2	34.3	-31.7	-31.3	-170.3	-151.9				
Average MSC		5.4	58.0	-32.4	-32.3	-160.8	-148.9				

### Appendix B.4

Thickness, time of deposition and sedimentation rate of Govone lithological cycles.  
MSC: Messinian salinity crisis.

Cycles	Thickness	Time of deposition <sup>1</sup>	Sedimentation rate		Average sedimentation rate
	m	kyr	m/kyr	cm/kyr	cm/kyr
Gm32	1.02	21	0.05	4.9	MSC
Gm31	0.73	23	0.03	3.2	4.1
Gm30	0.51	12	0.04	4.2	
Gm29	0.60	17	0.04	3.6	pre-MSC
Gm28	0.84	22	0.04	3.8	3.1
Gm27	0.58	20	0.03	2.9	
Gm26	0.83	36	0.02	2.3	

Cycle Gm33 was excluded from the calculation due to slumping in the marly interval

<sup>1</sup>: time of deposition was calculated as difference between the shales midpoint reported in Manzi et al. (2013), according to the proposed age model.





## APPENDIX C

Appendix C contains organic and inorganic geochemical proxies and the  $\delta^{13}\text{C}_{\text{bulk rock}}$ -total inorganic carbon (TIC) correlation discussed in Chapter 3. Details on references mentioned in this Appendix can be found in the Reference list.

### Appendix C.1

Contents archaeol ( $\text{C}_{20-20}$  arch.), glycerol dibiphytanyl glycerol tetraethers (iso-GDGT), lycopane (Ly),  $n\text{-C}_{31}$  alkane ( $n\text{-C}_{31}$  alk.), and tetrahymanol. GDGT-0/crenarchaeol and lycopane/ $n\text{-C}_{31}$  ratios are displayed. Cren.: crenarchaeol; Cren': crenarchaeol isomer; d.n.a.: data not available.

Samples	$\text{C}_{20-20}$ arch. (%)	iso-GDGTs (%)						(μg/g TOC)				
		[0]	[1]	[2]	[3]	Cren.	Cren'	[0]/ cren. ratio	Tetra hyma nol	Ly.	$n\text{-C}_{31}$ alk.	Ly./ $n\text{-C}_{31}$ ratio
Gm33.2	26.2	29.1	8.7	8.8	1.7	22.7	2.8	1.3	2.8	d.n.a.	20.3	d.n.a.
Gm33.1	30.7	24.8	7.3	9.3	1.8	24.2	2.0	1.0	3.9	7.8	56.9	0.1
Gm32.5	34.0	27.0	5.4	5.8	1.0	25.1	1.8	1.1	1.8	0.2	16.1	0.0
Gm32.2	31.0	30.4	8.3	5.6	1.4	20.6	2.9	1.5	7.3	d.n.a.	24.9	d.n.a.
Gm32.1	24.5	29.4	8.2	7.5	1.8	25.1	3.5	1.2	4.2	8.2	27.9	0.3
Gm31.4	15.5	28.1	9.7	12.0	2.0	29.1	3.6	1.0	2.5	0.4	16.3	0.0
Gm31.2	20.4	31.2	9.5	10.1	2.0	22.9	3.9	1.4	3.3	6.0	16.7	0.4
Gm31.1	15.3	27.2	9.7	11.5	3.1	29.0	4.2	0.9	5.7	4.7	10.6	0.4
Gm30.3	24.6	25.3	8.7	9.3	2.2	26.4	3.5	1.0	1.9	0.4	16.8	0.0
Gm30.2	29.4	26.4	6.6	9.5	1.8	23.2	3.1	1.1	2.9	0.3	6.5	0.0
Gm30.1	23.6	30.4	10.7	8.3	1.9	23.1	1.9	1.3	26.5	0.8	12.5	0.1
Gm29.3	19.7	26.8	8.2	11.4	2.3	28.2	3.3	1.0	1.1	0.2	4.8	0.0
Gm29.2	35.9	21.6	8.3	7.9	2.7	20.9	2.7	1.0	11.3	25.0	20.9	1.2
Gm29.1	28.1	22.7	9.7	9.8	3.1	23.7	2.9	1.0	6.9	18.2	19.0	1.0
Gm28.4	19.8	24.5	9.0	13.7	2.6	26.5	3.9	0.9	2.3	0.1	3.8	0.0
Gm28.2	42.9	18.0	7.6	8.6	2.4	18.3	2.3	1.0	4.1	4.6	13.7	0.3
Gm28.1	36.4	23.2	5.5	10.1	2.4	19.6	2.7	1.2	12.0	d.n.a.	17.9	d.n.a.
Gm27.3	7.8	26.4	11.9	14.5	2.5	32.9	4.0	0.8	2.0	0.1	11.6	0.0
Gm27.1	23.1	26.0	8.6	12.7	2.7	22.8	4.0	1.1	7.5	3.0	14.6	0.2
Gm26.3	15.7	29.2	8.1	11.7	1.6	30.4	3.2	1.0	1.3	0.0	6.5	0.0
Gm26.1	14.9	28.9	11.2	12.2	2.7	26.3	3.8	1.1	5.9	6.8	15.6	0.4

**Appendix C.2**

Total carbon (TC), total inorganic carbon (TIC), total organic carbon (TOC), and mineralogy of the carbonate phase (calcite *vs.* dolomite) in Govone sediments.

Samples	TC (wt%)	TIC (wt%)	TOC (wt%)	Intensity in counts of the main peaks	
				Calcite	Dolomite
Gm33.2	7.4	5.2	2.2	-	3410
Gm33.1	1.7	0.4	1.3	-	707
Gm32.6	6.8	5.5	1.3	-	3558
Gm32.5	3.1	1.8	1.3	-	3185
Gm32.4	6.9	5.3	1.6	-	3433
Gm32.3	5.8	3.2	2.6	-	2396
Gm32.2	2.4	0.4	2.0	-	825
Gm32.1	3.3	1.3	2.0	-	2017
Gm31.5	3.4	2.1	1.3	-	3172
Gm31.4	4.8	3.2	1.6	-	2277
Gm31.3	6.5	4.8	1.7	-	2873
Gm31.2	3.5	1.2	2.3	-	1132
Gm31.1	6.3	3.5	2.7	-	2898
Gm30.3	3.7	2.3	1.4	-	2057
Gm30.2	6.7	4.5	2.1	-	3418
Gm30.1	5.7	3.6	2.1	-	2693
Gm29.4	6.1	4.7	1.5	-	3289
Gm29.3	8.5	6.0	2.5	-	4157
Gm29.2	4.1	1.4	2.7	-	1404
Gm29.1	5.1	2.0	3.1	-	2015
Gm28.5	5.5	3.8	1.7	-	2610
Gm28.4	7.1	4.7	2.4	-	3135
Gm28.3	3.0	1.7	1.3	-	1955
Gm28.2	6.3	3.5	2.8	-	2910
Gm28.1	5.8	3.5	2.3	490	2824
Gm27.4	3.1	1.9	1.2	1708	749
Gm27.3	4.6	3.0	1.6	1114	1963
Gm27.2	3.3	2.2	1.1	1873	746
Gm27.1	6.0	3.1	2.9	1270	1798
Gm26.4	3.8	2.8	1.0	2023	1680
Gm26.3	5.7	3.7	1.9	244	2902
Gm26.2	3.6	1.9	1.8	1826	761
Gm26.1	4.7	2.2	2.4	2115	1246

**Appendix C.3**Bulk rock carbon ( $\delta^{13}\text{C}$ ) and oxygen ( $\delta^{18}\text{O}$ ) stable isotopes in Govone sediments.

Samples	cycle	$\delta^{13}\text{C}$ (‰)	$\delta^{18}\text{O}$ (‰)	
Gm33.2	Gm 33	-4.3	3.4	<u>Additional notes:</u> * samples from Bernardi (2013) <i>Correction factors for <math>\delta^{18}\text{O}</math> values:</i> Samples from Bernardi (2013) were corrected by $-0.8\text{‰}$ according to Sharma & Clayton (1965) for analyses performed at $T = 323.15 \text{ °K}$ . The new samples were corrected for $-1.2\text{‰}$ . This values was obtained as the difference between the fractionation among $\text{CO}_2$ and solid dolomite according to Rosenbaum & Sheppard, (1986) ( $10^3 \ln \alpha = 6.65 \times 10^5 \times (1/T^2) + 4.23$ ) and $\text{CO}_2$ and solid calcite according to Kim et al. (2007) ( $10^3 \ln \alpha = 3.59 \times (10^3/T) - 1.79$ ) for a reaction temperature of $T = 348.15 \text{ °K}$
Gm32.6	Gm 32	-4.2	3.5	
Gm32.5	Gm 32	-2.6	4.7	
GM 32.2*	Gm 32	-5.2	2.9	
Gm32.4	Gm 32	-4.2	5.5	
Gm32.3	Gm 32	-2.8	5.4	
GM 32.1*	Gm 32	-1.4	2.9	
Gm31.5	Gm 31	-0.4	3.6	
GM 31.1*	Gm 31	-0.4	3.7	
GOV B 12.1*	Gm 31	-4.4	5.1	
Gm31.3	Gm 31	-1.5	4.9	
Gm31.2	Gm 31	-0.8	3.2	
GOV B 11.4*	Gm 31	-0.9	-3.1	
GOV B 11.2*	Gm 30	-0.4	3.8	
GOV B 10.5*	Gm 30	-1.4	4.9	
GOV B 10.4*	Gm 30	-0.4	2.6	
GOV B 10.3*	Gm 29	-0.4	3.8	
Gm29.3	Gm 29	-2.7	4.9	
GM 29*	Gm 29	-2.3	5.1	
GOV B 9.4*	Gm 29	-0.9	5.0	
GOV B 9.3*	Gm 28	-1.3	4.9	
GOV B 9.2*	Gm 28	0.3	0.0	
GOV B 9.1*	Gm 28	-2.2	4.9	
GOV B 8.2*	Gm 27	0.3	-4.3	
GOV B 8.1*	Gm 27	-0.4	-0.3	
GOV B 7.4*	Gm 27	-1.7	2.5	
GOV B 7.3*	Gm 26	0.3	-4.5	
GOV B 7.2*	Gm 26	-2.1	5.4	
GOV B 7.1*	Gm 26	-0.2	-3.9	
average pre-MSC		-1.0	2.1	
average MSC		-2.4	3.5	

### Appendix C.4

Correlation between bulk rock  $\delta^{13}\text{C}$  values and total inorganic carbon (TIC).

Samples	cycle	$\delta^{13}\text{C}$ (‰)	TIC (%)
GOV B 9.3*	Gm 28	-1.3	3.8
GOV B 9.4*	Gm 29	-0.9	1.4
Gm29.3	Gm 29	-2.7	6.0
GOV B 10.4*	Gm 30	-0.4	3.6
GOV B 11.4*	Gm 31	-0.9	3.5
Gm31.2	Gm 31	-0.8	1.2
Gm31.3	Gm 31	-1.5	4.8
Gm31.5	Gm 31	-0.4	2.1
Gm32.3	Gm 32	-2.8	3.2
Gm32.4	Gm 32	-4.2	5.3
Gm32.5	Gm 32	-2.6	1.8
Gm32.6	Gm 32	-4.2	5.5
Gm33.2	Gm 33	-4.3	5.2

Shales				Marls			
GOV B 9.4*	Gm 29	-0.9	1.4	GOV B 9.3*	Gm 28	-1.3	3.8
GOV B 10.4*	Gm 30	-0.4	3.6	Gm29.3	Gm 29	-2.7	6.0
GOV B 11.4*	Gm 31	-0.9	3.5	Gm31.3	Gm 31	-1.5	4.8
Gm31.2	Gm 31	-0.8	1.2	Gm31.5	Gm 31	-0.4	2.1
Gm32.3	Gm 32	-2.8	3.2	Gm32.4	Gm 32	-4.2	5.3
Gm33.2	Gm 33	-4.3	5.2	Gm32.5	Gm 32	-2.6	1.8
				Gm32.6	Gm 32	-4.2	5.5

Correlation coefficient shales	Correlation coefficient marls
-0.7	-0.6

Additional notes

\* samples from Bernardi, 2013

TIC contents in italics were measured on samples from this study (labeled GmXX) corresponding to samples from the same stratigraphic level analysed by Bernardi (2013); Gm28.5 for GOV B 9.3\*; Gm29.2 for GOV B 9.4\*; Gm30.1 for GOV B 10.4\*; Gm31.1 for GOV B 11.4\*. We do not consider samples with co-occurrence of calcite and dolomite, and samples from Bernardi (2013) for which TIC contents are offset to contents measured in this study.



## APPENDIX D

Appendix D contains details on the geological setting, methodologies, and the organic geochemical proxies discussed in Chapter 4. Moreover, details on inferred sources for lipid biomarkers other than tricyclic biphytane are presented. References mentioned in this Appendix can be found in the Reference list.

### Appendix D.1

#### *The Messinian sediments of the Piedmont Basin*

The studied sections are located in proximal (Pollenzo) and distal (Govone) parts of the southern margin of the Piedmont Basin (NW Italy), an Alpine retroforeland basin filled with Cenozoic sediments (Fig. AD.1; Dela Pierre et al., 2011; Sabino et al., 2020b). The Messinian sediments are represented by outer shelf to slope shale/marl lithological cycles belonging to the Sant'Agata Fossili Marls Formation, testifying progressive basin restriction (Fig. AD.1; Dela Pierre et al., 2011). The lithological cyclicity reflects precession-paced climate fluctuations, with shales deposited under moister climate conditions (precession minima) and marls deposited under drier conditions (precession maxima; Natalicchio et al., 2019; Sabino et al., 2020b). Starting from 5.97 Ma, shale/marl couplets make upslope transition to shale/gypsum lithological cycles, assigned to the Primary Lower Gypsum unit (Fig. AD.1; Dela Pierre et al., 2011). The lithological cyclicity of the unit, deposited during the first stage of the Messinian salinity crisis (MSC; 5.97–5.60 Ma; Roveri et al., 2014a), was attributed to precession-driven climate fluctuations as well, with gypsum corresponding to precession maxima and arid conditions (Krijgsman et al., 1999). In deeper-water settings (> 200 m), gypsum deposition was delayed, possibly because of sulfate consumption driven by intense bacterial sulfate reduction favored by pronounced water-column stratification after the MSC onset (Fig. AD.1; de Lange and Krijgsman, 2010; Sabino et al., 2020a). The Messinian succession of the Piedmont Basin terminates with resedimented evaporites and fluvio-deltaic deposits, representing the acme (5.60–5.55 Ma) and the final stage (5.55–5.33 Ma) of the MSC, respectively (Fig. AD.1; Dela Pierre et al., 2011).

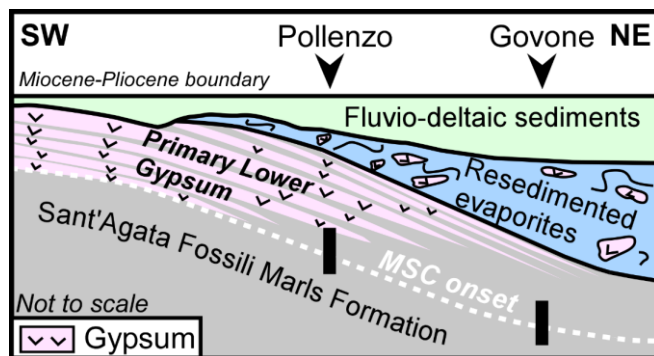


Figure AD.1 – Schematic cross section of the Piedmont Basin showing the Messinian stratigraphy (modified from (Sabino et al., 2020a)). The thick black bars indicate the investigated stratigraphic intervals of the proximal Pollenzo and distal Govone sections. MSC: Messinian salinity crisis.

## Appendix D.2

### Lipid biomarker extraction, separation, and analyses

Lipid biomarkers were extracted applying the procedure described in detail in Sabino et al. (2020b). After basic hydrolysis with 6% potassium hydroxide in methanol, the samples were repeatedly extracted through ultrasonication with dichloromethane:methanol (3:1, v:v) until the organic solvent phase became colorless. The basic hydrolysis products and the extracts were combined and the solution was acidified with 10% hydrochloric acid to a pH 2 for transferring also liberated fatty acids to the organic solvent phase. The latter, containing the extracted lipids, was evaporated and separated in an *n*-hexane-soluble and a dichloromethane-soluble fraction. Using a Supelco glass cartridge (6 ml, 500 mg, DSC-NH<sub>2</sub>), the *n*-hexane-soluble fraction was separated into (1) hydrocarbon, (2) ketone, (3) alcohol, and (4) carboxylic acid sub-fractions. The alcohol fraction was derivatized for 1 h at 70 °C by adding a mixture of pyridine and N,O-bis(trimethylsilyl)trifluoroacetamide (BSTFA) (1:1; v/v), dried and re-dissolved in *n*-hexane for analyses. The other sub-fractions are not further discussed herein. Gas chromatography-amenable compounds (in particular archaeols; Fig. AD.2) in the Govone samples were identified using a Thermo Scientific Trace GC Ultra coupled to a Thermo Scientific DSQ II mass spectrometer (GC-MS) through comparison of retention times and published mass spectral data. Quantification was achieved with a Fisons Instruments GC 8000 series equipped with a flame-ionization detector (GC-FID). Internal standards used for quantification were 1-nonadecanol, DAGE C<sub>16-16</sub>, and DAGE C<sub>18-18</sub>. The carrier gases were helium and hydrogen for the GC-MS and GC-FID analyses, respectively. Both devices were equipped with an Agilent HP-5MS UI fused silica column with a length of 30 m, a diameter of 0.25 mm, and a film thickness of 0.25 µm. The GC temperature program was: 50 °C (3 min); from 50 °C to 230 °C (held 2 min) at 25 °C/min; from 230 °C to 320 °C (held 20 min) at 6 °C/min. GC-amenable compounds in the Pollenzo samples were identified using an Agilent 7890 A GC system coupled to an Agilent 5975C inert MSD mass spectrometer. Quantification was done using an Agilent 7820 A GC-FID system. Both systems were equipped with an Agilent HP-5MS UI (see above for details). Internal standards were identical as mentioned above. The GC temperature program for all fractions was: 60 °C (1 min) to 150 °C at 10 °C/min, then to 320 °C (held 25 min) at 4 °C/min.

### Diphytanyl glycerol diether (DGD) and glycerol dibiphytanyl glycerol tetraether (GDGT) preparation and analysis

10% vol. of 57 total lipid extracts (TLE) from a sub-set of samples from Natalicchio et al. (2019; Pollenzo: 43 samples) and Sabino et al. (2020a; Govone: 14 samples) was used to obtain DGDs and GDGTs (Fig. AD.2) according to the method reported in Sabino et al. (2020a). Briefly, after dissolution in *n*-hexane, an internal standard (C<sub>46</sub> GDGT; 12 mg/L) was added and 10 µL for each sample were analyzed using a Varian MS Workstation 6.91 HPLC system coupled to a Varian 1200L triple quadrupole mass spectrometer. Compound separation was achieved with a Grace Prevail Cyano column (150 mm × 2.1 mm; 3 µm particle size) and a guard column, held at 30 °C. The solvent gradient program was: linear change from 97.5% A (100% *n*-hexane) and 2.5% B (90% *n*-hexane: 10% 2-propanol; v/v) to 75% A and 25% B from 0 to 35 min; then linearly to 100% B in 5 min and held for 8 min.

Thereafter, back to 97.5% A and 2.5% B to re-equilibrate the column for 12 min. Solvent flow (0.3 mL/min) was kept constant during the entire run time (60 min). A mass spectrometer equipped with an atmospheric pressure chemical ionization (APCI) interface operated in positive ion mode was used for GDGTs identification. The APCI parameters were: N<sub>2</sub> as nebulizing gas with a pressure of 60 psi; temperature fluctuating between 35 °C and 40 °C, 50 °C as API housing temperature, 200 °C for the drying gas of the API, with a pressure of 12 psi; the APCI auxiliary gas temperature was 400 °C, and its pressure was 18 psi. A standard mixture of synthetic archaeol (CAS 99341-19-2), DAGE C<sub>18:18</sub> (CAS 6076-38-6), DAGE C<sub>18:18-4ene</sub> (CAS 15818-46-9), and synthetic C<sub>46</sub> GDGT (CAS 138456-87-8) was used to evaluate the response factors (around 1.5:1 between archaeol and C<sub>46</sub> GDGT) after every four to five samples. The scanned spectral range was set at *m/z* 500 to 750 and 950 to 1500. Lipid abundances (Appendix D.3 and D.4) were determined selecting base peaks (*m/z*) of GDGTs, including ions symmetrically with ± 1.0 of target *m/z*.

#### Ether cleavage of GDGTs and DGDs

For the analyses of archaeol-derived phytane (only for Govone) and biphytanes (Fig. AD.2), isoprenoid DGDs and GDGTs (Pollenzo: 21 samples; Govone 14 samples) were subjected to ether cleavage following the procedure in Birgel et al. (2014). Briefly, polar compounds were isolated through liquid chromatography from 10% vol. of the TLE, after eluting hydrocarbons. The polar fraction was reacted for 4 h at 110 °C with hydriodic acid and acetic acid glacial, 500 mL each. Excess iodine was removed with 1 mL aqueous 5% sodium thiosulfate and the alkyl iodides were reduced to hydrocarbons with lithium aluminum hydride in 2 mL tetrahydrofuran for 3h at 110 °C under an argon atmosphere. The tetrahydrofuran was collected and water was added to completely deactivate excess lithium aluminum hydride. The samples were dried with sodium sulfate and the solvent evaporated. The same GC–MS analytical setting and temperature program described above were applied for the investigation of ether-cleaved samples. Phytane and biphytanes were identified through comparison of retention times and published mass spectral data (Schouten et al., 1998a).

#### Desulfurization of asphaltenes

Desulfurization was performed for the dichloromethane-soluble fractions (asphaltenes), according to the procedure described in Sabino et al. (2020a). Briefly, after dissolving asphaltenes in 8 mL tetrahydrofuran/methanol (1:1, *v/v*), 200 mg each of anhydrous nickel chloride and sodium borohydride were added and left react for 1 h. The samples were centrifuged, the supernatant collected, and the solid residue extracted twice with dichloromethane/methanol (1:1, *v/v*), combining the new supernatants with the initial extract. An aqueous solution was added to separate and collect the organic layer. Excess solvents were eliminated through a rotary evaporator and the residual organic phase was filtered through dry sodium sulfate to remove water. Hydrocarbons released after desulfurization were collected through column chromatography using *n*-hexane/dichloromethane (9:1, *v/v*) as eluent and silica gel as stationary phase. Hydrocarbons, dissolved in *n*-hexane, were analyzed by using the previously described GC–MS device and the following program: from 60 °C (1 min) to 150 °C at 15 °C/min and then up to 320 °C (held 40 min) at 4 °C/min. Compound identification was achieved through



comparison of retention times and published mass spectral data, with a focus on C<sub>27</sub> to C<sub>29</sub> steranes and phytane (Fig. AD.2).

#### Compound specific $\delta^{13}\text{C}$ values

Compound specific  $\delta^{13}\text{C}$  values were determined, when possible, on acyclic and cyclic biphytanes (after ether cleavage), phytane (after ether cleavage, only Govone, and after desulfurization), C<sub>20-20</sub> and C<sub>20-25</sub> archaeols (only Pollenzo), and C<sub>27</sub> to C<sub>29</sub> steranes released after desulfurization (Appendix D.5 and D.6). Measurements were conducted at the University of Hamburg (27 samples) and the University of Vienna (12 samples, in italics in Appendix D.5 and D.6).  $\delta^{13}\text{C}$  values are reported in ‰ vs. the Vienna Pee Dee Belemnite (V-PDB) standard. Measurements at the University of Hamburg were performed using an Agilent 6890 GC, equipped with an Agilent HP-5MS UI fused silica column (length of 30 m × 0.25 mm diameter; 0.25 μm film thickness) coupled via a Thermo Finnigan Combustion III to a Thermo Finnigan Delta Plus XL isotope mass spectrometer (GC-IRMS). The following temperature program was applied: from 50 °C (held 2 min) to 320 °C (held 35 min) with a rate of 12 °C/min. An externally calibrated standard mixture of 15 *n*-alkanes (C<sub>16</sub> to C<sub>30</sub>) with known isotopic composition was measured after every three to four samples to check for instrument precision. When possible, analyses were conducted at least in duplicates; analytical standard deviation for the measured compounds was ≤1.4‰. Analyses at the University of Vienna (Department of Terrestrial Ecosystem Research) were performed using a Thermo Fisher Trace GC Ultra connected via a Thermo Fisher GC Isolink interface to a Thermo Fisher Delta V Advantage mass spectrometer. The GC system was equipped with the same column described above and the carrier gas was helium. The GC temperature program was: from 60 °C (held 1 min) to 150 °C at 10 °C/min and then up to 320 °C (held 25 min) at 4 °C/min. After 5 samples, an externally calibrated standard mixture of 25 *n*-alkanes (C<sub>14</sub> to C<sub>38</sub>) with known isotopic composition was measured to check instrument precision. When possible, samples were measured at least in duplicate; analytical standard deviation was ≤2.4‰. The  $\delta^{13}\text{C}$  values of archaeol and extended archaeol were measured as their trimethyl silyl ethers and were corrected for carbons added after derivatization.

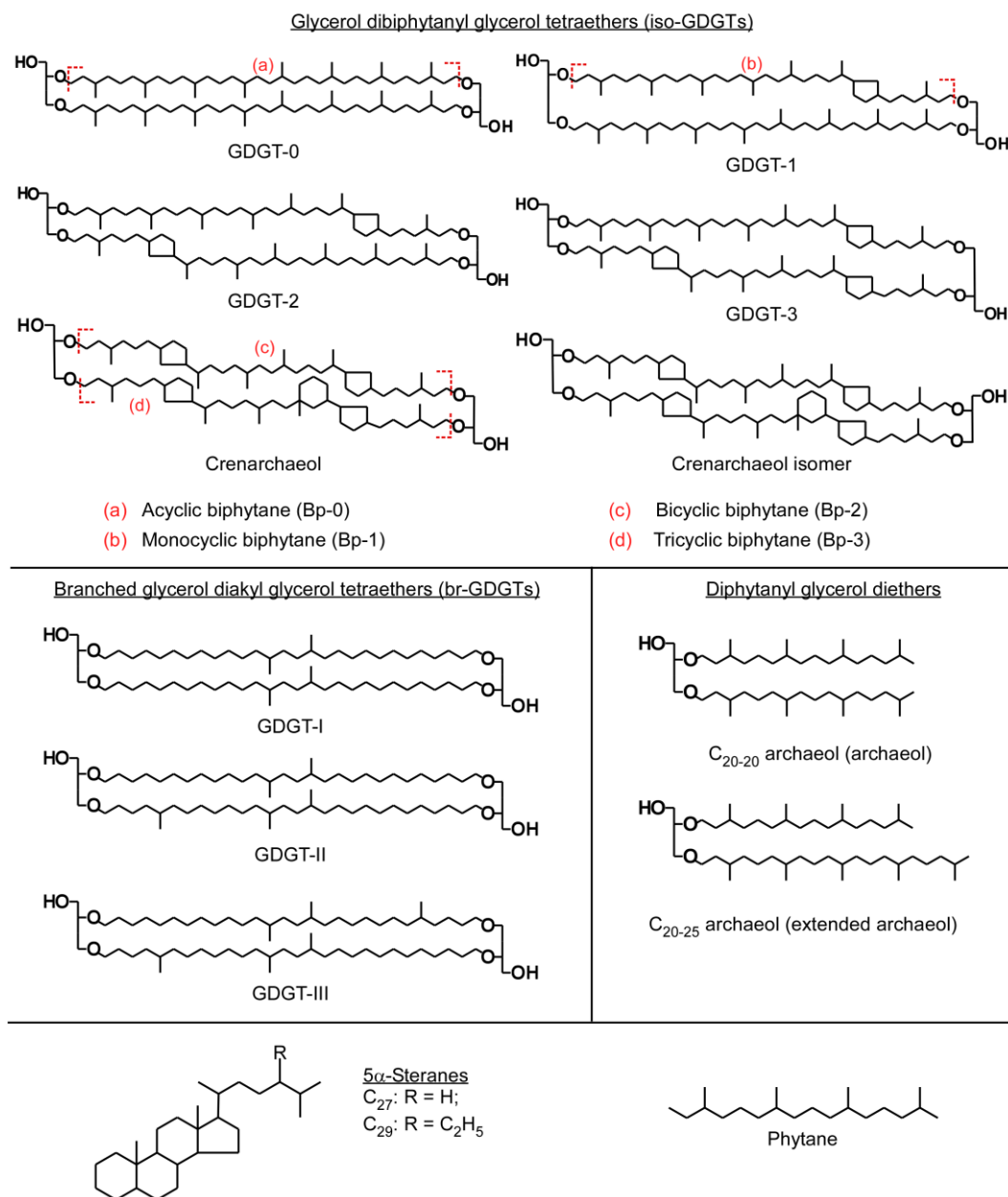


Figure AD.2 – Structure of analyzed lipid biomarkers.

**Appendix D.3**

Abundance of glycerol dibiphytanyl glycerol tetraethers (iso-GDGTs). Cren.: crenarchaeol; Cren': crenarchaeol isomer. [2]/[3]: GDGT-2/GDGT-3.

Samples	iso-GDGTs ( $\mu\text{g/g TOC}$ )				Cren.	Cren'.	[2]/[3] ratio
	[0]	[1]	[2]	[3]			
<i>Pollenzo section</i>							
Pg1.2.2	50	6	0.8	0	0.3	0	-
Pg1_2.1	4.4	4	2.8	2	6	0.7	1.4
Pg1_1.5	15.7	3.5	2.8	1.9	6.4	0.8	1.5
Pg1_1.4	9	2.4	2.2	1.3	5.2	0.8	1.7
Pg1.1.2	50.9	11.4	20.6	4.7	29	5.3	4.3
Pg1_1.1	38.9	10.4	13	2.8	21.7	3.8	4.6
Pm7_6.4	14.5	1.7	2.4	0.4	5.7	0.3	6.4
Pm7_6.2	9.1	0.2	0.2	0.1	0	0	2.5
Pm7_6.1	5.7	0.8	0.4	0.3	1	0.1	1.2
Pm7_5.1	17.1	4.4	3.3	0	9.5	1.2	-
Pm7_4.1	18	7.2	4.9	3.3	10	1.4	1.5
Pm7_3.3	21.6	4.3	8.2	4.1	21.4	4.9	2
Pm7_3.2	19	8.2	11.8	2.3	21.8	1	5.2
Pm7_3.1	25	3.9	4	1.1	8.6	0.7	3.6
Pm7_2.1	55.8	11.7	18.5	4.4	35.1	4.9	4.2
Pm7_1.2	77.3	14.7	20.6	6.2	42.2	7.8	3.3
Pm7_1.1	20.2	4.9	6.6	1.8	14.8	2.3	3.6
Pm6_8.1	34.5	6.7	5.9	2	12.9	1.6	2.9
Pm6_7.1	19.2	5.4	5.9	2.5	11.7	2	2.3
Pm6_6.1	12.7	3.2	3.6	1.4	8.2	1.2	2.6
Pm6_5.2	40.3	3.8	6.9	0.8	17.5	0.4	8.6
Pm6_5.1	11	3.4	3.7	0.8	8.6	1	4.6
pm6_4.2	44.5	15	24.3	4.3	34	7.7	5.6
Pm6_4.1	22.9	6.7	8.7	2.9	20.2	2	3
Pm6_3.1	46.4	15.6	16.9	6.2	38.1	4.2	2.7
Pm6_2.2	33.5	7.8	8.7	1.6	23.5	1.6	5.4
Pm6_2.1	26.2	6.7	4.4	1.2	25.5	0.7	3.8
Pm6_1.1	28.9	6.8	4.2	1.4	23.1	0.7	3
Pm5_3.1	87.5	17.2	12.2	4.1	66.1	2.5	3
Pm5_2.5	24.6	7	4.4	1.4	17.4	1.1	3.2
Pm5_2.4	34.4	8.8	7.9	2.5	25.6	2.4	3.1
Pm5_2.1	41.1	11.1	8.7	2.4	29.8	2.3	3.6
Pm5_1.8	38.1	12.2	11.3	3.3	31.4	3	3.4
Pm5_1.6	44.8	13.5	13.5	4.3	36.4	4.7	3.2
Pm5_1.5	23.9	8.3	8.8	2.1	22.7	2.6	4.2
Pm5_1.2	72.5	23.2	33.9	7.3	63.3	10.3	4.6
Pm5_1.1	31.6	11.2	13.9	3.9	28.6	4.7	3.6
Pm4_3.1	9.3	2.7	1.5	0.5	6.9	0.4	2.9
Pm4_2.2	17.6	4.9	3.5	1	15.3	0.7	3.5
Pm4_2.1	14.2	3.3	1	0	12.9	2.3	-
Pm4_0.3	28.1	9.4	10.8	2.3	24.7	3.7	4.7
Pm4_0.2	29.8	10.3	11.7	3	26.9	3.9	3.8
Pm4_0.1	38.8	13	17.4	4	35.6	5.5	4.4

## [Appendix D.3 – continuation]

Samples	iso-GDGTs ( $\mu\text{g/g TOC}$ )					Cren.	Cren'	[2]/[3] ratio
	[0]	[1]	[2]	[3]				
<i>Govone section</i>								
Gm33.2	16.4	4.9	5.0	0.9	12.8	1.6	5.3	
Gm33.1	16.5	4.9	6.2	1.2	16.1	1.3	5.3	
Gm32.5	5.4	1.1	1.2	0.2	5.0	0.4	6.1	
Gm32.2	17.9	4.9	3.3	0.8	12.1	1.7	4.1	
Gm32.1	19.7	5.5	5.0	1.2	16.8	2.4	4.2	
Gm31.4	20.5	7.1	8.8	1.5	21.2	2.6	5.9	
Gm31.2	22.0	6.7	7.1	1.4	16.1	2.8	5.1	
Gm31.1	18.6	6.6	7.9	2.1	19.8	2.8	3.7	
Gm30.3	8.4	2.9	3.1	0.7	8.8	1.2	4.2	
Gm30.2	8.0	2.0	2.9	0.5	7.0	0.9	5.4	
Gm30.1	22.9	8.0	6.3	1.5	17.4	1.4	4.3	
Gm29.3	5.6	1.7	2.4	0.5	5.8	0.7	4.9	
Gm29.2	17.0	6.5	6.3	2.2	16.5	2.1	2.9	
Gm29.1	16.7	7.1	7.2	2.3	17.4	2.1	3.2	

**Appendix D.4**

Abundance of C<sub>20-20</sub> (archaeol) and C<sub>20-25</sub> (extended archaeol) archaeols and branched glycerol dialkyl glycerol tetraethers (br-GDGTs). Branched and isoprenoid tetraether (BIT) index calculated according to Hopmans et al. (2004).

Samples	Archaeols ( $\mu\text{g/g TOC}$ )		br-GDGTs ( $\mu\text{g/g TOC}$ )			BIT index
	C <sub>20-20</sub>	C <sub>20-25</sub>	I	II	III	
<i>Pollenzo section</i>						
Pg1.2.2	437.1	51.9	2.6	4.4	4.2	1.0
Pg1_2.1	474.9	56.0	3.1	4.1	1.0	0.6
Pg1_1.5	152.7	25.7	1.7	2.2	1.8	0.5
Pg1_1.4	56.1	21.8	0.9	1.2	1.1	0.4
Pg1.1.2	13.1	0	6.0	6.1	4.3	0.4
Pg1_1.1	72.0	3.0	10.4	11.0	7.8	0.6
Pm7_6.4	16.5	4.1	3.2	2.3	2.8	0.6
Pm7_6.2	244.4	17.3	2.6	2.4	1.8	1.0
Pm7_6.1	103.2	7.2	1.5	1.4	1.1	0.8
Pm7_5.1	251.1	22.6	2.0	2.3	2.7	0.4
Pm7_4.1	243.9	28.3	5.4	3.7	3.0	0.5
Pm7_3.3	73.4	22.7	5.9	6.7	5.1	0.5
Pm7_3.2	48.1	8.1	6.5	7.0	50.9	0.7
Pm7_3.1	35.3	0	19.9	16.1	13.1	0.9
Pm7_2.1	46.0	0	13.1	13.6	9.8	0.5
Pm7_1.2	51.5	0	16.3	17.7	11.3	0.5
Pm7_1.1	61.0	0	7.9	9.1	6.6	0.6
Pm6_8.1	42.7	0	23.6	29.6	20.4	0.9
Pm6_7.1	259.7	45.0	8.5	10.3	8.5	0.7

*[Appendix D.4 – continuation]*

Samples	Archaeols ( $\mu\text{g/g TOC}$ )		br-GDGTs ( $\mu\text{g/g TOC}$ )			BIT index
	C <sub>20-20</sub>	C <sub>20-25</sub>	I	II	III	
<i><u>Pollenzo section</u></i>						
Pm6_6.1	228.6	53.7	5.7	4.8	4.5	0.6
Pm6_5.2	546.2	44.9	40.1	40.5	35.1	0.9
Pm6_5.1	31.7	0	4.5	4.1	3.0	0.6
pm6_4.2	32.6	0	10.5	12.2	8.3	0.5
Pm6_4.1	76.1	0	17.9	18.3	16.9	0.7
Pm6_3.1	31.0	0	19.1	20.9	17.9	0.6
Pm6_2.2	75.0	17.7	13.9	14.5	11.6	0.6
Pm6_2.1	63.2	0	10.4	11.2	10.2	0.6
Pm6_1.1	22.4	0	7.9	7.9	7.0	0.5
Pm5_3.1	30.1	0	13.2	15.3	8.9	0.4
Pm5_2.5	25.1	0	5.2	6.0	4.9	0.5
Pm5_2.4	32.1	0	15.8	19.5	15.3	0.7
Pm5_2.1	22.0	0	7.1	9.6	7.9	0.5
Pm5_1.8	22.4	0	9.2	12.4	12.3	0.5
Pm5_1.6	24.1	0	19.8	23.6	18.2	0.6
Pm5_1.5	24.9	0	17.5	19.6	15.3	0.7
Pm5_1.2	22.6	0	32.0	38.5	26.8	0.6
Pm5_1.1	29.8	0	17.2	20.7	15.0	0.6
Pm4_3.1	20.2	0	19.6	22.2	16.9	0.9
Pm4_2.2	10.0	0	7.8	10.4	8.6	0.6
Pm4_2.1	13.9	0	5.3	6.4	5.8	0.6
Pm4_0.3	30.2	0	20.0	19.4	16.2	0.7
Pm4_0.2	27.8	0	14.0	15.2	10.3	0.6
Pm4_0.1	33.5	0	41.0	53.5	36.5	0.8
<i><u>Govone section</u></i>						
Gm33.2	14.7	0	3.0	3.4	2.2	0.4
Gm33.1	20.4	0	7.7	8.7	6.0	0.6
Gm32.5	6.8	0	2.9	3.8	3.2	0.7
Gm32.2	18.3	0	4.0	5.1	3.1	0.5
Gm32.1	16.4	0	5.2	6.4	4.5	0.5
Gm31.4	11.3	0	4.9	7.5	6.6	0.5
Gm31.2	14.4	0	3.0	3.0	2.1	0.3
Gm31.1	10.5	0	2.9	3.3	1.8	0.3
Gm30.3	8.2	0	2.8	4.4	4.6	0.6
Gm30.2	8.9	0	0.1	3.0	2.5	0.4
Gm30.1	17.8	0	2.7	3.4	2.5	0.4
Gm29.3	4.1	0	1.1	1.7	1.6	0.3
Gm29.2	28.2	0	3.0	3.2	2.0	0.3
Gm29.1	20.6	0	4.0	4.5	3.2	0.4

**Appendix D.5**

Compound specific carbon ( $\delta^{13}\text{C}$ ) stable isotopes of biphytanes (Bp). SD: standard deviation. Samples measured at the University of Vienna in italics.

Samples	$\delta^{13}\text{C}$ biphytanes (‰)							
	Bp-0		Bp-1		Bp-2		Bp-3	
		SD		SD		SD		SD
<i>Pollenzo section</i>								
Pg1_2.1	-25.9	0.3	-17.4	0.0	-15.2	0.4	-15.4	0.8
Pg1_1.5	-26.1	0.4	-16.5	0.3	-14.7	0.1	-15.0	0.1
Pg1_1.1	-26.2	0.3	-22.9	0.3	-22.2	0.3	-22.4	0.3
Pm7_6.2	-30.9	0.4	-	-	-	-	-	-
<i>Pm7_6.1</i>	-27.8	<i>0.1</i>	-	-	<i>-18.3</i>	<i>0.6</i>	-	-
<i>Pm7_5.1</i>	-24.2	<i>0.4</i>	-	-	-	-	-	-
<i>Pm7_4.1</i>	-25.4	<i>0.5</i>	<i>-18.0</i>	<i>0.3</i>	<i>-16.9</i>	<i>0.4</i>	<i>-16.2</i>	<i>0.2</i>
<i>Pm6_8.1</i>	-28.7	<i>0.2</i>	<i>-23.4</i>	<i>0.3</i>	<i>-22.3</i>	<i>0.2</i>	<i>-21.4</i>	<i>0.2</i>
<i>Pm6_7.1</i>	-24.7	<i>0.2</i>	<i>-25.2</i>	<i>1.0</i>	<i>-16.1</i>	<i>1.8</i>	<i>-15.7</i>	<i>1.8</i>
<i>Pm6_6.1</i>	-24.6	-	<i>-17.1</i>	-	<i>-17.2</i>	-	<i>-17.1</i>	-
Pm6_5.1	-26.4	0.2	-23.8	0.9	-23.4	0.5	-23.3	0.3
Pm6_4.1	-26.5	0.2	-23.9	0.1	-22.4	0.2	-23.2	0.0
Pm6_2.1	-21.0	0.3	-17.1	0.2	-17.5	0.4	-17.1	0.3
<i>Pm6_1.1</i>	-21.3	-	<i>-20.3</i>	-	<i>-19.4</i>	-	<i>-18.9</i>	<i>0.0</i>
<i>Pm5_3.1</i>	-23.0	<i>0.5</i>	<i>-20.3</i>	<i>0.0</i>	<i>-21.3</i>	<i>0.1</i>	<i>-20.7</i>	<i>0.0</i>
<i>Pm5_2.5</i>	-23.1	-	<i>-20.6</i>	-	<i>-21.1</i>	-	<i>-20.5</i>	-
Pm5_1.6	-22.8	0.4	-21.4	0.3	-21.7	0.4	-21.3	0.3
<i>Pm4_3.1</i>	-21.7	<i>0.3</i>	<i>-21.5</i>	<i>0.8</i>	<i>-20.9</i>	<i>0.0</i>	<i>-20.9</i>	-
<i>Pm4_2.2</i>	-20.1	<i>0.1</i>	<i>-21.1</i>	<i>0.1</i>	<i>-18.5</i>	<i>0.1</i>	<i>-19.1</i>	<i>0.0</i>
<i>Pm4_2.1</i>	-21.1	<i>0.1</i>	<i>-20.3</i>	<i>0.0</i>	<i>-20.0</i>	<i>0.1</i>	<i>-20.0</i>	<i>0.1</i>
Pm4_0.3	-25.4	0.0	-23.8	0.1	-22.8	0.1	-22.8	0.1
<i>Govone section</i>								
Gm33.2	-24.1	0.4	-21.6	0.6	-21.4	0.4	-21.5	0.5
Gm33.1	-23.2	0.3	-22.1	0.2	-20.9	0.8	-20.4	0.3
Gm32.5	-23.7	0.5	-22.6	0.4	-21.3	0.4	-21.2	0.1
Gm32.2	-22.8	0.4	-22.1	0.5	-22.1	0.5	-21.3	0.1
Gm32.1	-22.0	0.4	-20.9	0.4	-20.7	0.2	-20.6	0.2
Gm31.4	-22.8	0.5	-22.3	0.1	-22.7	0.5	-22.6	0.4
Gm31.2	-24.1	0.2	-22.9	0.4	-22.3	0.4	-22.6	0.6
Gm31.1	-23.9	0.4	-21.5	0.7	-22.7	0.3	-21.6	0.7
Gm30.3	-23.6	0.2	-22.6	0.4	-21.5	0.1	-21.4	0.1
Gm30.2	-24.8	0.2	-22.3	0.2	-23.2	0.6	-22.5	0.6
Gm30.1	-26.4	0.4	-25.3	0.4	-25.9	0.2	-26.0	0.3
Gm29.3	-24.2	0.1	-23.1	0.4	-24.2	0.3	-23.3	0.4
Gm29.2	-23.5	0.3	-23.7	0.6	-22.5	0.4	-22.4	0.5
Gm29.1	-22.6	0.1	-22.5	0.5	-21.4	0.5	-22.1	0.7

**Appendix D.6**

Compound specific carbon ( $\delta^{13}\text{C}$ ) stable isotope values. \*: lipids after desulfurization; l.c.: too low contents for  $\delta^{13}\text{C}$  measurements; Ph: phytane; SD: standard deviation.

Samples	$\delta^{13}\text{C}$ archaeols (‰)		$\delta^{13}\text{C}$ phytane*		$\delta^{13}\text{C}$ 5 $\alpha$ -C <sub>27</sub>	$\delta^{13}\text{C}$ 5 $\alpha$ -C <sub>29</sub>	
	C <sub>20-20</sub>	C <sub>20-25</sub>	(‰)	(‰)	sterane* (‰)	sterane* (‰)	(‰)
	SD	SD	SD	SD	SD	SD	SD
<i>Pollenzo section</i>							
Pg1_2.2	-19.4	0.4	-	-	-	-	-
Pg1_1.5	-18.0	0.4	-	-	-26.0	0.0	-23.9
Pg1_1.4	-24.0	0.1	-	-	-	-	-
Pg1.1.2	-31.0	0.4	-	-	-	-	-
Pg1_1.1	-26.1	0.7	-	-	-	-	-
Pm7_6.1	-20.1	0.3	-21.1	0.3	-	-	-
Pm7_5.1	-19.4	0.0	-	-	-	-	-
Pm7_4.1	-20.0	0.4	-22.2	0.3	-24.4	0.4	-24.3
Pm6_8.1	-22.1	0.4	-	-	-	-	-
Pm6_7.1	-19.3	0.3	-18.4	0.2	-24.8	0.0	-23.5
Pm6_6.1	-18.4	0.3	-17.1	0.1	-	-	-
Pm6_5.1	-	-	-	-	-27.4	0.1	-25.7
Pm6_4.1	-26.8	0.2	-	-	-	-	-
Pm6_1.1	-25.4	0.4	-	-	-	-	-
Pm5_3.1	-23.4	0.2	-	-	-	-	-
Pm4_3.1	-27.2	2.4	-	-	-	-	-
Pm4_2.2	-23.2	0.1	-	-	-	-	-
Pm4_2.1	-26.7	0.2	-	-	-	-	-
Pm4_0.3	-27.9	0.0	-	-	-	-	-
Samples	$\delta^{13}\text{C}$ ether-cleaved Ph		$\delta^{13}\text{C}$ phytane*		$\delta^{13}\text{C}$ 5 $\alpha$ -C <sub>27</sub>	$\delta^{13}\text{C}$ 5 $\alpha$ -C <sub>29</sub>	
	(‰)	(‰)	(‰)	(‰)	sterane* (‰)	sterane* (‰)	(‰)
	SD	SD	SD	SD	SD	SD	SD
<i>Govone section</i>							
Gm33.2	-29.6	0.5	-29.1	0.3	-28.2	1.0	-29.2
Gm33.1	-28.8	0.6	l.c.	l.c.	l.c.	l.c.	l.c.
Gm32.5	-28.8	0.8	l.c.	l.c.	l.c.	l.c.	l.c.
Gm32.2	-27.6	0.3	-29.4	0.8	-24.8	0.5	-27.4
Gm32.1	-28.1	0.4	-30.3	0.6	-26.5	0.7	-28.1
Gm31.4	-27.1	0.5	l.c.	l.c.	l.c.	l.c.	l.c.
Gm31.2	-28.6	0.3	-29.7	0.9	-27.2	0.7	-28.0
Gm31.1	-29.8	0.4	-31.6	-	-25.0	1.0	-28.6
Gm30.3	-29.5	0.0	l.c.	l.c.	l.c.	l.c.	l.c.
Gm30.2	-26.8	0.2	l.c.	l.c.	l.c.	l.c.	l.c.
Gm30.1	-28.0	0.2	l.c.	l.c.	l.c.	l.c.	l.c.
Gm29.3	-28.1	0.6	l.c.	l.c.	l.c.	l.c.	l.c.
Gm29.2	-29.8	0.2	-31.0	-	-26.7	0.3	-29.1
Gm29.1	-28.4	0.3	-29.6	0.1	-31.2	0.5	-31.1

## Appendix D.7

### Lipid input from soil archaea: acyclic, monocyclic, and bicyclic biphytanes

The  $\delta^{13}\text{C}$  values of biphytanes (Bps) reported in Appendix D.5 reveal that Bp-2 exhibits the values most similar to values of Bp-3 ( $\Delta_{\text{Bp-2-Bp-3}} \leq 1.1\text{‰}$ ). Therefore, Bp-2 has probably the same source as Bp-3 – crenarchaeol of marine group I (MGI) Thaumarchaeota – and the bias by input from soil Thaumarchaeota on  $\delta^{13}\text{C}_{\text{Bp-2}}$  values is also negligible. This is confirmed by the positive correlation between the lowest BIT values and the lowest  $\delta^{13}\text{C}_{\text{Bp-2}}$  values (pre-MS:  $r = 0.5$ ,  $r^2 = 0.3$ ; MS:  $r = 0.3$ ,  $r^2 = 0.1$ ; Fig. AD.7A), which is opposite to the correlation expected in case of a major contribution from soil Thaumarchaeota. Conversely,  $\delta^{13}\text{C}_{\text{Bp-1}}$  and particularly  $\delta^{13}\text{C}_{\text{Bp-0}}$  values differ from  $\delta^{13}\text{C}_{\text{Bp-3}}$  values (Appendix D.5), with the strongest deviations observed in the more proximal part of the basin, where  $\Delta_{\text{Bps}}$  up to 9.5‰ for Bp-1 and 11.1‰ for Bp-0 were determined. Furthermore, the BIT index indicates overall stronger terrestrial input in the MS interval, particularly in more proximal settings of the Piedmont Basin (Appendix D.4), and shows a very weak negative correlation with  $\delta^{13}\text{C}_{\text{Bp-1}}$  values ( $r = -0.2$ ,  $r^2 = 0.0$ ; Fig. AD.7B) and a moderate negative correlation with  $\delta^{13}\text{C}_{\text{Bp-0}}$  values ( $r = -0.7$ ,  $r^2 = 0.5$ ; Fig. AD.7C). Altogether, the data point to contributions from additional soil-derived sources, especially for Bp-0 and for the more proximal areas; the low  $\delta^{13}\text{C}_{\text{Bp-0}}$  values are the cause of the observed negative correlations. Interestingly, methanogenic Euryarchaeota commonly thrive in soils, but are typically less abundant than the dominant group I soil Thaumarchaeota (Bates et al., 2011). Methanogenic Euryarchaeota synthesize mostly GDGT-0 and few GDGT-1, yielding acyclic and monocyclic biphytanes with  $\delta^{13}\text{C}$  values ranging between  $-36\text{‰}$  and  $-26\text{‰}$  in modern soils (Fig. AD.7B, C; Oppermann et al., 2010; Pancost et al., 2000; Pancost and Sinninghe Damsté, 2003; Weijers et al., 2010). Hence, the negative correlations possibly suggest a bias from soil methanogenic Euryarchaeota particularly after the MS onset. However, a marked contribution exclusively from soil methanogenic Euryarchaeota seems unlikely considering the negligible contribution of group I soil Thaumarchaeota. According to the archaeal community reconstructed for the Piedmont Basin at the MS onset (Natalicchio et al., 2017; Sabino et al., 2020a), the more negative  $\delta^{13}\text{C}$  values of Bp-1 and Bp-0 are probably related to contributions from sediment-dwelling methanogenic Euryarchaeota, Thermoplasmatales, or heterotrophic planktonic marine Euryarchaeota; the latter for Bp-0 only (Besseling et al., 2020; Zeng et al., 2019).



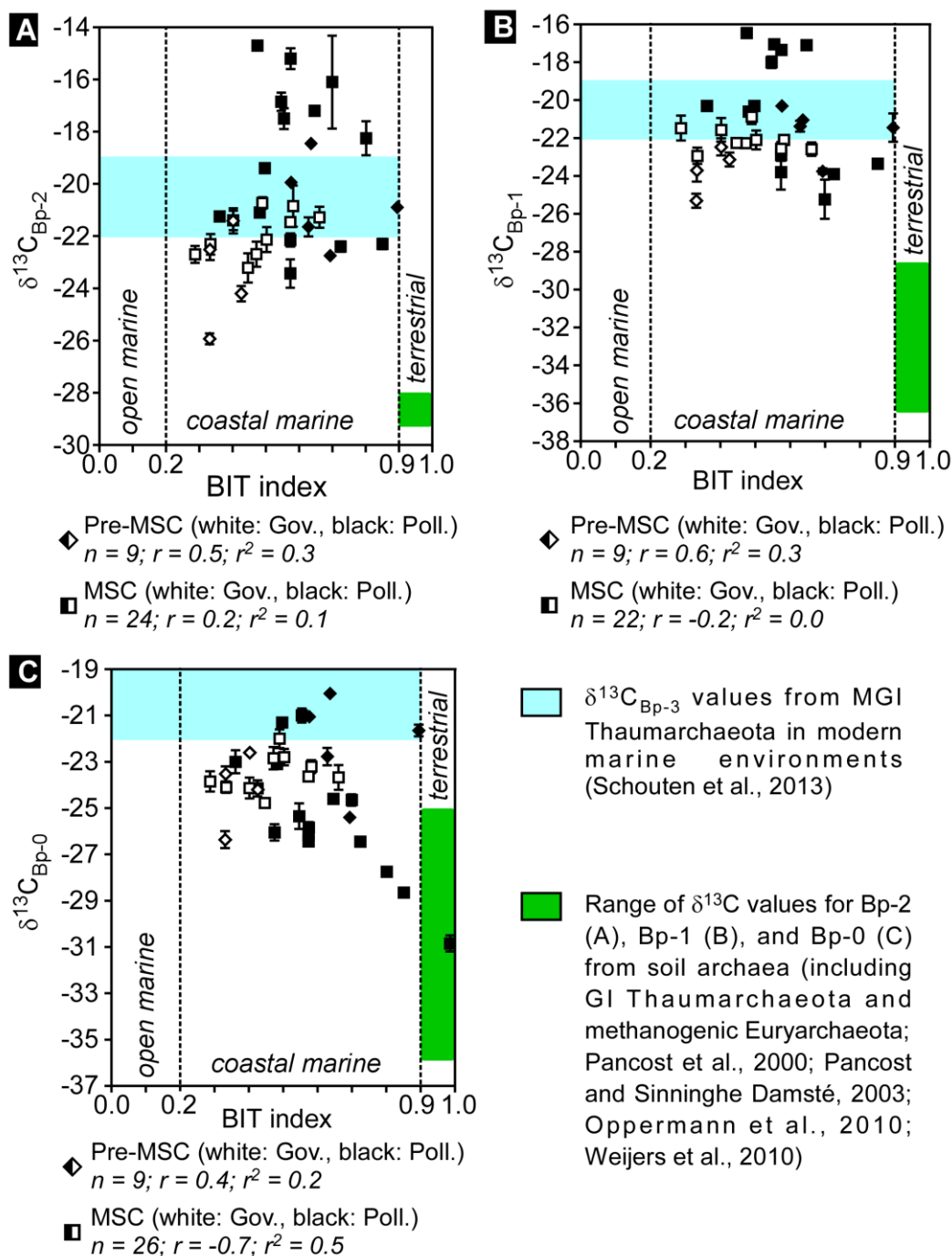


Figure AD.7 – Branched and isoprenoid tetraether (BIT) index *vs.* the carbon stable isotope compositions ( $\delta^{13}\text{C}$ ) of bicyclic (Bp-2, A), monocyclic (Bp-1, B), and acyclic (Bp-0, C) biphytanes. GI: group I; Gov.: Govone; MGI: marine group I; MSC: Messinian salinity crisis; Poll.: Pollenzo.

#### Dominant sources for steranes and phytane released after desulfurization

Regular ( $5\alpha$ )  $\text{C}_{27}$  and  $\text{C}_{29}$  steranes and phytane were released after desulfurization of asphaltenes from proximal (Pollenzo) and distal (Govone) parts of the Piedmont Basin. Despite a relatively wide variability, the  $\delta^{13}\text{C}$  values of the released steranes and phytane show overall  $^{13}\text{C}$  enrichment toward younger samples and the highest values were recorded at the same stratigraphic level as observed for the lipids of

MGI Thaumarchaeota from the more proximal parts of the Piedmont Basin (Appendix D.5 and D.6). The common patterns suggest that the dominant source organisms of steranes and phytane were occupying the same environment as the MGI Thaumarchaeota community recording  $^{13}\text{C}$  enrichment (cf. Schouten et al., 1998b), i.e. the upper water column (< 200 m). Here, photosynthetic primary producers are the main source for steranes and phytane (e.g., Knoll et al., 2007; Volkman, 2003), whose respective  $\delta^{13}\text{C}$  values can differ by as much as  $\pm 4\text{-}5\%$ , even when produced by the same organism (Schouten et al., 1998b). The difference between the  $\delta^{13}\text{C}$  signature of steranes and phytane in most cases fall in this range and their  $\delta^{13}\text{C}$  values co-vary, supporting a common source represented by algae dwelling in the upper water column. Occasionally phytane exceeds the range expected for such a common source, suggesting additional contributions. Interestingly, phytol, the precursor of phytane, is also synthesized by terrestrial plants, typically showing low  $\delta^{13}\text{C}$  values in the case of  $\text{C}_3$  vegetation ( $\delta^{13}\text{C}$  between  $-34\%$  and  $-30\%$ ; Collister et al., 1994). Hence, the  $^{13}\text{C}$  depletion observed for phytane could be due to an additional contribution from  $\text{C}_3$  plants, whose input was high at that time in the Piedmont Basin (Natalicchio et al., 2019; Sabino et al., 2020b). To sum up, planktonic eukaryotes were the dominant source of phytane and  $\text{C}_{27}$  and  $\text{C}_{29}$  steranes released from desulfurization, whose carbon stable isotope signatures reflect the  $\delta^{13}\text{C}$  variability of the inorganic carbon pool reconstructed from thaumarchaeal lipids.



## ACKNOWLEDGMENTS

---

The completion of this project and the writing of this dissertation was possible thanks to the valuable support of many people who accompanied me through this exciting journey. I would like to acknowledge the Landesgraduiertenförderung of the state of Hamburg and the merit scholarship program from the University of Hamburg, which provided the doctoral scholarships. The thesis is further based upon work from COST Action ‘Uncovering the Mediterranean salt giant’ (MEDSALT) supported by COST (European Cooperation in Science and Technology).

For a start, I would like to thank my supervisors, Prof. Dr Jörn Peckmann and Prof. Dr. Francesco Dela Pierre. Jörn, thank you very much for welcoming in your research group, being always supportive with all my ideas, and helping me in growing in my career as a scientist. Francesco, we know each other’s since long. Thanks for always believing in me as a scientist, for your endless patience, and for always pushing and supporting me in overcoming the many challenges I faced in the past years.

Special thanks to Dr. Daniel Birgel and Dr. Marcello Natalicchio. You were always there, not just as colleagues. It was a pleasure to share these four years with you and find some invaluable time to relax and laugh together, as that unforgettable day, telling you about the eggs (or better the omelette!) I received. Your guidance through this project was precious to me. Sabine Beckmann, your tireless technical support was instrumental for the successful outcome of the analyses related to the project, thank you. I would also like to express my gratitude to the many people I collaborated with during my doctoral project. Sorry for not mentioning you all explicitly in this acknowledgment.

In this exciting journey I had several mates, sharing with me joys and sorrows. You are the dearest to me, Lydia Baumann and Alexmar Cordova-Gonzales. We started somehow together and shared plenty of unforgettable moments at work, but also outside. Not enough words could express my gratitude for choosing to be not just colleagues, but friends. Thank you! Nicola Krake, Simon Rouwendaal, although we met halfway, your cheerfulness undoubtedly enriched this experience. Thanks for sharing meals and coffee breaks together in the last very tough year! Thanks as well to my other colleagues and friends, Dorothea Bunzel, Fabio Francescangeli, Paul Göllner, Felix Schulte, and Claudio Sambito.

Last, but not least, thanks from the bottom of my heart to my family and friends in Italy. You were never too far away and always made me feel your unconditioned support, even in the darkest hours. It was always a joy to be back and realize that it still was as I had just left. To conclude, thanks to the Italian Sun! You never stop shining when I was back.



## VERSICHERUNG AN EIDES STATT – AFFIRMATION ON OATH

---

Hiermit versichere ich an Eides statt, dass ich die vorliegende Dissertation mit dem Titel: „Climate forcing on water column and sedimentary environments of an ancient semi-enclosed basin: insights from the late Miocene (Messinian) Mediterranean Basin“ selbstständig verfasst und keine anderen als die angegebenen Hilfsmittel – insbesondere keine im Quellenverzeichnis nicht benannten Internet-Quellen – benutzt habe. Alle Stellen, die wörtlich oder sinngemäß aus Veröffentlichungen entnommen wurden, sind als solche kenntlich gemacht. Ich versichere weiterhin, dass ich die Dissertation oder Teile davon vorher weder im In- noch im Ausland in einem anderen Prüfungsverfahren eingereicht habe und die eingereichte schriftliche Fassung der auf dem elektronischen Speichermedium entspricht.

I hereby declare an oath that I have written the present dissertation on my own with the title: "Climate forcing on water column and sedimentary environments of an ancient semi-enclosed basin: insights from the late Miocene (Messinian) Mediterranean Basin" and have not used other than the acknowledge resources and aids. All passages taken literally or analogously from other publications are identified as such. I further declare that this thesis has not been submitted to any other German or foreign examination board and that the submitted written version corresponds to that on the electronic repository.

Hamburg, den 08.02.2021

  
*Mathia Sabino*



